Springer Proceedings in Physics 149

Alessandro Talamelli
Martin Oberlack
Joachim Peinke *Editors*

Progress in Turbulence V

Proceedings of the iTi Conference in Turbulence 2012

Springer

Springer Proceedings in Physics

Volume 149

For further volumes:
http://www.springer.com/series/361

Alessandro Talamelli · Martin Oberlack
Joachim Peinke
Editors

Progress in Turbulence V

Proceedings of the iTi Conference in Turbulence 2012

Springer

Editors
Alessandro Talamelli
Department of Industrial Eng. (DIN)
Università di Bologna
Forlì
Italy

Joachim Peinke
Institute of Physics
University of Oldenburg
Oldenburg
Germany

Martin Oberlack
Department of Mechanical Engineering
TU Darmstadt
Darmstadt
Germany

ISSN 0930-8989 ISSN 1867-4941 (electronic)
ISBN 978-3-319-01859-1 ISBN 978-3-319-01860-7 (eBook)
DOI 10.1007/978-3-319-01860-7
Springer Cham Heidelberg New York Dordrecht London

Library of Congress Control Number: 2013946664

Printed on acid-free paper

Springer is part of Springer Science+Business Media (www.springer.com)

Dedication

In memory of Rudolf Friedrich - University of Münster

On 16th of August 2012 just a few weeks before our 5th iTi Conference Rudolf Friedrich, 55, unexpectedly passed away.

He was a very good friend with whom one could spend nice evenings taking about all the world and his brother, as well as, about profound scientific problems like turbulence. We lost a colleague with whom we loved to cooperate, an excellent researcher who looked forward to find some time to work on the problem of turbulence. Turbulence as a cooperative systems of coupled subsystems was a main challenge for him. As he stated: "Turbulence remains a highly interesting and modern problem, which has been the origin of many actual scientific ideas without being solved". For him

the comprehension of the pressure term was a, if not the, central challenging issue. The large range of interdisciplinary applications inspired him in many ways.

He succeeded to pass his enthusiasm to his students and his colleagues and thus initiated many new ideas. As a deep thinking theoretician he was highly interested in applications and experimental work. He liked very much the interdisciplinary aspect of science, which also characterized his work, which ranged from neural science, over mechanical machining of materials, to mathematical problems like the fractional substantial derivative. A main focus of his work was devoted to the turbulence problem, where he found beside other results the spiral turbulence and the stochastic description by means of a Fokker-Planck equation.

With him we lost a charming friend, a committed colleague, an excellent scientist and a founding member of the interdisciplinary turbulence initiative.

Alessandro, Martin and Joachim
Forlì, Darmstadt, Oldenburg, 11thJuly 2013

Preface

This volume collects the latest contributions presented in the 5^{th} iTi Conference in Bertinoro, continuing a tradition that has been started in Bad Zwischenahn/Germany with the first edition of the conference in 2003. Since 2008 the conference has been held in the beautiful town of Bertinoro/Italy favoring the interactions between participants mostly coming from the engineering and physicist communities.

About 65 scientists coming from 12 countries have presented their latest contribution covering several fundamental aspects in turbulent flows. The contributions have been submitted to external peer reviewers and in the end 38 (together with 2 invited papers) have been collected in this fifth issue on Progress in Turbulence.

It must be stated that since Progress in Turbulence IV online publication on Apr 25, 2012, there has been a total of 1472 chapter downloads from this book on SpringerLink, the online platform, which means that the book is one of the top 25% most downloaded eBooks in the Springer eBook Collection in 2012.

The present volume is dedicated to the memory of Prof. Rudolf Friedrich who prematurely died in Münster/Germany on the 16^{th} of August 2012. In his honor the conference has started with a special session dedicated to his work. The volume contains one paper describing his main contributions.

As Wind Energy has been a focal topic during the iTi Conference in 2010, this 5^{th} iTi Conference started with a one-day workshop on symmetries and conservation laws as it experiences an increasing interest in recent turbulence research activities.

In the spirit of the iTi initiative, the volume is produced after the conference so that the authors have the possibility to incorporate comments and discussions raised during the meeting.

Turbulence presents a large number of aspects and problems, which are still unsolved and which challenge research communities in engineering and physical sciences both in basic and applied research. The book presents recent advances in theory related to new statistical approaches, effect of non-linearities and presence of symmetries. This edition presents new contributions related to the physics and control of laminar-turbulent transition in wall-bounded flows, which may have a significant impact on drag reduction applications. Turbulent boundary layers, at increasing Reynolds number, are the main subject of both computational and experimental long

research programs aimed at improving our knowledge on scaling, energy distribution at different scales, structure eduction, roughness effects to name only a few.

Like previous editions several numerical and experimental analysis of complex flows, mostly related to applications, are presented.

Based on the successful previous conferences, we intend to continue with this initiative for subsequent years with the 6^{th} iTi Conference planned for September 2014.

The structure of the present book is as such that contributions have been bundled according to covering topics i.e. I Theory, II Stability, III Wall bounded flows, IV, Complex flows, V Acoustic, VI Numerical methods.

Finally, we would like to thank all authors for their contributions to this volume and the reviewers whose comments have significantly contributed to the overall scientific quality of the proceedings. We would like to thank Thomas Ditzinger from Springer for his patience during the production of the book. Finally we gratefully acknowledge the staff from CEUB and University of Bologna for helping us to carry out this conference.

Alessandro Talamelli
Martin Oberlack
Joachim Peinke
(Forlì, Darmstadt, Oldenburg, 2013)

Contents

Topic II: Stability

Topic III: Wall Bounded Flows

Topic V: Acoustic

Topic VI: Numerical Methods

Statistical Description of Turbulent Flows
A Short Review in Memory of Rudolf Friedrich

Oliver Kamps and Michael Wilczek

Abstract. In this article we review two different approaches to the statistical description of turbulent flows in terms of evolution equations for probability density functions (PDFs), namely a description of the turbulent cascade by a Fokker-Planck equation, as well as kinetic equations in terms of the theoretical framework of the Lundgren-Monin-Novikov hierarchy. In both cases conditional averages are the building blocks that allow to make a connection to experimental or numerical data. Professor Dr. Rudolf Friedrich made central contributions to both of these approaches, which we want to highlight here.

1 Introduction

The spatio-temporal complexity of turbulence necessitates a statistical description of the flow field in terms of statistical quantities like averages or PDFs. In this article we review two different approaches to the description of turbulence based on PDFs. Both approaches aim at deriving evolution equations for the PDF describing the observable of interest. The first one, referred to as *Fokker-Planck approach*, is motivated by the theory of stochastic processes and was introduced by Friedrich and Peinke [1]. Here, the central idea is to understand the velocity increment statistics as a stochastic process in scale, whose properties can be estimated from experimental data. In more detail, the Fokker-Planck approach starts with the N-point PDF f_N containing the full information on the physical problem. If we interpret this N-point PDF as a PDF describing the probability of a realization of N steps of a stochastic process, we could ask whether this process obeys the Markov property. This would mean that one can split up the N-point PDF into a product of two-point transition PDFs which would be a tremendous reduction of the complexity of the problem.

Oliver Kamps
Center for Nonlinear Science, University of Münster, 48149 Münster
e-mail: okamp@uni-muenster.de

Michael Wilczek
Institute for Theoretical Physics, University of Münster, 48149 Münster
e-mail: mwilczek@uni-muenster.de

A. Talamelli et al. (eds.), *Progress in Turbulence V*,
Springer Proceedings in Physics 149,
DOI: 10.1007/978-3-319-01860-7_1,

The crucial question in this context is under which conditions this assumption is fulfilled, e.g., how large the distance between two steps has to be taken to observe a Markov process. If the transition PDF is additionally close to Gaussian, its time evolution can be described by a Fokker-Planck equation. If this is possible, we arrive at a closed evolution equation from which the whole N-point PDF can be computed.

The second approach is inspired by the *Bogoliubov-Born-Green-Kirkwood-Yvon (BBGKY) hierarchy* of statistical mechanics [2] and was introduced into turbulence research by Lundgren [3], Monin [4] and Novikov [5]. Therefore we refer to this approach as the *Lundgren-Monin-Novikov (LMN) hierarchy*. The main feature of this approach is that the evolution of the PDF can be related to averages involving the Navier-Stokes dynamics, for example by considering the temporal evolution of a so-called fine-grained PDF. Averaging these fine-grained evolution equations then leads to the usual closure problem of turbulence, which either can be expressed in terms of a coupling to higher-order multi-point PDFs or in terms of unclosed conditional averages. Especially the latter are accessible to DNS investigations and their investigation has led to interesting insights on the connection of turbulence dynamics and statistics. Combining these two approaches was one of the goals of Rudolf Friedrich's recent research, but now remains an open problem for future work.

2 The Fokker-Planck Approach

Starting with a paper by Friedrich and Peinke [1] the Fokker-Planck approach was mainly pursued to describe the velocity increment statistics in scale. The characterization of the complexity of a turbulent flow in terms of velocity increments is intimately related to the idea of a cascade and the transport of energy between scales. We define the longitudinal velocity increment as

$$U(\mathbf{r},\mathbf{x},t) = [\mathbf{v}(\mathbf{x}+\mathbf{r},t) - \mathbf{v}(\mathbf{x},t)] \cdot \frac{\mathbf{r}}{r}, \tag{1}$$

In case of a stationary, homogeneous and isotropic flow the one-point PDF can now be written as

$$f(u;r) = \langle \delta(u - U(\mathbf{r},\mathbf{x},t)) \rangle \tag{2}$$

e.g., the increment statistics depends only on the absolute value r of the distance vector $\mathbf{r}$. Here the average is taken with respect to time and space. Our goal is to describe the increment statistics on different length scales r_N, with $r_{i+1} > r_i$ and $\Delta r = r_{i+1} - r_i$ where the increments have the same starting point $\mathbf{x}$. A full description of the statistics is encoded in the N-point PDF

$$f(u_{r_N}, u_{r_{N-1}}, \ldots, u_{r_1}) = p(u_{r_N} | u_{r_{N-1}}, \ldots, u_{r_1}) f(u_{r_{N-1}}, \ldots, u_{r_1}). \tag{3}$$

Here we used the shorthand notation u_{r_i} to denote the dependence on the parameter r_i. Since the N-point PDF is a rather complex object the question for a possible simplification of (3) arises quite naturally. One could ask under which conditions does the relation

$$p(u_{r_N}|u_{r_{N-1}},\dots,u_{r_1}) = p(u_{r_N}|u_{r_{N-1}}) \tag{4}$$

hold so that the N-point statistics can be described as a Markov process

$$f(u_{r_N},u_{r_{N-1}},\dots,u_{r_1}) = p(u_{r_N}|u_{r_{N-1}})p(u_{r_{N-1}}|u_{r_{N-2}})\dots p(u_{r_2}|u_{r_1})f(u_{r_1}) \tag{5}$$

in scale. In a practical application, instead of (4) the relation $p(u_{r_i}|u_{r_{i-1}},u_{r_{i-2}}) = p(u_{r_i}|u_{r_{i-1}})$ or the Chapman-Kolmogorov equation can be checked numerically. The equality of the PDFs can be tested by hypothesis tests like the Wilcox test or methods that calculate the distance between both PDFs like the Kullback-Leibler measure. For details we refer the reader to [1, 6, 7].

2.1 The Markov-Einstein Length

Based on experimental data from hot wire measurements of free jet turbulence it was possible to show that for length scales $\Delta r \geq l_{ME}$ the Markov property is fulfilled [1]. Further investigations [6] indicate that this scale is proportional to the Taylor microscale l_λ which was confirmed in an extensive study of experimental data from various experiments [8]. This leads to the insight that the complete information about the increment statistics for scales larger than l_λ and therefore in the whole inertial range is encoded in two-point transition PDFs.

The occurrence of a finite length scale reflects the fact that for many physical systems a description in terms of stochastic processes or more specific as Markov processes is only valid for time and length scales above typical microscopic time and length scales of the problem. This was already realized by Einstein [9] when he developed a quantitative description of Brownian motion. He explicitly stated that the stochastic description is only valid for scales above the mean free path length. For this reason the length scale l_{ME} is termed Markov-Einstein coherence length [8].

2.2 The Fokker-Planck Equation

Given the fact that the two-point transition PDFs are sufficient to reproduce the N-point statistics we now seek for a dynamical equation for these transition probabilities. From the theory of stochastic processes we know that such a dynamical description is given by the Kramers-Moyal expansion [10] with an infinite number of coefficients D^n. For Gaussian transition PDFs or equivalently in case of vanishing D^4 the expansion reduces to the Fokker-Planck equation

$$\frac{\partial}{\partial r_i}p(u_{r_i}|u_{r_{i-1}}) = \left[-\frac{\partial}{\partial u_{r_i}}D^1(u_{r_i}) + \frac{\partial^2}{\partial u_{r_i}^2}D^2(u_{r_i})\right]p(u_{r_i}|u_{r_{i-1}}) \tag{6}$$

with drift-coefficient D^1 and the diffusion-coefficient D^2 which can be estimated from data [1, 6]. It was shown that D^1 and D^2 are sufficient to reproduce the increment PDFs in the whole inertial range. The general structure of the coefficients can be approximated by polynomials of the form

$$D^1(u,r) = a_1(r)u \tag{7}$$
$$D^2(u,r) = b_1(r) + b_2(r)u + b_3(r)u^2 \tag{8}$$

showing the r-dependence of the process. A detailed discussion of the dependence of this approximation on the Reynolds number can be found in [11]. Due to the fact that we have a finite Markov-Einstein length, some subtleties are involved in the estimation procedure. Nevertheless, given both coefficients it is not only possible to reproduce the increment statistics but also to determine all transition probabilities and the whole N-point PDF.

2.3 Further Investigations

Beside homogeneous, isotropic turbulence the Fokker-Planck approach was also applied to other types of turbulent flows. For example, it could be shown that the transition to turbulence in the wake behind a cylinder is characterized by a transition in the functional structure of the drift coefficient [12]. For fractal grid generated turbulence it could be shown that in contrast to classical fully developed turbulence the drift- and diffusion coefficients are independent of R_λ [13]. Also solar wind turbulence [14] and passive scalar turbulence [15] exhibit the Markov property on small scales.

It is worth mentioning that the spin-off of the investigations started by [1] was the development of a systematic approach to the estimation of Fokker-Planck and Langevin equations from data which has been successfully applied to various scientific fields ranging from medicine to finance [7]. This is a further example of the stimulating character of basic turbulence research for other scientific fields.

3 The LMN Hierarchy

One of the main strengths of the Fokker-Planck approach is that it is data-driven, i.e. in a sense it can be regarded as a closure scheme based on experimental observations. One would also like, however, to connect to the basic dynamical equation, the Navier-Stokes equation, to obtain a statistical framework based on first principles.

This is the route followed by studying PDF equations in terms of the LMN hierarchy. As mentioned above, this framework is based on works by Lundgren [3], Monin [4] and Novikov [5], which appeared in the late 1960's. Back then, the equations of the hierarchy only were accessible to analytical closure schemes, but later on also could be combined with data obtained by direct numerical simulations, as has been demonstrated by Novikov and co-workers in their study of vorticity statistics from three-dimensional turbulence [16, 17]. This idea was picked up in the group of Rudolf Friedrich and has been followed on in recent years with application to the statistics of vorticity in two- and three-dimensional turbulence [18, 19], velocity [20, 21], and temperature in Rayleigh-Bénard convection [22]. These works have been summarized recently in [23], to which we refer the interested reader. Here, we

will focus on a presentation of the main ideas and a number of general features of this approach. We also refer to the textbook by Pope [24] for further reading.

3.1 Basic Concepts

While for the Fokker-Planck equation the starting point was the experimental observation of velocity fluctuations, we now start our discussion with the Navier-Stokes equation

$$\frac{\partial}{\partial t}\mathbf{u}(\mathbf{x},t)+\mathbf{u}(\mathbf{x},t)\cdot\nabla\mathbf{u}(\mathbf{x},t)=-\nabla p(\mathbf{x},t)+\nu\Delta\mathbf{u}(\mathbf{x},t)+\mathbf{F}(\mathbf{x},t)\,. \tag{9}$$

For a statistical description we introduce the fine-grained one-point PDF

$$\hat{f}_1(\mathbf{v}_1;\mathbf{x}_1,t)=\delta(\mathbf{u}(\mathbf{x}_1,t)-\mathbf{v}_1)\,, \tag{10}$$

which can be used to obtain the full one-point PDF by an ensemble average:

$$f_1(\mathbf{v}_1;\mathbf{x}_1,t)=\langle\hat{f}_1(\mathbf{v}_1;\mathbf{x}_1,t)\rangle \tag{11}$$

The N-point PDF is now obtained as a straightforward generalization by averaging the product of one-point fine-grained PDFs

$$f_1(\mathbf{v}_1,\ldots,\mathbf{v}_n;\mathbf{x}_1,\ldots,\mathbf{x}_n,t)=\left\langle\prod_{i=1}^{N}\delta(\mathbf{u}(\mathbf{x}_i,t)-\mathbf{v}_i)\right\rangle\,. \tag{12}$$

Following [3] one can derive an evolution equation for the fine-grained PDF. Subsequent averaging leads to an equation for the full PDF of the form

$$\begin{aligned}\frac{\partial}{\partial t}f_1(\mathbf{v}_1;\mathbf{x}_1,t)+\mathbf{v}_1\cdot\nabla_{\mathbf{x}_1}f_1(\mathbf{v}_1;\mathbf{x}_1,t)=\\ -\nabla_{\mathbf{v}_1}\cdot\left\langle(-\nabla_{\mathbf{x}_1}p(\mathbf{x}_1,t)+\nu\Delta_{\mathbf{x}_1}\mathbf{u}(\mathbf{x}_1,t)+\mathbf{F}(\mathbf{x}_1,t))\hat{f}_1(\mathbf{v}_1;\mathbf{x}_1,t)\right\rangle\,.\end{aligned} \tag{13}$$

Here we encounter the closure problem of turbulence because the average on the right-hand side of (13) still contains the fine-grained PDF $\hat{f}_1$. There are in principle two ways of proceeding; either one can express the unclosed expressions in terms of higher-order statistics, or one can introduce conditional averages. The former procedure easily becomes clear at the example of the pressure term. As the pressure field is governed by a Poisson equation, it can be expressed in terms of the velocity field according to

$$p(\mathbf{x},t)=\frac{1}{4\pi}\int\mathrm{d}\mathbf{x}'\frac{\nabla_{\mathbf{x}'}\cdot[\mathbf{u}(\mathbf{x}',t)\cdot\nabla_{\mathbf{x}'}\mathbf{u}(\mathbf{x}',t)]}{|\mathbf{x}-\mathbf{x}'|} \tag{14}$$

which shows that the pressure field is a non-local expression of the velocity field. Statistically, this leads to the coupling to the two-point PDF [3]. A similar reasoning

can be applied to the diffusive term, so that this coupling to the two-point PDF can formally be written as

$$\left\langle (-\nabla_{\mathbf{x}_1} p(\mathbf{x}_1,t) + \nu \Delta_{\mathbf{x}_1} \mathbf{u}(\mathbf{x}_1,t) + \mathbf{F}(\mathbf{x}_1,t)) \hat{f}_1(\mathbf{v}_1;\mathbf{x}_1,t) \right\rangle = \mathrm{C}_1[f_2,\mathbf{F}_1], \tag{15}$$

where C_1 is the non-local operator including the coupling due to pressure, diffusion and the information of the external forcing field. Deriving the evolution equation for the two-point PDF f_2 then leads to a coupling to the three-point PDF f_3 and so forth, finally establishing the famous hierarchy of PDF equations.

The second possibility, again at the example of the pressure term, is to use a conditional average to split the term into

$$\langle -\nabla_{\mathbf{x}_1} p(\mathbf{x}_1,t) \hat{f}_1(\mathbf{v}_1;\mathbf{x}_1,t) \rangle = \langle -\nabla_{\mathbf{x}_1} p(\mathbf{x}_1,t) | \mathbf{v}_1,\mathbf{x}_1,t \rangle f_1(\mathbf{v}_1;\mathbf{x}_1,t) \tag{16}$$

leading to a closure of (13) once the conditional averages are specified. Expressing the closure problem in terms of conditional averages makes it more accessible to physical intuition and modeling. For instance, for the above expression we need to answer the question: What is the average value of the pressure gradient given a fixed value of velocity? Furthermore, the conditional averages are accessible by direct numerical simulations, although this also can be quite challenging. However, by exploiting statistical symmetries, the dimensionality of these unknowns can be considerably reduced. This route has been taken to explain slight deviations from Gaussianity of the single-point velocity PDF as well as strong departures from Gaussianity of the single-point vorticity PDF [19, 20, 21].

3.2 General Structure of the Hierarchy

If we combine the coupling to higher-order PDFs with conditional averaging, we can specify the hierarchy up to a given level according to

$$\frac{\partial}{\partial t} f_1 + \mathbf{v}_1 \cdot \nabla_{\mathbf{x}_1} f_1 = \mathrm{C}_1[f_2,\mathbf{F}_1] \tag{17}$$

$$\frac{\partial}{\partial t} f_2 + \mathbf{v}_1 \cdot \nabla_{\mathbf{x}_1} f_2 + \mathbf{v}_2 \cdot \nabla_{\mathbf{x}_2} f_2 = \mathrm{C}_2[f_3,\mathbf{F}_1,\mathbf{F}_2] \tag{18}$$

going up to

$$\frac{\partial}{\partial t} f_{N-1} + \sum_{i=1}^{N-1} \mathbf{v}_i \cdot \nabla_{\mathbf{x}_i} f_{N-1} = \mathrm{C}_{N-1}[f_N,\mathbf{F}_1,\ldots,\mathbf{F}_{N-1}]. \tag{19}$$

Here $\mathrm{C}_i[f_{i+1},\mathbf{F}_1,\ldots,\mathbf{F}_i]$ describes the coupling to the next order including the dependence on the forcing. Then introducing the conditional averages on the N-th level yields

$$\frac{\partial}{\partial t} f_N + \sum_{i=1}^{N} \mathbf{v}_i \cdot \nabla_{\mathbf{x}_i} f_N = -\sum_{i=1}^{N} \nabla_{\mathbf{v}_i} \cdot \left\{ \langle -\nabla_{\mathbf{x}_i} p_i + \nu \Delta_{\mathbf{x}_i} \mathbf{u}_i + \mathbf{F}_i | \mathbf{v}_1,\ldots,\mathbf{v}_N \rangle f_N \right\}, \tag{20}$$

by which we have obtained a set of N kinetic equations. If we do not introduce conditional averages, this hierarchy in principle continues to infinity. As a side remark we would like to note that this is a direct consequence of the fact that we describe turbulence in terms of a *field* and not in terms of a finite number of fluid particles. However, one can argue that from a physical point of view a finite set of points should suffice, for example, when the Eulerian field is sampled fine enough to smoothly resolve the Kolmogorov scale. So one interesting question for future research is whether it is possible to formulate a reasonable closure at large, but finite N which in principle contains all relevant physical information.

On the other hand, it would be interesting to combine also the multi-point PDF equations with DNS results, which, however, turns out to be quite challenging as tremendous amounts of data are needed for statistical convergence. Some progress recently was made for the two-point statistics of two-dimensional turbulence [18]. For more details on the LMN hierarchy, we would like to invite the reader to [23], which gives a broader overview of the contribution of Rudolf Friedrich and his group to this research field.

4 Conclusion and Outlook

We have presented a short overview of two approaches dealing with evolution equations for probability density functions describing statistical properties of fully developed turbulence. The motivation and starting point of the two approaches is quite different: The Fokker-Planck approach mainly is motivated by the desire to establish a self-consistent closure from experimental data, whereas the investigation of the LMN hierarchy mainly has been motivated by the aim of making contact to the Navier-Stokes dynamics. Despite these quite different motivations, both approaches lead to evolution equations for probability density functions and hence share some interesting formal analogies.

One of the most interesting questions for future work is to investigate whether these two approaches can be combined. Is it, for example, possible to derive a closure scheme for the LMN equations based on the Markov property? Or conversely: What is the physical meaning of the Markov property? Can the LMN hierarchy eventually be used to prove the Markov property from first principles? A progress with respect to these questions will surely lead to a deeper understanding of the statistics of fully developed turbulence.

References

1. Friedrich, R., Peinke, J.: Description of a turbulent cascade by a Fokker-Planck equation. Phys. Rev. Lett. 78(5), 863–866 (1997)
2. Pitaevskii, L.P., Lifshitz, E.M.: Physical Kinetics (Course of Theoretical Physics), vol. 10. Butterworth-Heinemann (1981)
3. Lundgren, T.S.: Distribution functions in the statistical theory of turbulence. Phys. Fluids 10(5), 969–975 (1967)

4. Monin, A.S.: Equations of turbulent motion. Prikl. Mat. Mekh. 31(6), 1057 (1967)
5. Novikov, E.A.: Kinetic equations for a vortex field. Sov. Phys. Dokl. 12(11), 1006–1008 (1968)
6. Renner, C., Peinke, J., Friedrich, R.: Experimental indications for Markov properties of small-scale turbulence. J. Fluid Mech. 433, 383–409 (2001)
7. Friedrich, R., Peinke, J., Sahimi, M., Tabar, M.R.R.: Approaching complexity by stochastic methods: From biological systems to turbulence. Phys. Rep. 506(5), 87–162 (2011)
8. Lück, S., Renner, C., Peinke, J., Friedrich, R.: The Markov-Einstein coherence length – a new meaning for the Taylor length in turbulence. Phys. Lett. A 359(5), 335–338 (2006)
9. Einstein, A.: Über die von der molekularkinetischen Theorie der Wärme geforderte Bewegung von in ruhenden Flüssigkeiten suspendierten Teilchen. Ann. Phys. 17, 549–560 (1905)
10. Risken, H.: The Fokker-Planck Equation: Methods of Solutions and Applications, 2nd edn. Springer Series in Synergetics. Springer (1996)
11. Renner, C., Peinke, J., Friedrich, R., Chanal, O., Chabaud, B.: Universality of small scale turbulence. Phys. Rev. Lett. 89(12), 124502 (2002)
12. Lück, S., Peinke, J., Friedrich, R.: Uniform statistical description of the transition between near and far field turbulence in a wake flow. Phys. Rev. Lett. 83, 5495–5498 (1999)
13. Stresing, R., Peinke, J., Seoud, R.E., Vassilicos, J.C.: Defining a new class of turbulent flows. Phys. Rev. Lett. 104(19), 194501 (2010); data analysis
14. Strumik, M., Macek, W.M.: Testing for markovian character and modeling of intermittency in solar wind turbulence. Phys. Rev. E 78, 026414 (2008)
15. Tutkun, M., Mydlarski, L.: Markovian properties of passive scalar increments in grid-generated turbulence. New J. Phys. 6, 49 (2004)
16. Novikov, E.A., Dommermuth, D.G.: Conditionally averaged dynamics of turbulence. Mod. Phys. Lett. B 8(23), 1395 (1994)
17. Mui, R.C.Y., Dommermuth, D.G., Novikov, E.A.: Conditionally averaged vorticity field and turbulence modeling. Phys. Rev. E 53(3), 2355–2359 (1996)
18. Friedrich, R., Voßkuhle, M., Kamps, O., Wilczek, M.: Two-point vorticity statistics in the inverse cascade of two-dimensional turbulence. Physics of Fluids 24(12), 125101 (2012)
19. Wilczek, M., Friedrich, R.: Dynamical origins for non-Gaussian vorticity distributions in turbulent flows. Phys. Rev. E 80, 016316 (2009)
20. Wilczek, M., Daitche, A., Friedrich, R.: On the velocity distribution in homogeneous isotropic turbulence: correlations and deviations from Gaussianity. J. Fluid Mech. 676, 191–217 (2011)
21. Wilczek, M., Daitche, A., Friedrich, R.: Theory for the single-point velocity statistics of fully developed turbulence. Europhys. Lett. 93(3), 34003 (2011)
22. Lülff, J., Wilczek, M., Friedrich, R.: Temperature statistics in turbulent Rayleigh-Bénard convection. New J. Phys. 13(1), 015002 (2011)
23. Friedrich, R., Daitche, A., Kamps, O., Lülff, J., Vokuhle, M., Wilczek, M.: The Lundgren-Monin-Novikov hierarchy: Kinetic equations for turbulence. Comptes Rendus Physique 13(9-10), 929–953 (2012)
24. Pope, S.: Turbulent Flows. Cambridge University Press, Cambridge (2000)

Extreme Events for Two-Particles Separations in Turbulent Flows

Luca Biferale, A.S. Lanotte, R. Scatamacchia, and F. Toschi

Abstract. Results from high resolution numerical simulations of tracer particles emitted from localised sources in homogeneous and isotropic flows are presented. A huge number of tracers are emitted in order to reach an unprecedented statistics concerning particles pairs motion. We show that the far tails of the particles pair separation Probability Distribution Function can not be described by a Richardson-like distribution, even if finite Reynolds effects are introduced. We argue that to describe extreme event statistics, velocity temporal correlations and non-Gaussian fluctuations must be taken into account.

1 Introduction

The relative separation between two fluid particles by turbulent flows has been firstly addressed by L.F. Richardson [1] (see [2, 3] for recent reviews). The main question is the following: given a pair of tracer particles released, at time $t_0 = 0$ at a small separation distance r_0 (smaller of the Kolmogorov dissipative scale, η), what is the probability, $P(r_0, t_0; r, t)$ to find it at a given distance r at a later time t?

Luca Biferale
Dept. Physics and INFN, University of Rome 'Tor Vergata', 00133 Rome, Italy
e-mail: biferale@roma2.infn.it

A.S. Lanotte
ISAC-CNR, Str. Prov. Lecce - Monteroni, and INFN, Sez. Lecce, 73100 Lecce, Italy
e-mail: a.lanotte@isac.cnr.it

R. Scatamacchia
Dept. Physics, University of Rome 'Tor Vergata', 00133 Rome, Italy
e-mail: riccardoscatamacchia@gmail.com

F. Toschi
Department of Physics, and Department of Mathematics and Computer Science,
Eindhoven University of Technology, 5600 MB Eindhoven, The Netherlands
e-mail: f.toschi@tue.nl

A. Talamelli et al. (eds.), *Progress in Turbulence V*,
Springer Proceedings in Physics 149,
DOI: 10.1007/978-3-319-01860-7_2,

The knowledge of such Probability Density Function (PDF) is of crucial importance for many geophysical applications [4, 5, 6]. It is a highly complex statistical problem due to its dependence on the velocity fluctuations evaluated at the particle positions, along their whole past history [7]. Here we will investigate only the classical case of passive particles, with no feedback on the flow and in the dilued limit, neglecting collisions. Richardson proposed to model the particle separation, at inertial subrange distances $\eta \ll r \ll L_0$, as a Fokker-Planck diffusive process characterised by an effective inertial range diffusivity, $D_{Ric}(r) = \frac{1}{2}\frac{d\langle r^2\rangle}{dt}$, with

$$D_{Ric}(r) \sim \beta r^{4/3}. \tag{1}$$

Here L_0 is the large-scale of the flow and $\beta = k_0\varepsilon^{1/3}$, where k_0 is a non dimensional constant and ε is the mean kinetic energy dissipation. It is possible to relate Richardson and Kolmogorov 1941 theory [8], by using dimensional estimate [7, 9]. Namely, $D_{Ric}(r) \sim \tau(r)\langle(\delta_r v)^2\rangle$, where $\tau(r) \sim \varepsilon^{-1/3}r^{2/3}$ is the local eddy-turn-over-time at the inertial range scale r, and $\langle(\delta_r v)^2\rangle \propto \varepsilon^{2/3}r^{2/3}$ is the second order Eulerian longitudinal structure function. The resulting long time growth of the mean squared separation is: $\langle r^2(t)\rangle = g\varepsilon t^3$, where $g \simeq 0.5$ is the Richardson constant [10, 11, 12, 13, 14]. Since [1], many experimental and numerical studies have focused on the statistics of pair dispersion in turbulent flows [15, 16, 12, 17, 18, 14], also considering the problem of multiparticle dispersion [19, 20]. More recently, effects related to inertia have also been considered in dispersion studies [21, 22, 23]. Here we would like to understand if the Richardson's approach is suitable for the statistics of the extreme events also, i.e. those pairs of tracers with separation much larger/smaller than the average one, $\langle r^2(t)\rangle^{1/2}$.

To proceed with our analysis, it is worth recalling that Richardson's approach can be reinterpreted as the evolution of tracers in a Gaussian, homogeneous and

Fig. 1 Two different bunches emitted in two different locations from a source of size $\sim \eta$, recorded at time $t = 75\tau_\eta$. On the left, a bunch emitted in a strong shear-rate region; on the right, a bunch emitted in a weak shear region. Direct Numerical Simulations are performed on a cubic fully periodic grid at 1024^3 points, at a Reynolds-Taylor number $Re_\lambda \sim 300$. For further details see [30].

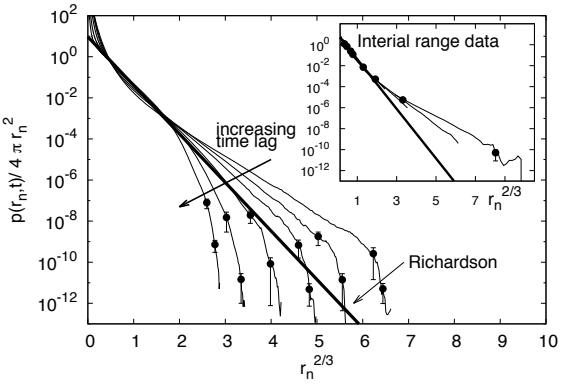

Fig. 2 Log-lin plot of $P(r_n,t)$ versus the rescaled variable r_n (see text), for $t = (20,30,40,60,90,120)\tau_\eta$. The distribution $P(r_n,t)$ has been divided by a factor r_n^2 to highlight the large separation range. Richardson prediction (3) becomes time-independent if rescaled in this way (solid curve). Inset: same PDFs plotted only for separations r_n that belong to the inertial subrange at any time lag chosen.

isotropic velocity field, delta-correlated in time, with two-point correlation given by $\langle \delta_r v_i(t) \delta_r v_j(t') \rangle = \delta(t-t')[D_\parallel(r)\hat{r}_i\hat{r}_j + D_\perp(r)(\delta_{ij} - \hat{r}_i\hat{r}_j)]$, where the longitudinal and transverse second order structure functions $D_\parallel(r)$ and $D_\perp(r)$ are such that $D_\perp(r) = D_\parallel(r) + 1/2\, r\, \partial_r D_\parallel(r)$, because of incompressibility [24].

The pair separation PDF for tracers advected by such a velocity field satisfies the following diffusive Fokker-Planck equation [24, 7]

$$\partial_t P(r,t) = r^{-2} \partial_r r^2 D_\parallel(r) \partial_r P(r,t)\,. \tag{2}$$

Moreover, if the eddy-diffusivity has a power-law behavior, $D_\parallel(r) = D_0 r^\xi$ with $0 \leq \xi < 2$, the Richardson equation (2) with initial condition $P(r,t_0) \propto \delta(r-r_0)$ can be solved [25, 26]. The solution has an asymptotic large time form (independent of the initial condition r_0 at t_0) of the kind

$$P_{Ric}(r,t) \propto \frac{r^2}{\langle r^2(t) \rangle^{\frac{3}{2}}} \exp\left\{ -b \left(\frac{r}{\langle r^2(t) \rangle^{\frac{1}{2}}} \right)^{2-\xi} \right\}, \tag{3}$$

where b is a constant determined in terms of D_0 [25]. In this infinite Reynolds number scaling scenario (no cut-offs are present), tracer pairs separate in an *explosive* way: $\langle r^2(t) \rangle \propto t^{2/(2-\xi)}$. It is easy to recognise that, for $\xi = 4/3$, this behaviour is the one originally proposed by Richardson. At small scales, where the turbulent flow is differentiable and the eddy diffusivity is $D_\parallel(r) = D_0 r^2$, the PDF assumes a log-normal shape, $P(r,t|r_0,0) \propto \exp\left\{ -(\log(r/r_0) - \lambda t)^2/(2\Delta\, t) \right\}$, [7]; here λ is the maximal Lyapunov exponent and Δ is connected to fluctuations of the strain field. In this case the rate of separation is strongly fluctuating from point-to-point and

from time-to-time being connected to the fluctuations of the Lyapunov exponents [7, 27].

There are many reasons for which the Richardson distribution can not *exactly* describe the behaviour of tracer pairs in real flows. The most important are: (i) the nature of the temporal correlations of the fluid flow [24, 9, 28, 18]; (ii) the non-Gaussian fluctuations of turbulent velocities; (iii) the small-scales effects induced by the dissipation subrange, and (iv) the large-scales effects induced by the flow correlation lenght and/or the flow geometry. These last two are of course connected to finite Reynolds effects [29].

In this paper, we review some recent results about finite Reynolds effects on the rate of occurrence of *rare* extreme events [30]. Moreover, we present a generalization of the Richardson approach by introducing an *effective* turbulent diffusivity, taking into account also of viscous and large-scale turbulent properties.

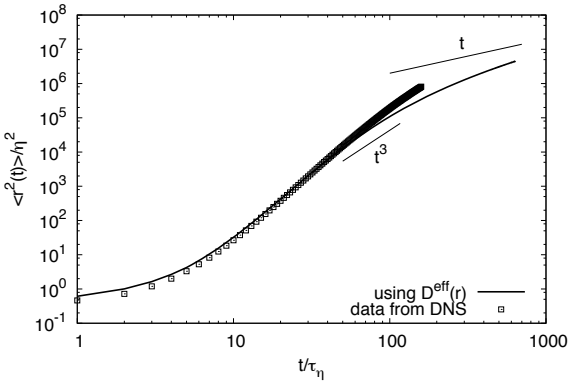

Fig. 3 Log-log plot of the second moment of relative dispersion $\langle r^2(t)\rangle$. Symbols are from DNS data, while the continuous line is obtained from integrating the diffusive evolution with the eddy diffusivity model of eq. (4). Notice the change in the asymptotic evolution obtained with (4) due to the saturation of the effective diffusivity at large separation scales.

2 DNS Results

We have performed a series of Direct Numerical Simulations (DNS) of homogeneous and isotropic turbulence, seeding the fluid with bunches of tracers, emitted in different locations (see [30] for details). In Fig. 1, a glance on the complexity of the problem is given. In the left panel, there is a typical bunch emitted in a region of strong shear: we observe an abrupt transition in the particle dispersion occurring at a time $t \sim 10\,\tau_\eta$ after the emission, when most of the pairs reaches a relative distance of the order of $\sim 10\eta$. Later on, we again note the presence of many pairs with mutual separations much larger than the mean one. In the right panel, there is a bunch with an anomalous history: at difference with the previous case, here tracers tend to

stay at mutual distance of the order of η for a very long time. This happens when pairs are injected in a spatial region characterised by a very small stretching rate.

In Fig. 2, we quantify these observation by plotting the PDF $P(r,t)$ rescaled in terms of the variable $r_n(t) = r(t)/\langle r^2(t)\rangle^{1/2}$, and compared against the asymptotic prediction (3). The deviations from Richardson's model are evident in the strong discrepancies at large scales, for all times. In the inset of the same figure, a more stringent test is shown. We plot the same PDFs but restricting the pair distances to scales belonging to the inertial subrange, $30\eta < r < 300\eta$.

Let us remark that previous studies could access events up to separation distances $r/\langle r^2(t)\rangle^{1/2} < 3$ (see e.g. [2]). Our study improves of about four order of magnitude (in probability) the intensity of detectable events, highlighting strong deviations from Richardson's shape previously inaccessible. Such departures from the *ideal infinite-Reynolds* distribution proposed by Richardson call for a better quantification. In particular, to assess the importance of finite Reynolds effects, we have integrated the Richardson equation (2) using an *effective* eddy-diffusivity $D^{eff}(r)$ which modifies the classical expression (1) by including small- and large-scales cut-offs:

$$\begin{aligned} D_{\parallel}^{eff}(r) &\sim r^2 \qquad\quad r \ll \eta \\ D_{\parallel}^{eff}(r) &\sim r^{4/3} \qquad \eta \ll r \ll L_0 \\ D_{\parallel}^{eff}(r) &\sim const. \quad r \gg L_0\,. \end{aligned} \tag{4}$$

In this way, the eddy-diffusivity spans all statistical behaviours from the smooth one in the dissipative range, up to the saturated one at scales larger than the flow correlation lenght L_0. A popular fitting formula that reproduces well the Eulerian data, and that matches the expected scaling for both $\tau(r)$ and $\langle(\delta_r v)^2\rangle$, is (see also [31]):

$$\langle(\delta_r v)^2\rangle = c_0 \frac{r^2}{((r/\eta)^2 + c_1)^{2/3}} \left[1 + c_2 \left(\frac{r}{L_0}\right)^2\right]^{-1/3} \tag{5}$$

supplemented with a similar expression for the eddy turn over time:

$$\tau(r) = \frac{\tau_\eta}{((r/\eta)^2 + c_1)^{-1/3}} \left[1 + d_2 \left(\frac{r}{L_0}\right)^2\right]^{-1/3}. \tag{6}$$

The $\mathcal{O}(1)$ parameters c_0, c_1, c_2 are fitted from the Eulerian statistics; the parameter d_2 is fixed such as to correctly reproduce the evolution of the mean square separation, $\langle r^2(t)\rangle$, over the whole time range $\tau_\eta \le t \le T_L$, see Fig. 3. Note that the hypothesis of Gaussian statistics still holds true in this approach, since the velocity field distribution is fixed by $D^{eff}(r)$ only.

In Fig. 4, there is the solution, $P_{eff}(r,t)$, of the diffusive equation (2) obtained using $D^{eff}(r)$ and for different choices for the parameter d_2: these modelling solutions are compared with the PDF obtained from the numerical simulation, and with

the ideal Richardson prediction. Despite the excellent agreement for the second moment $\langle r^2(t)\rangle$ obtained from DNS and that obtained using the stochastic model (2) and (4), the PDF far tails are still different. For large separations the agreement with the DNS data is qualitatively better but still quantitatively off, particularly when focusing on the sharp change at the cut-off scale where the left tail becomes steeper and steeper: this effect is still absent in the evolution given by (4). This is a keypoint which tells us that to reproduce the observed PDF for large excursions, it is not enough to impose a saturation of eddy-diffusivity at large scales. The behavior of pair dispersion must then be crucially dependent on the nature of the Lagrangian turbulent velocity in the inertial subrange.

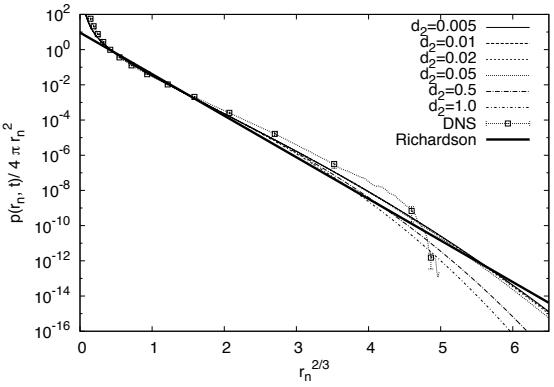

Fig. 4 Lin-log plot of $P_{eff}(r,t)$ as obtained from the integration of (3) with $D^{eff}(r)$ at changing the d_2 parameter (thin line, and different dashed lines) and the DNS data (symbols). The Richardson PDF is also plot (thick solid line).

3 Conclusions

We have reviewed recent results from a numerical simulation designed in order to quantitatively explore the stastistics of rare events in turbulent pair dispersion. Here we concentrated on the pairs that separate much "faster" than typical ones (for the case of "slow" pairs see also [30]). We showed the existence of an important departure from the Richardson-like inertial and idealised behavior described in eqn. (3). A step forward is obtained introducing a finite-Reynolds effective eddy-diffusivity kernel, which correctly takes into account both the viscous and integral scale physics. In this way, a better qualitative agreement with real data is observed. A different attempt using the diffusive nature of Lagrangian relative velocities has been recently proposed [18, 14]. Alternatively, suggestions based on a memory kernel to overcome the presence of unphysical infinite speed events [28, 32] has also been proposed. Further studies will be needed to quantify this issues. Single particles absolute dispersion and or dependence on the Stokes time for inertial particles are

other two important points that may deliver new insights in the physics of particles dispersions [35].

Acknowledgements. We thank M. Cencini, J. Bec and R. Benzi for very useful discussions. We acknowledge the EU COST Action MP0806 "Particles in turbulence" and CINECA (Italy) within the HPC program ISCRA Project. This research was supported in part by the Project of Knowledge Innovation Program (PKIP) of Chinese Academy of Science, Grant No. KJCX2.YW.W10.

References

1. Richardson, L.F.: Proc. R. Soc. London A 110, 709 (1926)
2. Salazar, J.P.L.C., Collins, L.R.: Annu. Rev. Fluid Mech. 41, 405 (2009)
3. Benzi, R.: In: Davison, P., Kaneda, Y., Moffatt, K., Sreenivasan, K. (eds.) A voyage through Turbulence. Cambridge Univ. Press (2011)
4. Sullivan, P.J.: J. Fluid Mech. 47, 601 (1971)
5. Ollitrault, M., Gabillet, C., Colin De Verdiére, A.: J. Fluid Mech. 533, 381 (2005)
6. LaCasce, J.H., Mar, J.: J. Mar. Res. 68, 433 (2010)
7. Falkovich, G., Gawędzki, K., Vergassola, M.: Rev. Mod. Phys. 73, 913 (2001)
8. Frisch, U.: Turbulence. Cambridge University Press, Cambridge (1995)
9. Sokolov, I.M.: Phys. Rev. E 60, 5528 (1999)
10. Ott, S., Mann, J.: J. Fluid Mech. 422, 207 (2000)
11. Boffetta, G., Sokolov, I.M.: Phys. Rev. Lett. 88, 094501 (2002)
12. Biferale, L., Boffetta, G., Celani, A., Devenish, B.P., Lanotte, A.S., Toschi, F.: Phys. Fluids 17, 115101 (2005)
13. Schumacher, J.: Phys. Rev. Lett. 100, 134502 (2008)
14. Bitane, R., Bec, J., Homann, H.: Geometry and violent events in turbulent pair dispersion, arXiv:1209.2296
15. Jullien, M.C., Paret, J., Tabeling, P.: Phys. Rev. Lett. 82, 2872 (1999)
16. Nicolleau, F., Vassilicos, J.C.: Phys. Rev. Lett. 90, 024503 (2003)
17. Ouellette, N., Xu, H., Bourgoin, M., Bodenschatz, E.: New J. Phys. 8, 109 (2006)
18. Bitane, R., Bec, J., Homann, H.: Timescales of Turbulent Relative Dispersion, arXiv:1206.7062
19. Pumir, A., Shraiman, B., Chertkov, M.: Phys. Rev. Lett. 85, 5324 (2000)
20. Biferale, L., Boffetta, G., Celani, A., Devenish, B.P., Lanotte, A.S., Toschi, F.: Phys. Fluids, 17, 111701 (2005)
21. Bec, J., Biferale, L., Lanotte, A.S., Scagliarini, A., Toschi, F.: J. Fluid Mech 645, 497 (2010)
22. Derevich, I.V.: Fluid Dyn. 43, 357 (2008)
23. Fouxon, I., Horvai, P.: Phys. Rev. Lett. 100, 040601 (2008)
24. Kraichnan, R.H.: Phys. Fluids 11, 945 (1968); Phys. Fluids 9, 1937 (1966)
25. Balkovski, E., Lebedev, V.: Phys. Rev. E 58, 5776 (1998)
26. Bennett, A.: Lagrangian fluid dynamics. Cambridge University Press, Cambridge (2006)
27. Bec, J., Biferale, L., Boffetta, G., Cencini, M., Musacchio, S., Toschi, F.: Phys. Fluids 18, 091702 (2006)
28. Ilyin, V., Procaccia, I., Zagorodny, A.: Phys. Rev. E 81, 030105 (2010)
29. Sawford, B.L., Yeung, P.K., Hackl, J.F.: Phys. Fluids 20, 065111 (2008)
30. Scatamacchia, R., Biferale, L., Toschi, F.: Phys. Rev. Lett. 109, 144501 (2012)

31. Meneveau, C.: Phys. Rev. E 54, 3657 (1996)
32. Ogasawara, T., Toh, S.: J. Phys. Soc. Jpn. 75, 083401 (2006)
33. Bec, J., Biferale, L., Boffetta, G., Celani, A., Cencini, M., Lanotte, A.S., Musacchio, S., Toschi, F.: J. Fluid Mech. 550, 349 (2006)
34. Biferale, L., Scagliarini, A., Toschi, F.: Phys. Fluids 22, 065101 (2010)
35. Scatamacchia, R., Lanotte, A.S., Biferale, L., Toschi, F.: (in preparation)

Higher Order Moments of Velocity Fluctuations and Their Gradients in Turbulent Wall-Jets

Zeinab Pouransari, Luca Biferale, and Arne V. Johansson

Abstract. The concept of local isotropy is addressed in a turbulent wall-jet. Direct numerical simulations (DNS) of a reacting turbulent wall-jet flow are used to evaluate the probability density functions (PDF) and higher order moments of the velocity and of the gradient in our set-up, in order to illustrate different aspects of the degree of isotropy at small scales. We observe a strong persistency of small-scale anisotropy up to $y/y_{1/2} \approx 1.5$, where $y_{1/2}$ is the half width of the jet.

1 Introduction

The idea of local isotropy is an interesting topic, since, if it holds, small scales in turbulent flows can be described by universal parameters [1,2]. The turbulent plane wall-jet is a test case that has close resemblance to a wide range of mixing and combustion applications. In the present study, DNS data is used to investigate the PDF shapes and the characteristics of the higher order moments at different downstream positions and at different wall-normal planes [3].

To provide an overview of the turbulent wall-jet flow, some of the mean profiles are shown in Fig. 1. The position of the maximum streamwise velocity and the position of zero shear stress in the turbulent wall-jet flow do not exactly coincide. This behavior has some similarities to what has been previously reported for the jet flows. We observed in Figs. 1(a,b) that in the self-similar region ($x/h > 20$), the latter lies below the former, and in between, a region with negative mean production. The zero-crossing in the skewness of the streamwise velocity gradient also lies close to these positions, see black curve in Fig. 4(a).

Zeinab Pouransari · Arne V. Johansson
Linné Flow Centre, KTH Mechanics, SE-100 44 Stockholm, Sweden
e-mail: zeinab@mech.kth.se

Luca Biferale
Department of Physics and INFN, University of Rome "tor vergata", Italy

A. Talamelli et al. (eds.), *Progress in Turbulence V*,
Springer Proceedings in Physics 149,
DOI: 10.1007/978-3-319-01860-7_3,

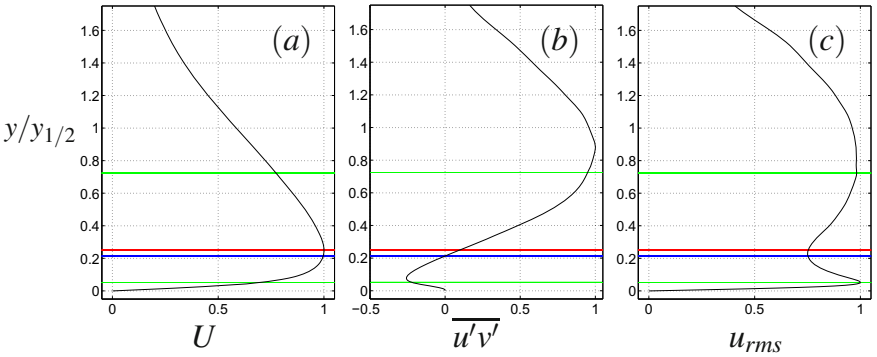

Fig. 1 (a) Mean cross-stream profiles of streamwise velocity, (b) Reynolds shear stress and (c) streamwise fluctuation intensity at $x/h = 25$. The red and blue lines show the position of the local maximum mean streamwise velocity and the local zero shear position, respectively. The green lines show the positions of the streamwise fluctuation intensity maxima.

2 Probability Density Functions

The PDF of the streamwise velocity fluctuation and its wall-normal gradient are shown in Fig.2(a) and (b), where we can observe a good collapse of the PDF curves in a large portion of the domain [3]. Rather different characteristics for the PDF of the velocities and gradients are observed in the inner region ($y/y_{1/2} < 0.4$). The PDF of the gradients have longer tails, caused by the inhomogeneity near the wall, also associated with larger flatness factors than for the velocity fluctuations, see Fig. 3. The occurrence of large flatness factors around $y/y_{1/2} = 1.5$ and beyond this positions, indicates high intermittency even for large-scale velocity fields. This also shows that a large number of realizations is needed to have statistical convergence in this region. The PDF of the derivatives are more influenced by the small scales.

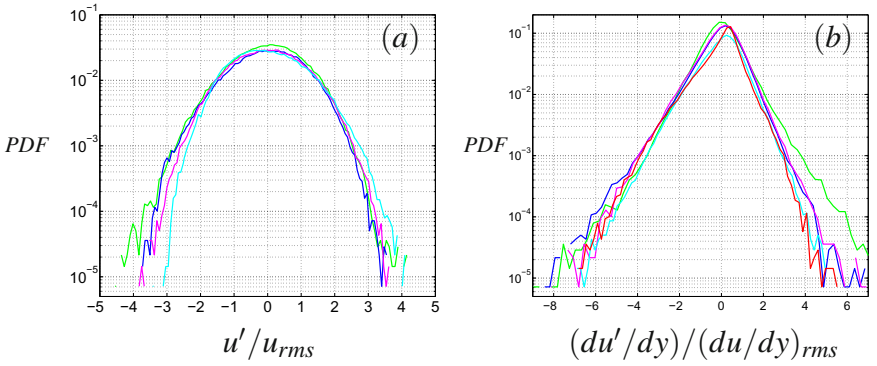

Fig. 2 Probability density functions of (a) the streamwise velocity and (b) the wall-normal gradient of the streamwise velocity at downstream position $x/h = 25$. Color code as follows, green: $y/y_{1/2} = 0.25$, blue: $y/y_{1/2} = 0.5$, magenta: $y/y_{1/2} = 0.75$, cyan: $y/y_{1/2} = 1$, red: $y/y_{1/2} = 1.5$.

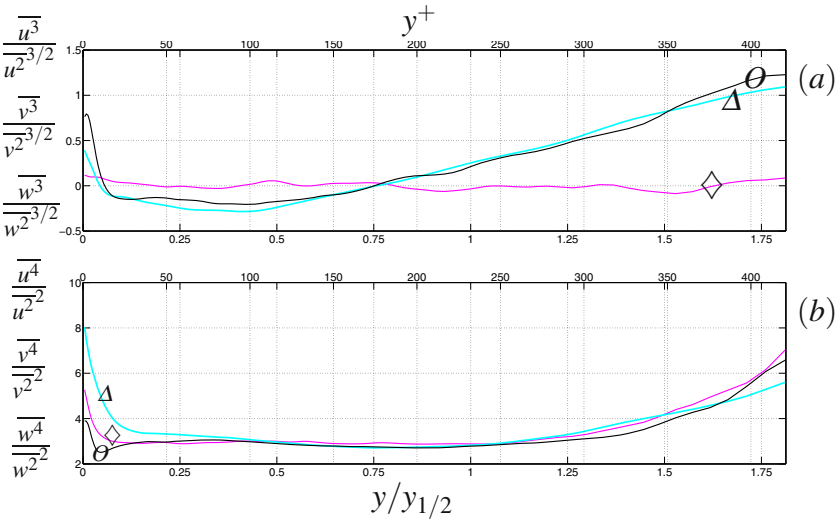

Fig. 3 Distributions of third and forth-order moments, (a) skewness and (b) flatness of the velocity fluctuations at $x/h = 25$. Color code as follows, streamwise: black (O), wall-normal: cyan (Δ) and spanwise: magenta ($\diamondsuit$). Here y^+ is yu_τ/ν and $y_{1/2}$ is the half-height of the jet.

3 Higher Order Moments

In order to investigate the intermittency effects at different wall-normal levels, the skewness and flatness of the velocity fluctuations and the velocity gradients are shown in Figs. 3 and 4, respectively. From studying the skewness factor of the streamwise velocity and its transversal gradient, one can get conclusions on the large-scale and small-scale anisotropy of the flow. Note that, the skewness of the velocity fluctuations is connected to the large-scale anisotropy and the skewness of the transverse velocity gradients to the small scale anisotropy.

Skewness and Flatness Factors of Velocities

The positive skewness of the streamwise velocity close to the wall is an indication of anisotropic large-scale velocities. This is a rather universal behavior for all wall-bounded flows. The zero crossings of the streamwise velocity skewness coincide with two maxima of the streamwise turbulent intensity (Fig. 3). The inner maximum around $y^+ = 14$ is similar to that in the turbulent boundary layer. In the turbulent wall-jet flow, a second zero-crossing occurs around $y/y_{1/2} = 0.75$, see Fig. 1(c). The zero crossing of the skewness factor and the local minimum in flatness profiles, Fig. 3(b), is an indication that around the region where turbulence intensity has a local maximum, the PDF shape remains fairly symmetric. As seen in Fig. 3(b), the wall normal velocity in the near wall region, has a higher flatness factor than the other two components, which has a clear similarity with other wall-bounded flows. In the outer region of the wall-jet, large positive values of flatness are observed for all three components, which is due to the intermittency at the interface between turbulent and laminar regions, just as it is at the edge of turbulent boundary layer.

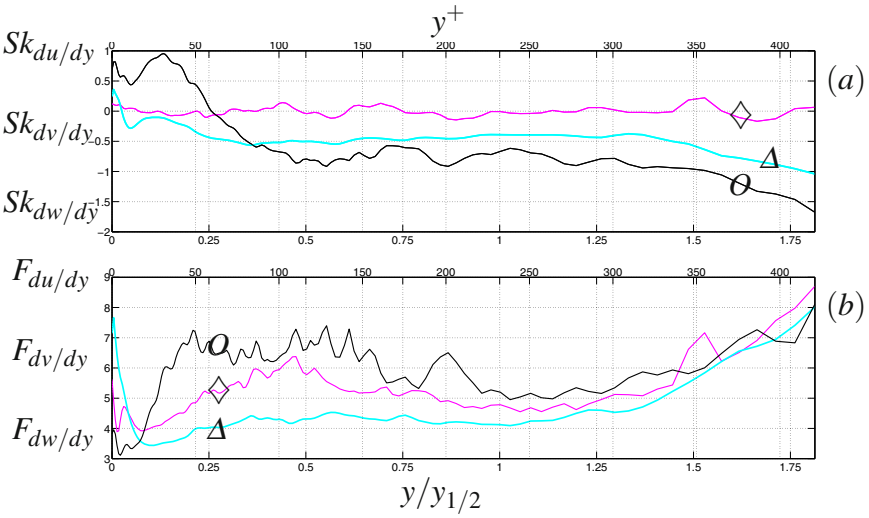

Fig. 4 Distributions of skewness (a) and flatness (b) of the wall-normal gradients of the velocity components at $x/h = 25$. Color code as in Fig. 3.

Skewness and Flatness Factors of Velocity Gradients

The skewness and flatness factor of the velocity gradients in the wall-normal direction are shown in Fig. 4. Let us stress that in a purely isotropic ensemble, all odd moments of the transverse gradients are exactly vanishing, so a measure of the skewness of du/dy gives a direct quantitative information on the degree of anisotropy. The skewness of the streamwise velocity gradient, $Sk_{du/dy}$ crosses zero close to $y/y_{1/2} = 0.25$, where also the turbulent shear is zero. For a wide region above this position $0.4 < y/y_{1/2} < 1.4$, there is a plateau with a negative value about -0.5, indicating a strong small-scale anisotropy. The anisotropy of the small scales seems to be of the same order as the anisotropy of the large scales, but interesting enough, starting from the wall region up to $y/y_{1/2} = 0.25$, the skewness of du/dy is positive, which indicates a significant influence of the mean flow inhomogeneity for the small scales. At the position where the mean Reynolds shear stress (transversal shear) changes sign, the skewness of du/dy (transversal gradient) changes sign too. The high values of all the velocity gradient flatness is a further indication of high non-Gaussian statistics at small-scales.

Acknowledgements. Financial supports by Swedish National Research program of Combustion Science and Technology (CECOST) and computer time provided by SNIC are acknowledged.

References

1. Biferale, L., Procaccia, I.: Anisotropy in Turbulent Flows and in Turbulent Transport. Phys. Rep. 414, 43 (2005)
2. Shen, X., Warhaft, Z.: The anisotropy of the small scale structure in high Reynolds number $Re_\lambda \sim 1000$ turbulent shear flow. Phys. Fluids 12(11) (2000)
3. Pouransari, Z., Brethouwer, G., Johansson, A.V.: Direct numerical simulation of an isothermal reacting turbulent wall-jet. Phys. Fluids 23 (2011)

Local and Non-local Interactions in the Batchelor Regime of the Passive Scalar

Robert Rubinstein and Wouter J.T. Bos

Abstract. Following a suggestion of Yukio Kaneda, Kraichnan's interpretation of Batchelor's analysis of high Schmidt number passive scalar turbulence is described in terms of local and non-local interactions. The formulations of Batchelor and Kraichnan are then compared through their predictions of the diffusive range following the Batchelor range and of the reduction of mean-square advection in scalar turbulence. Although comparison based on the diffusive range proves inconclusive, the predictions of reduction of mean-square advection may support Kraichnan's formulation; however, a definite conclusion is not yet possible.

1 Introduction

Passive advection of a scalar θ by a turbulent velocity field $\boldsymbol{u}$ is governed by

$$\dot{\theta}(\boldsymbol{k}) + \kappa k^2 \theta(\boldsymbol{k}) = -i \int_{\boldsymbol{k}=\boldsymbol{p}+\boldsymbol{q}} d\boldsymbol{p}\, \boldsymbol{u}(\boldsymbol{p}) \cdot \boldsymbol{q}\theta(\boldsymbol{q}) \tag{1}$$

where κ denotes the scalar diffusivity. Scalar and velocity correlations are denoted by $U_{ij}(\boldsymbol{k}) = \langle u_i(\boldsymbol{k}) u_j(-\boldsymbol{k}) \rangle$ and $U_\theta(\boldsymbol{k}) = \langle \theta(\boldsymbol{k})\theta(-\boldsymbol{k}) \rangle$. Spectra are defined as usual by the properties $\langle \boldsymbol{u} \cdot \boldsymbol{u} \rangle = \int d\boldsymbol{k}\, U_{mm}(\boldsymbol{k}) = 2\int_0^\infty E(k)dk$ and $\langle \theta^2 \rangle = \int d\boldsymbol{k}\, U_\theta(\boldsymbol{k}) = 2\int_0^\infty E_\theta(k)dk$. The rate of destruction of scalar fluctuations is $\chi = 2\kappa \langle |\nabla\theta|^2 \rangle$.

In the limit of high Schmidt number $\kappa \gg \nu$, where ν is the fluid viscosity, Batchelor's analysis [1] showed that for $k \gg k_d \propto (\varepsilon/\nu^3)^{1/4}$, a scaling range in which

Robert Rubinstein
Newport News, VA USA
e-mail: robert.rubinstein41@gmail.com

Wouter J.T. Bos
CNRS-LMFA, Ecole Centrale de Lyon, Université de Lyon, Ecully, France

A. Talamelli et al. (eds.), *Progress in Turbulence V*,
Springer Proceedings in Physics 149,
DOI: 10.1007/978-3-319-01860-7_4,

$$E_\theta(k) = \mathsf{C}\sqrt{\frac{\nu}{\varepsilon}}\chi k^{-1} \tag{2}$$

is possible provided that the total strain due to the velocity field, $\sqrt{\int_0^\infty dk\, k^2 E(k) dk} = \sqrt{\frac{\varepsilon}{\nu}}$ exceeds the viscous frequency κk^2. Here and throughout, C denotes a constant, not necessarily the same constant whenever it appears. This condition requires $k \ll k_B \propto (\varepsilon/\nu\kappa^2)^{1/4} \propto k_d \mathrm{Sc}^{1/2}$. Recent numerical simulations [2] confirm the existence of the *Batchelor spectrum* Eq. (2) in this wavenumber range.

2 Batchelor and Kraichnan Formulations

Batchelor gave a physical argument for Eq. (2) based on the idea that the velocity field statically strains 'blobs' of scalar at the average rate $\sqrt{\varepsilon/\nu}$. Assuming that this strain gives rise to a constant flux χ, dimensional analysis leads to Eq. (2). This argument postulates a kind of 'rapid distortion theory' in which scalar 'blobs' are deformed by a uniform strain; hence, the velocity field acts on the scalar field as a mean field ('mean' here in the sense of Reynolds averaging). Batchelor scaling can also be established following [1] by an elementary closure approach. Non-diffusive conservation of scalar variance implies that the scalar spectrum satisfies

$$\dot{E}_\theta(k) = -\frac{\partial}{\partial k}\mathscr{F}_\theta - 2\kappa k^2 E_\theta(k). \tag{3}$$

The simplest possible hypothesis is

$$\mathscr{F}_\theta = \mathsf{C}\eta(k) k E_\theta(k) \tag{4}$$

where $\eta(k)$ is a suitably defined frequency. In a Batchelor range $\eta(k) = \sqrt{\varepsilon/\nu}$. Then the constant flux condition $\chi = \mathsf{C}\sqrt{\varepsilon/\nu} k E_\theta(k)$ leads at once to Eq. (2). We will call this analysis the *Batchelor formulation*.

A systematically derived alternative to the heuristic closure Eq. (4) is the scalar Test-Field Model [3]

$$\dot{U}_\theta(\boldsymbol{k}) = \int_{\boldsymbol{k}=\boldsymbol{p}+\boldsymbol{q}} d\boldsymbol{p}\, \Theta(\boldsymbol{k},\boldsymbol{p},\boldsymbol{q}) U_{ij}(\boldsymbol{p}) k_i k_j [U_\theta(\boldsymbol{q}) - U_\theta(\boldsymbol{k})] \tag{5}$$

where $\Theta(\boldsymbol{k},\boldsymbol{p},\boldsymbol{q})$ is a triad relaxation time determined by the theory. Since the energetic wavenumbers in the velocity field are much smaller than those in the Batchelor range, we consider wavevector triads in which $\boldsymbol{p} \approx 0$, $\boldsymbol{q} \approx \boldsymbol{k}$. In this limit, some simplifications of Eq. (5) lead to

$$\mathscr{F}_\theta(k) = -\mathsf{C}\sqrt{\frac{\varepsilon}{\nu}} k^4 \frac{\partial}{\partial k}\left(\frac{E_\theta(k)}{k^2}\right) \tag{6}$$

[3, 4]. This is a modified form of the Leith scalar diffusion model [5]. It is easily verified that Eq. (6) is consistent with Batchelor scaling of a steady, non-diffusive constant flux scalar spectrum. Since Kraichnan [6] derives an equation of this form for a white-in-time Gaussian velocity field, we will call this the *Kraichnan formulation*.

Eq. (6) is diffusive because triad interactions with $|\boldsymbol{p}| \leq \Delta p$ spread scalar excitation at wavevector k over an interval $k - \Delta p \leq \lambda \leq k + \Delta p$. But in Eq. (4), although a range of wavenumbers contributes to the total strain, triad interactions between the scalar and these velocity modes are ignored, and consequently the entire strain field acts as if it were a mean field concentrated at $\boldsymbol{p} = 0$. Although usage of these terms is not unambiguous, we might describe the interactions in Kraichnan's formulation as 'local,' and those in Batchelor's as 'non-local:' the distinction is whether velocity-scalar triad interactions are considered, or not.

3 Comparison of the Formulations

Kraichnan [6] presented these formulations as alternatives (a static or a rapidly varying straining field) that might well apply under different conditions. Nevertheless, it is natural to ask which formulation better describes advection in a random velocity field, such as turbulence, which is neither exactly static nor white noise in time.

Batchelor considered the diffusive range following the constant scalar flux range. For this range, the steady form of Eq. (3) with the flux model Eq. (4) gives $\mathsf{C}\frac{d}{dk}\left(\sqrt{\frac{\varepsilon}{\nu}}kE_\theta\right) = -2\kappa k^2 E_\theta$ with the solution $E_\theta(k) = k^{-1}e^{-(2/\mathsf{C})(k/k_B)^2}$ (recall that $k_B = (\varepsilon/(\nu\kappa^2)^{1/4})$. The flux model Eq. (6) gives instead an equation with a leading order asymptotic solution $E_\theta(k) \sim k^2 e^{-(k/\sqrt{\mathsf{C}}k_B)}$. Thus, Eq. (6) predicts slower decay in the diffusive range than Eq. (4). DNS data [2] support this prediction. However, this finding does not necessarily establish Kraichnan's formulation instead of Batchelor's: an extension of Batchelor's argument had already been suggested in [6], namely, that if the strain rate in Batchelor's theory is taken to be a random variable γ with mean $\langle\gamma\rangle = \sqrt{\varepsilon/\nu}$, then although the k^{-1} range is preserved (since it is linear in γ), the dissipation range is not; Gotoh has shown [7] that the pdf of γ can be chosen so that the expected scalar spectrum is $E_\theta(k) = \int \langle E_\theta(k)|\gamma\rangle P(\gamma)d\gamma \sim k^{-3/2}e^{-ak/k_B}$, with a theoretically predicted constant a. Although the prefactor is not the same as Kraichnan's, this approach makes the Batchelor formulation consistent with the exponential decay of the Kraichnan formulation.

This observation causes us to seek another way to distinguish these physically very different pictures. Higher order statistics like the mean square advection

$$\langle(\boldsymbol{u}\cdot\nabla\theta)^2\rangle = \int d\boldsymbol{k} \int_{\boldsymbol{k}=\boldsymbol{p}+\boldsymbol{q}=-\boldsymbol{p}'-\boldsymbol{q}'} d\boldsymbol{p}d\boldsymbol{p}'\ \langle \boldsymbol{u}(\boldsymbol{p})\cdot\boldsymbol{q}\theta(\boldsymbol{q})\boldsymbol{u}(\boldsymbol{p}')\cdot\boldsymbol{q}'\theta(\boldsymbol{q}')\rangle \quad (7)$$

offer a possibility. If we evaluate this fourth order moment by assuming independence of Fourier modes as in the quasinormality theory, we will obtain $\langle(\boldsymbol{u}\cdot\nabla\theta)^2\rangle = \int d\boldsymbol{k} \int_{\boldsymbol{k}=\boldsymbol{p}+\boldsymbol{q}} d\boldsymbol{p}\, U_{ij}(\boldsymbol{p}) q_i q_j U_\theta(\boldsymbol{q})$. In reality, cumulant corrections to Eq. (7) exist and are well predicted by closure [8]. These cumulants give a reduction of mean-square advection compared to the value assuming quasinormality.

Concerning cumulants in Batchelor's theory, we can only extrapolate, since Batchelor never wrote anything about this issue. But if we evaluate Eq. (7) in the RDT-like limit $\boldsymbol{p},\boldsymbol{p}' = 0$, $\boldsymbol{q} = -\boldsymbol{q}' = \boldsymbol{k}$ which characterizes Batchelor's theory, we will obtain $\langle \boldsymbol{u}(\boldsymbol{p})\cdot\boldsymbol{q}\theta(\boldsymbol{q})\boldsymbol{u}(\boldsymbol{p}')\cdot\boldsymbol{q}'\theta(\boldsymbol{q}')\rangle \to U_{ij}k_i k_j U_\theta(\boldsymbol{k})$ where U_{ij} is evaluated at zero wavenumber and is therefore actually a mean field as suggested earlier. This conclusion is not changed if the velocity field depends on a fluctuating total strain γ, because evaluation of the mean square advection then gives $\int d\gamma P(\gamma) U_{ij}(\gamma) k_i k_j U_\theta(\boldsymbol{k})$. In either case, we obtain zero cumulants.

Thus, although the Batchelor formulation can predict the same exponential decay in the diffusive range as the Kraichnan formulation if the strain rate fluctuates, the formulations differ in their predictions of mean-square advection: Kraichnan's predicts cumulants corresponding to suppression of mean-square advection, but Batchelor's predicts zero cumulants, even if the strain rate fluctuates.

Can we use this conclusion to decide which formulation is the more accurate? Although DNS data do clearly exhibit the 'suppression of advection' we have described in the inertial-convective range, no suitable high Schmidt number DNS data has yet been interrogated with respect to this property; thus, we cannot be certain that the predicted cumulant corrections actually exist. Moreover, the cumulant predicted by closure appears to diminish as the Schmidt number increases; thus, the discrepancy between the Batchelor and Kraichnan formulations may not actually be so large. To conclude, existing knowledge does not favor one formulation over the other and further research will be needed to decide between them.

Acknowledgements. We would like to thank Timothy Clark, Toshiyuki Gotoh, and Yukio Kaneda for numerous discussions of the issues discussed in this paper.

References

[1] Batchelor, G.K.: J. Fluid Mech. 5, 113–133 (1959)
[2] Donzis, D.A., Sreenivasan, K.R., Yeung, P.K.: Flow Turb. Comb. Flow Turb. Comb. 85, 549–566 (2010)
[3] Newman, G.R., Herring, J.R.: J. Fluid Mech. 94, 163–194 (1979)
[4] Clark, T.T., Rubinstein, R., Weinstock, J.: J. Turbulence 10, N31 (2009)
[5] Leith, C.E.: Phys. Fluids 11, 1612–1617 (1968)
[6] Kraichnan, R.H.: Phys. Fluids 11, 945–953 (1968)
[7] Gotoh, T.: private communication (2012)
[8] Bos, W.J.T., Rubinstein, R., Fang, L.: Phys. Fluids 24, 075104 (2012)

The KOSL Scaling, Invariant Measure and PDF of Turbulence

Björn Birnir

In 1941 Kolmogorov and Obukhov [9, 12] proposed that there exists a statistical theory of turbulence that should allow the computation of all the statistical quantities that can be computed and measured in turbulent systems. These are quantities such as the moments, the structure functions and the probability density functions (PDFs) of the turbulent velocity field. The Kolmogorov-Obukhov '41 theory predicted that the structure functions of turbulence, that are the moments of the velocity differences at distances separated by a lag variable l, should scale with the lag variable to a power $p/3$ for the pth structure function, multiplied by a universal constant. This was found to be inconsistent with observations and in 1962 Kolomogorov and Obukhov [10, 13] presented a refined scaling hypothesis, where the multiplicative constants are not universal and the scaling exponents are modified to $\zeta_p = p/3 + \tau_p$, by the intermittency correction τ_p that are due to intermittency in the turbulent velocity. It was still not clear what the values of τ_p should be, because the log-normal exponents suggested by Kolmorogov turned out again to be inconsistent with observations. Then in 1994 She and Leveque [16] found the correct (log-Poissonian) formulas for τ_p that are consistent with modern simulations and experiments.

In this paper we will outline how the statistical theory of Kolmogorov and Obukhov is derived from the Navier-Stokes equation without getting into any of the technical details. We start with the classical Reynolds decomposition of the velocity into the mean (large scale) flow and the fluctuations or small scale flow. Then we develop a stochastic Navier-Stokes equation [6], for the small scale flow. If we assume that dissipation take place on all scales in the inertial range (defined below) then it turns out that the noise in this stochastic Navier-Stokes equation is determined by well-known theorems in probability. The additive noise in the stochastic Navier-Stokes equation is generic noise given by the central limit theorem and the large deviation principle. The multiplicative noise consists of jumps multiplying the

Björn Birnir
CNLS and Department of Mathematics
UC Santa Barbara
e-mail: birnirb@gmail.com

A. Talamelli et al. (eds.), *Progress in Turbulence V*,
Springer Proceedings in Physics 149,
DOI: 10.1007/978-3-319-01860-7_5,

velocity, modeling jumps in the velocity gradient. We will explain how this form of the noise follows from very general hypothesis.

Once the form of the noise in the stochastic Navier-Stokes equation for the small scales is determined, we can estimate the structure functions of turbulence and establish the Kolmogorov-Obukhov '62 scaling hypothesis with the She-Leveque intermittency corrections [5]. Then one can compute the invariant measure of turbulence writing the stochastic Navier-Stokes equation as an infinite-dimensional Ito process and solving the linear Kolmogorov-Hopf [8] functional differential equation for the invariant measure. Finally the invariant measure can be projected onto the PDF. The PDFs turn out to be the normalized inverse Gaussian (NIG) distributions of Barndorff-Nilsen [1, 2], and compare well with PDFs from simulations and experiments. The details of the proofs can be found in [5] and the background material can be found in [6].

A general incompressible fluid flow satisfies the Navier-Stokes Equation

$$u_t + u \cdot \nabla u = \nu \Delta u - \nabla p, \qquad u(x,0) = u_0(x)$$

with the incompressibility condition $\nabla \cdot u = 0$. Eliminating the pressure using the incompressibility condition gives

$$u_t + u \cdot \nabla u = \nu \Delta u + \nabla \Delta^{-1} \text{trace}(\nabla u)^2, \qquad u(x,0) = u_0(x).$$

The turbulence is quantified by the dimensionless Taylor-Reynolds number $Re_\lambda = \frac{U\lambda}{\nu}$ [14].

Following the classical Reynolds decomposition [15], we decompose the velocity into mean flow U and the fluctuations u. Then the velocity is written as $U+u$, where U describes the large scale flow and u describes the small scale turbulence. We must also decompose the pressure into mean pressure P and the fluctuations p, then the equation for the large scale flow can be written as

$$U_t + U \cdot \nabla U = \nu \Delta U - \nabla P - \nabla \cdot (\overline{u \otimes u}), \tag{1}$$

where in coordinates $\nabla \cdot (\overline{u \otimes u}) = \frac{\partial \overline{u_i u_j}}{\partial x_j}$, that is ∇ is dotted with the rows of $\overline{u_i u_j}$ and $R_{ij} = \overline{u \otimes u}$ is the Reynolds stress, see [3]. The Reynolds stress has the interpretation of a turbulent momentum flux and the last term in (1) is also know as the eddy viscosity. It describes how the small scales influence the large scales. In addition we get divergence free conditions for U, and u

$$\nabla \cdot U = 0, \qquad \nabla \cdot u = 0.$$

Together, (1) and the divergence free condition on U give Reynolds Averaged Navier-Stokes (RANS) that forms the basis for most contemporary simulations of turbulent flow.

Finding a constitutive law for the Reynolds stress $\overline{u \otimes u}$ is the famous closure problem in turbulence and we will solve that by writing down a stochastic equation for the small scale velocity u. The hypothesis is that the large scale influence the

small scales directly, through the fluid instabilities and the noise in fully developed turbulence. An example of this mechanics, how the instabilities magnify the tiny ambient noise to produce large noise, in given in [4], see also Chapter 1 in [6].

Now consider the inertial range in turbulence. In Fourier space this is the range of wave numbers k: $\frac{1}{L} \leq |k| \leq \frac{1}{\eta}$, where $\eta = (\nu^3/\varepsilon)^{1/4}$ is the Kolmogorov length scale, ε is the energy dissipation and L the size of the largest eddies, see [6]. If we assume that dissipation takes place on all length scale in the inertial range then the form of the dissipation processes are determined by the fundamental theorems of probability. Namely, if we impose periodic boundary conditions (different boundary conditions correspond to different basis vectores), then the central limit theorem and the large deviation principle stipulate that the additive noise in the Navier-Stokes equation for the small scale must be of the form:

$$\sum_{k\neq 0} c_k^{\frac{1}{2}} db_t^k e_k(x) + \sum_{k\neq 0} d_k |k|^{1/3} dt \; e_k(x),$$

where $e_k(x) = e^{2\pi i k\cdot x}$ are the Fourier coefficient and $c_k^{\frac{1}{2}}$ and d_k are coefficients that ensure the series converge in 3 dimensions. The first term describes the mean of weakly coupled dissipation processes given by the central limit theorem and the second term describes the large deviations of that mean, given by the large deviation principle, see [6]. Thus together the two terms give a complete description of the mean of the dissipation process similar to the mean of many processes in probability. The factor $|k|^{1/3}$ implies that the mean dissipation has only one scaling. The Fourier coefficients of the first series contain independent Brownian motions b_t^k and thus the noise is white in time in the infinitely many directions in function space. The noise cannot be white in space, hence the decaying coefficients $c_k^{1/2}$ and d_k, because if it was the small scale velocity u would be discontinuous in 3 dimension, see [5]. This is contrary to what is observed in nature.

The other part of the noise, in fully developed turbulence, is multiplicative and models the excursion (jumps) in the velocity gradient or vorticity concentrations. If we let N_t^k denote the integer number of velocity excursion, associated with kth wavenumber, that have occurred at time t, so that the differential $dN^k(t) = N^k(t+dt) - N^k(t)$ denotes the number of excursions in the time interval $(t, t+dt]$, then the process $df_t^3 = \sum_{k\neq 0}^M \int_{\mathbb{R}} h_k(t,z)\bar{N}^k(dt,dz)$, gives the multiplicative noise term. One can show that any noise corresponding to jumps in the velocity gradients must have this multiplicative noise to leading order, see [5]. A detailed derivation of both the noise terms can be found in [5] and [6].

Adding the additive noise and the multiplicative noise we get the stochastic Navier-Stokes equations describing the small scales in fully developed turbulence

$$du = (\nu\Delta u - u\cdot\nabla u + \nabla\Delta^{-1}\mathrm{tr}(\nabla u)^2)dt + \sum_{k\neq 0} c_k^{\frac{1}{2}} db_t^k e_k(x) + \sum_{k\neq 0} d_k|k|^{1/3} dt \; e_k(x)$$
$$+ u(\sum_{k\neq 0}^M \int_{\mathbb{R}} h_k \bar{N}^k(dt,dz)) - U\cdot\nabla u - u\cdot\nabla U, \;\; u(x,0) = u_0(x), \quad (2)$$

where we have used the divergence free condition $\nabla \cdot u = 0$ to eliminate the small scale pressure p. Each Fourier component e_k comes with its own Brownian motion b_t^k and a deterministic bound $|k|^{1/3}dt$.

The next step is to figure out how the generic noise interacts with the Navier-Stokes evolution. This is determined by the integral form of the equation (2),

$$u = e^{Kt}e^{\int_0^t dq}M_t u^0 + \sum_{k\neq 0}\int_0^t e^{K(t-s)}e^{\int_s^t dq}M_{t-s}(c_k^{1/2}d\beta_s^k + d_k\mu_k ds)e_k(x), \qquad (3)$$

where K is the operator $K = \nu\Delta + \nabla\Delta^{-1}tr(\nabla u\nabla)$, and we have omitted the terms $-U\cdot\nabla u - u\cdot\nabla U$ in (2), to simplify the exposition. We solve (2) using the Feynmann-Kac formula, and the Cameron-Martin formula (or Girsanov's Theorem) from probability theory, see [6], to get (3). The Cameron-Martin formula gives the Martingale $M_t = exp\{-\int_0^t u(B_s,s)\cdot dB_s - \frac{1}{2}\int_0^t |u(B_s,s)|^2 ds\}$. The Feynmann-Kac formula gives the exponential of a sum of terms of the form $\int_s^t dq^k = \int_0^t\int_{\mathbb{R}} \ln(1+h_k)N^k(dt,dz) - \int_0^t\int_{\mathbb{R}} h_k m^k(dt,dz)$, see [5] or [6] Chapter 2 for details. The form of the processes

$$e^{\int_0^t\int_{\mathbb{R}}\ln(1+h_k)N^k(dt,dz) - \int_0^t\int_{\mathbb{R}}h_k m^k(dt,dz)} = e^{N_t^k \ln\beta + \gamma\ln|k|} = |k|^{\gamma}\beta^{N_t^k} \qquad (4)$$

was found by She and Leveque [16], for $h_k = \beta - 1$. It was pointed out by She and Waymire [17] and by Dubrulle [7] that they are log-Poisson processes. The upshot of this computation is that we see the Navier-Stokes evolution acting on the additive noise to give the Kolmogorov-Obukhov '41 scaling, and the Navier-Stokes evolution acting on the multiplicative noise to produce the intermittency corrections through the Feynmann-Kac formula. Together these two scaling combine to give the scaling of the structure functions in turbulence,

Lemma 1 (The Kolmogorov-Obukhov-She-Leveque scaling). *The scaling of the structure functions is*

$$S_p \sim C_p|x-y|^{\zeta_p}, \qquad \zeta_p = \frac{p}{3} + \tau_p = \frac{p}{9} + 2(1-(2/3)^{p/3}).$$

$\frac{p}{3}$ *being the Kolmogorov scaling and* τ_p *the intermittency corrections. The scaling of the structure functions is consistent with Kolmogorov's* $4/5$ *law,* $S_3 = -\frac{4}{5}\varepsilon|x-y|$, *to leading order, were* $\varepsilon = -\frac{d\mathcal{E}}{dt}$ *is the energy dissipation.*

The first structure functions is estimated by

$$S_1(x,y,\infty) \leq \frac{2}{C}\sum_{k\in\mathbb{Z}^3\setminus\{0\}}\frac{|d_k|(1-e^{-\lambda_k t})}{|k|^{\zeta_1}}|\sin(\pi k\cdot(x-y))|.$$

We get a stationary state as $t\to\infty$, and for $|x-y|$ small, $S_1(x,y,\infty) \sim \frac{2\pi^{\zeta_1}}{C}\sum_{k\in\mathbb{Z}^3\setminus\{0\}} |d_k||x-y|^{\zeta_1}$, where $\zeta_1 = 1/3 + \tau_1 \approx 0.37$. Similarly, $S_2(x,y,\infty) \sim \frac{4\pi^{\zeta_2}}{C^2}\sum_{k\in\mathbb{Z}^3\setminus\{0\}}[{d_k}^2 + (\frac{C}{2})c_k]|x-y|^{\zeta_2}$, when $|x-y|$ is small, where $\zeta_2 = 2/3+\tau_2 \approx 0.696$, and $S_3(x,y,\infty) \sim \frac{2^3\pi}{C^3}\sum_{k\in\mathbb{Z}^3\setminus\{0\}}[|d_k|^3 + 3(C/2)c_k|d_k|]|x-y|$. For the pth structure functions, we get that S_p is estimated by

$$S_p \leq \frac{2^p}{C^p} \sum_{k\in\mathbb{Z}^3\setminus\{0\}} \frac{\sigma^p \cdot (-i\sqrt{2}\mathrm{sgn}\, M)^p\, U\left(-\frac{1}{2}p, \frac{1}{2}, -\frac{1}{2}(M/\sigma)^2\right)}{|k|^{\zeta_p}} |\sin^p(\pi k\cdot(x-y))|.$$

where U is the confluent hypergeometric function, $M = |d_k|(1-e^{-\lambda_k t})$ and $\sigma = \sqrt{(C/2)c_k(1-e^{-2\lambda_k t})}$. The details of these estimates are given in [5].

The integral equation can be considered to be an infinite-dimensional Ito process, see [6]. This means that we can find the associated Kolmogorov backward equation for the Ito diffusion associated with the equation (3) and this equations that determines the invariant measure of turbulence, see [5], is linear. This was first attempted by Hopf [8] wrote down a functional differential equation for the characteristic function of the invariant measure of the deterministic Navier-Stokes equation. The Kolmogorov-Hopf (backward) equation for (2) is

$$\frac{\partial\phi}{\partial t} = \frac{1}{2}\mathrm{tr}[P_t C P_t^* \Delta\phi] + \mathrm{tr}[P_t \bar{D}\nabla\phi] + < K(z)P_t, \nabla\phi >, \tag{5}$$

see [5] and [6] Chapter 3, where $\bar{D} = (|k|^{1/3}D_k)$, $\phi(z)$ is a bounded function of z, $P_t = e^{-\int_0^t \nabla u\, dr} M_t \prod_k^m |k|^{2/3}(2/3)^{N_t^k}$. The variance and drift are defined to be

$$Q_t = \int_0^t e^{K(s)} P_s C P_s^* e^{K^*(s)} ds, \quad E_t = \int_0^t e^{K(s)} P_s \bar{D} ds. \tag{6}$$

In distinction to the nonlinear Navier-Stokes equation (2) that cannot be solved explicitly, the linear equation (5) can be solved. The solution of the Kolmogorov-Hopf equation (5) is

$$R_t\phi(z) = \int_H \phi(e^{Kt}P_t z + EI + y)\mathcal{N}_{(0,Q_t)} * \mathbb{P}_{N_t}(dy),$$

$\mathbb{P}_{N_t}$ being the law of the log-Poisson process (4). The invariant measure of turbulence that appears in the last equation can now be expressed explicitly,

Theorem 1. *The invariant measure of the Navier-Stokes equation on* $H_c = H^{3/2^+}(\mathbb{T}^3)$ *is,*

$$\mu(dx) = e^{<Q^{-1/2}EI,\, Q^{-1/2}x> - \frac{1}{2}|Q^{-1/2}EI|^2} \mathcal{N}_{(0,Q)}(dx) \sum_k \delta_{k,l} \sum_{j=0}^{\infty} p_{m_l}^j \delta_{(N_l - j)}$$

where $Q = Q_\infty$, $E = E_\infty$, $m_k = \ln|k|^{2/3}$ *is the mean of the log-Poisson processes (4) and* $p_{m_k}^j = \frac{(m_k)^j e^{-m_k}}{j!}$ *is the the probability of* $N_\infty^k = N_k$ *having exactly* j *jumps,* $\delta_{k,l}$ *is the Kroncker delta function.*

This shows that the invariant measure of turbulence is simply a product of two measure, one an infinite-dimensional Gaussian that gives the Kolmogorov-Obukhov scaling and the other a discrete Poisson measure that gives the She-Leveque

intermittency corrections. Together they produce the scaling of the structure functions in Lemma 1.

The quantity that can be compared directly to experiments is the probability density function (PDF). We take the trace of the Kolmogorov-Hopf equation (5), see [6] Chapter 3, to compute the differential equation satisfied by the PDE. The stationary equation satisfied by the PDF is

$$\frac{1}{2}\phi_{rr} + \frac{1+|c|}{r}\phi_r = \frac{1}{2}\phi. \tag{7}$$

Lemma 2. *The PDF is a Normalized Inverse Gaussian distribution NIG of Barndorff-Nilsen [1]:*

$$f(x) = \frac{(\delta/\gamma)}{\sqrt{2\pi}K_1(\delta\gamma)} \frac{K_1\left(\alpha\sqrt{\delta^2+(x-\mu)^2}\right)e^{\beta(x-\mu)}}{\left(\sqrt{\delta^2+(x-\mu)^2}/\alpha\right)} \tag{8}$$

where K_1 is modified Bessel's function of the second kind, $\gamma = \sqrt{\alpha^2-\beta^2}$.

(8) is the solution of (7) and the PDF that can be compared a large class of experimental data.

We finally explain how we get around the famous non-uniqueness problem of the Navier-Stokes equation. It is well known that the fluid velocity u solving the (stochastic) Navier-Stokes equation may not be unique in 3 dimensions. However, the invariant measure in Theorem 1 exists by Leray's '34 [11] theory, see Theorem 2 below. If the velocity is not unique different velocities give equivalent statistics. Thus the statistical theory is unique although the velocity u may not be.

Theorem 2. *The solution of the stochastic Navier-Stokes equation (2) satisfies the estimates*

$$E(|u|_2^2)(t) \le |u|_2^2(0)e^{-at} + \frac{1}{a}\left(\frac{2|T|}{\varepsilon}\sum_{k\neq 0} d_k|k|^{\frac{1}{3}} + \sum_{k\neq 0} c_k\right) + \frac{|T|}{a}\ln\left(\prod_{k=1}^{m}|k|^2\right)^{\frac{1}{9}},$$

and

$$(1-\varepsilon D)\sup_{[0,t]} E(|u|_2^2)(t) + 2\nu\int_0^t E(|\nabla u|)(s)ds \le |u|_2^2(0) + \left(\frac{|T|}{\varepsilon}\sum_{k\neq 0} d_k|k|^{\frac{1}{3}} + \sum_{k\neq 0} c_k\right)t + |T|\ln\left(\prod_{k=1}^{m}|k|^2\right)^{\frac{1}{9}},$$

where $D = \sum_{k\neq 0} d_k|k|^{1/3}$, E denotes the expectation, $a = 2\nu\lambda_1 - D$, λ_1 is the first eigenvalue of $-\Delta$, with vanishing boundary conditions, ε is a small number and $|T|$ is the volume of the torus (box with periodic boundary conditions).

The proof of the theorem is similar to the proof of the Leray theory in Chapter 4, in [6].

References

1. Barndorff-Nilsen, O.E.: Exponentially decreasing distributions for the logarithm of the particle size. Proc. R. Soc. London A353, 401–419 (1977)
2. Barndorff-Nilsen, O.E., Blaesild, P., Schmiegel, J.: A parsimonious and universal description of turbulent velocity increments. Eur. Phys. J. B 41, 345–363 (2004)
3. Bernard, P.S., Wallace, J.M.: Turbulent Flow. John Wiley & Sons, Hoboken (2002)
4. Birnir, B.: Turbulence of a unidirectional flow. In: Proceedings of the Conference on Probability, Geometry and Integrable Systems, MSRI, p. 55. MSRI Publications, Cambridge Univ. Press (December 2007), http://repositories.cdlib.org/cnls/
5. Birnir, B.: The Kolmogorov-Obukhov statistical theory of turbulence. J. Nonlinear Sci. (2013), doi:10.1007/s00332-012-9164-z
6. Birnir, B.: The Kolmogorov-Obukhov Theory of Turbulence. Springer, New York (2013)
7. Dubrulle, B.: Intermittency in fully developed turbulence: in log-Poisson statistics and generalized scale covariance. Phys. Rev. Letters 73(7), 959–962 (1994)
8. Hopf, E.: Statistical hydrodynamics and functional calculus. J. Rat. Mech. Anal. 1(1), 87–123 (1953)
9. Kolmogorov, A.N.: The local structure of turbulence in incompressible viscous fluid for very large Reynolds number. Dokl. Akad. Nauk SSSR 30, 9–13 (1941)
10. Kolmogorov, A.N.: A refinement of previous hypotheses concerning the local structure of turbulence in a viscous incompressible fluid at high Reynolds number. J. Fluid Mech. 13, 82–85 (1962)
11. Leray, J.: Sur le mouvement d'un liquide visqueux emplissant l'espace. Acta Math. 63(3), 193–248 (1934)
12. Obukhov, A.M.: On the distribution of energy in the spectrum of turbulent flow. Dokl. Akad. Nauk SSSR 32, 19 (1941)
13. Obukhov, A.M.: Some specific features of atmospheric turbulence. J. Fluid Mech. 13, 77–81 (1962)
14. Reynolds, O.: An experimental investigation of the circumstances which determine whether the motion of water shall be direct or sinuous, and the the law of resistance in parallel channels. Phil. Trans. Roy. Soc. Lond. 174(11), 935–982 (1883)
15. Reynolds, O.: On the dynamical theory of incompressible viscous fluids and the determination of the criterion. Phil. Trans. Roy. Soc. Lond. 186A, 123–164 (1885)
16. She, Z.-S., Leveque, E.: Universal scaling laws in fully developed turbulence. Phys. Rev. Letters 72(3), 336–339 (1994)
17. She, Z.-S., Waymire, E.: Quantized energy cascade and log-poisson statistics in fully developed turbulence. Phys. Rev. Letters 74(2), 262–265 (1995)

Depression of Nonlinearity and Advection in Isotropic Turbulence

Wouter J.T. Bos and Robert Rubinstein

Abstract. We investigate the depletion of nonlinearity in isotropic turbulence using a Markovianized version of the Direct Interaction Approximation (DIA). It is shown that this depletion is present in both the inertial range and dissipation range scales at high Reynolds numbers. The mixing of a passive scalar shows a similar depletion of advection.

1 Introduction

In turbulent flows, velocity and vorticity have a tendency to align in the small scales. This alignment, also called Beltramization, results in a weakening of the nonlinear term. Pelz *et al.* [1] suggested that this effect might importantly affect the turbulence dynamics. However, as outlined by Kraichnan and Panda [2], the depletion of nonlinearity in Navier-Stokes turbulence is much stronger than can be explained by local Beltramization. It was shown that it is an effect that is common to a wide class of systems, displaying quadratic nonlinearity. In [3] it was shown that the effect of depletion of nonlinearity can be adequately captured by closure theory. The results in that study were obtained at Reynolds numbers of approximately $R_\lambda = 20$. We use the approach outlined in [3] to obtain predictions for 4^{th} order correlations at much higher Reynolds numbers.

Wouter J.T. Bos
CNRS, LMFA, Ecole Centrale de Lyon, Université de Lyon, Ecully, France
e-mail: wouter.bos@ec-lyon.fr

Robert Rubinstein
Newport News, VA USA

A. Talamelli et al. (eds.), *Progress in Turbulence V*,
Springer Proceedings in Physics 149,
DOI: 10.1007/978-3-319-01860-7_6,

2 Method

In [3], the DIA was used to derive closed expressions for the nonlinearity spectrum. This spectrum is defined so that its integral yields the mean-square value of the complete nonlinear term in the Navier-Stokes equations,

$$\int w(k)dk = \overline{|\boldsymbol{u}\cdot\nabla\boldsymbol{u}+\nabla p|^2}. \tag{1}$$

The resulting expression depended in [3] on the two-time energy spectrum and the response funtion. In our approach, we use these DIA expressions and simplify them by assuming an exponential time dependence of the response function and the two-time energy spectrum, with a time-scale consistent with Kolmogorov's 1941 inertial range theory. The details of this procedure are outlined in [4, 5]. The resulting expression is numerically integrated and the results are presented in the following paragraph.

3 Depletion of Nonlinearity

In figure 1, we show $w(k)$, the spectrum of the nonlinear term, normalized by its Gaussian estimate $w_G(k)$. The ratio $w(k)/w_G(k)$ is a measure of the depletion of nonlinearity at different lengthscales. It is observed that in the dissipation range the nonlinearity drops to a value close to zero. In the inertial range the nonlinearity divided by its Gaussian estimate is close to a constant value. In [4] it is shown that the variance of the nonlinear term is sweeping-dominated. The depletion of nonlinearity is therefore directly related to a partial suppression of the sweeping of the small scales by the large scales. An open question is how this depletion of nonlinearity is related to the stabilization of coherent structures.

4 Depletion of Advection in Passive Scalar Mixing

The approach followed in the preceeding paragraph was subsequently applied to the mixing of a passive scalar in isotropic turbulence and closure expressions were derived [5]. In this case we study the suppression of the advection term compared to its Gaussian value. The spectrum we analyze is

$$\int w_\theta(k)dk = \overline{[\boldsymbol{u}\cdot\nabla\theta]^2}. \tag{2}$$

We consider the case of an isotropic passive scalar, forced at the large scales, advected by an isotropic turbulent velocity field. Results for mixing at Prandtl numbers varying from 0.01 to 100 are shown in Figure 2, as obtained by integrating the Eddy-Damped Quasi-Normal Markovian closure model. The energy spectrum and the passive scalar spectra show clear scaling behavior in agreement with Kolmogorov-Corrsin-Obukhov phenomenology in the inertial range. For large and

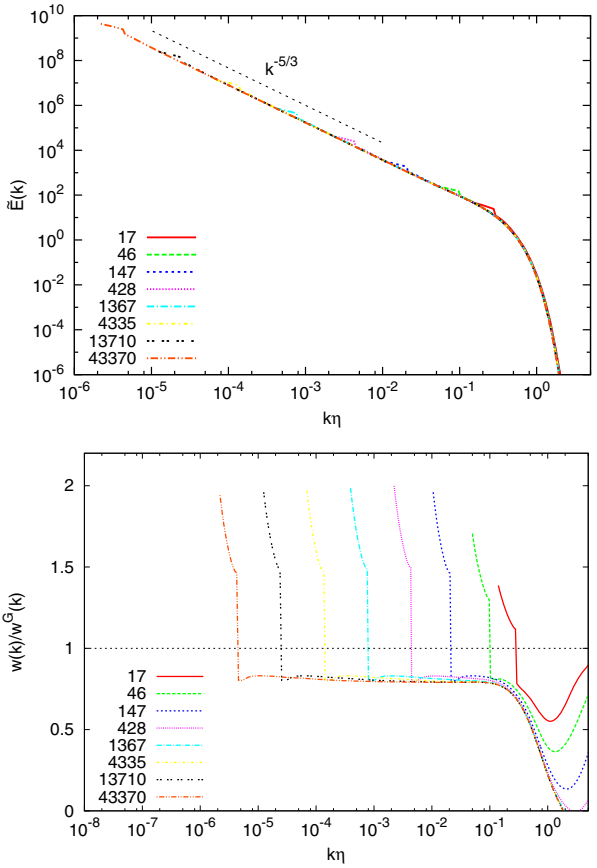

Fig. 1 Top: energy spectra of isotropic turbulence at Taylor-scale Reynolds numbers between 17 and 4.10^4. Bottom: comparison of the spectrum of the mean square nonlinear term of the Navier-Stokes equation in isotropic turbulence to its Gaussian value.

small Prandtl number, the scaling is in agreement with Batchelor and Batchelor-Howells-Townsend scaling, respectively. As for the mean-square nonlinear term, we observe a depletion of advection in both the inertial-convective range and the scalar dissipation range. The effect is weaker in the Batchelor range (in which the scalar spectrum is proportional to k^{-1}). The depletion of advection should manifest itself in the instantaneous flow fields as an enhanced probability to observe the scalar gradient to be aligned or anti-aligned with the velocity field, when commpared to a fully random scalar field, and this is currently under investigation. An interesting perspective is the investigation of the link between this reduction of advection and the enhancement of scalar gradients and fronts.

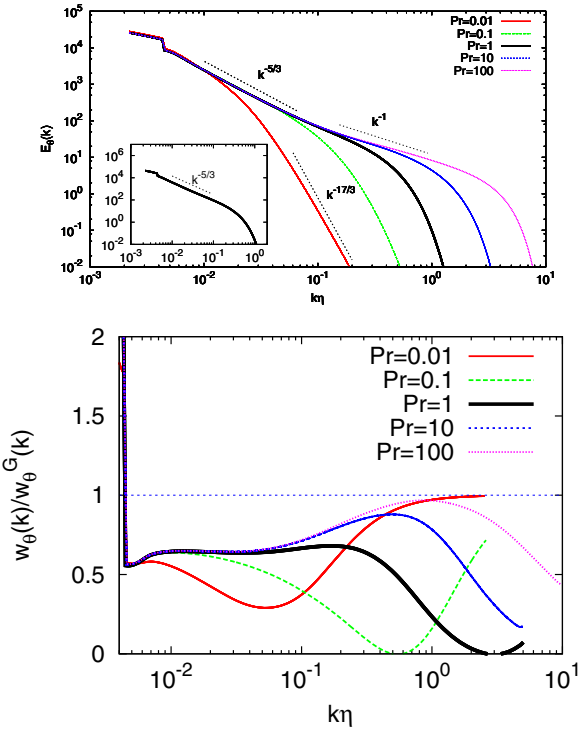

Fig. 2 Top: scalar variance spectra and energy spectrum (inset) of isotropic turbulence advecting an isotropic passive scalar at a Taylor-scale Reynolds number of 428 for different Prandtl numbers. Bottom: comparison of the spectrum of the mean square advection term of the scalar equation in isotropic turbulence to its Gaussian value.

References

1. Pelz, R.B., Yakhot, V., Orszag, S.A., Shtilman, L., Levich, E.: Velocity-vorticity patterns in turbulent flow. Phys. Rev. Lett. 54, 2505 (1985)
2. Kraichnan, R.H., Panda, R.: Depression of nonlinearity in decaying isotropic turbulence. Phys. Fluids 31, 2395–2397 (1988)
3. Chen, H., Herring, J.R., Kerr, R.M., Kraichnan, R.H.: Non-Gaussian statistics in isotropic turbulence. Phys. Fluids A 1, 1844–1854 (1989)
4. Bos, W.J.T., Rubinstein, R.: On the strenght of the nonlinearity in isotropic turbulence (submitted, 2012)
5. Bos, W.J.T., Rubinstein, R., Fang, L.: Reduction of mean-square advection in turbulent passive scalar mixing. Phys. Fluids 24, 075104 (2012)

"Symmetries and Conservation Laws" in the Closure Problem of Turbulence

Tomomasa Tatsumi

Abstract. The relative advantage of the statistical mechanical approach to fluid turbulence over the conventional statistical approach by means of the mean velocity products is briefly surveyed. In particular, it is shown that the requirements such as "symmetries and conservation laws" actually provide us with the necessary and sufficient conditions for the statistical mechanical approach.

1 Introduction

The present iTi School, prior to the iTi Conference 2012, is entitled as "*Symmetries and Conservation Laws*". This title is actually concerned with the closure problem in the statistical theory of turbulence.

1.1 Statistical Dynamics of Turbulence

The practical and traditional way of dealing with statistics of turbulence is to represent the turbulent velocity field in terms of the *mean velocity products* at several spatial points and a time.

$$
\begin{aligned}
&U^{(2)}_{i_1 i_2}\left(\mathbf{x}_1, \mathbf{x}_2; t\right) = \left\langle u_{i_1}\left(\mathbf{x}_1, t\right)\ u_{i_2}\left(\mathbf{x}_2, t\right)\right\rangle, \\
&U^{(n)}_{i_1 \ldots i_n}\left(\mathbf{x}_1, \ldots, \mathbf{x}_n; t\right) = \left\langle \Pi^{n}_{m=1} u_{i_m}\left(\mathbf{x}_m, t\right)\right\rangle, \quad \text{for} \ \ n \geq 3,
\end{aligned} \tag{1}
$$

where the suffixes i_m $(1 \leq m \leq n)$ denote the component $(1, 2, 3)$ of the orthogonal coordinates $\mathbf{x}_m$, so that $U^{(n)}_{i_1 \ldots i_n}$ represents an n-th order tensor while the mean velocity $U^{(1)}_{i_1}$ is taken to zero in homogeneous turbulence.

Tomomasa Tatsumi
Professor Emeritus, Kyoto University,
26-6 Chikuzendai, Momoyama, Fushimi, Kyoto 612-8032, Japan
e-mail: tatsumi@skyblue.ocn.ne.jp

A. Talamelli et al. (eds.), *Progress in Turbulence V*,
Springer Proceedings in Physics 149,
DOI: 10.1007/978-3-319-01860-7_7,

1.2 Closure of Equations for Mean Velocity-Products

Dynamical equations governing these mean velocity products are derived from the Navier-Stokes equation. Then, we encounter the problem of unclosedness of these dynamical equations, since the equation for the mean velocity-product of the n-th order $U^{(n)}_{i_1\ldots i_n}$ always includes those of the higher-order $U^{(n+1)}_{i_1\ldots i_{n+1}}$ as another unknown, thanks to the nonlinearity of the Navier-Stokes equation. In order to overcome this difficulty, usually a closure assumption is introduced for expressing the higher-order product $U^{(n+1)}_{i_1\ldots i_{n+1}}$ in terms of those of the lower orders and then the unknown product $U^{(n)}_{i_1\ldots i_n}$ is obtained as the solution of the closed equation.

A number of studies along this line of idea have been made so far by theoreticians over the world, and actually the products of these works constitute a substantial part of the achievements in statistical theory of turbulence (see, for instance, the surveys by Frisch (1995), Lesieur (1993), and McComb (1990)).

2 Statistical Mechanics of Turbulence

An entirely different statistical mechanical approach to turbulence is made by dealing with the *joint-probability distributions* of the multi-point velocities, $\mathbf{u}_m(t) = \mathbf{u}(\mathbf{x}_m, t)$ $(1 \le m \le n)$ as follows:

$$\begin{aligned} &f(\mathbf{v}_1, \mathbf{x}_1, t) = \langle \delta(\mathbf{u}_1(t) - \mathbf{v}_1)\rangle, \\ &f^{(2)}(\mathbf{v}_1, \mathbf{v}_2; \mathbf{x}_1, \mathbf{x}_2; t) = \langle \delta(\mathbf{u}_1(t) - \mathbf{v}_1)\,\delta(\mathbf{u}_2(t) - \mathbf{v}_2)\rangle, \\ &f^{(n)}(\mathbf{v}_1, \ldots, \mathbf{v}_n; x_1, \ldots, \mathbf{x}_n; t) = \langle \Pi_{m=1}^{n}\delta(\mathbf{u}_m(t) - \mathbf{v}_m)\rangle, \quad \text{for} \quad n \ge 3, \end{aligned} \tag{2}$$

where $\mathbf{v}_m$ denotes the probability variable corresponding to the random velocity $\mathbf{u}_m(t)$ $(1 \le m \le n)$.

The statistical mechanical equations governing these velocity distributions $f^{(n)}$ $(n \ge 1)$ have been obtained by Lundgren (1967) and Monin (1967) independently. It should be noted that these equations are also unclosed, since the equation for the distribution of a certain order $f^{(n)}$ always includes the higher-order distribution $f^{(n+1)}$ as another unknown. In this case, however, the unclosedness is much easier to deal with, since the higher-order distribution $f^{(n+1)}$ appears only in the "degenerate" form as a "substantially n-point distribution".

2.1 Cross-Independence Closure

Probably, the simplest relationship between the velocity distributions of different orders may be the *independence relation*,

$$f^{(2)}\left(\mathbf{v}_1,\mathbf{v}_2;\mathbf{x}_1,\mathbf{x}_2;t\right)=f\left(\mathbf{v}_1,t\right)f\left(\mathbf{v}_2,t\right), \tag{3}$$

which is generally valid for large distance $r=|\mathbf{x}_2-\mathbf{x}_1|\to\infty$ according to the asymptotic independence of the one-point distributions in this limit, but not valid otherwise, especially for vanishing distance $r\to 0$.

A relation having a wider range of validity has been proposed by Tatsumi (2001) by introducing the *cross-velocities* or the *sum* and *difference* of the velocities $(\mathbf{u}_1,\mathbf{u}_2)$, as

$$\mathbf{u}_+=\frac{1}{2}\left(\mathbf{u}_1+\mathbf{u}_2\right),\quad \mathbf{u}_-=\frac{1}{2}\left(\mathbf{u}_2-\mathbf{u}_1\right), \tag{4}$$

and considering the distributions of these cross-velocities as

$$\begin{aligned} g_+\left(\mathbf{v}_+;\mathbf{x}_1,\mathbf{x}_2;t\right)&=\left\langle\delta\left(\mathbf{u}_+\left(\mathbf{x}_1,\mathbf{x}_2,t\right)-\mathbf{v}_+\right)\right\rangle,\\ g_-\left(\mathbf{v}_-;\mathbf{x}_1,\mathbf{x}_2;t\right)&=\left\langle\delta\left(\mathbf{u}_-\left(\mathbf{x}_1,\mathbf{x}_2;t\right)-\mathbf{v}_-\right)\right\rangle. \end{aligned} \tag{5}$$

$$g^{(2)}\left(\mathbf{v}_+,\mathbf{v}_-;\mathbf{x}_1,\mathbf{x}_2;t\right)=\left\langle\delta\left(\mathbf{u}_+\left(t\right)-\mathbf{v}_+\right)\delta\left(\mathbf{u}_-\left(t\right)-\mathbf{v}_-\right)\right\rangle. \tag{6}$$

Then, the *cross-independence relation* is defined as

$$g^{(2)}\left(\mathbf{v}_+,\mathbf{v}_-;\mathbf{x}_1,\mathbf{x}_2;t\right)=g_+\left(\mathbf{v}_+;\mathbf{x}_1,\mathbf{x}_2;t\right)g_-\left(\mathbf{v}_-;\mathbf{x}_1,\mathbf{x}_2;t\right). \tag{7}$$

If we take into account the identity for the distributions $f^{(2)}$ and $g^{(2)}$,

$$f^{(2)}\left(\mathbf{v}_1,\mathbf{v}_2;\mathbf{x}_1,\mathbf{x}_2;t\right)d\mathbf{v}_1d\mathbf{v}_2=g^{(2)}\left(\mathbf{v}_+,\mathbf{v}_-;\mathbf{x}_1,\mathbf{x}_2;t\right)d\mathbf{v}_+d\mathbf{v}_-,$$

or equivalently,

$$f^{(2)}\left(\mathbf{v}_1,\mathbf{v}_2;\mathbf{x}_1,\mathbf{x}_2;t\right)=2^{-3}g^{(2)}\left(\mathbf{v}_+,\mathbf{v}_-;\mathbf{x}_1,\mathbf{x}_2;t\right), \tag{8}$$

according to the Jacobian $\partial\left(d\mathbf{v}_+,d\mathbf{v}_-\right)/\partial\left(d\mathbf{v}_1,d\mathbf{v}_2\right)=2^{-3}$, the relation (7) is rewritten as

$$f^{(2)}\left(\mathbf{v}_1,\mathbf{v}_2;\mathbf{x}_1,\mathbf{x}_2;t\right)=2^{-3}g_+\left(\mathbf{v}_+;\mathbf{x}_1,\mathbf{x}_2;t\right)g_-\left(\mathbf{v}_-;\mathbf{x}_1,\mathbf{x}_2;t\right), \tag{9}$$

which provides us with the *cross-independence closure relation* for the distribution $f^{(2)}$.

Unlike the independence relation (3), the cross-independence relations (7) and (9) are valid for both large and small distances $r\to\infty$ and $r\to 0$, but generally not in between. Fortunately, it will be shown below that the closure is applied only to the vanishing distances $|\mathbf{x}_{n+1}-\mathbf{x}_m|\to 0$ $(m=1,\ldots,n)$ of the higher-order $f^{(n+1)}$ terms in the equation for $f^{(n)}$.

2.2 Closed Equation for One-Point Velocity Distribution

The closed equation for the *one-point velocity distribution* f is obtained by applying the cross-independence relation (9) to the higher-order $f^{(2)}$ term in the Lundgren-Monin equation for the distribution f. For homogeneous isotropic turbulence, the closed equation is expressed in the following simple form:

$$\left[\frac{\partial}{\partial t}+\alpha\left(t\right)\left|\frac{\partial}{\partial \mathbf{v}}\right|^2\right] f\left(\mathbf{v},t\right)=0, \tag{10}$$

$$\alpha\left(t\right)=\frac{2}{3}\nu\lim_{|\mathbf{r}|\to 0}\left|\frac{\partial}{\partial \mathbf{r}}\right|^2\int\left|\mathbf{v}_-\right|^2 g_-\left(\mathbf{v}_-,\mathbf{r},t\right)d\mathbf{v}_-=\frac{1}{3}\varepsilon\left(t\right), \tag{11}$$

with the suffix of $\mathbf{v}_1$ being omitted and $\mathbf{r}=\mathbf{x}_2-\mathbf{x}_1$, where g_- denotes the velocity-difference distribution defined by Eq.(5) and $\varepsilon\left(t\right)$ is the *mean energy-dissipation rate* defined by

$$\varepsilon\left(t\right)=\nu\sum_{i,j=1}^{3}\left\langle\left(\frac{\partial u_i\left(\mathbf{x},t\right)}{\partial x_j}\right)^2\right\rangle=-\frac{dE\left(t\right)}{dt}, \tag{12}$$

for homogeneous turbulence, and $E\left(t\right)$ is the *kinetic energy of turbulence* defined by

$$E\left(t\right)=\frac{1}{2}\left\langle\left|\mathbf{u}\left(\mathbf{x},t\right)\right|^2\right\rangle=\frac{1}{2}\sum_{i=1}^{3}\left\langle u_i\left(\mathbf{x},t\right)^2\right\rangle. \tag{13}$$

2.3 Energy Decay of Homogeneous Turbulence

The closed equation (10) for the distribution f seems to be a simple equation to be easily solved. This is, however, not the case.

First, it includes the *energy-dissipation rate,* $\varepsilon\left(t\right)=-dE\left(t\right)/dt$, as a parameter, so that we have to know the parameters $\varepsilon\left(t\right)$, or $E\left(t\right)$, as the function of time t, before solving the equation itself. In homogeneous turbulence which has no external energy source, the kinetic energy $E\left(t\right)$ and its time-derivative $\varepsilon\left(t\right)$ both have to decay in time, and all turbulent motions are driven by this decay of energy.

In the present case, the energy-decay law is immediately obtained from Kolmogorov's hypothesis of the inviscid energy-dissipation, $\varepsilon\left(t\right)>0$ for $\nu\to 0$, using the dimensional analysis, as

$$\varepsilon\left(t\right)=\varepsilon_0\ t^{-2}, \tag{14}$$

where t_0 and ε_0 denote certain initial values of t and $\varepsilon\left(t\right)$ respectively. Hence, it follows from Eqs.(12) and (13) that

$$E(t) = E_0\, t^{-1}, \quad E_0 = \varepsilon_0. \tag{15}$$

The inverse-linear decay law (15) of the kinetic energy $E(t)$ has been first obtained theoretically by Batchelor (1953) for the initial stage of the decay of turbulence. It has also been derived by Comte-Bellot & Corrsin (1966) from the condition of the vanishing integral-scales in the inviscid limit. Thus, the problem of the "conservation laws" has been completely fixed in the present context.

2.4 Self-similar Evolution of Velocity Distributions

The next problem is that the equation (10), having a negative diffusion coefficient $\alpha(t) < 0$, may lead to an ill-posed initial-value problem. In order to avoid such a possibility, we impose on the solution the self-similarity which is compatible with the energy-decay law (15). This is again the "symmetry" raised in the present One-Day School.

If we introduce the similarity variables as

$$\mathbf{w} = \mathbf{v}\, t^{1/2}, \quad \mathbf{w}_\pm = \mathbf{v}_\pm\, t^{1/2}, \quad \mathbf{s} = \mathbf{r}\, t^{-1/2}, \tag{16}$$

the distributions f and $g_\pm$ are written in the self-similar forms as follows:

$$f(\mathbf{v}, t) = t^{3/2}\, F(\mathbf{w}), \quad g_\pm(\mathbf{v}_\pm, \mathbf{r}, t) = t^{3/2}\, G_\pm(\mathbf{w}_\pm, \mathbf{s}). \tag{17}$$

Then, it follows from Eq.(11) that

$$\begin{aligned} \alpha(t) &= \frac{1}{3}\varepsilon(t) = \alpha_0\, t^{-2} = \frac{1}{3}\varepsilon_0\, t^{-2}, \\ \alpha_0 &= \frac{1}{3}\varepsilon_0 \;= \frac{2}{3}\nu \lim_{|\mathbf{s}|\to 0} \left|\frac{\partial}{\partial \mathbf{s}}\right|^2 \int |\mathbf{w}_-|^2\; G_-(\mathbf{w}_-, \mathbf{s})\, d\mathbf{w}_-. \end{aligned} \tag{18}$$

On substitution from Eqs.(16)–(18) and taking account of the isotropy of the operator, the equation (10) for the distribution f is written in the form of ordinary differential equation with respect to $w = |\mathbf{w}|$ as

$$\left[\frac{d^2}{dw^2} + \frac{2}{w}\frac{d}{dw} + \frac{1}{2\alpha_0}\left(w\frac{d}{dw} + 3\right)\right] F(w) = 0,$$

which is immediately factorized as

$$\left(\frac{d}{dw} + \frac{2}{w}\right)\left(\frac{d}{dw} + \frac{w}{2\alpha_0}\right) F(w) = 0. \tag{19}$$

2.5 Normal One-Point Velocity Distribution (N1)

The solution of Eq.(19) which is entitled to be a probability distribution is given by the solution of its homogeneous part,

$$\left(\frac{d}{dw}+\frac{w}{2\alpha_0}\right)F(w)=0, \tag{20}$$

that is,

$$F(w)=F_0(w)\equiv(4\pi\alpha_0)^{-3/2}\exp\left[-\frac{w^2}{4\alpha_0}\right], \tag{21}$$

which has been normalized by the condition: $\int_0^\infty F(w)\,4\pi w^2 dw=1$.

The self-similar distribution (21) is expressed in the original variables as

$$f(\mathbf{v},t)=f_0(\mathbf{v},t)\equiv\left(\frac{t}{4\pi\alpha_0}\right)^{3/2}\exp\left[-\frac{|\mathbf{v}|^2 t}{4\alpha_0}\right], \tag{22}$$

which may be called $N1$, and the corresponding one-dimensional distribution is given by

$$f(v,t)=f_0(v,t)\equiv\left(\frac{t}{4\pi\alpha_0}\right)^{1/2}\exp\left[-\frac{v^2 t}{4\alpha_0}\right], \tag{23}$$

both of which representing the *inertial-normal distributions* with the decreasing variance in time.

The distributions (22) and (23) change their forms self-similarly in time. At an initial time $t=0$, they represent an uniform distribution with infinitesimal probability density, grow up with time $t>0$ as the *normal distributions* with the decreasing variances or the *kinetic energy*, and eventually tend to the delta distributions around $|\mathbf{v}|=0$ in the limit of infinite time $t\to\infty$. The existing experimental results are generally in good agreement with the normality of the distribution $f(\mathbf{v},t)$ and its way of change in time.

2.6 Closed Equations for Cross-Velocity Distributions

The two-point velocity distribution $f^{(2)}$ defined by Eq.(2) is equivalently expressed by the cross-velocity distributions $g_\pm$ as Eq.(9). Thus, the set of the one-point velocity distribution f and the cross-velocity distributions $g_\pm$ constitutes the minimum deterministic mechanical system, irrespective to the higher-order velocity distributions.

The closed equations for the *cross-velocity distributions* $g_\pm$ can be derived from the closed equation for the distribution $f^{(2)}$, which is obtained by applying the cross-independence relation (9) to the higher-order $f^{(3)}$ terms in the Lundgren-Monin equation for the distribution $f^{(2)}$. However, unlike the case of the one-point distribution f, this closure scheme can be applied only for the distribution $f^{(2)}$ associated with a finite distance $r=|\mathbf{x}_2-\mathbf{x}_1|=O(L)$ as in

the global range, since otherwise, the application of the cross-independence relation to each of the higher-order $f^{(3)}$ terms should interact with each other. Thus, the case of small distance r of the distribution $f^{(2)}$ requires a more sophisticated treatment, that will be dealt with in the last subsection.

2.7 Normal Cross-Velocity Distributions (N2)

Now, if we restrict ourselves to the case of finite distance r of the distribution $f^{(2)}$ as for the *global range*, we can proceed in the same manner as for the distribution f and finally obtain the following closed equations for the cross-velocity distributions $g_{\pm}$:

$$\left[\frac{\partial}{\partial t}+\frac{1}{2}\alpha\left(t\right)\left|\frac{\partial}{\partial \mathbf{v}_{\pm}}\right|^{2}\right]\ g_{\pm}\left(\mathbf{v}_{\pm},t\right)=0, \tag{24}$$

where, the parameter $\alpha\left(t\right)$ is same as that defined by Eq.(11).

It is clearly seen from Eq.(24) that the equations governing the distributions g_{+} and g_{-} are the same with each other and both are associated with the the variance $\frac{1}{2}\alpha\left(t\right)$ which is a half of that for the distribution f given by Eq.(10). Thus, the self-similar solutions which are entitled to be probability distributions are derived, following the procedure for the distribution f, as follows:

$$g_{\pm}\left(\mathbf{v}_{\pm},t\right)=g_{\pm 0}\left(\mathbf{v}_{\pm},t\right)\equiv\left(\frac{t}{2\pi\alpha_{0}}\right)^{3/2}\exp\left[-\frac{\left|\mathbf{v}_{\pm}\right|^{2}t}{2\alpha_{0}}\right], \tag{25}$$

which may be called $N2$, and the one-dimensional distribution,

$$g_{\pm}\left(v_{\pm},t\right)=g_{\pm 0}\left(v_{\pm},t\right)\equiv\left(\frac{t}{2\pi\alpha_{0}}\right)^{1/2}\exp\left[-\frac{v_{\pm}^{2}t}{2\alpha_{0}}\right]. \tag{26}$$

It may easily be seen that the *second normal distributions* $N2$ of the distributions g_{+} and g_{-} are nothing but the convolution of the two independent *distributions* $N1$ at points $\mathbf{x}_1$ and $\mathbf{x_2}$ in the *global range*. Thus, the two-point statistics of homogeneous isotropic turbulence has been completely determined, so far as the global range is concerned. Then, the problem of the cross-velocity distributions in the *local range* is dealt with in the next subsection.

2.8 Local Cross-Velocity Distributions

As stated in §2.6, the closure process of the equation for the distribution $f^{(2)}$ leads to the non-zero interaction between the higher-order $f^{(3)}$ terms if the distance r associated with the distribution $f^{(2)}$ is so small as in the *local*

range. This interaction, however, can be dissolved if we transfer the variables $(\mathbf{v}_1, \mathbf{v}_2)$ in the $f^{(3)}$ terms into the cross-velocities $(\mathbf{v}_+, \mathbf{v}_-)$, since the latter are independent from each other for the small distance r. In this way, we can derive the closed equation for the local cross-velocity distributions $g^*_\pm$, where $*$ represents the local variables (see for details Tatsumi (2011)).

It should be noted that the closed equations for the $g^*_\pm$ are associated with the parameters,

$$\alpha^*_\pm(r^*, t^*) = \frac{2}{3} \lim_{|\mathbf{r}^{*\prime}| \to 0} \left| \frac{\partial}{\partial \mathbf{r}^{*\prime}} \right|^2 \int \left| \mathbf{v}^{*\prime}_{\pm -} \right|^2 g^*_{\pm -} \left(\mathbf{v}^{*\prime}_{\pm -}; \mathbf{r}^*, \mathbf{r}^{*\prime}; t^* \right) d\mathbf{v}^{*\prime}_{\pm -}$$
$$= \frac{2}{3} \lim_{|\mathbf{r}^{*\prime\prime}| \to 0} \left| \frac{\partial}{\partial \mathbf{r}^{*\prime\prime}} \right|^2 \int \left| \mathbf{v}^{*\prime\prime}_{\pm -} \right|^2 g^*_{\pm -} \left(\mathbf{v}^{*\prime\prime}_{\pm -}; \mathbf{r}^*, \mathbf{r}^{*\prime\prime}; t^* \right) d\mathbf{v}^{*\prime\prime}_{\pm -}, \quad (27)$$

which are functions of the distance $r^* = |\mathbf{x}^*_2 - \mathbf{x}^*_1|$.

The space-dependence of the parameters $\alpha^*_\pm = \frac{1}{3}\varepsilon^*_\pm$, being the extended *energy-dissipation rate*, actually represents the so-called "intermittency" of the energy-dissipation rate ε in a concrete manner. The full dynamics of the local cross-velocity distributions $g^*_\pm$ in the local range is dealt with in a separate paper.

3 Concluding Remarks

It is generally recognized that the closure process of turbulence must be supplemented by the physical requirements such as the "symmetries and conservation laws". This situation is found to be quite the same in the statistical mechanical approach of turbulence in terms of the multi-point velocity distributions.

In the two-point statistics of the latter approach, the closed equations for the one-point velocity distribution f and the two-point cross-velocity distributions $g_\pm$ are derived from the unclosed Lundgren-Monin equations using the *cross-independence* closure hypothesis (9), and then the closed equations are solved imposing the *self-similarity conditions* (16) due to the *energy decay law* (15), which are closely related with the "*symmetries and conservation laws*", constituting the subject of the One-Day School.

As the result, the distributions f and $g_\pm$ have been obtained as the self-consistent set of the inertial normal distributions with the parameters $\alpha_0 = \frac{1}{3}\varepsilon_0$ and $\frac{1}{2}\alpha_0 = \frac{1}{6}\varepsilon_0$, respectively in the *global range*. In the *local range*, the closed equations for the local cross-velocity distributions $g^*_\pm$ have been obtained exactly with the space-dependent parameters $\alpha^*_{\pm 0}(r^*)$, and the full solution of the distributions $g^*_\pm$ is being obtained in a separate paper.

Thus, the concept of the "*symmetries and conservation laws*" as the physical requirements for the closure process to turbulence seem to have been well established, so far as the statistical mechanical approach of turbulence is concerned.

References

Batchelor, G.K.: The Theory of Homogeneous Turbulence. Cambridge Univ. Pr. (1953)

Comte-Bellot, G., Corrsin, S.: The use of a contraction to improve the isotropy of grid generated turbulence. J. Fluid Mech. 25, 657–682 (1966)

Frisch, U.: Turbulence, The Legacy of A.N. Kolmogorov. Cambridge Univ. Pr. (1995)

Lesieur, M.: Turbulence in Fluids, Stochastic and Numerical Modelling. Kluwer Acad. Publ. (1993)

Lundgren, T.S.: Distribution functions in the statistical theory of turbulence. Phys. Fluids 10, 969–975 (1967)

McComb, W.D.: The Physics of Fluid Turbulence. Clarendon Pr., Oxford (1990)

Monin, A.S.: Equations of turbulent motion. PMM J. Appl. Math. Mech. 31, 1057–1068 (1967)

Tatsumi, T.: Mathematical physics of turbulence. In: Kambe, et al. (eds.) Geometry and Statistics of Turbulence, pp. 3–12. Kluwer Acad. Publ., Dordrecht (2001)

Tatsumi, T.: Cross-independence closure for statistical mechanics of fluid turbulence. J. Fluid Mech. 670, 365–403 (2011)

Lie Symmetries of the Lundgren−Monin−Novikov Hierarchy

N. Staffolani, M. Waclawczyk, Martin Oberlack,
R. Friedrich, and Michael Wilczek

Abstract. In this work we consider the statistical approach to turbulence represented by the Lundgren−Monin−Novikov (LMN) hierarchy of equations for the probability density functions (PDFs). After a review of the properties that the PDFs have to satisfy, we first show the basic Galilean invariance of the LMN equations; then we discuss the extended Galilean one and finally we present a transformation of the PDFs and examine the conditions which have to be satisfied so that this transformation represents a symmetry of the LMN hierarchy corresponding in the Multi−Point Correlation (MPC) approach to one of the so called statistical symmetries found using the Lie symmetry machinery in [6] for the infinite hierarchy of equations satisfied by the correlation functions from which some decay exponents of turbulent scaling law could be worked out.

1 Introduction

Let us take into consideration an ensemble of solutions to the incompressible Navier−Stokes (NS) equations defined over the entire infinite space $\mathbb{R}^3$ but obeying

N. Staffolani · M. Waclawczyk
Chair of Fluid Dynamics, Department of Mechanical Engineering, TU Darmstadt, Petersenstr. 30, 64287 Darmstadt, Germany
e-mail: nicola.staffolani@gmail.com, martaw@fdy.tu-darmstadt.de

Martin Oberlack
Chair of Fluid Dynamics, Department of Mechanical Engineering and Center of Smart Interfaces, TU Darmstadt, Petersenstr. 30, 64287 Darmstadt, Germany,
and GS Computational Engineering, TU Darmstadt, Dolivostr. 15, 64293 Darmstadt, Germany
e-mail: oberlack@fdy.tu-darmstadt.de

Michael Wilczek · R. Friedrich
Institute for Theoretical Physics, University of Münster, Wilhelm-Klemm-Str. 9, D-48149 Münster, Germany
e-mail: {mwilczek,fiddir}@uni-muenster.de

A. Talamelli et al. (eds.), *Progress in Turbulence V*,
Springer Proceedings in Physics 149,
DOI: 10.1007/978-3-319-01860-7_8,

different initial conditions. Let the velocity field of each member of the ensemble be denoted by $\mathbf{u}$. It is assumed that the statistical distribution of $\mathbf{u}$ over the ensemble at the initial time t_0 is given. The main aim is to understand how the statistical distribution of the velocity field evolves with time. In order to do so, let us define multi−point probability density functions (PDFs) in the following usual way: the 1−point PDF $f_1(\mathbf{x}_1,\mathbf{v}_1;t)$ is such that $f_1(\mathbf{x}_1,\mathbf{v}_1;t)\,\mathrm{d}\mathbf{v}_1$ expresses the probability to measure for the fluid element that occupies the position $\mathbf{x}_1$ at the time t a velocity inside the infinitesimal element $\mathrm{d}\mathbf{v}_1$ about $\mathbf{v}_1$. Let $\langle\cdot\rangle$ denote the operation of ensemble average; then the 1−point PDF can be written as:

$$f_1(\mathbf{x}_1,\mathbf{v}_1;t) = \langle \delta(\mathbf{u}(\mathbf{x}_1,t) - \mathbf{v}_1\rangle. \tag{1}$$

Analogously to eq. (1) the 2−point PDF, which denotes the joint probability to measure two given velocities at two defined points in space at the same time, can be expressed as:

$$f_2(\mathbf{x}_1,\mathbf{v}_1;\mathbf{x}_2,\mathbf{v}_2;t) = \langle \delta(\mathbf{u}(\mathbf{x}_1,t) - \mathbf{v}_1)\delta(\mathbf{u}(\mathbf{x}_2,t) - \mathbf{v}_2)\rangle,$$

and so on. To avoid cumbersome formulae the following notation will be used:

$$f_n \equiv f_n(1,\ldots,n) \equiv f_n\left(\mathbf{x}_1,\mathbf{v}_1;\ldots,\mathbf{x}_n,\mathbf{v}_n;t\right).$$

From the NS equation the LMN hierarchy [3, 4, 5] can be derived. The n−th equation for the n−point PDF f_n reads:

$$\left[\partial_t + \sum_{i=1}^{n} \mathbf{v}_i\cdot\nabla_i\right] f_n = -\sum_{j=1}^{n}\frac{\partial}{\partial \mathbf{v}_j}\cdot\left\{\lim_{\mathbf{x}_{n+1}\to\mathbf{x}_j} \nu\,\triangle_{n+1}\int \mathrm{d}\mathbf{v}_{n+1}\mathbf{v}_{n+1}f_{n+1} - \right.$$
$$\left. - \int \mathrm{d}\mathbf{x}_{n+1}\left(\nabla_j \frac{1}{4\pi\left|\mathbf{x}_j-\mathbf{x}_{n+1}\right|}\right)\int \mathrm{d}\mathbf{v}_{n+1}\left(\mathbf{v}_{n+1}\cdot\nabla_{n+1}\right)^2 f_{n+1}\right\}, \tag{2}$$

where ∇_i and $\triangle_i$ denote the differential operators with respect to the i−th coordinate. We also recall that the presence of f_{n+1} in the n−equation represents the closure problem of turbulence.

1.1 Properties of the PDFs

The physical meaning of the PDFs defined in section 1 requires them to satisfy four conditions:

1. the reduction or normalization property imposed by the concept of probability:

$$\int \mathrm{d}\mathbf{v}_1 f_1(\mathbf{x}_1,\mathbf{v}_1;t) = 1;$$
$$\int \mathrm{d}\mathbf{v}_2 f_2\left(\mathbf{x}_1,\mathbf{v}_1;\mathbf{x}_2,\mathbf{v}_2;t\right) = f_1\left(\mathbf{x}_1,\mathbf{v}_1;t\right);$$
$$\vdots \tag{3}$$

2. an infinite number of divergenceless or "continuity" conditions dictated by the incompressibility of the fluid:

$$\nabla_i \cdot \int \mathrm{d}\mathbf{v}_i \, \mathbf{v}_i \, f_n = 0, \quad \forall i \in \{1,\ldots,n\}, \forall n = 1,2,\ldots; \tag{4}$$

3. the "coincidence" property:

$$\begin{gathered} \lim_{\mathbf{x}_2 \to \mathbf{x}_1} f_2(1,2) = f_1(1)\,\delta(\mathbf{v}_2 - \mathbf{v}_1); \\ \lim_{\mathbf{x}_3 \to \mathbf{x}_1} f_3(1,2,3) = f_2(1,2)\,\delta(\mathbf{v}_3 - \mathbf{v}_1); \\ \vdots \end{gathered} \tag{5}$$

4. the "separation" property (here only for the 2−point PDF) which expresses the fact that the velocities of two fluid elements tends to become independent if the two points are set far apart from each other:

$$\lim_{|\mathbf{x}_1 - \mathbf{x}_2| \to \infty} f_2(1,2) = f_1(1) f_1(2). \tag{6}$$

2 Classical Symmetries of the LMN Hierarchy

In this section we discuss the invariance of the LMN hierarchy under time and space translations, Galilean transformations and extended Galilean transformations [7].

The invariance under time and space translations can be very easily inspected. As far as Galilean transformations are concerned, the left hand side of eq. (2) is also readily seen to be invariant, while for the right hand side we have to use the reduction property (3) for the viscous term and the reduction and continuity (4) ones for the pressure−gradient term.

The extended Galilean invariance is instead broken by the integral representation of the pressure−gradient term.

3 Statistical Symmetries of the LMN Hierarchy

In the multi−point correlation (MPC) approach [6] the MPC tensor of order $n+1$ $H_{i_{(0)}\ldots i_{(n)}} = \langle u_{i_{(0)}}(\mathbf{x}_0;t)\ldots u_{i_{(n)}}(\mathbf{x}_n;t)\rangle$ is defined as the average value of the product of the velocity field considered at n different points. By multiplying the NS equations by $u_{i_{(0)}}\ldots u_{i_{(n)}}$ and then averaging an infinite hierarchy of linear partial differential equations for the MPC tensors can be obtained. In [6] it has been shown that, applying the Lie algorithm [1, 2] to this infinite hierarchy, a set of symmetries which have been called statistical symmetries can be deduced. One of these symmetries, which leads to the log-law for stationary wall bounded turbulent shear flows, can be deducted; it reads:

$$H_{i_{(0)}\ldots i_{(n)}} \to H_{i_{(0)}\ldots i_{(n)}} + c_{i_{(0)}\ldots i_{(n)}}, \quad \forall n = 1,2,\ldots \tag{7}$$

where $c_{i_{(1)}\dots i_{(n)}}, \dots$ are constants independent one of each other. In what follows we show that there exists a symmetry transformation of the LMN eq. (2) that correponds to the symmetry transformations (7) for the MPC equations.

In the LMN vocabulary the MPC tensors $H_{i_{(0)}\dots i_{(n)}}$ are given by:

$$H_{i_{(0)}\dots i_{(n)}} = \langle u_{i_{(0)}}(\mathbf{x}_0;t)\dots u_{i_{(n)}}(\mathbf{x}_n;t)\rangle = \int \mathrm{d}\mathbf{v}_0 \dots \int \mathrm{d}\mathbf{v}_n \, f_n \, u_{i_{(0)}} \dots u_{i_{(n)}}.$$

Let us consider the transformation $f_i \to \hat{f}_i = f_i + \phi_i$ where $\phi_i = \phi_i(\mathbf{v}_1, \dots, \mathbf{v}_i)$. It can be easily checked that the transformation that corresponds to (7) is given by:

$$\begin{aligned}
\phi_1(\mathbf{v}_1) &= \phi_1(\mathbf{v}_1);\\
\phi_2(\mathbf{v}_1,\mathbf{v}_2) &= \phi_1(\mathbf{v}_1)\delta(\mathbf{v}_1-\mathbf{v}_2)\\
&\vdots\\
\phi_n(\mathbf{v}_1,\dots,\mathbf{v}_n) &= \phi_1(\mathbf{v}_1)\delta(\mathbf{v}_1-\mathbf{v}_2)\delta(\mathbf{v}_2-\mathbf{v}_3)\dots\delta(\mathbf{v}_{n-1}-\mathbf{v}_n)\\
&\vdots
\end{aligned} \tag{8}$$

The LMN eq. (2) is invariant under the transformations (8). Indeed, on the left hand side the differential operators ∂_t and ∇_i applied to $\phi_n(\mathbf{v}_1, \dots, \mathbf{v}_n)$ give a null contribution. On the right hand side the same applies, this time with respect to ∇_{n+1}. However, in order for the transformed functions to still be PDFs two conditions must be imposed, namely:

$$0 \le f_i + \phi_i, \ \forall \{\mathbf{x}_1, \dots, \mathbf{x}_i\}, \{\mathbf{v}_1, \dots, \mathbf{v}_i\} \in \mathbb{R}^{3i}; \ i = 1, 2, \dots; \ t \ge t_0; \tag{9}$$

$$\int \mathrm{d}\mathbf{v}\,[f(\mathbf{v}) + \phi(\mathbf{v})] = 1 \Rightarrow \int \mathrm{d}\mathbf{v}\,\phi(\mathbf{v}) = 0. \tag{10}$$

Moreover, as the functions ϕ_i do not depend on the space variables, the property of separation (6) is not satisfied. Therefore, the invariance of the LMN eq. (2) under the transformations (8) is true only at moderate separations between the spatial points.

References

1. Bluman, G.W., Cheviakov, A.F., Anco, S.C.: Applications of Symmetry Methods to Partial Differential Equations. Springer, New York (2010)
2. Hydon, P.E.: Symmetry Methods for Differential Equations: A Beginner's Guide. Cambridge University Press (2000)
3. Lundgren, T.S.: Distribution functions in the statistical theory of turbulence. Physics of Fluids 10(5), 969–975 (1967)
4. Monin, A.S.: Equations of turbulent motion. Prikl. Mat. Mekh. 31(6), 1057–(1967)

5. Novikov, E.A.: Kinetic equations for a vortex field. Soviet Physics-Doklady 12(11), 1006–1008 (1968)
6. Oberlack, M., Rosteck, A.: New statistical symmetries of the multi–point equations and its importance for turbulent scaling laws. Discrete and Continuous Dynamical Systems Series S 3(3), 451–471 (2010)
7. Pope, S.B.: Turbulent Flows. Cambridge University Press (2000)

An Investigation into Non-linear Growth Rate of 2D and 3D Single-Mode Richtmyer–Meshkov Instability

M.G. Probyn and B.J.R. Thornber

Abstract. Richtmyer–Meshkov instability (RMI) promotes turbulent mixing and is seen across a variety of events ranging from supernova to inertial confinement fusion. In particular understanding RMI is important for ICF where enhanced mixing tends to reduce power output in energy applications. In the case of ICF the shock-wave will be reflected and this wave may interact with the mixing front causing deposition of yet more vorticity. A number of models of reshock have been proposed and work by Latini et al [3] compares numerical results to the experimental work by Collins and Jacobs [2]. Previous work has shown that after reshock the mixing rate is increased and is in agreement with predictions. In this paper a 5^{th} order MUSCL scheme [9] is used on a mesh moving with plane averaged fluid velocity. Results are then presented for an investigation into non-linear growth of the mixing zone following reshock using an setup comparable to that of Collins and Jacobs to evaluate the behaviour of the numerical scheme for SM-RMI. Subsequently the code is used to evaluate the growth rate for a range of different initial conditions (amplitude/wavelength) and different reshock times. The effective growth rate will be presented as a function of the initial mode linearity. This is an important feature of reshocked interfaces. Also considered are the initial growth rate for 3D SM-RMI. The numerical studies detail the development of the mixing layer width (W) both prior to and after reshock. Prior to reshock the mixing layer is known to develop as $w \propto t^{\theta}$ with $\theta \sim 0.28$ for the bubble growth and this is compared to the results of the numerical scheme [10].

M.G. Probyn · B.J.R. Thornber
Department of Fluid Mechanics and Computational Science, Cranfield University, Bedfordshire, MK43 0AL, U.K.
e-mail: {m.g.probyn,b.j.r.thornber}@cranfield.ac.uk

A. Talamelli et al. (eds.), *Progress in Turbulence V*,
Springer Proceedings in Physics 149,
DOI: 10.1007/978-3-319-01860-7_9,

1 Introduction

The Richtmyer–Meshkov instability (RMI) is a special case [4, 7] of the Rayleigh–Taylor instability (RTI) [6, 8]. In the case of RTI the driving force is a difference in density between two fluids, with a heavy fluid tending to sink into a light one as a result of a gravitational or other acceleration force. RMI occurs when a shock wave is used to initiate the mixing, and can be considered as the impulsive limit of RTI. Other instabilities may subsequently act, particularly Kelvin–Helmholtz instability (KHI) may arise due to shear and eventually the fluid will break down in to a fully turbulent layer.

2 Methodology

Code. The results obtained for this work were achieved using a Cranfield in-house code (CHOC) an Implicit Large Eddy Simulation (ILES) solver with a 5^{th} order MUSCL scheme. A standard Eulerian solver and an ALE solver have been developed and are compared. The equations used are based on the five-equation model of Allaire [1] and further details of the code can be found in Thornber *et al.* [9]. The development of a moving mesh code is essential to reduce the computational time in particular for convergent geometries.

Initial Conditions. The initial conditions used in these tests are based on Collins and Jacobs mach number 1.21 single-mode (SM) Sod-shock case [2]. The shock passes from a light gas (75% air and 25% acetone) into a heavy gas (SF_6). The initial amplitude of the perurbation is 2.0 mm and the wavelength is 59.0 mm, fitting into a cross-sectional area of 89.0 mm. The interface sits 750 mm from the end wall.

3 Results

Images of the volume fraction at a central slice are compared at low and high resolution (128 and 256 cells per wavelength respectively) with the PLIF experimental results of Collins and Jacobs [2] as shown in Figure 1. It can clearly be seen that a higher resolution is required to achieve similar results. This gives a good visualisation of the development of the fluid and an early qualitative comparison.

The moving mesh was tested for simple cases such as the standard Sod-shock case to validate behaviour. A grid study was completed for the case of Section 2 using three resolutions on a stationary grid (S1[64x512], S2[128x1024], S3[256x2048]) as well as on a moving grid (M1, M2, M3). Moving grids contained the same number of cells in the transverse direction as their stationary equivalents but a quarter of the cells in the direction of the shock. There is a large translation of the region of interest in this direction, using a moving mesh a high cell density can track this. The results of the grid study showing convergence are shown in Figure 2.

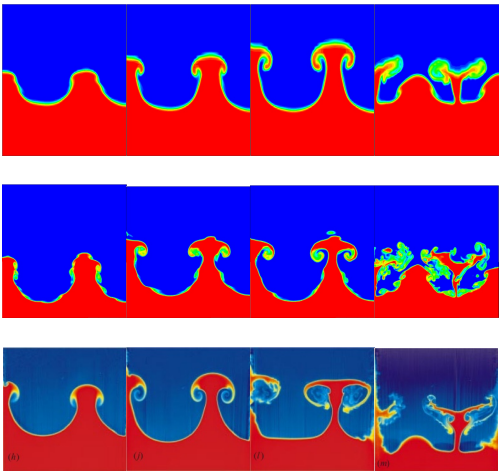

Fig. 1 Volume Fraction Slices: Time = 3,5,7,8ms (Left to Right)
(Top: Low Res. CFD; Middle: High Res. CFD; Bottom: Experiment [2])

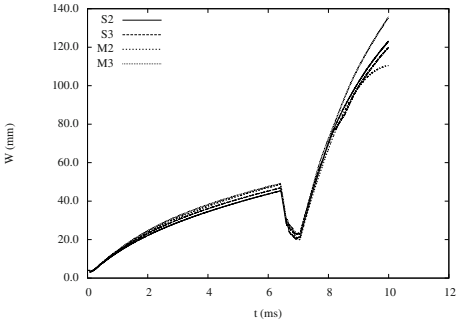

Fig. 2 Grid convergence is achieved between the medium and high resolution cases (low resolution omitted here). Reasonable agreement can be seen between a moving mesh using 1/4 of the number of cells as a moving grid right up to t=8ms. At late-time 2D schemes divergence since large coherent structures remain and propagate through vortex advection.

The comparison between moving and stationary grids show good agreedment with 1/4 of the number of cells, in this case leading to a compute time of around 1/4. Further gains are expected for use with convergent geometries.

A study of the effect of the initial amplitude on the growth rate was undertaken. Initial amplitudes should be governed by a linear growth rate $\propto ka_0$ [7]. For multi-mode (MM) reshock cases growth rates are believed to be independent of the conditions at reshock [5]. This is shown to be true here for low amplitude cases however for high amplitude cases the mixing layer shear component becomes more significant such that the physics is fundamentally different.

A coefficient of non-linearity is obtained by dividing the initial growth rate obtained through CFD by that of Richtmyer's formula $\dot{\eta} = ka_0 \Delta u A t^+$. This is shown

in Figure 4. This coefficient may be suitable for use as a simple means of predicting the growth of a reshocked case by considering the equivalent Richtmyer's formula by pre-multiplying by this coefficient [11].

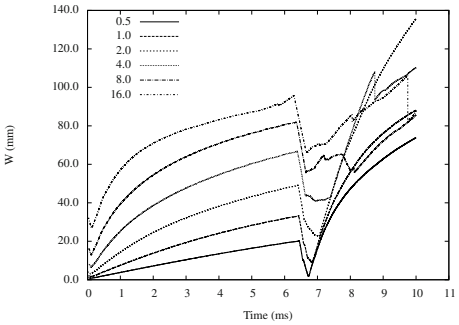

Fig. 3 Growth of the mixing layer plotted for initial amplitudes ranging from 0.5 mm up to 16.0 mm. Initial growth rates are approximately linear up to $a_0 = 4$ mm as expected. After that the large initial amplitudes create non-linearity's, there is now a large shear component which leads to KHI. Reshock of the linear cases can be seen to create a growth rate independent of the initial amplitude.

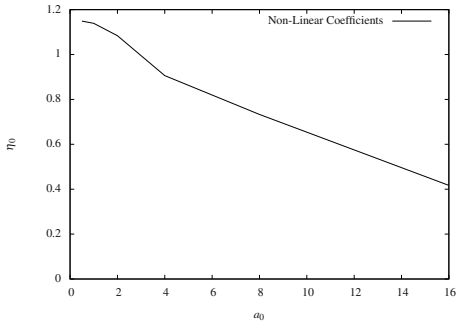

Fig. 4 Initial growth rates converted to a function of non-linearity show the behaviour rapidly departs from that of linear prediction. Linearity is expected whilst $ka_0 \ll 1$ corresponding to $a_0 \ll\sim 9$. in this simulation. Highly non-linear initial shock is investigated since it may provide a model for reshock [11]

4 Conclusions

A moving mesh algorithm has been implemented into CHOC a Cranfield solver to reduce computational time. Results are compared to the work of Collins and Jacobs [2]. Growth rates for non-linear cases have been tested and it can be seen that non-linearity breaks down as expected and that growth rates for linear cases after reshock are independent of the initial amplitude as expected from Mikaelian's work [5].

Acknowledgements. The authors would like to recognise the assistance of Prof.D.L.Youngs and Dr.R.J.R.Williams of AWE(UK) and Prof.D.Drikakis of Cranfield University. This work is funded by AWE(UK) and the EPSRC.

References

1. Allaire, G., Clerc, S., Kokh, S.: A five-equation model for the simulation of interfaces between compressible fluids. J. Comp. Physics 181, 577–616 (2002)
2. Collins, B.D., Jacobs, J.W.: PLIF flow visualization and measurement of the Richtmyer–Meshkov instability of an air/sf_6 interface. J. Fluid Mech. 464, 113–136 (2002)
3. Latini, M., Schilling, O., Don, W.S.: High-resolution simulations and modeling of reshocked single-mode Richtmyer-Meshkov instability: Comparison to experimental data and to amplitude growth model predictions. Phys. Fluids 19 (2007)
4. Meshkov, E.E.: Instability of the interface of two gases accelerated by a shock wave. Fluid Dynamics 4(5), 101–104 (1972)
5. Mikaelian, K.O.: Turbulent mixing generated by Rayleigh–Taylor and Richtmyer–Meshkov instability. Physica D 36, 343–357 (1989)
6. Rayleigh, L.: Instability of the interface of two gases accelerated by a shock wave. Proc. Roy. Math. Soc. 14, 170–177 (1883)
7. Richtmyer, R.D.: Taylor instability in shock-acceleration of compressible fluids. Comm. Pure Appl. Math. 13, 297–319 (1960)
8. Taylor, G.I.: The instability of liquid surfaces when accelerated in a direction perpendicular to their planes. Proc. R. Soc. London, Series A 201, 192–196 (1950)
9. Thornber, B., Bilger, R.W., Masri, A.R., Hawkes, E.R.: An algorithm for les of premixed compressible flows using the conditional moment closure model. J. Comp. Physics 230, 7687–7705 (2011)
10. Thornber, B., Drikakis, D., Youngs, D.L., Williams, R.J.R.: Growth of a richtmyer-meshkov turbulent layer after reshock. Phys. Fluids 23(9) (2011)
11. Thornber, B., Drikakis, D., Youngs, D.L., Williams, R.J.R.: Physics of the single-shocked and reshock Richtmyer–meshkov instability. J. Turbulence 12(10) (2012)

DNS of Turbulent By-Pass Transition at the Entrance of a Plane Channel

A. Cadiou, M. Buffat, L. Le Penven, and J. Montagnier

Abstract. Direct numerical simulations of boundary layers transition and their interaction in a very elongated plane channel are presented. Wall-normal velocity perturbations of small amplitude and with a spanwise wavelength of the order of the boundary layer thickness are introduced in one of the boundary layer. They generate steady elongated streaks by a transient growth mechanism. In the non-linear regime, a varicose instability mechanism pushes the low speed streaks away from the wall. Mushroom-shaped structures appear in the outer region of the laminar boundary layer. They are subjected to sinuous instabilities leading to transition. The turbulent boundary layer evolves further downstream and initiates the by-pass transition of the second boundary layer. An orthogonal decomposition of the velocity field is used to characterize the transition.

1 Introduction

Developing channel flows are of interest in a large number of application areas. Many aspects of these flows are not yet fully understood, such as the flow stability characteristics in the entrance region. It is well known that for the plane Poiseuille flow, linear stability theory gives a critical Reynolds number of $Re_c = 5772$ [12] whereas, in experiments, a plane channel flow can become already turbulent at $Re = 1000$ [11]. This has been explained by the non-normal property of the linearized Navier-Stokes operator that allows transient growth of initial perturbations [15]. Entrance flows however significantly differ from the asymptotic Poiseuille flow. For uniform inlet flow conditions and at high enough Reynolds numbers, the turbulent transition actually takes place inside the boundary layers [3] and well before the fully developed regime. When the boundary layers are distant, the nature of their

A. Cadiou · M. Buffat · L. Le Penven · J. Montagnier
Laboratoire de Mécanique des Fluides et d'Acoustique, Université de Lyon, CNRS,
École Centrale de Lyon, INSA de Lyon, 43 bv. du 11 Nov. 1918, 69622 Villeurbanne, France
e-mail: anne.cadiou@ec-lyon.fr

A. Talamelli et al. (eds.), *Progress in Turbulence V*,
Springer Proceedings in Physics 149,
DOI: 10.1007/978-3-319-01860-7_10,

transition and of their initial development is expected to have some similarity to the freestream Blasius boundary layer case. For Blasius flow, the linear stability theory gives a critical Reynolds number at $Re_x = 92000$ [14], but for entrance flows the boundary layers are modified, in particular because of the small favorable pressure gradient existing inside the plane channel. This is known to have a stabilizing effect on the boundary layers [6]. Another aspect of the entrance flows that differs from the Blasius case is linked to the fact that two boundary layers are actually co-existing in the velocity profiles. This raises the question of their mutual interaction in the transition scenario of the flow. In this is study, we describe the way the turbulence generated by the transition of one of the boundary layer initiates the transition of the second boundary layer.

2 Flow Configuration and Numerical Method

We consider the boundary layers developing on the upper and lower walls at the entrance of a plane channel of width $2h$ (fig. 1). The flow enters at large Reynolds number $Re_h = 10000$ (based on the channel half-width and the mean velocity), so that near the entrance, the boundary layers are well separated. They merge inside the channel if it is long enough.

The simulation is performed with a DNS spectral code based on a Galerkin formulation of the incompressible Navier-Stokes equations developed in our team [10] [4] [9]. The numerical method is based on a general property of the decomposition of solenoidal vector fields [13], derived from the Helmholtz-Hodge theorem. The velocity is expressed as an L_2-orthogonal sum of two incompressible fields. One of which is function of the normal component of the velocity and the other one of the normal component of the vorticity. By analogy with the stability analysis of parallel shear flows, the two velocities are named respectively the Orr-Sommerfeld (OS) and Squire (SQ) velocity field.

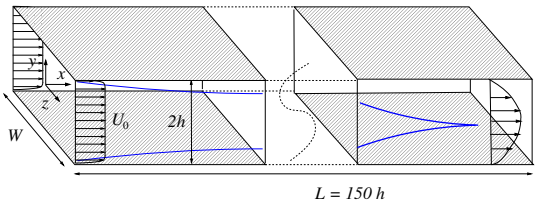

Fig. 1 Computational domain $150h \times 2h \times 3.2h$ with $17280 \times 192 \times 384$ modes

3 Base Flow and Inlet Perturbations

Blasius profiles ($\delta_{0.99} = h/10$ and $Re_\theta = 138$) are imposed at the inlet section of the computational domain which is located at $x_0 = 4h$ from the channel entrance. Without inlet perturbation, the flow remains laminar. The Reynolds number Re_x, based on

the distance x from the entrance, ranges from $4\,10^4$ up to $1.5\,10^6$. A small favorable pressure gradient gives a slightly lower shape factor of the laminar boundary layers compared the Blasius profiles. Its influence on the linear neutral stability curve is strong, reducing the critical Reynolds number by ten. However, the transient energy growth remains as large as for the Blasius case, so that the by-pass transition is not significantly delayed (estimated Falkner-Skan parameter: $\beta \sim 0.07$).

A well-defined perturbation is applied to the upper boundary layer. It is based on an optimal mode [5] obtained by solving the Orr-Sommerfeld/Squire equations for the entrance laminar profile. It is made of steady pairs of contra-rotating longitudinal vortices inside the boundary layer, with a spanwise wavenumber $\beta \approx 2/\delta$ and zero streamwise wavenumber α. It essentially consists in an OS velocity perturbation. In the present simulation, its amplitude is small ($\sim 1.7\%$), but it induces a large linear transient growth and creates a large longitudinal SQ velocity field, that corresponds to steady streaks. An additional smaller random perturbation ($< 0.1\%$) is superimposed to the first one to trigger transition of the upper boundary layer. It occurs near the entrance of the channel at $x/h \sim 10$.

No perturbation is imposed to the other boundary layer, which remains laminar in a large part of the channel. Near $x/h \sim 100$ the low frequency fluctuations induced by the turbulent upper boundary layer interact with the laminar lower boundary layer, and generate modulated streaks. Then by-pass transition of the lower boundary layer is observed. The corresponding value of Re_x is $\sim 10^6$. Afterwards turbulence occupies all the channel width and a turbulent channel flow develops.

4 Characterization of the Transition Scenario

The disturbance velocity is defined as the velocity departure from the time-averaged, spanwise-averaged velocity. The streamwise evolutions of the OS and SQ parts of the disturbance velocity, spatially averaged inside the boundary layer thickness, are shown on figure 2. Before the turbulent transition point (near $x/h \approx 8$), the disturbance velocity field mainly contains a SQ streamwise component $\overline{u}_{SQ}$, as seen on figure 2a. The first instability on the upper wall corresponds to steady streaks generated from the optimal inlet perturbation. As noted before, the transient growth is strong ($\overline{u}_{SQ}$ increases from 2% to 20%, up to $x/h \approx 2$). An inflection point appears near $x/h \approx 2$, in the wall normal profile of the spanwise averaged streamwise velocity, as a consequence of nonlinear effects. The SQ velocity field experiences transient varicose instabilities in the wall-normal direction, that push low speed streaks away from the wall and form mushroom-shaped structures. It changes the mean velocity profile and consequently, the energy of the disturbance velocity $\overline{u}_{SQ}$ decreases. Further downstream near $x/h \approx 6$, the heads of these low speed streaks are subjected to sinuous instabilities in the spanwise direction and turbulent transition occurs near $x/h \approx 8$, characterized by an increase of all the components of the disturbance velocity.

The sinuous instability is clearly seen near $x/h \sim 8$ on instantaneous streamwise velocity contours in a plane parallel to the wall (figure 3a) , whereas the transitional

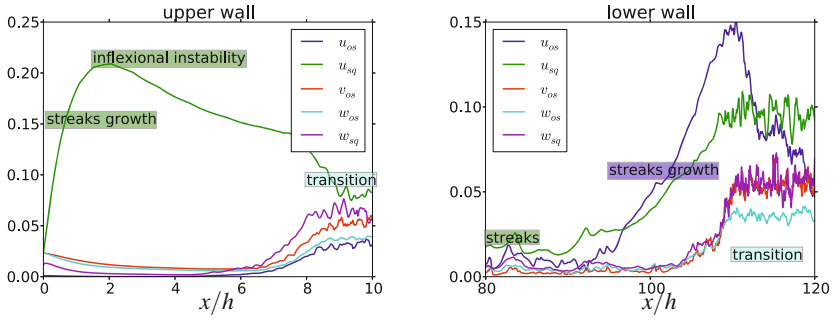

(a) upper wall at the entrance of the domain **(b)** lower wall, near the transition at $x/h \leq 100$

Fig. 2 Streamwise evolution of $\overline{\boldsymbol{u}}_{OS}$ and $\overline{\boldsymbol{u}}_{SQ}$ to the disturbance velocity, spatially averaged inside the boundary layer thickness

varicose instability is only apparent on the streamwise planes (figure 3c). At $x/h = 1$, the structure of the streaks corresponds to the linear transient growing phase. Non-linear growth is observed at $x/h = 4$ with a mushrhroom-like shape of the streaks enhanced by the transient varicose instabilities. Further downstream these structures are subject to sinuous instabilities, tilt, twist, interact with the wall and the neighboring structures and develop into complex forms as they move downstream into the fully turbulent region.

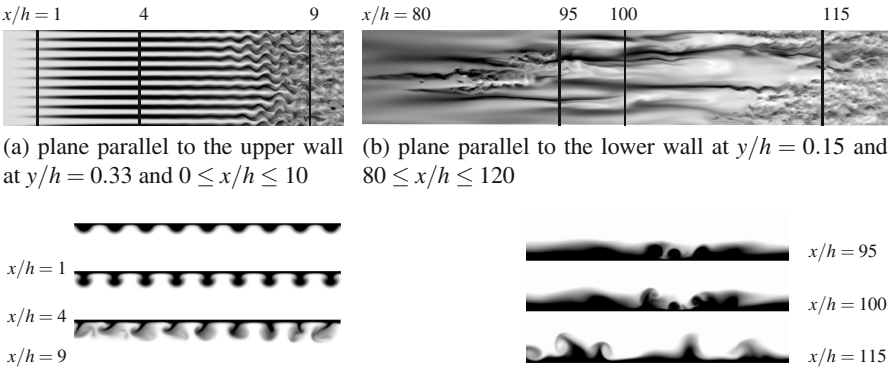

(a) plane parallel to the upper wall at $y/h = 0.33$ and $0 \leq x/h \leq 10$

(b) plane parallel to the lower wall at $y/h = 0.15$ and $80 \leq x/h \leq 120$

(c) streamwise planes. upper wall.

(d) streamwise planes. lower wall.

Fig. 3 Visualization of the instantaneous streamwise velocity u

The transition of lower boundary layer is observed at $x/h \approx 100$. It results from the interaction with the upper turbulent boundary layer. On figure 2b, the growth of the SQ streamwise component $\overline{u}_{SQ}$ is observed, characteristic of the formation of

streaks in the boundary layer. Near the transition point, a fast growth of the streamwise component $\overline{u}_{OS}$ is noticed, indicating that the streaks are unsteady and wavy. Further downstream, turbulent transition occurs characterized by the fast growth of all the velocity components of $\overline{\boldsymbol{u}}_{OS}$ and $\overline{\boldsymbol{u}}_{SQ}$.

Vizualisations of the instantaneous streamwise velocity in the lower boundary layer near the transition location is shown figure 3b and 3d. The formation of low speed streaks is seen in the plane parallel to the wall (3b). It can be observed that the streaks are larger than near the entrance as the boundary layer is thicker. The streaks are also modulated in the streamwise direction. This is similar to the formation of non stationary streaks. Turbulent spots are observed upstream of the fully turbulent boundary layer. The breakdown of the streaks follows the same scenario than for the upper-wall transition. As seen on figure 3d in the streamwise plane $x/h = 95$, low speed streaks appears in the near wall region of the boundary layer, due to the lift-up mechanism induced by normal velocity oscillations of very small amplitude but with a length scale of the order of the boundary layer thickness. Then non linear transient growth and transient varicose instabilities push these low speed streaks away from the wall to form the mushroom-shaped structures seen in the plane $x/h = 100$. Further downstream they are subject to sinuous instabilities as seen in the plane $x/h = 115$.

5 Conclusion

DNS of the by-pass transition and interaction of the two boundary layers developing from the entrance of an elongated plane channel at high Reynolds number is discussed. The transition scenario is described using an orthogonal decomposition of the disturbance velocity field [13]. A perturbation of small amplitude ($< 2\%$) based on an optimal mode is imposed at the inlet, inside the upper boundary layer, leading to a fast growth of infinitely elongated streaks. The growth of varicose mode of flow perturbations is first observed, followed by sinuous instabilities that eventually lead to the transition near the channel entrance $x/h \sim 10$. This differs from the stability analysis of steady streaks ([2], [8], [7]) in which the streaky profiles are obtained from the steady linear optimal perturbation [1] and extracted at a position where the streaks reach a maximum of energy. These studies indicate that either large amplitude streaks or large amplitude spanwise perturbations are required to destabilize a streaky boundary layer through sinuous instabilities. In our simulations, perturbations are imposed at the inlet section and they correspond to the optimal mode obtained for the inlet velocity profile, whose boundary layer thickness is δ. Therefore, the perutbations are located inside the boundary layer at the inlet section. They induce the streaks generation, their transient growth and their breakdown. The transition of the lower boundary layer occurs near $x/h \sim 100$, initiated by perturbations coming from the upper boundary layer. These perturbations lead to modulated streaks at $Re_x \sim 10^6$. This kind of simulations is, to the author's knowledge, the first DNS of boundary layer by-pass transition induced by "real" external turbulence generated inside the computational domain. The numerical

simulations of such an experiment require billions of modes and is now possible thanks to massively parallel ressources.

Acknowledgements. The simulations were performed on BlueGene/P platforms thanks to GENCI and PRACE HPC resources (at IDRIS in France and at JSC in Germany). The authors would also like to thank the computer center P2CHPD at Université Claude Bernard Lyon 1, member of the Fédération Lyonnaise de Modélisation et Sciences Numériques, for providing computer facilities.

References

1. Andersson, P., Berggren, M., Henningson, D.S.: Optimal disturbances and bypass transition in boundary layers. Physics of Fluids 11, 134–150 (1999)
2. Andersson, P., Brandt, L., Bottaro, A., Henningson, D.S.: On the breakdown of boundary layers streaks. J. Fluid Mech. 428, 29–60 (2001)
3. Asai, M., Floryan, J.M.: Certain aspects of channel entrance flow. Phys. Fluids 16(4), 1160–1163 (2003)
4. Buffat, M., Le Penven, L., Cadiou, A.: An efficient spectral method based on an orthogonal decomposition of the velocity for transition analysis in wall bounded flow. Comput. Fluids 42, 62–72 (2011)
5. Butler, K.M., Farrell, B.F.: Three-dimensional optimal perturbations in viscous shear flow. Phys. Fluids A 4, 1637–1650 (1992)
6. Corbett, P., Bottaro, A.: Optimal perturbations for boundary layers subject to stream-wise pressure gradient. Phys. Fluids 12, 120–130 (2000)
7. Cossu, C., Brandt, L., Bagheri, S., Henningson, D.S.: Secondary threshold amplitudes for sinuous streak breakdown. Physics of Fluids 23, 074103 (2011)
8. Hoepffner, J., Brandt, L., Henningson, D.S.: Transient growth on boundary layer streaks. J. Fluid Mech. 537, 91–100 (2005)
9. Montagnier, J., Cadiou, A., Buffat, M., Le Penven, L.: Towards petascale simulation for transition analysis in wall bounded flow. Int. Journ. for Num. Meth. in Fluids (2012) (in revision)
10. NadiaSpectral, `http://www.ufrmeca.univ-lyon1.fr/~buffat/NadiaSpectral`
11. Nishioka, M., Asai, M.: Some observations of the subcritical transition in plane poiseuille flow. J. Fluid Mech. 150, 441–450 (1985)
12. Orszag, S.A.: Accurate solution of the Orr-Sommerfeld stability equation. J. Fluid Mech. 50, 689–703 (1971)
13. Le Penven, L., Buffat, M.: Orthogonal decomposition of a solenoidal 3D vector field in terms of projections of vector and its curls onto arbirary field lines. Submitted to J. Phys. A: Math. Gen. (2012)
14. Schmid, P.J., Henningson, D.S.: Stability and Transition in Shear Flows. Springer (2001)
15. Schmid, P.J.: Linear stability theory and bypass transition in shear flows. Phys. Plasmas 7, 1788–1794 (2000)

Numerical Investigation of the AFRODITE Transition Control Strategy

S. Camarri, J.H.M. Fransson, and A. Talamelli

Abstract. The experiments carried out within the AFRODITE[2] project are aimed at exploring the effectiveness of properly shaped velocity miniature vortex generators in delaying transition to turbulence in a boundary layer. The present work details the direct numerical simulation setup designed to support and reproduce the AFRODITE experiments and provide results showing that the proposed DNS is in good agreement with the experiments. The results of the DNS also show that even a minimal delay of the transition point results in an overall gain in terms of drag when MVGs are installed on the plate.

1 Introduction

Transition delay in boundary layers has always been of major scientific interest in engineering sciences. Recently, it has been shown in the literature that longitudinal high speed streaks in a boundary layer (BL), with proper shape and amplitude, damp Tollmien-Schlitching (TS) waves, (see e.g. [1]), leading to an evident delay of the transition point in a Blasius-like BL [4]. AFRODITE project[2], is devoted to the full experimental characterization of this and related passive control strategies for transition delay. Presently, the velocity streaks in the experiments (EXPs) are generated by Miniature Vortex Generators (MVGs), i.e. pairs of triangular winglets, mounted in one or more spanwise rows on a flat plate and an extensive experimental activity is carried out on this configuration (see e.g. [3, 5]).

S. Camarri
DICI - Universit di Pisa, 56122 Pisa, Italy
e-mail: s.camarri@ing.unipi.it

J.H.M. Fransson
Linné Flow Centre, KTH Mechanics, Stockholm, Sweden

A. Talamelli
DIN - Università di Bologna, I-47100 Forlì, Italy

A. Talamelli et al. (eds.), *Progress in Turbulence V*,
Springer Proceedings in Physics 149,
DOI: 10.1007/978-3-319-01860-7_11,

The present work documents part of a numerical activity aimed at providing full numerical support to the EXPs of AFRODITE. In this paper the DNS setup designed to reproduce the EXPs of AFRODITE is described, and the results of its validation provided. This is the starting point to obtain numerical data, which can be used in synergy with the EXPs for investigating in details the transition delay mechanism. Moreover, the same tool can be used to explore configurations alternative to those presently under investigation in AFRODITE.

2 Results and Discussion

With reference to Fig. 1, where a sketch of the experimental configuration and the related frame of reference are reported, the considered geometry of the MVGs is characterized by the following dimensions: $h = 1.3$ mm, $d = 3.25$ mm, $h = 3.25$ mm, $D = 13$ mm and $x_{\mathrm{MVG}} = 222$ mm. The thickness of the winglet is equal to $t = 0.3$ mm. The incoming velocity is $U_\infty = 7.7$ m/s and the EXP is carried out in air in atmospheric conditions (kinematic viscosity: $\nu \simeq 1.46 \cdot 10^{-5}$ m^2/s). The ratio between h and the BL reference height at the MVGs position $\delta(x_{\mathrm{MVG}}) = \sqrt{\nu x_{\mathrm{MVG}}/U_\infty}$ is $h/\delta(x_{\mathrm{MVG}}) \simeq 2.00$, so that the MVGs' height is approximately 0.4 times the total thickness (δ_{99}) of the boundary later.

The numerical code used to perform the DNS of the considered flow is NEK5000, which is an open-source spectral element solver for the unsteady incompressible Navier-Stokes equations, employing hexahedral HP elements based on tensorial product of Gauss-Lobatto Legendre nodes. Details on the code can be found at the following URL: `http://nek5000.mcs.anl.gov/index.php/Main_Page`.

In this work we present the results obtained by two DNS simulations. The first simulation (SA) is carried out on a flow domain which extends in the streamwise direction from Reynolds number $Re_x \simeq 5.2 \cdot 10^4$ (measured from the leading edge) to $Re_x \simeq 3.0 \cdot 10^5$. A fully-developed Blasius profile is imposed at the inlet of the domain, which is in excellent agreement with the EXPs, and standard outflow conditions are imposed at the outlet ($p\mathbf{n} - Re^{-1}(\mathbf{n} \cdot \nabla \mathbf{u}) = 0$, $\mathbf{n}$ being the outer normal to the domain, p the pressure and $\mathbf{u}$ the velocity vector) and on the top boundary of the domain, located at a distance $H = 19.3\,h$ from the wall. In the spanwise direction, the domain is $D/2$ wide, thus comprising only one winglet of the MVGs and symmetric boundary conditions are imposed. Symmetry holds as far as the streaks generated by the MVGs are stable, as it is the case for the considered flow conditions. Besides experimental evidence, the stability of the streaks has also been verified a-posteriori by performing simulations including up to 10 couples of MVGs (not detailed in this work for the sake of brevity). Finally, no-slip boundary conditions are imposed on the wall. The grid is made by $3.5 \cdot 10^4$ elements employing 6 collocation points in each direction ($1.8 \cdot 10^7$ global dofs).

The second simulation (SB), is made in two steps, using two partially overlapping domains placed in cascade in the spanwise direction. The first domain extends in the streamwise direction from $(x - x_{\mathrm{MVG}}) = -6.5\,h$ to $(x - x_{\mathrm{MVG}}) = 14\,h$, while the second starts at $(x - x_{\mathrm{MVG}}) = 10.2\,h$ ($Re_x = 1.2 \cdot 10^5$) and finishes at $Re_x = 3.0 \cdot 10^5$. The first

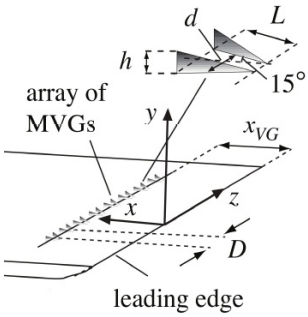

Fig. 1 Sketch of the flow configuration

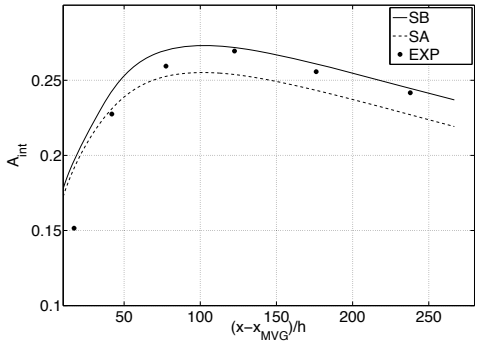

Fig. 2 Streak amplitude evolution

domain employs $8.2 \cdot 10^4$ elements of order 6 ($4.0 \cdot 10^7$ dofs) and the second $1.5 \cdot 10^4$ elements ($7.7 \cdot 10^6$ dofs). The boundary conditions and the dimensions in the other directions are the same as for SA. A first simulation is run on the first subdomain, and when the steady state is reached this solution is employed to fix the inflow conditions for the second domain. The motivation of simulation SB is to check the effect of a highly refined resolution near the MVG. In particular, to have an order of magnitude of the resolution, 4 elements (20 collocation points) are employed on the thickness t of the winglet.

The amplitude of the streaks is calculated using the following definition:

$$A_{int}(x) = \frac{1}{U_\infty L_z} \int_0^{L_z} \left[\int_0^{9\delta(x)} \frac{|U(x,y,z) - U_m(x,y)|}{\delta(x)} dy \right] dz \tag{1}$$

where the mean velocity $U_m(x,y)$ is the velocity averaged in the spanwise direction. The amplitude of the simulated streaks past the MVGs is reported for both SA and SB in Fig. 2 and compared with experimental data obtained by hot-wire anemometry. In the simulation SA the streak amplitude is estimated with a maximum error approximately equal to 4%, which is already in good agreement with the EXPs if we consider the complexity of both EXPs and DNS. Concerning the EXPs, the first two points closest to the MVG are not considered in the discussion since they can be affected by measurement errors due to the strong velocity gradients in that region and to the spatial resolution of the hot wire measurements. The results from SA show a systematic, even if slight, underestimation of the streak amplitude. Cross-checking the results obtained in SA with a 3D BL solver (results not reported for the sake of brevity), it was possible to deduce that, if a spatial resolution problem is present in SA, this must be necessarily localized in proximity of the MVG. This conclusion led us to setup the simulation SB described above. As shown in Fig. 2, increasing the resolution around the MVG (SB) leads to the prediction of slightly stronger streamwise vortices which, in turn, lead to stronger streaks with a slightly lower decay rate in the far wake of the MVG, thus allowing an evident accuracy recovery

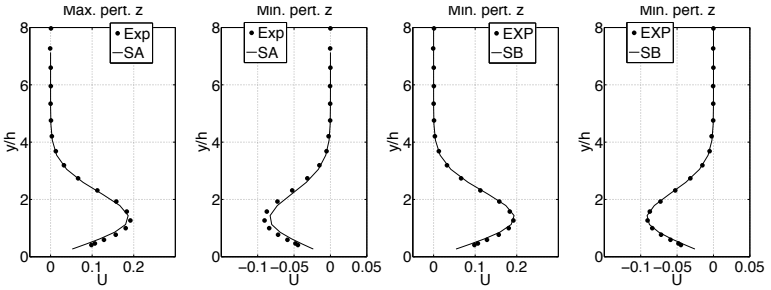

Fig. 3 Profiles of streamwise velocity perturbations along the wall-normal direction in the high and low speed streaks at $(x - x_{\mathrm{MVG}}) = 238$h: comparison with experiments

of SB with respect to the EXPs. For a more detailed comparison between EXPs and DNS, we report in Fig. 3 two profiles for each of the SA and SB simulations of the streamwise velocity perturbations with respect to U_m (normalized using U_∞), at a streamwise distance from the MVG equal to $238h$. The two profiles are measured at the spanwise sections where the maximum and minimum of the perturbation are observed. The figures show a satisfactory agreement between DNS and EXPs and that with a finer mesh around the MVGs the two sets of data overlap.

The DNS results described (SA) have been used to estimate the minimum transition delay that is necessary in order to obtain a net gain in terms of drag when the MVGs are used. To this purpose, we consider a plate with a length from the leading edge which is representative of the laminar part in a Blasius BL, i.e. $Re_x = 4.5 \cdot 10^5$. Concerning the plate with MVGs, the DNS is used to compute the drag coefficient in the computational domain SA, the Blasius solution is adopted to estimate the drag between the leading edge of the plate and the beginning of the computational domain and finally, in the region between the end of the computational domain and $Re_x = 4.5 \cdot 10^5$, we assume that the decay of the friction coefficient follows the same behaviour with Re_x as the unperturbed Blasius BL. Considering the wetted surface as a reference surface, the drag coefficient of the plate with MVGs is estimated to be $C_d \simeq 2.03 \cdot 10^{-3}$, with a contribution of the force exerted directly on the MVG which is two orders of magnitude lower and thus negligible. The corresponding value for the Blasius BL is $C_d \simeq 1.98 \cdot 10^{-3}$, so the MVGs lead to an increase of the drag coefficient of only 2.5% over the considered plate length. Thus, even a minimal delay in transition results in a net gain in terms of drag coefficient, proving the strong potential of this transition delay strategy.

J.H.M. Fransson acknowledges the financial support of the AFRODITE programme by the European Research Council. S. Camarri acknowledges the financial support provided by the "C.M. Lerici" Foundation and the computational resources provided by CASPUR (Roma, Italy) and by CINECA (Bologna, Italy) computing centers. Dott. S. Spagnolo is kindly acknowledged for his support.

References

1. Cossu, C., Brandt, L.: On Tollmien-Schlichting-like waves in streaky boundary layers. Eur. J. Mech. /B Fluids 23, 815–833 (2004)
2. Fransson, J.H.M., Fallenius, B.E.G., Shahinfar, S., Sattarzadeh, S.S., Talamelli, A.: Advanced fluid research on drag reduction in turbulence experiments afrodite. J. Phys.: Conf. Ser. 318, 032,007 (2011)
3. Fransson, J.H.M., Talamelli, A.: On the generation of steady streamwise streaks in flat-plate boundary layers. J. Fluid Mech. 698, 211–234 (2012)
4. Fransson, J.H.M., Talamelli, A., Brandt, L., Cossu, C.: Delaying transition to turbulence by a passive mechanism. Phys. Rev. Lett. 96, 064,501 (2006)
5. Shahinfar, S., Sattarzadeh, S.S., Fransson, J.H.M., Talamelli, A.: Revival of classical vortex generators now for transition delay. Phys. Rev. Lett. 109, 074,501 (2012)

Transition to Turbulence Delay Using Miniature Vortex Generators – AFRODITE –

J.H.M. Fransson, S. Shahinfar, S.S. Sattarzadeh, and A. Talamelli

Abstract. A laminar boundary layer has a relatively low skin-friction drag coefficient (c_f) with respect to a turbulent one, and for increasing Reynolds number the difference in c_f rapidly increases, and the difference can easily amount to an order of magnitude in many industrial applications. This explains why there is a tremendous interest in being able to delay transition to turbulence, particularly by means of a passive mechanism, which has the advantage of accomplishing the control without adding any extra energy into the system. Moreover, a passive, control does not have to rely on typically complicated sensitive electronics in sensor-actuator systems. Within the AFRODITE project [3] we now present the first experimental results where we are able to show that miniature vortex generators (MVGs) are really coveted devices in obtaining transition delay.

1 Introduction

Classical vortex generators, known for their efficiency in delaying or even inhibiting boundary layer separation, are here shown to be coveted devices for transition to turbulence delay. The present devices are miniature with respect to classical vortex generators but are really effecitve in modulating the laminar boundary layer in the direction orthogonal to the base flow and parallel to the surface. The modulation generates an additional term in the perturbation energy equation, which counteracts the wall-normal production term, and hence stabilizes the flow. Our experimental results show that these devices are really effective in delaying transition but we also reveal their Achilles' heel [7].

J.H.M. Fransson · S. Shahinfar · S.S. Sattarzadeh
Linné Flow Centre, KTH Mechanics, Stockholm, Sweden
e-mail: jensf@kth.se

A. Talamelli
DIN - Università di Bologna, I-47100 Forlì, Italy

A. Talamelli et al. (eds.), *Progress in Turbulence V*,
Springer Proceedings in Physics 149,
DOI: 10.1007/978-3-319-01860-7_12,

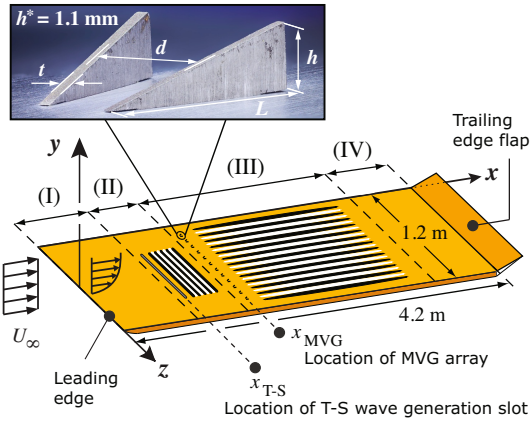

Fig. 1 Schematic of the flat plate boundary layer with the (I–IV) regions described in the text. The black and white stripy pattern perpendicular to the main stream downstream of the disturbance slot in region (II) indicates the T-S waves. In region (III) a similar stripy pattern aligned with the main stream indicates the alternating high and low speed streaks. Inset shows a photo of a MVG pair. $x_{T-S} = 190$ mm and $x_{MVG} = 222$ mm from the leading edge. $h = 1.1,\ 1.3,\ 1.5$, $L = d = 3.25$ and $t = 0.3$ [mm]. The distance between neighboring MVG pairs is $\Lambda = 13$ mm.

The physical mechanism of the stabilizing effect is known [1] and has previously been shown to be strong enough to delay transition to turbulence in wind tunnel experiments [4], where the base flow was modulated by means of cylindrical roughness elements. Later this result has been confirmed numerically in [6]. The experimental design (as well as the numerical simulation) was, however, fairly laboured, since the artificial disturbance was introduced downstream of the cylindrical roughness array avoiding any potential non-linear interaction of the incoming disturbance with the roughness array. In a recent study the flow configuration and experimental setup has challenged the passive flow control method by generating controlled disturbances upstream of the boundary layer modulators and showed promising results in being capable of delaying transition to turbulence [7]. This work is financially supported by the European Research Council and is performed within the AFRODITE research programme, which stands for Advanced Fluid Research On Drag reduction In Turbulence Experiments.

2 Experimental Setup

The experiments were performed in the Minimum-Turbulence-Level wind tunnel at KTH, renown for its low background turbulence intensity. This level depends on the free stream velocity (U_∞) and the streamwise velocity component amounts to less than 0.025% of U_∞ at the nominal free stream velocity of 25 m s^{-1}. In this wind tunnel investigation we test the effectiveness of miniature vortex generators

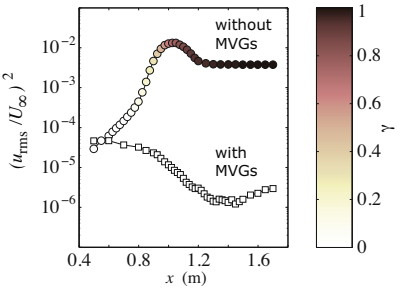

Fig. 2 Energy evolution in the downstream direction with and without MVGs plotted with (□)- and (○)-symbols, respectively, at $U_\infty = 7.7$ m s^{-1}. The same high initial forcing amplitude and frequency ($F = 102$) of the T-S wave were applied. MVGs: $h = 1.3$ mm giving a maximum A_{ST} of 21%. With the present configuration $h/\delta \approx 2$, where $\delta = \sqrt{x_{MVG}\,\nu/U_\infty}$. The color bar applied on the symbols corresponds to the intermittency (γ) of the velocity signal.

(MVGs) to stabilize T-S waves with the aim to obtain transition delay in flat plate boundary layers. In Figure 1 a sketch of the flat plate is shown and, here, the flow domain can be divided into four regions. In region (I) a 2D laminar boundary layer develops on the flat plate, while in (II) T-S waves are generated by means of blowing and suction through a spanwise slot in the plate located at x_{T-S}. Throughout this study we use the non-dimensional frequency $F = (2\pi f\nu/U_\infty^2)\times 10^6$, where f Hz is the forcing frequency and ν the kinematic viscosity. For the present MVG configuration $F \approx 102,\ 135,\ 178$ were tested. In region (III) the 3D streaky base flow with alternating high and low speed streaks are generated by the MVG array located at x_{MVG}. In region (IV) the amplitude of the streaky base flow has finally decayed and the 2D base flow found in region (I) will eventually be recovered, unless the streaks breakdown to turbulence.

The unsteady blowing and suction is created by a sealed loudspeaker connected to the slot via vinyl hoses (as described in [2]). The loudspeaker is driven by a computer generated sinusoidal output signal via an amplifier and the measurements are triggered based on the phase of this output signal.

The distance between neighboring MVG pairs is $\Lambda = 13$ mm. In this investigation we have considered three different MVG heights $h = 1.1,\ 1.3$ and 1.5 mm giving rise to successively intensified vortices provided that U_∞ is kept constant, which in turn results in stronger modulations of the originally 2D base flow.

The experiments were performed in the low speed closed circuit Minimum-Turbulence-Level wind tunnel at KTH, renown for its low background disturbance level and well suited for stability experiments [5]. Phase-triggered single hot-wire anemometry has been used as measurement technique due to its good accuracy and resolution (temporal as well as spatial). Note, that the boundary layer thickness in the present experiments is in the range 4–9 mm.

3 Results

In this experimental investigation we show that miniature classical vortex generators really are suitable devices in accomplishing transition delay and plausible to work in real flow applications. MVGs are clearly superior to circular roughness elements, since the flow is allowed to pass right through them, possibly reducing the absolute instability region behind the devices and allowing for twice as high amplitude streaks to be generated, but still with some margin to the threshold amplitude beyond which the streaky base flow becomes unstable. This makes the streaky base flow much more robust for external perturbations, a prerequisite for real flow applications. Furthermore, in the present setup the T-S waves are being generated upstream of the MVG array, leaving the complex receptivity process of the incoming wave by the MVG array, which really challenges the present passive flow control method. Despite this, transition delay is convincingly accomplished (see Figure 2).

Acknowledgements. JHMF acknowledges the European Research Council for their financial support of the AFRODITE project through a Starting Independent Researcher Grant.

References

1. Cossu, C., Brandt, L.: On Tollmien-Schlichting-like waves in streaky boundary layers. Eur. J. Mech. /B Fluids 23, 815–833 (2004)
2. Fransson, J.H.M., Brandt, L., Talamelli, A., Cossu, C.: Experimental study of the stabilisation of Tollmien-Schlichting waves by finite amplitude streaks. Phys. Fluids 17, 054,110 (2005)
3. Fransson, J.H.M., Fallenius, B.E.G., Shahinfar, S., Sattarzadeh, S.S., Talamelli, A.: Advanced fluid research on drag reduction in turbulence experiments afrodite. J. Phys.: Conf. Ser. 318, 032,007 (2011)
4. Fransson, J.H.M., Talamelli, A., Brandt, L., Cossu, C.: Delaying transition to turbulence by a passive mechanism. Phys. Rev. Lett. 96, 064,501 (2006)
5. Lindgren, B., Johansson, A.V.: Evaluation of the flow quality in the mtl wind-tunnel. Technical Report KTH/MEK/TR–02/13–SE, KTH, Department of Mechanics, Stockholm (2002)
6. Schlatter, P., Deusebio, E., de Lange, R., Brandt, L.: Numerical study of the stabilisation of boundary-layer disturbances by finite amplitude streaks. Int. J. Flow Contr. 2, 259–288 (2010)
7. Shahinfar, S., Sattarzadeh, S.S., Fransson, J.H.M., Talamelli, A.: Revival of classical vortex generators now for transition delay. Phys. Rev. Lett. 109, 074,501 (2012)

Large-Scale Structures in High Reynolds Number Wall-Bounded Turbulence

Nicholas Hutchins

Abstract. Through comparison of two turbulent boundary layers at vastly different Reynolds numbers, we note that the key features of the very large-scale structures appear to be universal (when scaled with the boundary layer thickness δ). The modulating influence of these large-scale features is analysed through means of conditional averages. It is proposed that the much discussed 'amplitude modulation', whereby the large scales modulate the intensity of the small-scale velocity fluctuations, is primarily a near-wall phenomenon, and that further from the surface this may be better described as a 'preferential arrangement'. In this interpretation, it becomes evident that there is a strong link between the very large-scales that populate the log region and the large-scale interfacial bulging that occurs at the edge of the boundary layers. Conditional averages are presented confirming this finding.

1 Introduction

From observations of pre-multiplied energy spectra, Kim and Adrian (1999) made the surprising observation that energetic fluctuations existed at very long length-scales (up to $14R$) in turbulent pipe flows. They called these features very large scale motions (VLSMs). In an attempt to learn more about these features, Hutchins and Marusic (2007b) deployed rakes of hotwires in the logarithmic region of high Reynolds number boundary layers, showing that these energetic events take the form of large-scale streak type structures which they termed 'superstructures'. Further experiments have shed additional light on these coherent motions, demonstrating that they modulate the small-scale near-wall cycle and are accompanied by very large-scale roll-modes (see for example Hutchins and Marusic, 2007a). It has also been noted that these features have a strong footprint at the wall (Hutchins and Marusic,

Nicholas Hutchins
Department of Mechanical Engineering, University of Melbourne, Victoria, Australia
e-mail: nhu@unimelb.edu.au

A. Talamelli et al. (eds.), *Progress in Turbulence V*,
Springer Proceedings in Physics 149,
DOI: 10.1007/978-3-319-01860-7_13,

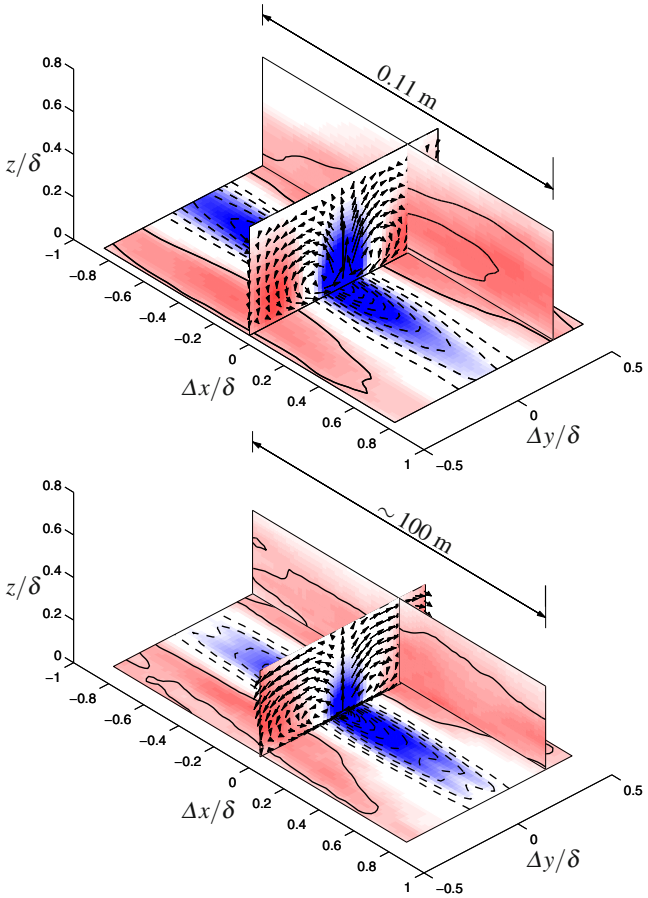

(*a*) $Re_\tau \approx 1000$
$\delta = 0.068$ m

Laboratory dual-plane PIV data of Hambleton et al (2006)

(*a*) $Re_\tau \approx 7.7 \times 10^5$
$\delta = 60$ m

ASL sonic anemometer data from Hutchins et al (2012)

Fig. 1 Linear stochastic estimate (LSE) showing the conditional large-scale structure in the logarithmic region of (*a*) a laboratory flat plate zero-pressure-gradient turbulent boundary layer at moderate Reynolds number ($Re_\tau \approx 1000$) and (*b*) the near-neutral atmospheric surface layer over smooth flat terrain at very high Reynolds number ($Re_\tau \approx 7.7 \times 10^5$). Shaded contours show velocity fluctuations (as a percentage of the condition vector) with the same colour axis for both flows. Blue shows negative velocity fluctuations and red shows positive. Cross-plane vectors show the associated large-scale roll-mode. The condition point is in the logarithmic region for both flows, at $z/\delta \approx 0.1$ for the laboratory and at $z/\delta \approx 0.036$ for the atmospheric data.

2007a; Hutchins et al, 2011) and carry a great deal of Reynolds stress (Balakumar and Adrian, 2007). Examples of these features at two very different Reynolds numbers are shown in figure 1, which shows the conditionally averaged structure based on a negative velocity fluctuation in the logarithmic region. Figure 1(*a*) shows the laboratory orthogonal-plane PIV data of Hambleton et al (2006) at $Re_\tau = 1100$

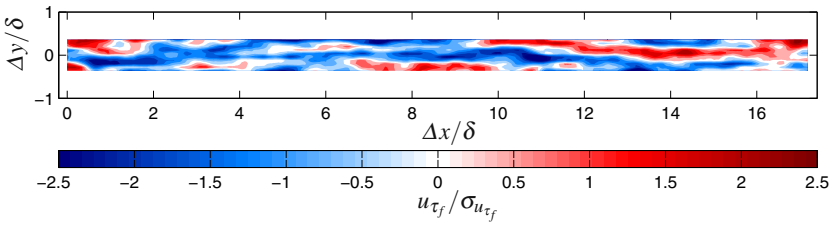

Fig. 2 Example filtered fluctuating shear stress signal from the spanwise array of Hutchins et al (2011). Colour shows Gaussian filtered fluctuating skin friction velocity normalised by the standard deviation. Signals are projected in x using Taylors Hypothesis and a convection velocity of approximately $U_c^+ = 20$.

($Re_\tau = \delta U_\tau/\nu$, where δ is the boundary layer thickness, U_τ is the friction velocity and ν is the kinematic viscosity). Figure 1(b) shows field data from the atmospheric surface layer (ASL) experiments of Hutchins et al (2012) with estimated $Re_\tau \approx O(10^6)$. The time signals of fluctuating velocity from the sonic anemometers are converted to the spatial domain using Taylor's hypothesis and a convection velocity given by the measured mean at $z/\delta = 0.036$. Note that the boundary layer thickness for the low Reynolds number data is 0.06 m, while for the ASL data the layer thickness is estimated at 60 m (yielding a conditional average in plot b that is 100 m in length). Despite this separation in scale and Reynolds number, it is clear that the conditionally averaged large-scale events are very similar between these two boundary layers. In both cases, a highly elongated negative velocity fluctuation is flanked on either side in the spanwise direction by similarly elongated high momentum regions. These elongated features are tall in the wall-normal direction (extending to $z/\delta \approx 0.5$) and are accompanied by large-scale roll modes.

2 Large-Scale / Small-Scale Interaction

We will here explore the interaction between the large-scale structures and the smaller scale features of wall bounded turbulence. We will make use of data from Hutchins et al (2011), comprising a spanwise array of wall-mounted hot-film shear stress sensors and a single traversing hot-wire probe positioned above this array. Figure 2 shows isocontours of instantaneous wall shear stress fluctuation as measured by the spanwise array. These data are presented as fluctuating friction velocity filtered with a Gaussian of size $0.5\delta \times 0.16\delta$ in x and y respectively (u_{τ_f} denotes the filtered signal) and normalised by the standard deviation (σ_{u_τ}). Time-series data from the skin friction sensor array are projected into the spatial domain using Taylor's hypothesis and a convection velocity of $U_c^+ = 20$ (the convection velocity previously measured for the large-scale fluctuations by Hutchins et al, 2011). Long meandering low and high shear stress events are evident in Figure 2, with length-scales that seem to exceed 6δ. The strong similarity between these features and the superstructures recorded in the logarithmic region by Hutchins and Marusic

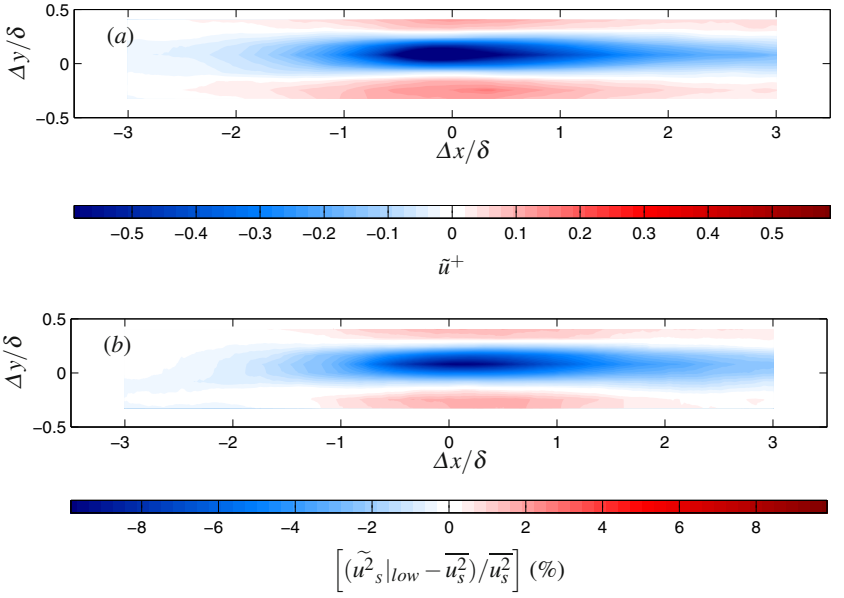

Fig. 3 Conditionally averaged (*a*) velocity fluctuations and (*b*) magnitude of the small-scale energy at $z^+ \approx 15$, conditioned on a negative skin friction fluctuation ($u_{\tau_f} < 0$) at $\Delta x = \Delta y = 0$

(2007b) suggests that the skin friction sensors are successfully detecting the footprints of the superstructure events. Figure 3(*a*) shows the conditionally averaged hot-wire measured velocity fluctuations at $z^+ \approx 15$ based on the occurrence of a large-scale negative shear stress event at the wall ($u_{\tau_f} < 0$ at $\Delta y = \Delta x = z = 0$). This figure offers a glimpse of the conditional form of the superstructure event very close to the surface. The negative shear stress fluctuations are associated with elongated regions of streamwise velocity deficit, flanked on either side in the spanwise direction by regions of increased momentum.

To investigate the connection between the large-scale and small-scale turbulence, we next decompose the measured hotwire signals into a large and small-scale component. This process is illustrated in figure 4. The original raw fluctuating velocity signal (shown on the left) is decomposed in to a large- (top right) and small-scale (bottom right) component using a spectral filter with a wavelength $\lambda_x^+ = 7000$. The choice of this wavelength is based on analysis of energy spectra presented in Hutchins and Marusic (2007b) and Mathis et al (2009) indicating that for $Re_\tau = 14000$ this cut-off wavelength is effective in separating small-scale energy associated with the near-wall cycle from the large-scale superstructure events. There has been much research (Brown and Thomas, 1977; Bandyopadhyay and Hussain, 1984; Hutchins and Marusic, 2007a; Mathis et al, 2009; Chung and McKeon, 2010; Hutchins et al, 2011) to suggest that close to the wall the large scales amplitude modulate the small-scale activity in turbulent boundary layers. All of these studies

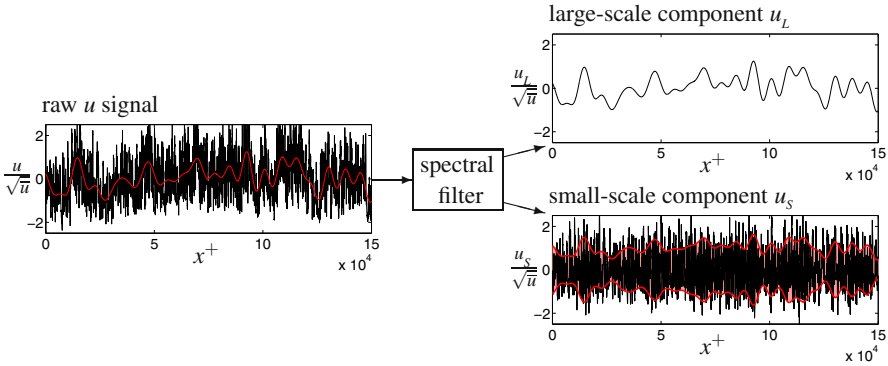

Fig. 4 Decomposition of hot-wire signal into small and large-scale components using a spectral low-pass filter at $\lambda_x^+ \approx 7000$

have observed that there is a strong correlation between the envelope of the small-scale signal and the phase-shifted large-scale signal. Close to the wall, the phase shift seems to tend to zero, such that there is a direct correlation between the filtered envelope of u_S and the large-scale signal u_L. This scenario is illustrated in the bottom-right plot of figure 4 where the red shaded region shows the predicted envelope of the small-scale signal u_S based on the large-scale fluctuation. Although in this figure the amplitude modulation is difficult to discern, a conditional average of the small-scale activity based on a large-scale negative shear-stress fluctuation can demonstrate this trend.

Figure 3(b) shows the square of the small-scale signal u_S^2 conditioned on the occurrence of $u_{\tau_f} < 0$. The tilde notation here indicates that a quantity has been conditionally averaged on the occurrence of a negative large-scale skin friction fluctuation at $\Delta y = \Delta x = 0$. This conditional average represents the modulation of the small-scale variance at $z^+ = 15$ associated with a low-speed (low skin friction) superstructure event. The data in figure 3(b) are presented as a percentage variation about the (unconditional) average small-scale variance $\overline{u_S^2}$. A comparison between figure 3(a) and (b) reveals that at $z^+ = 15$, there is a strong positive correlation (with zero phase shift) between the conditionally averaged large-scale velocity fluctuation and the envelope of the small scale turbulence. The large-scale elongated low momentum region (at $\Delta y = 0$ in figure 3(a), and extending approximately $\pm 2 - 3\delta$ upstream and downstream of $\Delta x = 0$) is clearly accompanied by a region of reduced small-scale activity. Figure 3(b) indicates that the conditioned small-scale variance in this region is decreased by up to 10%. Conversely, the high momentum regions that flank the elongated low-speed regions in the spanwise direction of figure 3 exhibit increased small-scale variance. This form of modulation is relatively straight-forward to understand from simple arguments based on the modified velocity gradient at the wall. The low-speed region of the superstructure event will cause a large-scale region of reduced shear at the wall. This large-scale region will have reduced friction velocity and an increased viscous length-scale. Since the near-wall

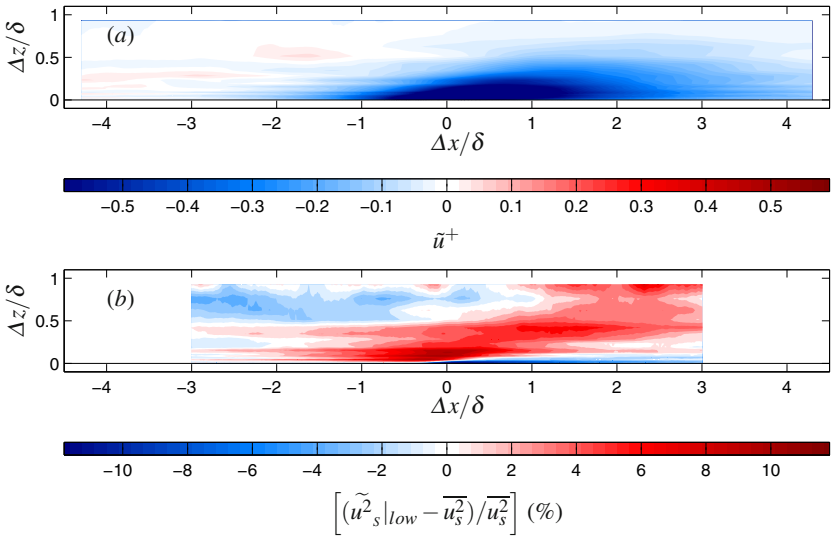

Fig. 5 (*a*) The velocity fluctuations and (*b*) the percentage change in the small-scale streamwise velocity variance, ensemble averaged on a streamwise/wall-normal plane at $\Delta y = 0$ and conditioned on a negative skin friction fluctuation ($u_\tau < 0$) at $\Delta x = \Delta y = 0$

cycle is believed to scale on viscous units (with a size proportional to ν/U_τ and a magnitude proportional to U_τ), it is reasonable to assume that in these regions the near-wall cycle will have a reduced magnitude (leading to a reduced amplitude of small-scale fluctuating components close to the wall). Effectively, the near-wall events (which have a very short time-scale compared to the superstructures) will experience these regions as if the Reynolds number had been reduced. If this argument is correct, one would also expect a frequency modulation effect, since the near-wall structures would be longer in this region and convect somewhat slower (reflecting the reduced U_τ). This would lead to lower frequency small-scale fluctuations in these regions. Such a frequency modulation effect has been recently verified by Ganapathisubramani et al (2012).

At locations further from the surface, the modulation effect becomes more complicated to explain. Figure 5(*a*) shows the ensemble averaged velocity fluctuations on a streamwise / spanwise plane at $\Delta y = 0$, conditioned on a large-scale region of reduced skin friction at $\Delta x = \Delta y = 0$. A tall low-momentum region on the plane of symmetry accompanies the $u_{\tau_f} < 0$ event at the origin. This elongated region extends beyond the log region into the wake of the boundary layer (particularly in the downstream). This region has a pronounced inclination in the downstream direction, as has been noted from many previous conditional averages and two-point correlations (see for example Kovasznay et al, 1970; Christensen and Adrian, 2001). This shape is typical of the low-speed regions that have been previously observed to occur within hairpin packets (Adrian, 2007). Figure 5(*b*) shows the modulation of the small-scale turbulent energy accompanying this large-scale inclined low-momentum

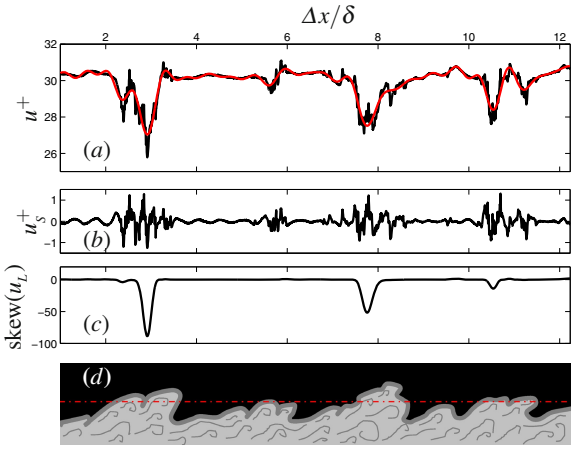

Fig. 6 (*a*) fluctuating velocity signal at $z/\delta \approx 0.77$ (large-scale component u_L is shown in red); (*b*) decomposed small-scale component u_S; (*c*) skewness of the large-scale component; (*d*) a schematic of edge of boundary, showing the turbulent / non-turbulent interface. Red dot-dashed line shows hot-wire measurement at $z/\delta = 0.77$.

region. Only very close to the surface is the negative large-scale velocity fluctuation directly associated with reduced small-scale intensity. Further from the wall, a more complicated interplay seems to develop. Most noticeably, the upstream inclined back of the low-speed region (of figure 5*a*) seems to be predominantly associated with increased small-scale activity. Bandyopadhyay and Hussain (1984) and Chung and McKeon (2010) have explained this shift in behaviour as an increasing phase difference with z between the large-scale u fluctuation and the envelope of the small-scale turbulence. Hutchins et al (2011) have suggested that further from the wall (in the log and wake region), the increased small-scale amplitude is closely aligned with the shear layers (the negative du/dx) that exist along the inclined back of the low momentum region.

There is a fine line here between notions of 'amplitude modulation' and simple 'preferred arrangements'. The hairpin packet paradigm suggests that increased vortical activity should be located along the inclined back of the large-scale low momentum region. The increased small-scale activity observed in this region in figure 5(*b*) may be more indicative of these arrangements. The suggestion could be that close to the surface, the large scale shear stress fluctuations genuinely do modulate the near-wall cycle in a manner that gives rise to amplitude modulated small-scale fluctuations. Further from the surface, the variations in small-scale activity might be better understood as preferential arrangements. The analysis below suggests that at the edge of the layer, at least, this might be a more apt description.

Notions of 'amplitude modulation' aside, the remarkable result from figure 5(*b*) is that there is an apparent link between the large-scale shear stress fluctuation at the wall, and increased small-scale activity at the edge of the boundary layer. This would seem to suggest a strong link between the superstructure events and the interfacial bulging that is known to occur in the highly intermittent turbulent / non-turbulent interface at the edge of the boundary layer. To explore this, figure 6(*a*) shows the fluctuating velocity signal close to the edge of the layer at $z/\delta = 0.77$. The signal is highly intermittent, with quiescent regions that are punctuated by periods of

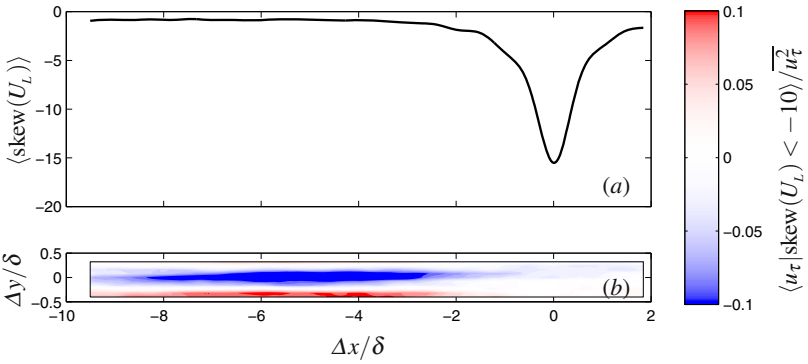

Fig. 7 (*a*) shows condition event $\langle \text{skew}(u_L) < -10 \rangle$ at $z/\delta = 0.77$, used to identify the interfacial bulge; (*b*) shows the shear stress at the wall conditioned on the bulge event

intense turbulence. This distinctive signal is a result of the hot-wire measuring a path through the turbulent / non-turbulent interface as illustrated by the red dot-dashed line in the schematic of figure 6(*d*). The small-scale component of the velocity signal is shown in Figure 6(*b*), highlighting that at these locations, almost all small-scale activity is associated with the interfacial bulging (reinforcing the 'preferential arrangement' description). Figure 6(*c*) shows the skewness of the large-scale component (the large-scale component is shown in red on plot *a*). It is observed that high negative values of this quantity are an excellent marker of the turbulent bulges. We use this signal to conditionally average the skin friction fluctuations at the wall (based on situations where skew(u_L) exceeds some negative threshold). The resulting conditionally averaged skin friction signal at the wall is shown in figure 7(*b*). It is clear that the interfacial bulge (shown in figure 7*a* and occurring at $\Delta x = 0$), is accompanied by a noticeable large-scale skin friction footprint at the wall (centered some distance upstream) with a form that is very similar to the previously observed superstructure event. This conditional average leads us to believe that the very large-scale features that are known to populate the logarithmic region (with a footprint down to the wall) are associated with the bulging that characterises the turbulent / non-turbulent interface at the edge of the boundary layer.

3 Conclusions

The observed superstructure type events, consisting of highly elongated regions of positive velocity fluctuation, and accompanied by large-scale roll-modes are universal features of turbulent boundary layers. They have been observed with a very similar form in laboratory measurements ranging from $1000 < Re_\tau < 14000$, and also in near-neutral ASL measurements at Reynolds numbers up to $Re_\tau \approx O(10^6)$. While the notion of amplitude modulation may provide a reasonable explanation for the interaction between these very large-scales and the near-wall cycle close to the surface, we would favour an interpretation based on 'preferential arrangement'

further from the surface. The preliminary results shown here suggest a link between the superstructure events and interfacial bulging at the edge of the turbulent boundary layer.

Acknowledgements. This research was supported under the Australian Research Council's Discovery Projects funding scheme (project numbers DP110102448 and DP1093585). NH is the recipient of an Australian Research Council Future Fellowship (project number FF110100432).

References

Adrian, R.J.: Hairpin vortex organization in wall turbulenc. Phys. Fluids 19, 041,301 (2007)

Balakumar, B.J., Adrian, R.J.: Large- and very-large-scale motions in channel and boundary-layer flows. Philosophical Transactions of the Royal Society A: Mathematical, Physical and Engineering Sciences 365(1852), 665–681 (2007)

Bandyopadhyay, P.R., Hussain, A.K.M.F.: The coupling between scales in shear flows. Phys. Fluids 27(9), 2221–2228 (1984)

Brown, G.L., Thomas, A.S.W.: Large structure in a turbulent boundary layer. Phys. Fluids 20(10), 243–252 (1977)

Christensen, K.T., Adrian, R.J.: Statistical evidence of hairpin vortex packets in wall turbulence. J. Fluid Mech. 431, 433–443 (2001)

Chung, D., McKeon, B.J.: Large-eddy simulation of large-scale structures in long channel flow. J. Fluid Mech. 661, 341–364 (2010)

Ganapathisubramani, B., Hutchins, N., Monty, J., Chung, D., Marusic, I.: Amplitude and frequency modulation in wall-turbulence. J. Fluid Mech. 712, 61–91 (2012)

Hambleton, W.T., Hutchins, N., Marusic, I.: Multiple plane PIV measurements in a turbulent boundary layer. J. Fluid Mech. 560, 53–64 (2006)

Hutchins, N., Marusic, I.: Evidence of very long meandering features in the logarithmic region of turbulent boundary layers. J. Fluid Mech. 579, 1–28 (2007a)

Hutchins, N., Marusic, I.: Large-scale influences in near-wall turbulence. Phil. Trans. R. Soc. A 365, 647–664 (2007b)

Hutchins, N., Monty, J., Ganapathisubramani, B., Ng, H., Marusic, I.: Three-dimensional conditional structure of a high-Reynolds-number turbulent boundary layer. J. Fluid Mech. 673, 255–285 (2011)

Hutchins, N., Chauhan, K., Marusic, I., Monty, J., Klewicki, J.: Towards reconciling the large-scale structure of turbulent boundary layers in the atmosphere and laboratory. Boundary Layer Meteorol. 145(2), 273–306 (2012)

Kim, K.C., Adrian, R.: Very large-scale motion in the outer layer. Phys. Fluids 11, 417–422 (1999)

Kovasznay, L.S.G., Kibens, V., Blackwelder, R.F.: Large-scale motion in the intermittent region of a turbulent boundary layer. J. Fluid Mech. 41, 283–326 (1970)

Mathis, R., Hutchins, N., Marusic, I.: Large-scale amplitude modulation of the small-scale structures in turbulent boundary layers. J. Fluid Mech. 628, 311–337 (2009)

Study of the Outer Self-regeneration of Turbulence in Wall Flows

A. Cimarelli, Elisabetta De Angelis, A. Talamelli, and C.M. Casciola

Abstract. A new approach for the study of the overlap layer of wall-turbulence is proposed. The multi-dimensional description of turbulence given by the Kolmogorov equation generalized to wall-flows is used and shown relevant for the identification of very robust features of the overlap layer. Numerical data of a turbulent channel are used. Despite the low Reynolds, a well-defined outer energy source region appears. The possibility to analyze its effects on the energy tranfer among scales and wall-distances is shown important to clarify the influences of the external region on the inner layer.

1 Introduction

One of the most peculiar aspects of turbulence in wall flows is the ability of the turbulent fluctuations to regenerate themselves forming self-sustained processes. In wall flows, the production of turbulent fluctuations is embedded in the system rather than being provided by an external agent. The dynamics of these self-sustaining mechanisms have been extensively investigated and these processes are known to be responsible for the turbulent drag.

It is well known that the near-wall layer is crucial to the dynamics of attached shear flows, being the seat of the highest rate of turbulent energy production and of the maximum turbulent intensities. The possibility to identify very robust kinematic features in the proximity of a wall fed the hope of the scientific community to give a complete and consistent dynamical description of the underlying physics of these processes. Indeed, the turbulent

A. Cimarelli · Elisabetta De Angelis · A. Talamelli
DIEM, Università di Bologna, Viale Risorgimento, 40136 Bologna, Italy
e-mail: {andrea.cimarelli2,e.deangelis,
alessandro.talamelli}@unibo.it

C.M. Casciola
DIMA, Università di Roma "La Sapienza" Via Eudossiana 18, 00184 Roma, Italy
e-mail: carlomassimo.casciola@uniroma1.it

A. Talamelli et al. (eds.), *Progress in Turbulence V*,
Springer Proceedings in Physics 149,
DOI: 10.1007/978-3-319-01860-7_14,

fluctuations near a wall have been found to organize in well defined coherent motions consisting of quasi-streamwise vortices and high/low velocity regions alternating in the spanwise direction. From these observations, a conceptual model has been developped. As shown in [1], these turbulent structures form a self-sustaining cycle mantaining near-wall turbulence without the need of any input from the core flow, i.e. it is an autonomous cycle.

From the technological point of view, the near-wall cycle is crucial since it controls the magnitude of the wall stress. But, coherent structures exist also at larger scales in the so-called overlap layer and have been found to form an outer self-sustaining mechanism of regeneration of very large turbulent fluctuations. The phenomenology resembles the near-wall cycle though its characteristic dimensions are larger. The coherent motions involved in this outer cycle should scale with external variables and, as a consequence, its field of action should increase as the extent of the log-layer with Reynolds. Hence, the understanding of these outer dynamics is crucial for the modelling of wall-turbulence at the asymptotic regime of very large Reynolds number.

Several approaches have been used to identify the main features of the overlap layer such as the study of the turbulent intensity profiles, of the outer energy spectra scaling and of the dynamical features of the large coherent motion, see [2]. Here, we aim at extending these analysis by considering a multi-dimensional approach given by the generalized Kolmogorov equation. The possibility to study how the turbulent energy is generated, transferred and dissipated among different scales and wall-distances, will be shown relevant for the understanding of the overlap layer physics, see also [3].

2 Kolmogorov Equation

The Kolmogorov equation is the balance equation for the second order structure function, $\langle \delta u^2 \rangle$, with $\delta u^2 = \delta u_i \delta u_i$, where the fluctuating velocity increment at position X_s and vector separation r_s is $\delta u_i = u_i(X_s + r_s/2) - u_i(X_s - r_s/2)$. This equation allows to identify the energy transport processes and production mechanisms in the compound space of scales and position. Indeed, two distinct transport processes exist in wall-turbulence. One corresponds to the energy transfer in the space of scales and the other is associated with the spatial redistribution of energy due to inhomogeneity. For the channel flow the equation reads, see [4] for the details,

$$\begin{aligned} &\frac{\partial \langle \delta u^2 \delta u_i \rangle}{\partial r_i} + \frac{\partial \langle \delta u^2 \delta U \rangle}{\partial r_x} + 2\langle \delta u \delta v \rangle \left(\frac{dU}{dy} \right)^* + \frac{\partial \langle v^* \delta u^2 \rangle}{\partial Y_c} \\ &= -4\langle \epsilon^* \rangle + 2\nu \frac{\partial^2 \langle \delta u^2 \rangle}{\partial r_i \partial r_i} - \frac{2}{\rho} \frac{\partial \langle \delta p \delta v \rangle}{\partial Y_c} + \frac{\nu}{2} \frac{\partial^2 \langle \delta u^2 \rangle}{\partial {Y_c}^2} \ . \end{aligned} \tag{1}$$

where the mean velocity $U(y)$ ($y = x_2$) is along the $x = x_1$ axis, $Y_c = X_2$ is the wall-normal coordinate of the mid-point, ν is kinematic viscosity

and $\epsilon = \nu(\partial u_i/\partial x_j)(\partial u_i/\partial x_j)$ is the pseudo-dissipation. Here * denotes the arithmetic average of a variable at the points $X_s \pm r_s/2$. As shown in [5], to emphasize its conservative nature, equation (1) is restated in terms of a four-dimensional vector field, $\mathbf{\Phi} = (\Phi_{r_x}, \Phi_{r_y}, \Phi_{r_z}, \Phi_c)$, defined in a four dimensional space (r_x, r_y, r_z, Y_c),

$$\nabla_4 \cdot \mathbf{\Phi}(\mathbf{r}, Y_c) = \xi(\mathbf{r}, Y_c) \ , \tag{2}$$

where $\xi = 2\langle \delta u \delta v \rangle \left(dU/dy\right)^* - 4\langle \epsilon^* \rangle$ is the energy source/sink. The projection of the flux in the space of scales is the scale-space transfer vector,$\mathbf{\Phi}_r = (\Phi_{r_x}, \Phi_{r_y}, \Phi_{r_z}) = \langle \delta u^2 \delta \mathbf{u} \rangle - 2\nu \nabla_r \langle \delta u^2 \rangle$. The projection in physical space is the spatial flux $\Phi_c = \langle v^* \delta u^2 \rangle + 2\langle \delta p \delta v \rangle / \rho - \nu / 2 \partial \langle \delta u^2 \rangle / \partial Y_c$. The data used are those of a channel flow direct numerical simulation (DNS) at $Re_\tau = 550$. The computational domain is $8\pi h \times 2h \times 4\pi h$ with a resolution in the homogeneous directions, $\Delta x^+ = 13.5$ and $\Delta z^+ = 6.7$.

3 Results and Final Comments

In the present work we limit our analysis to the (r_z, Y_c)-space by setting $r_x = r_y = 0$. As shown in the left plot of figure 1, the isocontours of ξ highlight two regions of energy source. The first stronger one in the near-wall region is the engine of wall-turbulence and will be hereafter called the driving scale-range (DSR). Indeed, only one singular point exists in the augmented space from which the energy fluxes take origin. The field lines of figure 1 stem from the DSR in the buffer layer and diverging sustain the whole turbulent motion in the other regions of the combined physical/scale space. Let us emphasize that the clear matching of scales and positions, $r_z^+ \sim 40$ and $Y_c^+ \sim 12$, suggests a strong connection with the near-wall cycle.

An interesting feature emerging from the present analysis is the existence of a rescaled replica of the processes described for the DSR, associated with a second peak in the energy source, called hereafter outer scale-range (OSR), see the contours of figure 1. Despite the low Reynolds number considered, the OSR belongs to a putative overlap layer and appears to be the result of an outer production mechanism well separated from the near-wall one.

Let us now investigate the nature of the turbulent structures involved in the OSR. According to Townsends attached eddy hypothesis, the production scales should behave linearly with wall-distance. The present data actually confirm this prediction with the spanwise scale of the energy source increasing to a very good degree linearly with wall-distance, $r_z^+ \sim 80 + Y_c^+$. A second consequence of the attached eddy hypothesis is the appereance of a k^{-1}-behavior at the large scales of the energy cospectrum and, hence, for turbulent production. In the present framework, this spectral law corresponds to a scale-production which follow a logarithmic behavior [6],

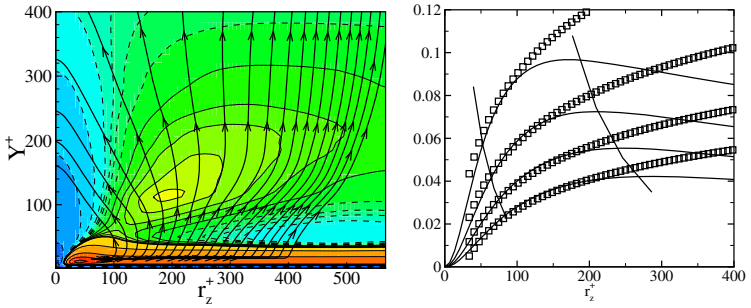

Fig. 1 Left: energy source contours, ξ, and field line of the energy flux Φ in the $r_x = r_y = 0$-plane. Right: r_z-scaling of production, $2\langle\delta u\delta v\rangle\,(dU/dy)^*$, for four different positions within the overlap layer. The squares represent the log-law (3) while the two vertical lines are $r_z^+ = ky^+$ and the scale of maximum energy source, $r_z^+ = 80 + Y_c^+$.

$$\langle\delta u\delta v\rangle\frac{dU}{dy} = u_\tau^2(C + D\log(r/y))/\kappa y \qquad \text{for} \qquad y < r < h \tag{3}$$

where κ is the Karman's constant. In the right of 1, the production in the overlap layer is reported and shown to follow this law for intermediate scales.

In conclusion, the outer energy source occurs at wall normal positions and scales that make it suspect of a result of an outer self-regenerating mechanism composed by attached eddies. As a consequence, its field of action should increase as the extent of the log-layer with Reynolds. The presence of the OSR violates the equilibrium assumption of the overlap layer. The OSR continuously injects energy feeding and diverging the field lines of the energy fluxes, see streamtraces of figure 1. In accordance with these observations, the large Reynolds number state of wall-turbulence should appears dominated by the overall production associated to the OSR. In this context the influences of the external region to the near-wall turbulence consist in a modulation and modification of the energy fluxes topology, i.e. a confination of the energy transfer emerging from the near-wall energy source.

References

1. Jiménez, J., Pinelli, A.: The autonomous cycle of near-wall turbulence. J. Fluid Mech. 389 (1999)
2. Smits, A.J., McKeon, B.J., Marusic, I.: HighReynolds Number Wall Turbulence. Annu. Rev. Fluid Mech. 43 (2011)
3. Cimarelli, A., De Angelis, E., Casciola, C.M.: Assessment of the turbulent energy paths from the origin to dissipation in wall-turbulence. J. of Phys.: Conference Series 318 (2011)

4. Marati, N., Casciola, C.M., Piva, R.: Energy cascade and spatial fluxes in wall turbulence. J. Fluid Mech. 521 (2004)
5. Cimarelli, A., De Angelis, E., Casciola, C.M.: Paths of energy in turbulent channel flows. J. Fluid Mech. 715 (2013)
6. Davidson, P.A., Nickels, T.B., Krogstad, P.A.: The logarithmic structure function law in wall layer turbulence. J. Fluid Mech. 550 (2006)

Turbulent Boundary Layers in Long Computational Domains

Philipp Schlatter and Qiang Li

Abstract. A new highly resolved large-eddy simulation is presented for a spatially developing turbulent boundary layer, covering in one single domain the range of Reynolds number $Re_\theta = 180$ to 8300. Turbulence statistics are in close agreement with experiments and other simulations. The evolution of the large outer-layer structures is examined using spectra. It is found that the near-wall region is very intermittent, and at high Re_θ dominated by strong modulation of the turbulence intensity through the outer structures. The corrugated appearance of the boundary-layer edge is thus directly linked to the turbulence regeneration in the immediate wall vicinity.

1 Introduction

Wall-bounded turbulence emerges *e.g.* along the surface of moving ships and airplanes or in pipelines. To emphasise the practical relevance of wall turbulence it must be clear that the prediction of skin friction and drag is directly related to fuel consumption or the power needed to transport gases through pipelines. Canonical wall-bounded flows are the flat-plate boundary layer, pipe and channel flows. While these flows are in essence theoretical abstractions and do not appear as such in reality it is necessary to study them separately by means of experiments, simulations or theory, since they constitute basic building blocks of more complete, *i.e.* real, flows. For instance, more complex geometries such as the turbulent flow along a curved wing might be approximated by a boundary layer with a suitable pressure gradient.

Simulations of turbulent flows are particularly helpful identifying physical processes occurring in near-wall turbulence, as the whole velocity field is available for analysis. In particular higher Reynolds numbers are necessary to obtain a clear separation of scales related to the near-wall turbulence cycle (*i.e.* scaling in wall units) and the mechanisms and structures related to the outer region of the boundary layer,

Philipp Schlatter · Qiang Li
Linné Flow Centre, KTH Mechanics, Stockholm, Sweden
e-mail: pschlatt@mech.kth.se

A. Talamelli et al. (eds.), *Progress in Turbulence V*,
Springer Proceedings in Physics 149,
DOI: 10.1007/978-3-319-01860-7_15,

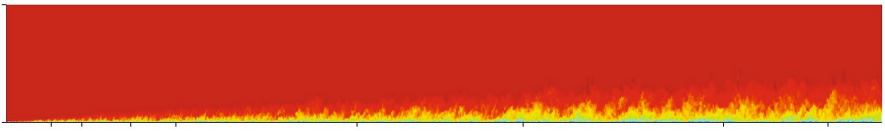

Fig. 1 Side view of the complete domain showing colours of the streamwise velocity; blue corresponds to zero velocity and red to the free-stream velocity. The streamwise positions indicated by the black ticks are: $Re_\theta = 1000$, 1410, 2000, 2500, 4300, 5800, 7500, 8300.

i.e. living in the logarithmic region and beyond. However, it remains crucial to properly validate simulation data with corresponding experimental results to ascertain that the turbulence at high Reynolds number has reached its developed state.

2 Simulation Setup

In order to contribute to the available simulation data, a new series of numerical simulations of spatially evolving turbulent boundary layers is discussed, reaching up to the highest Reynolds numbers in wall-resolved simulations. In a similar way as in experiments, we let the flow enter the domain as an unperturbed laminar Blasius flow, which is then disturbed to transition to turbulence via a trip forcing [5,6]. In this way, we avoid the use of a recycling/rescaling technique to generate turbulent unsteady inflow conditions. A close correspondence of the flow characteristics as in experimental setups is expected [3], with a minimum amount of ad-hoc parameters to specify. However, as documented in our recent study [6], the flow response to tripping is most efficient when performed at lower Reynolds number, *i.e.* close to the leading edge of the plate. Therefore, our simulation technique requires very long computational domains, essentially reproducing a wind-tunnel setup. In the present case, the domain starts at a low (laminar) $Re_\theta = 180$, directly followed by the tripping location. Transition to turbulence is assumed to be complete by about $Re_\theta = 700$, and a state approximately independent of initial conditions is reached somewhere around $Re_\theta = 1500$. The outflow of our domain is located at the (computationally very) high $Re_\theta = 8500$. In this single long domain, illustrated in Fig. 1, the boundary layer is allowed to develop naturally from the tripping location to the higher Reynolds numbers *without* any re-injection or recycling procedures. In consequence, albeit expensive, this computational setup allows us to study, *e.g.*, the mean flow development and the scaling behaviour of the fluctuating energy over a long spatial distance free from any pseudo-periodic (parasitic) effects.

However, such domains require a large number of grid points: We employ a grid with a total of $13824 \times 513 \times 1152$ collocation points in physical space in the streamwise, wall-normal and spanwise directions. As in our previous studies [5], the spectral code SIMSON is employed, giving very high accuracy coupled with efficient massive parallelisation (parallel efficiency up to 60% on 4096 cores on an Infiniband cluster). The grid resolution in viscous units is $\Delta x^+ = 18$ and $\Delta z^+ = 8$ which is good, but not quite as high as for proper direct numerical simulation (DNS).

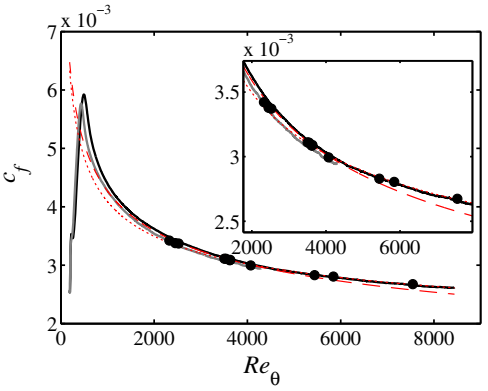

Fig. 2 Skin-friction coefficient c_f. (black) present LES, (gray) DNS [5], (symbols) experiments [2, 3], (dotted) $c_f = \kappa^{-1}(\ln Re_\theta + C)^{-2}$ with $\kappa = 0.384$ and $C = 4.127$, (dashed) $c_f = 0.024 Re_\theta^{-1/4}$.

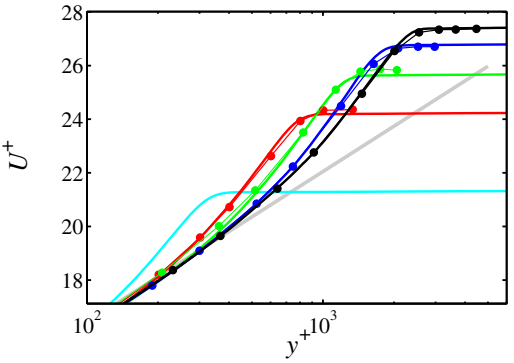

Fig. 3 Zoom of the mean velocity profiles at $Re_\theta = 1000$, 2500, 4000, 5800, 7500, symbols from experiments by Örlü [2, 3]. Gray corresponds to the log law ($\kappa = 0.41$, $B = 5.2$).

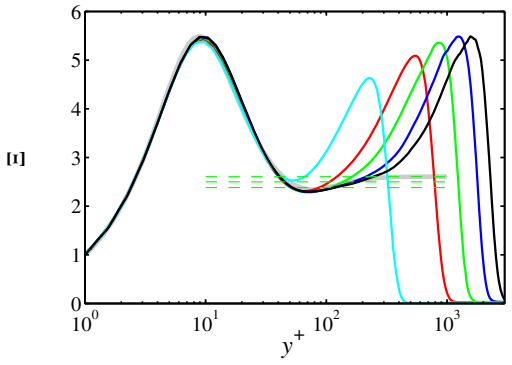

Fig. 4 Log-law indicator function $\Xi = y^+(\mathrm{d}U^+/\mathrm{d}y^+)$ for the same Re_θ. Gray corresponds to Monkewitz *et al.* [1].

Therefore, the ADM-RT subgrid-scale model [4] is employed, adding some limited dissipation only at the smallest scales improving the accuracy of our results. This model is based on high-order high-pass filters and thus adapts itself to the local resolution and will effectively be inactive if not needed. Note that the chosen resolution in this study corresponds to highly resolved large-eddy simulation (LES), and there are simulations in the literature with poorer resolution that are denoted DNS.

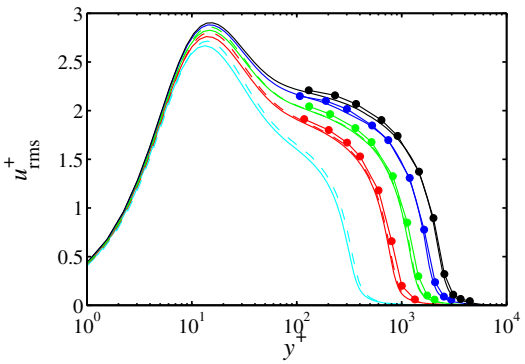

Fig. 5 Streamwise velocity fluctuations u_{rms} for $Re_\theta = 1000, 2500, 4000, 5800, 7500$. (solid) present LES, (dashed) DNS [5], (symbols) experiments by Örlü [2, 3] (only shown for $y^+ > 100$).

3 Results

The skin friction from the LES compared to DNS [5] and experiments [2, 3] together with the $1/7^{\mathrm{th}}$ power-law and log-law correlations is shown in Fig. 2. Good agreement can be established; interesting is that for lower $Re_\theta < 4000$ the $1/7^{\mathrm{th}}$ power-law correlation is accurate, whereas for higher Re_θ the log-law correlation is much more suitable. The generally good agreement with experiments can also be seen in the mean velocity profile U^+: In the near-wall and overlap region, the data shows the expected linear and logarithmic behaviour; discrepancies usually show up in the wake region, *i.e.* farthest away from the wall indicating incomplete development of the flow. Fig. 3 thus zooms in into that region, showing the good agreement between LES and experiments also in the outer region. Moreover, the vertical derivative of the mean velocity, the so-called log-law indicator function Ξ, closely follows the correlation proposed by Monkewitz *et al.* [1], as shown in Fig. 4. In case a genuine logarithmic region is present in the flow, Ξ would asymptote to a constant with value $1/\kappa$. The present results show that the diagnostic function is departing into the wake region just before reaching that plateau (expected to be around $\kappa \approx 0.38$), indicating that the Reynolds number is still too low to make definite statements about the (disputed) value of κ.

The turbulent fluctuations, shown in Fig. 5, also confirm the above mentioned agreement. Furthermore, the slow increase of the peak value in the buffer layer due to the outer influence can be seen together with a slight attenuation effect due to the lower resolution in the LES. Finally, Fig. 6 displays the premultiplied budget of the turbulent kinetic energy k, to emphasise the outer layer. In this figure, the activity of the subgrid-scale model is highlighted by the difference between the total dissipation and the resolved viscous dissipation (computed via the residual of the budget). It can be seen that its influence is small, but certainly not neglegible. Physically, the intermittent wake region, $y/\delta_{99} > 0.5$ is notable, as all budget terms except the viscous diffusion are contributing to the energy transfer. This is in stark contrast to internal flows such as channels or pipes.

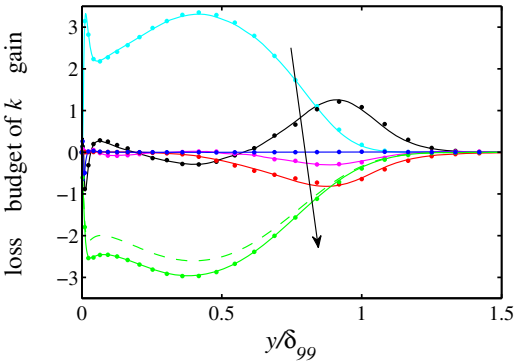

Fig. 6 (Premultiplied) budget of the turbulent kinetic energy k at $Re_\theta = 4000$; (lines) present LES, (symbols) DNS from [5]. In direction of arrow: production, turbulent diffusion, viscous diffusion, velocity-pressure correlation, convection, resolved dissipation, total dissipation (including SGS model dissipation).

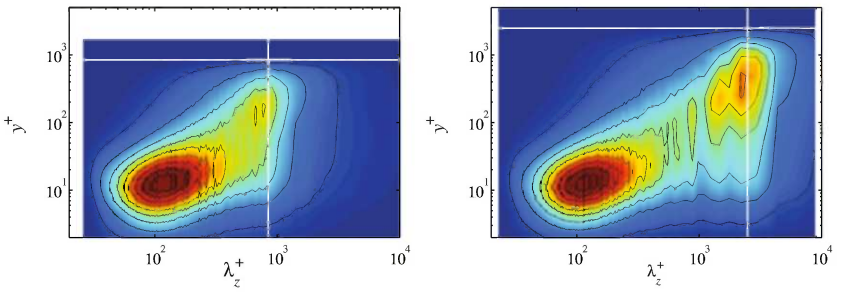

Fig. 7 Premultiplied spanwise spectra of the streamwise velocity at $Re_\theta = 2500$ and 8300, scaled in viscous units. The invariant inner peak is clearly visible together with an increasingly strong outer peak. The white line correspond to δ_{99}.

In a second part, structural information of the flow is discussed, exploiting the wide range of Reynolds number: Premultiplied energy spectra clearly highlight the presence of an invariant inner peak (corresponding to the near-wall streak cycle) together with a stronger outer peak, located at $\lambda_z \approx \delta_{99}$ and increasing in amplitude as the Reynolds number increases (not shown). The footprint of the outer-layer activities is getting very strong at $Re_\theta \approx 8000$: Visualisations of the evolving turbulent boundary layer, such as the ones presented in Fig. 8, persistently show the large-scale structures, but also another very dominant modulating effect: Near-laminar low-speed islands are clearly observed, which are alternating with regions of high intensity. A clear connection between these modulations at the wall, and the large-scale bulges in the outer region can be established. It should be noted that this large-scale modulation becomes more prominent with increasing Re_θ, motivating further studies, including postprocessing and new simulations. Proper modelling of turbulence can be improved with a better understanding of these mutli-scale processes.

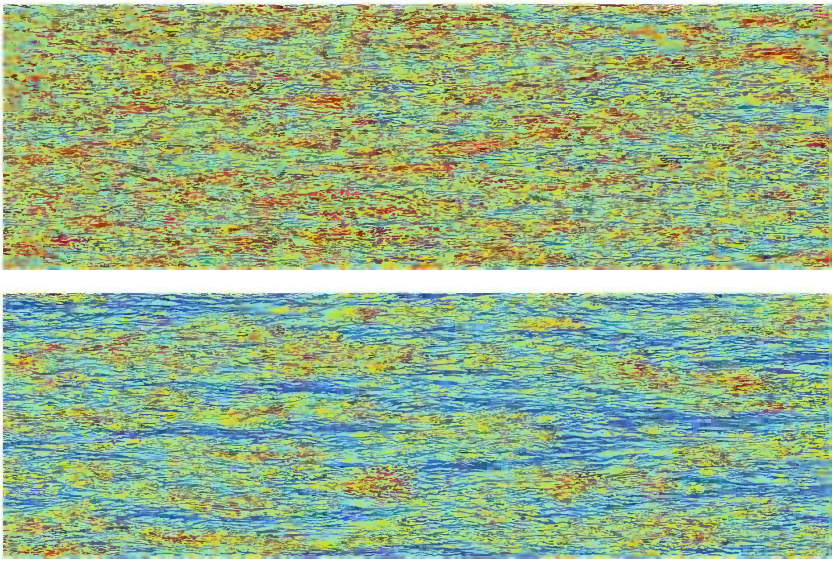

Fig. 8 View of the near-wall region in an x/z-plane at $y^+ = 15$. The colours indicate streamwise disturbance velocity from negative (blue) to positive (red). *Left:* $Re_\theta = 2500$, corresponding to $Re_\tau \approx 800$. *Right:* $Re_\theta = 8300$, or $Re_\tau = 2500$.

Acknowledgements. Ramis Örlü is gratefully acknowledged for providing the experimental data obtained in the MTL windtunnel at KTH. Computer time was provided by Swedish National Infrastructure for Computing (SNIC) through a generous grant by the Knut and Alice Wallenberg Foundation.

References

1. Monkewitz, P.A., Chauhan, K.A., Nagib, H.M.: Self-consistent high-Reynolds-number asymptotics for zero-pressure-gradient turbulent boundary layers. Phys. Fluids 19, 115101 (2007)
2. Örlü, R.: Experimental studies in jet flows and zero pressure-gradient turbulent boundary layers. Ph.D. Thesis, KTH Mechanics, Sweden (2009)
3. Örlü, R., Schlater, P.: Comparison of experiments and simulations for zero-pressure gradient turbulent boundary layers at moderate Reynolds numbers (2012) (submitted)
4. Schlatter, P., Stolz, S., Kleiser, L.: LES of transitional flows using the approximate deconvolution model. Int. J. Heat Fluid Flow 25, 549–558 (2004)
5. Schlatter, P., Örlü, R.: Assessment of direct numerical simulation data of turbulent boundary layers. J. Fluid Mech. 659, 116–126 (2010)
6. Schlatter, P., Örlü, R.: Turbulent boundary layers at moderate Reynolds numbers: Inflow length and tripping effects. J. Fluid Mech. 710, 5–34 (2012)

The Streamwise Turbulence Intensity – A Comparison between Smooth and Rough Wall Turbulent Boundary Layers

A. Segalini, R. Örlü, Ian P. Castro, and P. Henrik Alfredsson

Abstract. Clear differences in turbulence intensity profiles in smooth, transitional and fully rough zero-pressure gradient boundary layers are demonstrated, using the diagnostic plot (u'/U vs. U/U_∞ where u' and U are the local fluctuating and mean velocities and U_∞ is the free-stream velocity). A wide range of published data is considered and all zero-pressure gradient boundary layers yield outer flow u'/U values which are roughly linearly related to U/U_∞, just as for smooth walls, but with a significantly higher slope. The difference in slope is due largely to the influence of the roughness parameter (ΔU^+ in the usual notation) and all the data can be fitted empirically by using a modified form of the scaling, dependent only on $\Delta U^+/U_\infty^+$. It is observed that the turbulence intensity, at a location in the outer layer where U/U_∞ is fixed, rises monotonically with increasing $\Delta U^+/U_\infty^+$ regardless of the roughness morphology.

1 Introduction

The turbulent boundary layer over a rough wall is a canonical flow case that, despite its long history, is still a subject of numerous debates regarding the physical phenomena involved and its appropriate scaling. Compared to a turbulent boundary layer over a smooth wall with the same Reynolds number based on the thickness of the boundary layer, δ, and the friction velocity, u_*, the mean velocity over the rough wall is lower than the corresponding one measured at the same height over a smooth surface. This velocity difference is usually assumed to be constant from the roughness surface to a height $y = \delta$, and is referred to as the *roughness function*, ΔU^+, where the $+$ superscript indicates viscous scaling based on u_* and the

A. Segalini · R. Örlü · P. Henrik Alfredsson
Linné Flow Centre, KTH Mechanics, SE-100 44 Stockholm, Sweden
e-mail: segalini@mech.kth.se

Ian P. Castro
School of Engineering Sciences, University of Southampton, Southampton SO17 1BJ, U.K.

A. Talamelli et al. (eds.), *Progress in Turbulence V*,
Springer Proceedings in Physics 149,
DOI: 10.1007/978-3-319-01860-7_16,

kinematic viscosity, ν. The mean velocity profile of the boundary layer over a rough wall is often assumed to have the same structure as the equivalent smooth case with the offset provided by the roughness function as

$$\frac{U}{u_*} = \frac{1}{\kappa}\ln\left(y^+\right) + B - \Delta U^+ + \frac{2\Pi}{\kappa}W\left(\frac{y}{\delta}\right), \tag{1}$$

with a logarithmic region near the wall and a wake region for $y = \mathcal{O}(\delta)$. The y-origin is located between the valley and the peak of the roughness, at a distance d from the roughness minimum height [1]. Another major difference between the smooth and rough case is associated to the higher value of the wake parameter Π observed over rough surfaces [2].

It is generally believed that the direct effect of roughness can be observed in a layer with size 2-3k, where k is the roughness height, leading to the conclusion that high values of the ratio δ/k are required to reduce the effect of the roughness to the inner region of the boundary layer, which is dominated by viscous effects in the smooth wall case [3]. Away from the wall, and for a roughness with high enough δ/k, the turbulent flow will just be determined by the momentum transferred downward and absorbed by the drag of the roughness elements, a hypothesis usually referred to as Townsend's similarity hypothesis. The validity of such an assumption has been discussed in some recent investigations [2, 4, 5], but at the moment it is the only model available that describes at least part of the distribution of the velocity correlations in the boundary layer.

It is clear that the complete characterization of the flow over rough surfaces is a complicated task where a large number of parameters are involved, most of them related to the roughness characteristics, making any attempt to provide an *a priori* estimation of the turbulence intensity cumbersome. Despite the fact that a significant amount of experimental and numerical data are available, the research community has not been able yet to provide some trend without relying on specific data sets and, in particular, without the possibility to generalize the results.

Recently, Alfredsson *et al.* [6] have proposed a new fit of the streamwise velocity fluctuation profile, viz. a scatter plot between the mean velocity (normalized by an outer characteristic velocity scale, such as the free-stream velocity, U_∞) and the local streamwise turbulence intensity, u'/U, where u' is the streamwise velocity standard deviation. The new way to plot experimental and numerical data for u' yields a collapse of the data over a significant part of the boundary layer and, in a region starting within the logarithmic region out into the wake region, u'/U decreases linearly with U/U_∞: This feature gave the possibility to develop a simple estimation of the streamwise velocity variance profile once the mean velocity profile is given.

In the present work the diagnostic plot method is applied to data from rough surfaces to investigate the possibility that a similar fit might exist in this case as well, leading to some simple relationship between the mean velocity profile and the turbulence intensity. It is expected that the roughness characteristics should modify the plot, but the method should also be able to point out the leading parameters that

relate the turbulence intensity with the mean velocity, providing some insight into the physics of the turbulent boundary layer over rough surfaces.

2 Results and Discussions

Since the diagnostic method is still an empirical tool, a large number of experiments have been collected to provide evidence of the observed behavior. These experiments are listed in table 1 where it is shown that a large range of k^+, ΔU^+ and δ_{99}/k has been investigated.

Table 1 Details of the used experimental data

Experiment	Roughness	k^+	δ_{99}/k	ΔU^+
[4]	Sanded surface	8-62	130-162	0.14-4.6
[5]	Mesh	67-260	4-50	8-13.4
[5]	Random blocks	162-681	4.3-15	9.3-12.5
[5]	Grit	32-79	9-30	3-6.4
[8]	Braille	7-22	462-492	0.44-3.43
[9]	Grit	14-108	20-77	2.6-10.0
[10]	2D rods	103	130	13.9
[11]	Cubes	426-474	7-11	12-13.1
[12]	Sandpaper	60-385	16-54	5.2-13.0
[12]	Mesh	28-309	19-109	6.3-13.2
[13]	2D bars	11	160	7.7
[13]	2D bars	56	32	12.7
[13]	Staggered cubes	68	28	10.0

The diagnostic plot of all the available data, plotted regardless of the roughness characteristics and streamwise positions, is shown in figure 1. Each single

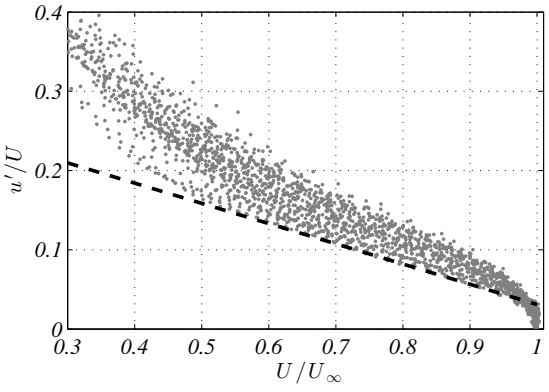

Fig. 1 Diagnostic plot of the available data plotted in traditional form. The dashed line indicates the smooth wall line given by Alfredsson *et al.* [7].

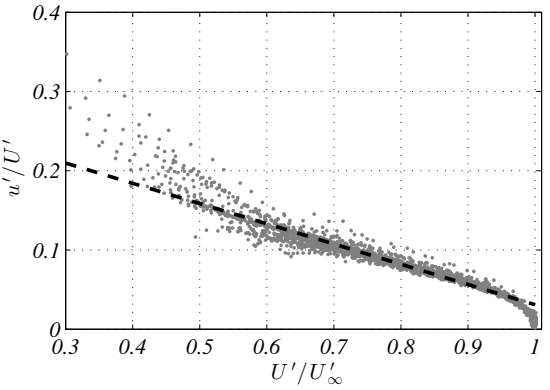

Fig. 2 Diagnostic plot of the available data in the proposed form with $U'^{+} = U^{+} + \Delta U^{+}$. The dashed line indicates the smooth wall line found by Alfredsson *et al.* [7].

experiment follows a linear behaviour, but the negative slope of the line appears to increase with the roughness strength. A surprising collapse of the data can, however, be achieved by including the roughness function in the mean velocity, namely by introducing the velocity $U'^{+} = U^{+} + \Delta U^{+}$, as shown in figure 2: In this case all the data agree much better, with a scatter that could be related to the uncertainty in the determination of ΔU^{+}, and overlaps the smooth wall line found by Alfredsson *et al.* [7]. This property is in agreement with Townsend's hypothesis since the variance is the same once the corrected mean velocity profile is the same. The fact that the wake parameter is higher, raises some doubt on the actual validity of Townsend hypothesis that nevertheless seems to be able to describe the leading observation.

By considering that the modified diagnostic plot indicates a scaling relationship, the local turbulence intensity at any mean velocity level, U/U_∞, can be found as

$$\frac{u'}{U} = \frac{U/U_\infty + \Delta U^{+}/U_\infty^{+}}{U/U_\infty}\left(a + b\frac{U/U_\infty + \Delta U^{+}/U_\infty^{+}}{1 + \Delta U^{+}/U_\infty^{+}}\right), \tag{2}$$

where $a = 0.286$ and $b = -0.255$ are the smooth wall constants given by Alfredsson *et al.* [7]. An example of equation (2) is reported in figure 3 where the good agreement between the measurements and the empirical line is evident.

Despite the different roughness characteristics, figures 1–3 demonstrate that the parameter ΔU^{+} (or its equivalent roughness length, y_0, defined by $\Delta U^{+} = \kappa^{-1}\ln y_0^{+} + B$) is a single measure of the roughness effect to the outer region of the boundary layer. The corrected diagnostic curves overlap with the smooth wall data covering the transitional to fully rough regimes, providing a simple and useful fit to estimate the turbulence intensity in the outer region of the turbulent boundary layer.

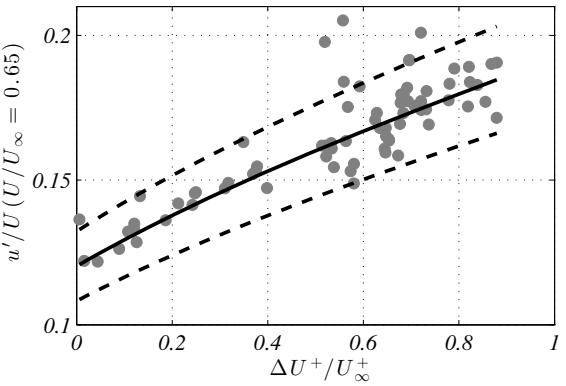

Fig. 3 Turbulence intensity of the available data at $U/U_\infty = 0.65$. The solid line indicates the extension of the smooth wall line of Alfredsson *et al.* [7] by accounting for ΔU^+, while the dashed lines indicate a $\pm 10\%$ deviation from the proposed fit.

Acknowledgements. A. Segalini and P. Henrik Alfredsson acknowledge the support from Vindforsk III, a research program sponsored by the Swedish Energy Agency. Prof. J. Morrison (Imperial College London) is acknowledged for the fruitful discussions on the modified diagnostic plot.

References

1. Jackson, P.S.: On the displacement height in the logarithmic velocity profile. J. Fluid Mech. 111, 15–25 (1981)
2. Castro, I.P.: Rough-wall boundary layers - mean flow universality. J. Fluid Mech. 585, 469–485 (2007)
3. Jiménez, J.: Turbulent flows over rough walls. Annu. Rev. Fluid Mech. 36, 173–196 (2004)
4. Schultz, M.P., Flack, K.A.: The rough-wall turbulent boundary layer from the hydraulically smooth to the fully rough regime. J. Fluid Mech. 580, 381–405 (2007)
5. Amir, M., Castro, I.P.: Turbulence in rough-wall boundary layers: universality issues. Exp. Fluids 51, 313–326 (2011)
6. Alfredsson, P.H., Segalini, A., Örlü, R.: A new scaling for the streamwise turbulence intensity in wall-bounded turbulent flows and what it tells us about the "outer" peak. Phys. Fluids 23, 041702 (2011)
7. Alfredsson, P.H., Örlü, R., Segalini, A.: A new formulation for the streamwise turbulence intensity distribution in wall-bounded turbulent flows. Eur. J. Mech. B/Fluids 36, 167–175 (2012)
8. Monty, J.P., Allen, J.J., Lien, K., Chong, M.S.: Modification of the large-scale features of high Reynolds number wall turbulence by passive surface obtrusions. Exp. Fluids 51, 1755–1763 (2011)
9. Brzek, B., Cal, R.B., Johansson, G., Castillo, L.: Inner and outer scalings in rough surface zero pressure gradient turbulent boundary layers. Phys. Fluids 19, 065101 (2007)
10. Krogstad, P.-Å., Efros, V.: About turbulence statsitics in the outer part of a boundary layer developing over 2d surface roughness. Phys. Fluids 24, 075112 (2012)
11. Cheng, H., Castro, I.P.: Near wall flow over urban-like roughness. Boundary-Layer Meteorol. 104, 229–259 (2002)
12. Flack, K.A., Schultz, M.P., Connelly, J.S.: Examination of a critical roughness height for outer layer similarity. Phys. Fluids 19, 095104 (2007)
13. Volino, R.J., Schultz, M.P., Flack, K.A.: Turbulence structure in boundary layers over periodic two- and three-dimensional roughness. J. Fluid Mech. 676, 172–190 (2011)

Influence of Tripping on Spatiotemporal Correlation between Velocity and Wall Pressure in a Turbulent Boundary Layer

Masaharu Matsubara, Yasuyuki Sendai, Kounosuke Matsumoto, and Taiki Mishiba

Abstract. In this study, investigation of tripping influence on a turbulent boundary layer was experimentally performed with five different tripping devices including classical circular rods and 'V' shape embossment. We focused on not only basic statistics such as mean velocity and fluctuation profiles, but also spatiotemporal correlation between the wall pressure and the streamwise velocity fluctuations. Measurements were made with a single hot wire and a spanwise array of 32 MEMS microphone sensors mounted on the wall. The results indicate that the velocity-pressure correlation is sensitively changed by the tripping devices, while the mean velocity profile is not affected except for very intense tripping with a thick rod. Though this tripping influence was confirmed only in the low range of Reynolds number, it warns that the transition process should be taken into account in researches on turbulent boundary layer flow.

1 Introduction

From extensive comparison of numerical results for turbulent boundary layer flow, there exist considerable discrepancies in both peak fluctuation value and outer layer profile [1]. One possible explanation for this inconsistency is that influence of upstream disturbance condition that strictly governs boundary layer transition is not negligible for downstream turbulent boundary layer. The aim of this study is to investigate tripping influence on not only basic statistics such as the mean velocity profile and the fluctuation distrubution, but also the spatiotemporal correlation between the wall pressure and the streamwise velocity fluctuation.

Masaharu Matsubara · Kounosuke Matsumoto · Taiki Mishiba
Shinshu University, Wakasato 4-17-1, Nagano, Japan
e-mail: mmatsu@shinshu-u.ac.jp

Yasuyuki Sendai
Matsuyama Co., Ltd. , Shiokawa 5155, Ueda, Japan

A. Talamelli et al. (eds.), *Progress in Turbulence V*,
Springer Proceedings in Physics 149,
DOI: 10.1007/978-3-319-01860-7_17,

2 Experimental Setup and Results

The experiment was performed in a closed wind tunnel, which had a vertically mounted test plate of a 2.1 m length and a 580 mm width. The sidewall faced to the test surface and the trailing-edge flap were adjusted to prevent separation around the leading edge and to obtain constant streamwise distribution of pressure in the free stream. The coordinate system is denoted by the streamwise, wall-normal and spanwise distances x, y and z from the origin at the center of the leading edge, respectively. The pressure sensor array had 32 holes of a 0.5 mm diameter with a 0.8 mm spanwise space. Each hole was connected to a MEMS microphone. The sensor array and the hot wire are located at $x = 1530$ mm. Five tripping sets were tested. One set labeled 'Case 1' consisted five plastic tapes embossed with letter 'V's. They were located between 315 mm $\leq x \leq$ 415 mm. Another set of 'Case 2' had seven plastic tapes but they were placed between 150 mm $\leq x \leq$ 400 mm. In Case 2, a strip of 100 grit sandpaper was sticked downstream of the tapes and this tripping is very similar to that used by Österund [2]. In both cases the tapes were placed at regular intervals. Case 3, 4 and 5 were of the classical tripping with a round cylinder of 1, 2 or 6 mm diameter, respectively. The cylinders were placed on the test plate surface at $x = 150$ mm. In all cases, the free stream velocities U_∞ were adjusted so that Reynolds number based on the momentum thickness, Re, was in the range of $2550 < Re < 3190$.

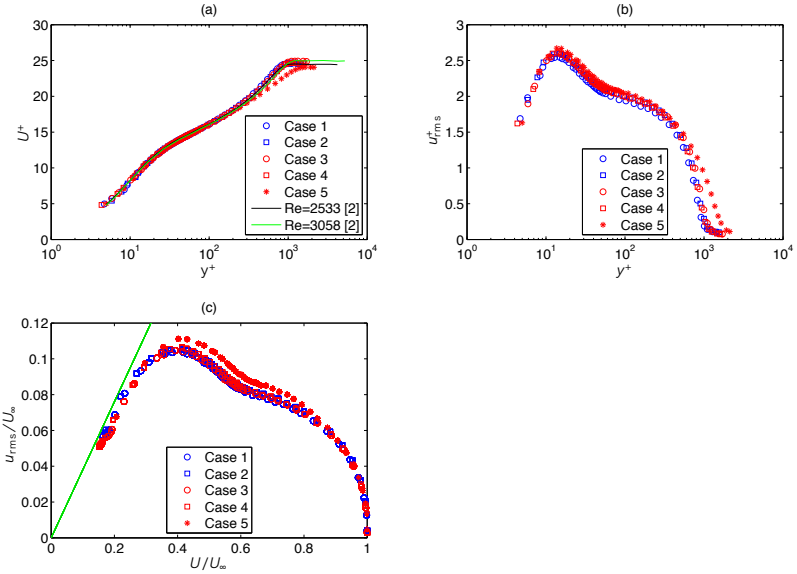

Fig. 1 The basic statistics. (a) Streamwise mean velocity profile. (b) Streamwise velocity fluctuation. (c) Diagnostic plot. The line is the slope $u_{\rm rms}/U = 0.38$.

As seen in Fig. 1 (a), the dimensionless velocity profiles, U^+, are collapsed well in the whole boundary layer except in Case 5 with the thickest rod. Distributions of the streamwise velocity fluctuation, u^+_{rms}, in Fig. 1 (b) also very similar except Case 5, though the fluctuation around $y^+ = 100$ in Case 1 is slightly lower than the other three cases. No drastic influence on the basic statistics in Case 1 to 4 is also confirmed in the diagnostic plot of Fig. 1 (c).

Figure 2 shows contour maps of the spatiotemporal correlation coefficient between the wall pressure and the streamwise velocity at $y^+ = 400$. Both temporal and spatial scales are normalized in the wall scale as $\Delta t^+ = \Delta t u_\tau U_\infty \nu$ and $\Delta z^+ = \Delta z u_\tau / \nu$. The time difference is defined as $\Delta t = t_u - t_p$, where t_u and t_p is the time of the streamwise velocity and the pressure, respectively. The fine spanwise step of 0.1 mm for the hot wire traversing realizes high spanwise resolution of these correlation maps. As seen Fig. 2 the correlation maps are obviously affected by the tripping configuration even the moderate tripping devices of Case 1, 2, 3 and 4. In Case 2 and 3 the positive peaks around $\Delta z^+ = 500$, $\Delta t^+ = 500$ shift father in

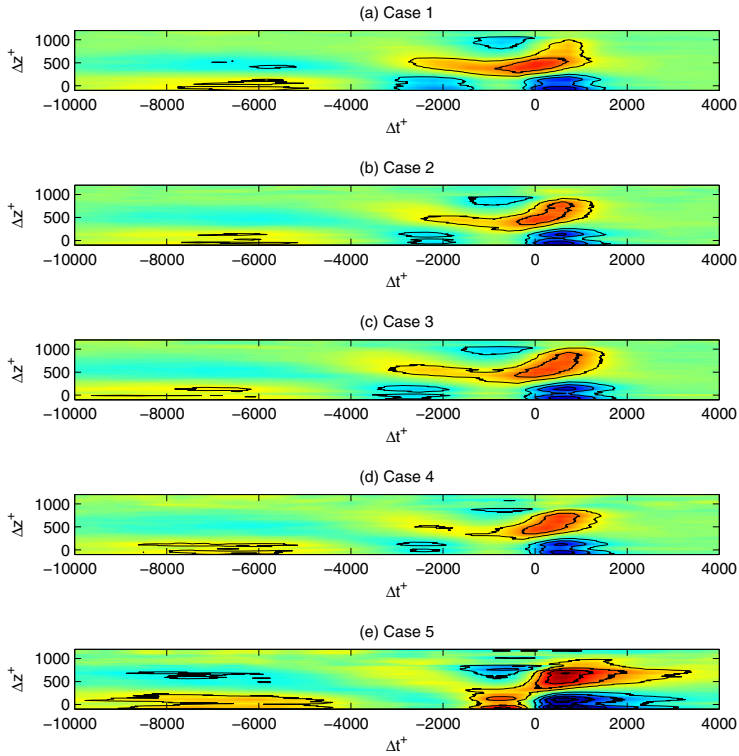

Fig. 2 Contour maps of cross-correlation maps between the streamwise velocity at $y^+ = 400$ and the wall pressure. Contour spacing is 1% and positive and negative regions are colored in red and blue, respectively.

the both streamwise and spanwise directions, compared with Case 1. Furthermore, for $\Delta t^+ < 0$ the correlation around $\Delta z^+ = 0$ in Case 1 is stronger than that in Case 2, 3 and 4. The correlation map in Case 5 is apparently different from others.

The results indicate that the cross-correlation is very sensitive to transition process. Velocity and velocity-pressure correlations are indispensable statistics for the turbulent analysis, so that great care of the tripping should be taken for both experiments and numerical investigation on a turbulent boundary layer.

3 Summary

Influence of a tripping on the zero-pressure-gradient turbulent boundary layer was investigated with the five sets of tripping devices. The basic statistics, the mean velocity profile and the velocity fluctuation distribution, are not affected by the tripping except for very intense tripping with the thick rod. However, the cross-correlation between the streamwise velocity and the wall pressure fluctuations are obviously changed by the alteration of the tripping devices. This influence suggests that disturbances excited in the transition process trace the turbulent boundary layer for a long streamwise distance and/or survive in a regeneration circle. Though this tripping influence was confirmed in the low range of Reynolds number, it warns that the transition process should be taken into account in researches on turbulent boundary layer flow, especially for analysis of detail statistics such as cross-correlations between velocities and pressure.

References

1. Schlatter, P., Örlü, R.: Assessment of direct numerical simulation data of turbulent boundary layers. J. Fluid Mech. 659, 116–126 (2010)
2. Österlund, J.M.: Experimental studies of zero pressure-gradient turbulent boundary layer flow. Ph. D. Thesis Royal Institute of Technology Department of Mechanics (1999), http://www.mech.kth.se/~jens/zpg/

Turbulent Production and Subgrid Dynamics in Wall Flows

A. Cimarelli and Elisabetta De Angelis

Abstract. The Kolmogorov equation generalized to wall-turbulence has been recently proven to give a detailed description of the multi-dimensional features of such flows[1]. As emerging from this approach, the small scales of wall turbulence are found to drive the quasi-coherent motion at large scales through a reverse energy transfer. At the base of this phenomenology is the focusing of production of turbulent fluctuations at small scales. These observations may have strong repercussion on both theoretical and modeling approaches to wall-turbulence. Here, we aim at using the Kolmogorov equation not only for the study of the mechanisms altering the energy transfer but also for modeling purpose.

1 Introduction

One of the main goals of large eddy simulation (LES) is the accurate and low-cost reproduction of the main features of turbulent flows. In LES, the velocity field, u_i, is decomposed into the sum of a filtered, $\bar{u}_i$, and a residual unresolved component, u_i^{sgs}, so that the resulting filtered field can be resolved on a relatively coarse grid. The evolution equations for $\bar{u}_i$ can be obtained by applying the filtering operation to the Navier-Stokes equations where the effects of the small unresolved scales appears in the subgrid stress tensor $\tau_{ij} = \overline{u_i u_j} - \bar{u}_i \bar{u}_j$ which must be modeled. Arguably, the most important effect of the subgrid scales on the large ones is the energy exchange, ϵ_{sgs}, between large resolved and small subgrid scales. In this context, most of the commonly used LES models assume that the main role of the subgrid scales is to remove energy from the large resolved motion and dissipate it. Indeed, according to the Kolmogorov theory, the small scales of turbulence dissipate

A. Cimarelli · Elisabetta De Angelis
DIEM, Università di Bologna, Viale Risorgimento, 40136 Bologna, Italy
e-mail: e.deangelis@unibo.it

A. Talamelli et al. (eds.), *Progress in Turbulence V*,
Springer Proceedings in Physics 149,
DOI: 10.1007/978-3-319-01860-7_18,

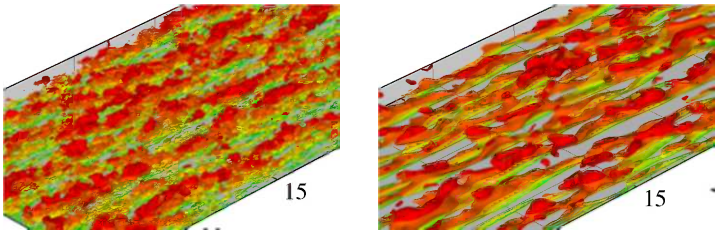

Fig. 1 Isosurfaces of the streamwise fluctuations in a turbulent channel with colors encoding wall-distance. Left: entire velocity field. Right: large scale coherent motion.

the energy flowing down from the largest ones at a rate proportional to the viscous dissipation ϵ. The filtering operation breaks off this energy transfer and, hence, the model should reproduce the draining of energy towards the removed dissipative scales. However, wall-flows have been recognized as extremely elusive. Indeed, in wall turbulent flows, the Richardson scenario of the energy cascade is completely modified up to a reverse energy flux from small to large scales. Even if it is well known that turbulent flows are characterized by events of energy back-scatter also in globally isotropic and homogeneous conditions, in the production region of wall turbulent flows these phenomena prevail resulting in a net energy flux from small to large scales. Here, we aim at discerning this phenomenon in order to define a new modeling approach for the subgrid stresses in wall flows.

2 Small-Scale Energy Sourcing

The spectral dynamics at the basis of the reverse energy cascade arise from the complex interactions between turbulent production in the space of scales and inhomogeneous fluxes in physical space. In this context, as shown in [1], the generalized Kolmogorov equation represents an ideal framework to address these two phenomena and is shown to be fundamental for the identification of the basic mechanisms responsible for the reverse energy cascade. Let us recall the main results. The Kolmogorov equation can be written as

$$\nabla_r \cdot \mathbf{\Phi}_r(\mathbf{r}, Y_c) + \frac{d}{dY_c}\Phi_c(\mathbf{r}, Y_c) = \xi(\mathbf{r}, Y_c) \tag{1}$$

where $\mathbf{\Phi}_r = \langle \delta u^2 \delta \mathbf{u} \rangle + \langle \delta u^2 \delta U \rangle - 2\nu \nabla_r \langle \delta u^2 \rangle$ is the transfer through the scales, $\Phi_c = \langle v^* \delta u^2 \rangle + 2\langle \delta p \delta v \rangle / \rho - \nu d\langle \delta u^2 \rangle / 2dY_c$ the flux in physical space and $\xi = -2\langle \delta u \delta v \rangle \left(dU/dy\right)^* - 4\langle \epsilon^* \rangle$ the balance between production and dissipation. When homogeneous and isotropic conditions are recovered, equation (1) reduces to $\partial \langle \delta u^2 \delta u_i \rangle / \partial r_i = -4\langle \epsilon^* \rangle$ which is analogous to the 4/5 law. This states that the energy flux through the scales equals the rate of energy dissipation. There is not direct energy injection and extraction amid the

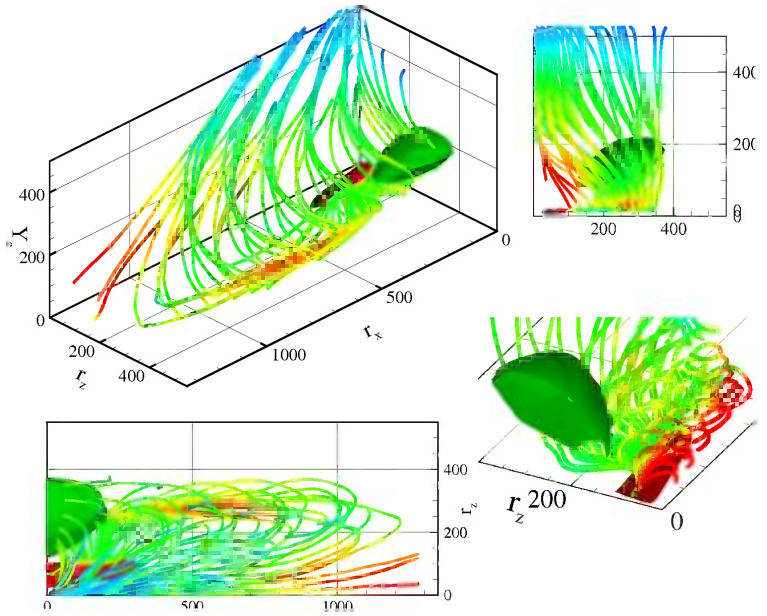

Fig. 2 Turbulent channel flow DNS at $Re_\tau = 550$, see [1] for the details of the simulations. (r_x, r_z, Y_c)-trajectories of the energy fluxes (colours according to strength increasing from blue to red). The two energy source – $\xi(r_x, r_z, Y_c)$ – iso-surfaces show the two maxima, in the inner ($\xi = 0.42$, red) and outer ($\xi = 0.006$, green) regions.

spectrum of scales. Whereas, as shown in figure 2, in wall-flows the turbulent production mechanisms concentrate at intermediate small scales, see red iso-surface. This small-scale source leads to a complex redistribution of energy in the compound space of scales and wall-distance, see field lines. From the source the energy fluxes diverge feeding longer and wider structures while ascending towards the bulk of the flow. Following a spiral-like behavior, the field lines end up in a Y_c-distributed dissipative range located at the smallest scales of motion.

3 Subgrid Scale Modeling and Final Comments

The driving idea of LES is to directly compute the large coherent motion whose features are specific of the problem considered, leaving to the small-scale (subgrid) models the duty to account in *almost universal* fashion for the dissipative energy sink, see figure 1. However, wall flows have a much richer physics accompanied by the focusing of energy generated at small scales near the wall which feed the large motion farther away from the wall. This leads to overwhelming difficulties for LES. Actually, the present approach

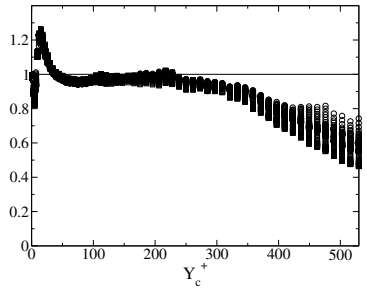

Fig. 3 Y_c-behaviour of the coefficient $C(Y_c)$ evaluated as $C(Y_c) = 1 + (\partial\langle v^*\delta u^2\rangle/\partial Y_c)/4\langle\epsilon^*\rangle$ for a subset of values of scales such as $r_x^+ < 1200$ and $r_z^+ < 600$

based on the Kolmogorov equation can be also used for modeling purpose. In particular, starting from the phenomenological relation for the energy transfer in wall-turbulence proposed in [1], we propose a new LES modeling approach. This new relation,

$$\frac{\partial\langle\delta u^2\delta u_i\rangle}{\partial r_i} = -\left[2\langle\delta u\delta v\rangle\left(\frac{dU}{dy}\right)^* + 4C(Y_c)\langle\epsilon^*\rangle\right], \tag{2}$$

though quite simple, accounts the scale-dependent dynamics of production which inject energy among the spectrum of scales. In equation (2), the presence of spatial fluxes (assumed to be weakly dependent on the scales considered) is taken into account with the constant $C(Y_c)$. As shown in figure 3, $C(Y_c)-1$ is positive in the buffer layer and negative in the bulk region consistently with the role of these layers as global origin and terminus, respectively, of the spatial flux. In this putative overlap layer, $50 < Y_c < 300$, our data show that $C(Y_c) - 1$ is almost vanishing consistently with the traditional notion of equilibrium layer.

Let us now consider how equation (2) can be used in a LES context. Equation (2) suggests to model turbulence using two different ingredients at the basis of the dynamics of small scales of wall turbulence. A linear isotropic mechanism analogous to the viscous stresses which models the sink behavior of the small scales and a nonlinear anisotropic one which accounts for their source behavior. By taking into account this double linear/nonlinear feature of the small scales, equation (2) has been already used in an *a priori* test, [2], to model the energy flux between resolved and subgrid scales, $\langle\epsilon_{sgs}\rangle$, showing the capability of this appraoch to reproduce the switch between draining, $-\langle\epsilon_{sgs}\rangle < 0$, and sourcing, $-\langle\epsilon_{sgs}\rangle > 0$, behavior of the subgrid motion when large filter lengths are considered. The subgrid stress tensor, $\tau_{ij}^\star$, is then decomposed in a linear eddy viscosity term which is responsible for the sink-like behaviour and a nonlinear anisotropic one which is responsible for the source-like one. A natural candidate for the nonlinear part is the velocity

increments tensor $\bar{Q}_{ij} = \delta\bar{u}_i\delta\bar{u}_j$, already used in [3]. Indeed, by evaluating the velocity increments for separation vectors r_i proportional to the grid interval, such a quantity allows for capturing implicitly the anisotropy of the mesh and, consequentely, of the flow. Hence, the model for the subgrid stresses should take a relatively standard form, see [4, 5],

$$\tau^{\star}_{ij} = C_{\Delta}\delta\bar{u}^{\star}_i\delta\bar{u}^{\star}_j - 2\nu_T\bar{S}^{\star}_{ij} \tag{3}$$

where the coefficient C_{Δ} could be set a priori using similarity or computed dynamically. Though the main goal of the paper is to present a new LES approach based on physical arguments, let us notice that very preliminary results in a turbulent channel are available. These results show the effectiveness of the present model and the value of the balance of the filtered second order structure function as a post-processing tool.

Acknowledgements. The DNS was performed on a computing time grant provided by CASPUR. We acknowledge that the present work has been carried under the auspices of MIUR through the PRIN08 funding scheme.

References

1. Cimarelli, A., De Angelis, E., Casciola, C.M.: Paths of energy in turbulent channel flows. J. Fluid Mech. 715 (2013)
2. Cimarelli, A., De Angelis, E.: Anisotropic dynamics and sub-grid energy transfer in wall-turbulence. Phys. Fluids 24 (2012)
3. Brun, C., Friedrich, R., da Silva, C.B.: A non-linear SGS model based on the spatial velocity increment. Theor. Comput. Fluid Dyn. 20 (2006)
4. Bardina, J., Ferziger, J.H., Reynolsa, W.C.: Improved subgrid scale models for large-eddy simulation. Am. Inst. Aeronaut. Asronaut. Pap. (1980)
5. Vreman, B., Geurts, B., Kuerten, H.: On the formulation of the dynamic mixed subgrid-scale model. Phys. Fluids 12 (1994)

Revisiting the Near-Wall Scaling of the Streamwise Variance in Turbulent Pipe Flows

S.S. Sattarzadeh, M. Ferro, R. Örlü, and P. Henrik Alfredsson

Abstract. Apparent contradictory results regarding the Reynolds number scaling of the near-wall peak of the variance distribution in turbulent pipe flows are discussed. Inconsistencies in the conclusions from the *Princeton SuperPipe* published between 2010–2012 are highlighted and new experimental evidence in the Kármán number range 500–2500 is supplemented. The new results support the view that the inner-scaled peak amplitude increases with Reynolds number as for channel and turbulent boundary layer flows, and in agreement with trends observed in recent direct numerical simulations and other experiments.

1 Introduction

Despite a large body of experimental investigations and more recently direct numerical simulations (DNS) there are still unresolved fundamental issues regarding *the* canonical flow case, the turbulent pipe flow. Among those are the distribution and scaling of the mean velocity (e.g. the value of the log-law constants) and the variance. In respect to the latter, two distinct issues have stirred the minds over recent years, namely the question whether the amplitude of the inner-scaled near-wall peak is Reynolds number (*Re*) invariant and whether a second (so called "outer") maximum emerges at higher *Re*, i.e. exceeding the highest available DNS by an order of magnitude [1]. While empirical evidences have established that the amplitude of the inner-scaled near-wall peak grows logarithmically with *Re* for both flat plate boundary layer and channel flows [2, 3], the situation for the turbulent pipe flow is less clear as concluded from a compilation of carefully selected data sets [4].

The main reason for this scatter is the fact that the effect of spatial resolution in the (predominantly hot-wire) measurements had not been (sufficiently) taken into account [3,5]. To resolve the controversy regarding the scaling of the near-wall peak

S.S. Sattarzadeh · M. Ferro · R. Örlü · P. Henrik Alfredsson
CCGEx & Linné Flow Centre, KTH Mechanics, SE-100 44 Stockholm, Sweden
e-mail: ramis@mech.kth.se

A. Talamelli et al. (eds.), *Progress in Turbulence V*,
Springer Proceedings in Physics 149,
DOI: 10.1007/978-3-319-01860-7_19,

of the variance distribution, hot-wire measurements with matched viscous scaled hot-wire lengths (L^+) were reported from the *Princeton SuperPipe*.[1] It was concluded [4] that "the magnitude of the peak is constant for all Reynolds numbers with a magnitude of 7.34 ± 0.13". Due to the finite length of the used hot-wires (with $L^+ = 20$) the authors stated that the real peak value "is expected to be closer to the value found with [their shortest employed hot-wire] $L^+ = 4$ which is 7.77 ± 0.37".

By applying the semi-empirical correction scheme for hot-wire measurements proposed in Ref. [6] one would instead obtain a slightly higher amplitude value of around 8.1. This is also the value obtained in a more recent investigation in which, besides conventional hot-wire probes, also a nano-scale thermal anemometry probe (NSTAP) was used in the *SuperPipe*. In fact, using the aforecited correction scheme, the authors concluded, that "the corrected hot-wire and NSTAP data collapse onto a single curve for each Reynolds number [...] with a peak value [...] $= 8.1\pm0.2$" [7]. While these and the aforementioned measurements from Princeton were restricted to Kármán numbers (R^+, where R denotes the pipe radius) up to 3300, more recent efforts provide variance profiles up to $R^+ = 10^5$ using NSTAPs [8, 9], whereas the near-wall peak was resolved up to (at least) $R^+ = 20000$. These efforts were seemingly "confirming the Reynolds number invariance of the inner peak magnitude" [8] or shown to "clearly demonstrate that the magnitude of the near-wall peak [...] remains constant" [9] (when corrected for spatial filtering effects).

2 Motivation

Despite the repeated reaffirmation of the *Re*-invariance through Refs. [4, 7–9], there remain some doubts: Firstly, the corrected (apparently *Re* invariant) peak value increased from 8.1 [4, 7] to around 8.4 [8] and then to around 9.0 [9]. Secondly, the quantitative results from preceding studies were not discussed in the succeeding studies, thereby leaving open whether the preceding (quantitative) conclusions are superseded. In conclusion, it can be summarised that the outcome of the *Princeton SuperPipe* experiments are inconclusive in respect to the amplitude of the near-wall peak as well as its *Re*-invariance. On the other hand, considering that the lowest considered R^+ value moved from around 700 [4], to 1100 [7, 8], and finally to around 2000 [9], one could equally well conclude – based on the same corrected data sets – that the near-wall peak value appears to increase with *Re*.

Recent DNS results from pipe flows compiled in Ref. [10], albeit limited to $R^+ \lesssim 1142$, and results from a detailed experimental investigation from Ng et al. [11] in the range $1000< R^+ <3000$ depict a clear increase with *Re*. In light of the aforementioned inconsistencies, there is consequently a clear need for additional experiments that focus on *Re* scaling by taking L^+ and L/d effects specifically into account and go beyond $R^+ = 1000$.

[1] The superscript '+' denotes quantities in wall units.

3 Results and Discussion

Hot-wire measurements in a turbulent pipe flow facility with a variety of hot-wire probes varying in diameter, length and length-to-diameter ratios in the range 1.25–5 micron, 0.24–1.50 mm and 128–600, respectively, have been performed in the pipe flow facility at KTH Mechanics. Details of the pipe flow facility, the measurement equipment and the measurement parameters covering the range from $500< R^+ <2500$, as well as the post-processing procedures are detailed in Refs. [12, 13].

The inner-scaled mean streamwise velocity profile measured with three different probes is depicted in Fig. 1*a)* to show the quality of the established flow field as well as the repeatability and (indirectly) accuracy of the measurements. Figure 1*b)*, showing the corresponding variance profiles, illustrates the significance of insufficient spatial resolution, but also demonstrates the good performance of the semi-empirical correction scheme [6] utilised in the Princeton experiments.

Considering now only the near-wall peak value of the variance profiles, Fig. 2*a)* depicts the measured values. Additionally, some of the data points with 3 or more measurements with exactly the same probe are connected and colour-coded in order to evince the various trends one can obtain if spatial resolution effects are not considered. Interestingly, these trends can easily be predicted by use of the empirical relation given in Ref. [3] (as function of L^+ and R^+) transformed into a relation as function of the (more practical) quantity L/R [5], as demonstrated in Fig. 2*b)*.

Correcting the measured data with the same scheme as the Princeton data, the scatter reduces drastically as shown in Fig. 3*a)*. Neglecting the data corresponding to the shortest L/d ratio, i.e. $L/d = 128$ (encircled cases), the scatter reduces even

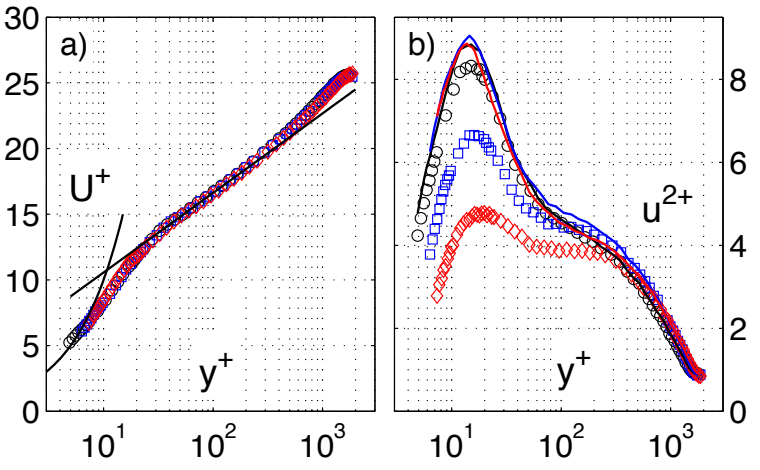

Fig. 1 Inner-scaled *a)* mean and *b)* variance profile for 3 measurements at around $R^+ = 1750$ with $L^+ = 14$ (○), 47 (□), and 94 (◇). Solid lines in subplot *a)* correspond to the linear velocity profile and log-law with $\kappa = 0.39$ and $B = 4.8$, and in *b)* to the corrected profiles obtained through the scheme proposed in Ref. [6].

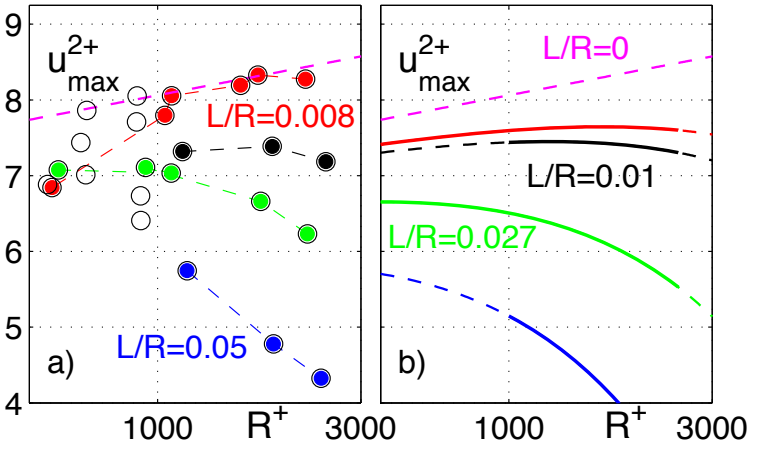

Fig. 2 *a)* Peak amplitude of measured inner-scaled variance profile as function of R^+. Points belonging to same physical probe are connected and colour-coded. Line for $L/R = 0$ is based on Ref. [3] for $L^+ = 0$. *b)* Prediction of the peak value for particular L/R ratios according to Ref. [5].

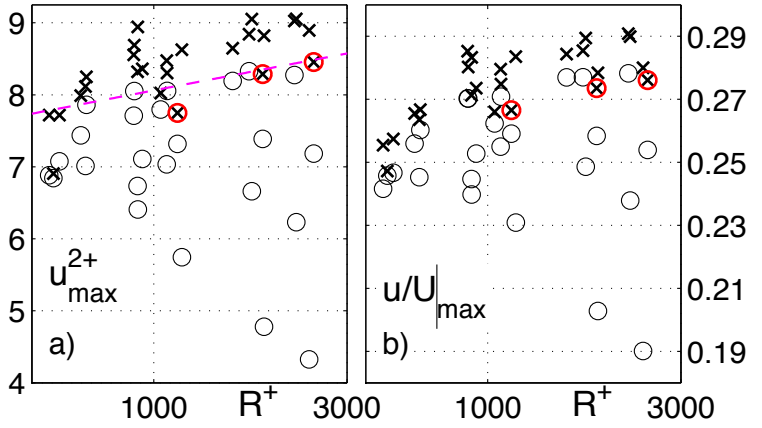

Fig. 3 For notation of data points see Fig. 2. *a)* Data corrected for L^+ effects ($\times$) according to scheme of Ref. [6]. Encircled cases correspond to $L/d = 128$. *b)* Turbulence intensity at peak location of variance profile, i.e. at same location as the data shown in subplot *a)*.

further. The observed effect of a too short L/d ratio is well known since the seminal work by Ligrani & Bradshaw [15], and has recently been revisited in Refs. [11, 14]. While an insufficient L/d ratio might at first glance appear to cause the same kind of attenuation as an insufficient L^+, the "attenuation due to long sensors is scale dependent", while the "attenuation caused by L/d effects occurs over a much broader range of wavelengths" as shown in Ref. [11].

The corrected results support the view that the near-wall peak amplitude of the variance in pipe flows increases with *Re*, as it does for channel and boundary layer flows at least for the *Re*-range considered here. Since, uncertainties in the measured or deduced friction velocity can easily mask *Re* effects if the considered *Re* range is relatively small (as is the case here), it is important to ensure that the local turbulence intensity (which is independent of the friction velocity), i.e. the root mean square value scaled by the local mean, is as well increasing. Figure 3*b)* shows the corresponding local turbulence intensity at the same wall-normal location as in Fig. 3*a)*, i.e. at the peak location, and confirms that the peak value is indeed increasing with *Re*, thereby supporting trends from recent direct numerical simulations (cf. compilation in Ref. [10]), the experiments by Ng et al. [11], and the formulation in Ref. [2] based on the diagnostic plot [16].

4 Conclusion and Outlook

Contrary to the view put forward in several of the *Superpipe* publications, new empirical evidence supports the view that the inner-scaled peak amplitude increases with *Re* at least up to $R^+ = 3000$. Since the *SuperPipe* experiments exceed the empirical evidence presented here and available elsewhere by an order of magnitude in *Re*, there is clearly a need for concerted experiments for $R^+ > 3000$ to settle this issue while taking L^+, L/d, and the frequency response of the employed hot-wire probe specifically into account. Such data will be available once the *Center for International Cooperation in Long Pipe Experiments* (CICLoPE) [17] goes into operation.

One additional cause for the disparity regarding the near-wall peak between various experiments might lie in the temperature gradient that can arise across the measurement plane in internal flows, i.e. between the inner pipe wall and the centreline. Preliminary results based on velocity and temperature fluctuation measurements by means of hot- and cold-wire measurements at KTH [13] have shown in the present experimental facility that temperature differences between the inner pipe wall and centreline of up to 2 K occurred at the highest flow rate. By exploiting the fact that the streamwise velocity and temperature fluctuations are nearly fully correlated [18] and taking the measured variances of both quantities into account, such a temperature gradient was found to lead to differences in the variance peak value of around 2 %. While the effect of temperature gradients on the mean streamwise velocity profile can be compensated for, if the mean temperature profile is known, it is a nearly impossible task to measure the spatially and temporally resolved temperature and velocity fluctuations simultaneously at the same location in order to facilitate the compensation of temperature fluctuations on the velocity measurements. Based on this observation, efforts have been initiated to study the effect of temperature gradients on the higher-order moments obtained through hot-wire anemometry by means of velocity and temperature fields from DNS of turbulent channel flows [19].

Acknowledgements. Part of this research was done within KTH CCGEx, a centre supported by the Swedish Energy Agency, Swedish Vehicle Industry and KTH.

Disclaimer: Parallel to the present paper, a *Letter* in *Experiments in Fluids* with a focus on the Princeton data, supplementary DNS data from various pipe flows and a discussion on the frequency response of hot-wire probes under pressurized conditions has been published by Örlü & Alfredsson [10].

References

1. Alfredsson, P.H., Segalini, A., Örlü, R.: A new scaling for the streamwise turbulence intensity in wall-bounded turbulent flows and what it tells us about the "outer" peak. Phys. Fluids 23, 041702 (2012)
2. Alfredsson, P.H., Örlü, R., Segalini, A.: A new formulation for the streamwise turbulence intensity distribution in wall-bounded turbulent flows. Eur. J. Mech. B 36, 167–175 (2012)
3. Hutchins, N., Nickels, T.B., Marusic, I., Chong, M.S.: Hot-wire spatial resolution issues in wall-bounded turbulence. J. Fluid Mech. 635, 103–136 (2009)
4. Hultmark, M., Bailey, S.C.C., Smits, A.J.: Scaling of near-wall turbulence in pipe flow. J. Fluid Mech. 649, 103–113 (2010)
5. Örlü, R., Alfredsson, P.H.: On spatial resolution issues related to time-averaged quantities using hot-wire anemometry. Exp. Fluids 49, 101–110 (2010)
6. Smits, A.J., Monty, J.P., Hultmark, M., Bailey, S.C.C., Hutchins, N., Marusic, I.: Spatial resolution correction for wall-bounded turbulence measurements. J. Fluid Mech. 676, 41–53 (2011)
7. Vallikivi, M., Hultmark, M., Bailey, S.C.C., Smits, A.J.: Turbulence measurements in pipe flow using a nano-scale thermal anemometry probe. Exp. Fluids 51, 1521–1527 (2011)
8. Smits, A.J., Hultmark, M., Vallikivi, M., Rosenberg, B.J., Bailey, S.C.C.: Pipe flow turbulence at extreme Reynolds numbers. Turbulence Shear Flow Phenomena 7, Ontario, Canada (2011)
9. Hultmark, M., Vallikivi, M., Bailey, S.C.C., Smits, A.J.: Turbulent pipe flow at extreme Reynolds numbers. Phys. Rev. Lett. 108, 094501 (2012)
10. Örlü, R., Alfredsson, P.H.: Comment on the scaling of the near-wall streamwise variance peak in turbulent pipe flows. Exp. Fluids 54, 1431 (2012)
11. Ng, H.C.H., Monty, J.P., Hutchins, N., Chong, M.S., Marusic, I.: Comparison of turbulent channel and pipe flows with varying Reynolds number. Exp. Fluids 51, 1261–1281 (2011)
12. Sattarzadeh, S.S.: Experimental study of complex pipe flows. M.Sc. thesis, Royal Institute of Technology, Stockholm (2011), `http://kth.diva-portal.org/smash/record.jsf?pid=diva2:430330`
13. Ferro, M.: Experimental study on turbulent pipe flow. M.Sc. thesis, Royal Institute of Technology, Stockholm (2012), `http://kth.diva-portal.org/smash/record.jsf?pid=diva2:558033`
14. Hultmark, M., Ashok, A., Smits, A.J.: A new criterion for end-conduction effects in hot-wire anemometry. Meas. Sci. Technol. 22, 055401 (2011)

15. Ligrani, P.M., Bradshaw, P.: Spatial resolution and measurement of turbulence in the viscous sublayer using subminiature hot-wire probes. Exp. Fluids 5, 407–417 (1987)
16. Örlü, R., Alfredsson, P.H.: The diagnostic plot – a litmus test for wall bounded turbulence data. Eur. J. Mech. B 29, 403–406 (2010)
17. Talamelli, A., Persiani, F., Fransson, J.H.M., Alfredsson, P.H., Johansson, A.V., Nagib, H.M., Rüedi, J.-D., Sreenivasan, K.R., Monkewitz, P.A.: CICLoPE–a response to the need for high Reynolds number experiments. Fluid Dyn. Res. 41, 021407 (2009)
18. Kawamura, H., Abe, H., Matsuo, Y.: DNS of turbulent heat transfer in channel flow with respect to Reynolds and Prandtl number effects. Int. J. Heat Fluid Flow 20, 196–207 (1999)
19. Malizia, F., Cimarelli, A., De Angelis, E., Schlatter, P., Örlü, R., Talamelli, A.: Computational study of temperature gradient effects on hot-wire measurements. preperation for Proc. 14th European Turbulence Conference, Lyon, France (2013)

Turbulence Control in Plane Couette Flow by Spanwise Reflection Symmetry Breaking

George Khujadze, George Chagelishvili, and Martin Oberlack

Abstract. We propose a new strategy shear flow turbulence control which can be realised by the following steps: (i) a specially designed, non-symmetric in spanwise direction seed velocity perturbations imposed at the boundaries of the flow; (ii) the configuration of the imposed perturbations ensures a gain of shear flow energy and the breaking of turbulence reflection symmetry – generates spanwise mean flow; (iii) the generated flow changes the self-sustaining dynamics and results in considerable reduction of the level of turbulence and its kinetic energy production. The generated spanwise mean flow is a result of an *action of intrinsic nonlinear processes* of forced turbulence and it is not directly introduced in the system – the activation of the intrinsic processes is the basic idea of the proposed strategy. A model, weak near-wall forcing was designed to impose in the flow the perturbations with required characteristics and the efficiency of the proposed scheme was demonstrated by direct numerical simulation using plane Couette flow as a representative example. The considerable reduction (up to 35%) of production of turbulent kinetic energy was obtained.

1 Introduction

Controll of wall-bounded turbulent flows is an important topic in modern fluid mechanics. Investigations of problems concerned with a reduction of consumption of fuel in aeronautical applications, or reduction of energetic costs at pipeline transportation of fluids, have a century long history. A wide variety of active and passive,

George Khujadze · Martin Oberlack
Chair of Fluid Dynamics, Technische Universität Darmstadt, Germany
e-mail: georgekh@yahoo.com, oberlack@fdy.tu-darmstadt.de

George Chagelishvili
Abastumani Astrophysical Observatory, Ilia State University,
Georgia & M. Nodia Institute of Geophysics, Tbilisi State University, Georgia
e-mail: chagelishvili@astro-ge.org

A. Talamelli et al. (eds.), *Progress in Turbulence V*,
Springer Proceedings in Physics 149,
DOI: 10.1007/978-3-319-01860-7_20,

linear and nonlinear flow control mechanisms have been suggested and developed over the years (Choi *et al.*, 1993; Gad-el-Hak, 2000).

Coherent structures in turbulence play an important role in wall-layer dynamics and most high skin-friction regions in near-wall turbulent layers are induced by nearby streamwise vortices (Kim, 2011; Garcia-Mayoral & Jimenez, 2011). Generally, streamwise vortices are formed and maintained by a self-sustained dynamics of turbulence which goes by linear/unstable and nonlinear processes associated with these structures. The common features of all drag-reduced flows are weakened near-wall streamwise vortices and streaks. Recently efforts have been made to control turbulence through different spanwise wall-based forcing methods (Karniadakis & Choi, 2003). These attempts address the modification of near-wall turbulence by direct creation of a spanwise mean flow using the models of the shark-skin riblets (Garcia-Mayoral & Jimenez, 2011), streamwise traveling waves (Quadrio *et al.*, 2009), etc. However, there could be an indirect way of a spanwise mean flow generation, for instance, by a week near-wall forcing that initiates the breaking of turbulence spanwise reflection symmetry that, finally, leads to the turbulence control: **(i)** a specially designed, non-symmetric in spanwise direction, near-wall weak forcing generates seed velocity perturbations that draw shear flow energy and undergo substantial transient growth; **(ii)** the amplified non-symmetric velocity perturbations lead to the breaking of turbulence reflection symmetry and the generation of mean spanwise flow; **(iii)** the latter, in turn, changes the statistics of the turbulence giving a considerable reduction of its level.

2 Model of Non-symmetric Near-Wall Forcing

Incompressible plane Couette flow with shear parameter A and Reynolds number $Re \equiv UL/\nu = AL^2/\nu$, based on the wall velocity U, the channel half-width L, and the kinematic viscosity ν is considered. (x,y,z) indexes of physical variables for streamwise, wall-normal and spanwise directions are used respectively.

The transient growth of perturbations (that is due to the non-normality of the linearised operators of shear flow system) is the basis of smooth shear flows dynamical activity. It is well-known that constant shear flows for sufficiently high Reynolds numbers support a set of perturbations that undergo large transient growth during the dynamical time of turbulence ($\mathcal{O}(1/A)$). A robust growth appears for $3D$ perturbations satisfying the following conditions: characteristic streamwise and spanwise scales of which are the same order but larger than the viscous dissipative length scale, $\ell_x \simeq \ell_z \gg \ell_\nu$, or, in terms of wavenumbers, $k_x, k_z \ll k_\nu$ ($k_\nu \equiv \sqrt{Re} \approx 1/\ell_\nu$); the perturbations are tilted with the background shear (Craik & Criminale (1986)), or in terms of wavenumbers, $k_y/k_x < 0$.

This type of seed (i.e., small amplitude) velocity perturbations can be imposed in the flow by the following model of the helical forcing:

$$F_x(x,y,z) = A_1 f(y) \cdot \sum_{n,m=0}^{N,M} Z_m \cdot \exp\left(-X_n^2 - Z_m^2\right) \exp\left(-\frac{\hat{X}_n^2}{l_x^2} - \frac{\hat{Z}_m^2}{l_z^2}\right), \quad (1)$$

$$F_y(x,y,z) = -A_2 \cdot f(y) \cdot \sum_{n,m=0}^{N,M} \exp\left(-X_n^2 - Z_m^2\right) \exp\left(-\frac{\hat{X}_n^2}{l_x^2} - \frac{\hat{Z}_m^2}{l_z^2}\right), \quad (2)$$

$$F_z(x,y,z) = -A_1 f(y) \cdot \sum_{n,m=0}^{N,M} X_n \cdot \exp\left(-X_n^2 - Z_m^2\right) \exp\left(-\frac{\hat{X}_n^2}{l_x^2} - \frac{\hat{Z}_m^2}{l_z^2}\right), \quad (3)$$

where $f(y) = \sin(\pi y)\exp\left[-(|y| - y_{peak})^2/l_y^2\right], y \in [-1,1]$. Functions $X_n, Z_m, \hat{X}, \hat{Z}$ on the bottom wall ($y = -1$) are defined as:

$$X_n(a,\phi) = x/a - 2n\cos\phi, \quad Z_m(a,\phi) = z/a - 1 - (4m+1)(1-\sin\phi),$$

$$\hat{X}_n(a,\phi) = x/a - (2n+1)\cos\phi, \quad \hat{Z}_m(a,\phi) = z/a - (4m+2)(1-\sin\phi),$$

while the functions $X_n, Z_m, \hat{X}, \hat{Z}$ on the top wall ($y = 1$) have the form:

$$X_n(a,\phi) = (L_x - x)/a - 2n\cos\phi, \;\; Z_m(a,\phi) = (L_z - z)/a - 1 - (4m+1)(1-\sin\phi),$$

$$\hat{X}_n(a,\phi) = (L_x - x)/a - (2n+1)\cos\phi, \;\; \hat{Z}_m(a,\phi) = (L_z - z)/a - (4m+2)(1-\sin\phi),$$

where $L_x = 2a(N-1)\cos\phi$ and $L_z = 4aM(1-\sin\phi)$ are sizes of the simulation box and $N+1$ and $M+1$ are numbers of the forcing centers in the streamwise and spanwise directions, respectively; a and ϕ define the forcing configuration (a defines the forcing "cell" size and ϕ – the forcing orientation in $x-z$ plane, e.g., at $\phi = \pi/4$ quasi equipartition of the forcing in the streamwise and spanwise directions occurs); l_x, l_y and l_z are sizes of the forcing localisations in the streamwise, wall-normal and spanwise directions respectively; A_1 and A_2 define the forcing amplitudes in the streamwise (spanwise) and wall-normal directions; $X_n(a,\phi)$ and $Z_m(a,\phi)$ define the location of the forcing symmetry centers and $\hat{X}_n(a,\phi)$ and $\hat{Z}_m(a,\phi)$ define the location of the forcing localisation centers in the streamwise and spanwise directions, respectively; y_{peak} defines the location of the forcing localisation center in the wall-normal direction. Fig. 1 displays the forcing design in xz-plane.

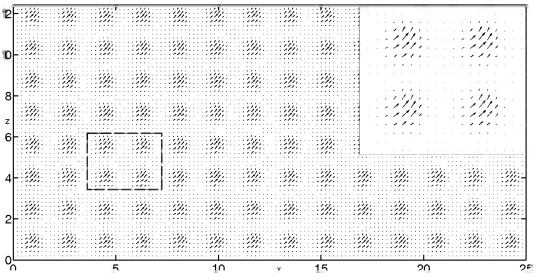

Fig. 1 Design of the helical forcing (with zoomed region in the upper right part of the plot) in the xz-plane at $y = -y_{\text{peak}} = -0.95$ and with the parameters $M = 7, N = 13, a = 1.2221$, $\phi = \pi/4$, $\ell_x = \ell_z = 1/\sqrt{10}$, $\ell_y = 0.2$, $A_1 = 0.4$, $A_2 = 0.008$

3 Numerical Simulations: Results and Analysis

Pseudo-spectral code developed at KTH, Stockholm was used in the simulations (Skote, 2001) of the controlled and unmanipulated flows at $Re = 750$. The simulation box $L_x \times L_y \times L_z = 8\pi \times 2 \times 4\pi$ and two different number of modes $N_x \times N_y \times N_z = 256 \times 97 \times 128,\ 512 \times 257 \times 256$ were used. The resolution was $\Delta x^+ = 5,\ \Delta y^+ = 0.03 - 1.6, \Delta z^+ = 5$. It was found that the production of turbulent kinetic energy is very sensitive to the forcing parameters. Here only the case with the significant reduction of turbulent kinetic energy production is presented.

In Fig. 2 the contours of spanwise velocity for the unmanipulated (top plot) and controlled (bottom plot) turbulence are shown in xy-plane with the levels in the range of $[-0.2, 0.2]$ and increment 0.02. Dashed and solid contours correspond to the negative and positive spanwise velocities correspondingly. In the case of unmanipulated flow, the contours with different signs are uniformly distributed in wall-normal direction (no mean spanwise flow in this case). A completely different picture is observed on the bottom plot. Firstly, the contours become rare indicating a reduction of the turbulence intensity. Secondly, the contours with negative values are located in the upper half of the flow and vice versa, which means the appearance of the mean flow in the spanwise direction. The statistics of Reynolds stress tensor components in unmanipulated (dashed lines) and forced (solid lines) cases are shown in Fig. 3 showing significant decrease of level of turbulence in the latter case. We have to emphasize the appearance of the nonzero non-diagonal stress components in the controlled case.

Fig. 4 shows the deviation of the controlled flow mean streamwise ($\Delta \overline{U}_x = \overline{U}_x^{contr} - \overline{U}_x^{turb}$) and spanwise ($\Delta \overline{U}_z = \overline{U}_z^{contr} - \overline{U}_z^{turb}$) velocity profiles from the unmanipulated ones. The maximum deviation of the mean streamwise velocity is small: $\Delta \overline{U}_{x,max} \approx 0.014$. In the unmanipulated case the mean spanwise velocity is zero, consequently its deviation is $\Delta \overline{U}_z = \overline{U}_z^{contr}$ with the maximum $\overline{U}_{z,max}^{contr} \approx 0.07$.

As for the production of turbulent kinetic energy, besides the classical term, $Pr_x = -\overline{u'_x u'_y} d\overline{U}_x/dy$, the additional component $Pr_z = -\overline{u'_y u'_z} d\overline{U}_z/dy$ appears due to the forcing. The power input in the flow can be defined by: $P^{in} = \overline{F_x u'_x} + \overline{F_y u'_y} + \overline{F_z u'_z} \equiv P_x^{in} + P_y^{in} + P_z^{in}$, where the term P_y^{in} is negligible. The terms characterising the energetics of the control process are presented in Fig. 5. The left plot displays P_x^{in} (dashed-dotted line) and Pr_x for the unmanipulated (dashed line) and controlled (solid line) flows. The right plot displays the same for the spanwise components.

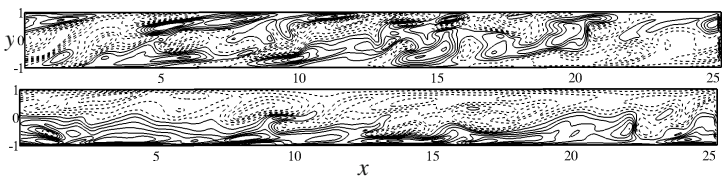

Fig. 2 Contours of spanwise velocity for unmanipulated (top plot) and controlled (bottom plot) flows. The levels are in the range $[-0.2, 0.2]$ with increment 0.02: —— positive, - - - negative.

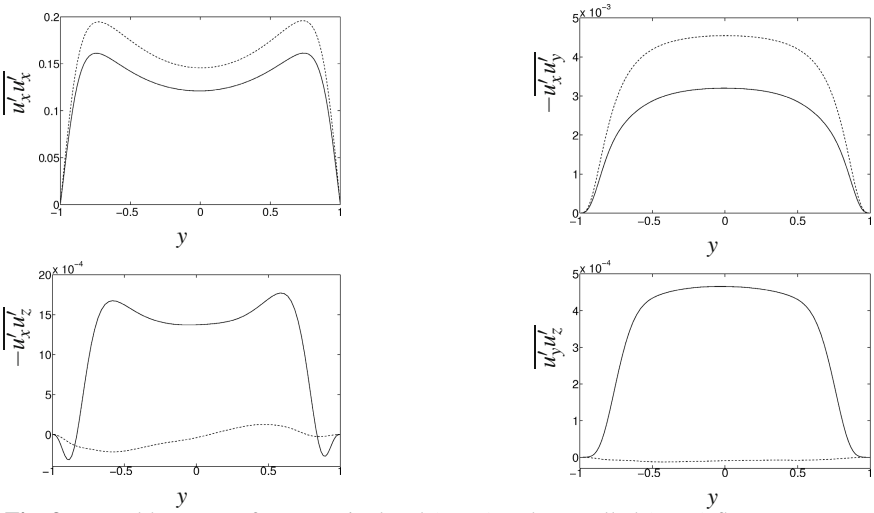

Fig. 3 Reynolds stresses for unmanipulated (– – –) and controlled (——) flows

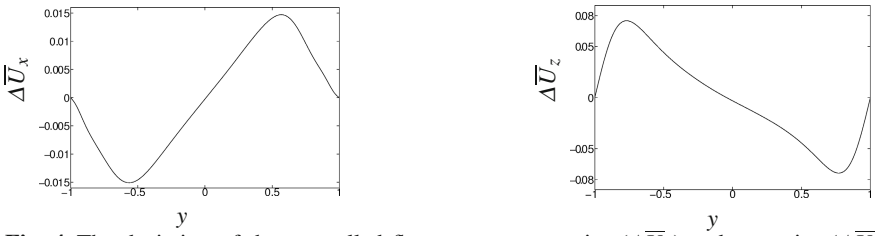

Fig. 4 The deviation of the controlled flow mean streamwise ($\Delta\overline{U}_x$) and spanwise ($\Delta\overline{U}_z$) velocity profiles from the unmanipulated ones

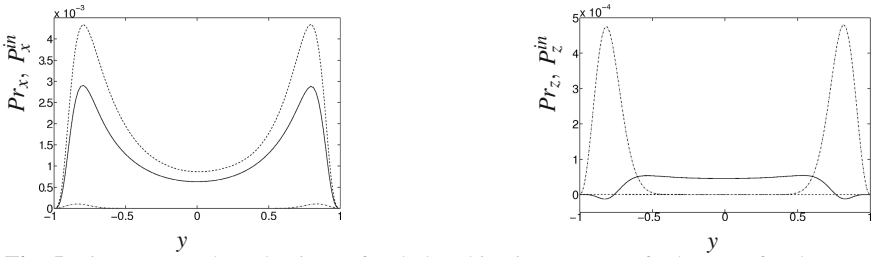

Fig. 5 Time averaged productions of turbulent kinetic energy. Left plot: Pr_x for the unmanipulated turbulent (– – –) and controlled (——) flows and input power, P_x^{in}, (—·—); Right plot: The same for the spanwise components.

The figure shows that $P_x^{in}, P_z^{in}, Pr_z \ll Pr_x$ and the turbulent kinetic energy production is substantially reduced in the controlled case. This result is confirmed by Fig. 6 that displays the time evolution of the space averaged production of turbulent kinetic energy. The time region $t \leq 3000$ corresponds to the unmanipulated turbulent flow.

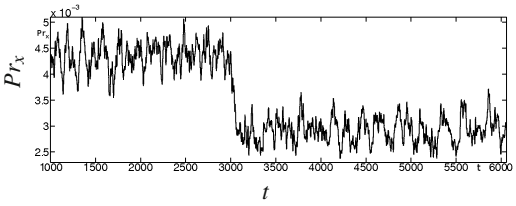

Fig. 6 Time evolution of Pr_x (averaged in space) for unmanipulated ($t < 3000$) and controlled ($t > 3000$) flows

At $t = 3000$ the forcing was switched on. The reduction of the level of turbulence about 35% was obtained.

4 Conclusions

The aim of this study was to propose a new strategy of the flow control by permanent imposition in the flow a specially designed seed velocity perturbations that have potential of transient growth and generation of helical turbulence with simultaneous creation of spanwise mean flow. This strategy is based on peculiarities of linear and nonlinear processes in the framework of the bypass concept of transition to turbulence in shear flows. According to this concept, the self-sustenance of the turbulence is a result of the flow non-normality induced transient growth of kinetic energy of perturbations and positive nonlinear feedback. The turbulence level depends on the nonlinear redistribution process in wavenumber space and the balance between the linear and nonlinear processes can be achieved at different levels (low or high). At the proposed control strategy the imposed specially designed velocity perturbations grow transiently and become active participant of the nonlinear redistribution process changing it and finally leading to the balance at the low level of turbulence.

References

Choi, H., Moin, P., Kim, J.: Direct numerical simulation of turbulent flow over riblets. J. Fluid Mech. 255, 503–539 (1993)

Craik, A.D.D., Criminale, W.O.: Evolution of Wavelike Disturbances in Shear Flows: A Class of Exact Solutions of the Navier-Stokes Equations. Proc. R. Soc. Lond. A 406, 13–26 (1986)

Gad-El-Hak, M.: Passive, Active and Reactive Flow. Cambridge Univ. Press, Cambridge (2000)

Garcia-Mayoral, R., Jimenez, J.: Hydrodynamic stability and breakdown of the viscous regime over riblets. J. Fluid Mech. 678, 317–347 (2011)

Karniadakis, G.E., Choi, K.-S.: Mechanisms on transverse motions in turbulent wall flows. Annu. Rev. Fluid Mech. 35, 45–62 (2003)

Kim, J.: Physics and control of wall turbulence for drag reduction. Phil. Trans. R. Soc. A 369, 1396–1411 (2011)

Quadrio, M., Ricco, P., Viotti, C.: Streamwise-travelling waves of spanwise wall velocity for turbulent drag reduction. J. Fluid Mech. 627, 161–178 (2009)

Skote, M.: Studies of turbulent boundary layer flow through direct numerical simulation. PhD thesis, Royal Institute of Technology, Stockholm, Sweden (2001)

The "Long Pipe" in CICLoPE: A Design for Detailed Turbulence Measurements

A. Talamelli, G. Bellani, and A. Rossetti

Abstract. A new facility to study high Reynolds number wall bounded turbulent flow has been designed. It will be installed in the laboratory of Center for International Collaboration on Long Pipe Experiments "CICLoPE" in Predappio (Italy). The facility consists of a large pipe, allowing to reach high Reynolds numbers, where all turbulent scales can be resolved with standard measurement techniques. The pipe operates with air at ambient conditions with a maximum speed of 60 m/s in order to avoid any compressibility effect. In order to maintain stable conditions over long period of time the pipe is part of a close loop circuit. The pipe will be located in a tunnel 60 m underground, thus ensuring very low level of external perturbations. The layout resembles an ordinary wind tunnel where the main difference is the long test section, which produces most of the friction losses. This requires the use of a multiple stage axial fan driven by two independent motors. Even though many of the various aerodynamic components are similar to those ordinary used in wind tunnel (corners, diffusers, turbulence manipulators, contraction, etc.) they have been designed aiming at obtaining a very good quality of the flow and minimizing the overall pressure losses.

1 Introduction

Even if the possibility to simulate and understand turbulence dynamics has recently taken a giant leap with the increase of computing power, the worlds largest computers still may completely simulate (through Direct Numerical Simulation, DNS) only flows at moderate Reynolds numbers and are not likely to reach the higher values of practical interest for decades to come. Moreover, the required computational time to obtain good statistical significance at high Reynolds numbers for higher moments and spectra still remains prohibitive.

A. Talamelli · G. Bellani · A. Rossetti
Department of Industrial Engineering, University of Bologna, I-47100 Forlí, Italy
e-mail: alessandro.talamelli@unibo.it

A. Talamelli et al. (eds.), *Progress in Turbulence V*,
Springer Proceedings in Physics 149,
DOI: 10.1007/978-3-319-01860-7_21,

As far as the interaction between the large, essentially inviscid, outer scales and the viscously influenced, highly anisotropic, near-wall structures, DNS has recently advanced to the point where a real scale separation between inner and outer scales can be seen and new findings are emerging on the role of their interaction [1]. However, although DNS is giving us valuable information, there are still a number of outstanding questions in turbulence research that can only be answered by studying turbulence at high Reynolds numbers experimentally under well controlled conditions.

Several possibilities exist to obtain high Re in a laboratory. However, if a full characterization of the turbulent flow is required then it is necessary to operate with a facility where the spatial sizes of the smallest scales are sufficiently large to be resolvable by the available measurement techniques. A measure of the smallest scale is the viscous length scale ($\ell_* = \nu/u_\tau$) and it can be shown that for a pipe flow experiment with radius R the following relation holds ($Re_\tau \sim Re$)

$$\ell_* = \frac{R}{Re_\tau} \tag{1}$$

so it is clear that in order to have large scales, for a fixed Reynolds number, the overall dimension of the facility should be chosen as large as possible.

The facility which is presently under construction in CICLoPE[1] is a large circular pipe, which will allow high Reynolds numbers to be reached and to resolve all turbulent scales with standard measurement techniques (see Figure 1). An advantage of the pipe flow compared to the other canonical cases, i.e. two-dimensional channel flow and flat-plate boundary layer flows, is that the wall shear stress can be determined directly from the pressure drop, which can be measured directly and very accurately.

2 The Facility

The main element of the apparatus is the long pipe, which consists of a 115 m long tube with an inner diameter of 0.9 m, result in in an L/D of about 125 [2]. The pipe is made of 5 m long carbon fiber modules held by precision positioning elements for accurate alignment. All pipe elements have two accesses with a diameter of 10 cm allowing measurement devices like traversing mechanism to be mounted every 5 m along the pipe. The main test section, at the end of the pipe, is 1.5 m long,

[1] CICLoPE, Center for International Cooperation in Long Pipe Experiments (www.ciclope.unibo.it), is an international cooperation between several Universities and research Institutions to establish a laboratory where large scale facilities for high Reynolds number experiments can be mounted. The laboratory is located in Predappio beside the old factory of the *Caproni Industry*, which was one of the major sites of aircraft production in Italy between 1930 and 1945. Two 130 m long tunnels were excavated under the mountains to keep the plant operative under bombing activities as well as to provide shelter for civilians during the 2nd World War. In 2006 the tunnels were given to the *University of Bologna* specifically for hosting the CICLoPE laboratory.

and can be easily removed and replaced with another, according to experiment type and/or measurement technique. This feature allows a maximal flexibility in terms of experiment and enables users to build their own instrumented test section for specific measurements. The mechanical requirements for the pipe are mainly fixed by the demand to have a hydrodynamically smooth surface and diameter accuracy. In order to achieve this, the sand equivalent surface roughness of the pipe k_s has to be lower than $3.5\ell_*$ according to recent results for a honed finished surface[3]. It was also shown that for such a surface $k_s/k_{RMS} \simeq 3$. Since the minimal scale for spatial resolution for the long pipe is $\ell_* = 12\ \mu$m, this means that the RMS surface roughness can be maximum 14 μm, values that can be obtained with moulded carbon fiber. The absolute accuracy of the diameter is not very stringent in itself, as long as its variation is small along the pipe. For a pipe flow, the convective term of the streamwise momentum equation, which should ideally be zero, should at least be small compared to the longitudinal pressure gradient. It can be shown easily that in order to get stream-wise mean velocity variations not greater than 0.2 % the diameter variation for a diameter of 0.9 *m* is about 0.9 *mm*.

The test section is linked to the return duct, one floor below, through a series of shape converter, diffusers and corners. Immediately after the test section a fast diffuser is mounted in order to reduce significantly the flow speed before the first corner. Inside, a set of guide vanes allow a wide angle expansion avoiding any possible flow separation. Some corners in the entire apparatus are characterized by the

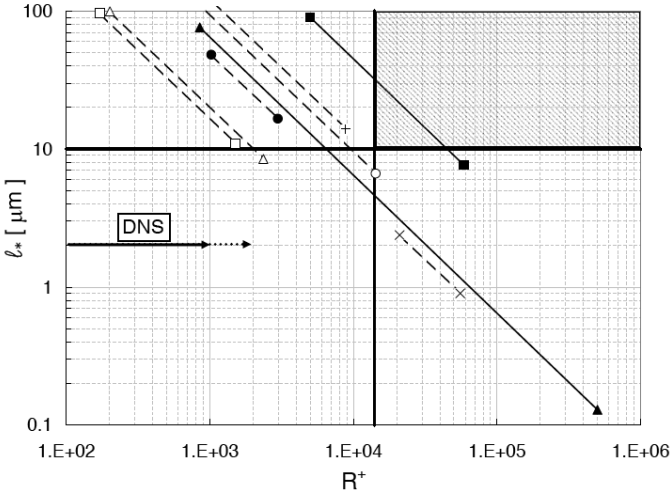

Fig. 1 Range of Reynolds number and viscous length scale of various pipe flow experiments (see [2] for symbols); ■: CICLoPE experiment. The solid vertical line refers to the criterion of a well developed overlap region ($R^+ > 14000$). Horizontal line gives the limit for $\ell_* > 10\ \mu$m which is the minimum for sufficient spatial resolution.

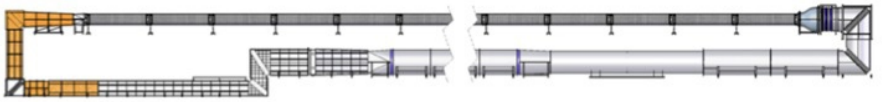

Fig. 2 Outline of the long pipe facility

presence of expanding guide vanes which allow the flow to be expanded during the corner phase while preserving an excellent quality of the flow. Expanding corners have been extensively studied by Lindgren [4]. The major benefit of using these corners is the possibility to compact the overall dimension and to reduce the friction losses without increasing the total pressure-loss. The return duct first runs under the floor of the main laboratory to allow access to the second tunnel and then rise above the floor of the main tunnel trough an "S"-shape made of two expanding corners.

A heat exchanger located downstream of the "S" controls the temperature of the flow with a target accuracy of $\pm 0.1^{\circ}$C. The main idea is to keep the temperature stable in order to maximize the accuracy of the Constant Temperature Anemometry, CTA, measurements in the test section. The heat exchanger consists of elliptical pipes where cold water is flowing at a constant rate ad where the flow is blowing perpendicularly to the grid. Since this is an element which increases the pressure losses it must be as large as possible, expanding the flow before and reducing significantly the flow speed.

The shape of the return duct is converted downstream of the heat exchanger from rectangular to circular and remains the same for the rest of the circuit. The fan is located along the return duct and ensures an optimal homogenization of the temperature in the flow. The fan produces a maximum pressure rise of 6500 Pa at a volume flow rate of 38 $m^3 s^{-1}$, corresponding to a velocity of 60 m/s in the test section. It has a diameter of 1.8 m and a power of about 300 kW. Since axial fans may create flow quality problems when subjected to large loads, it has been decided to divide it in 4 different stages driven by two independent motors. The motors are powered by two AC inverters, which controls the flow velocity with an accuracy of $\pm 0.1\%$.

The stagnation chamber, positioned after the fourth corner, has the objective to improve the quality of the flow in the test section. To this aim, inside the stagnation chamber there is a honeycomb section followed by five screens. The function of these flow manipulators is twofold: firstly they make the flow more homogeneous by introducing a pressure drop (slowing down the faster regions of the flow), secondly, they dampen flow fluctuation, reducing the turbulence level. When the flow passes through the last screen, it has been subjected to a non homogeneous strain which give a non isotropic state of the turbulent energy. For this reason, before entering in the contraction the flow passes through a straight part of the circuit (settling chamber).

After the settling chamber, the flow enters the contraction, which is crucial for the flow quality improvement in the test section. In order to avoid any possible separation of the flow (especially at the end) it has been chosen a shape taken from the MTL wind tunnel at the KTH Mekanik in Stockholm [4]. The contraction will

be realized in fiber glass material. Right after the contraction a metal interface will be positioned in order to host possible flow manipulators, like screens, turbulence generator, grids to change the initial conditions in a controlled matter.

Acknowledgements. We would like to acknowledge the input from the different researchers involved in CICLoPE: H. Nagib (Illinois Institute of Technology), I. Marusic (University of Melbourne), A.V. Johansson, H. Alfredsson and J. Fransson (Royal Institute of Technology), K.R. Sreenivasan and P. Monkewitz. J.D. Rüedi, Studio YES, A. Bassi and P. Proli are also acknowledged for their contribution during the design phase of the pipe.

References

1. Marati, N., Casciola, C.M., Piva, R.: Energy cascade and spatial fluxes in wall turbulence. J. Fluid Mech. 521 (2004)
2. Talamelli, A., Persiani, F., Fransson, J.H.M., Alfredsson, P.H., Johansson, A.V., Nagib, H.M., Rüedi, J.-D., Sreenivasan, K.R., Monkewitz, P.A.: CICLoPE - a response to the need for high Reynolds number experiments. Fluid Dynamics Research (2007), doi:10.1088/0169-5983/41/2/021407
3. Shockling, M.A., Allen, J.J., Smits, A.J.: Roughness effects in turbulent pipe flow. J. Fluid Mech. 564, 267–285 (2006)
4. Lindgren, B., Johansson, A.V.: Evaluation of a new wind tunnel with expanding corners. Exp. Fluids 36, 197–203 (2004)

Large Eddy Simulation of Accidental Releases

Bernd Leitl, Denise Hertwig, Frank Harms, Michael Schatzmann,
Gopal Patnaik, Jay Boris, Keith Obenschain, Susanne Fischer,
and Peer Rechenbach

Abstract. First responders need a more or less instant estimate of danger zones resulting from accidentally released hazardous materials in order to take immediate action, to coordinate rescue teams and to protect human population and critical infrastructure. To fulfill the need for a sufficient dispersion modeling accuracy while maintaining efficient access to reliable results in a first responders environment, systematic high resolution pre-accidental LES modeling can be combined with 'physical data reduction' in an emergency assessment tool. A typical example of such an approach adjusted to the geometry of the Hamburg inner city area will be presented. It gives a glimpse into the application of LES-modeling for real-world problems.

Keywords: LES-modeling, Flow and dispersion, Accidental releases, Emergency response tool, Urban environment.

1 Introduction

Manufacturing, storing and transportation of flammable and toxic gases involves the risk of accidental spills of hazardous materials. Releases of major concern occur in urban or industrial environments, with the consequence that the dispersion

Bernd Leitl · Denise Hertwig · Frank Harms · Michael Schatzmann
Meteorological Institute, KlimaCampus, University of Hamburg, Germany
e-mail: schatzmann@zmaw.de

Gopal Patnaik · Jay Boris · Keith Obenschain
The Laboratories for Computational Physics and Fluid Dynamics,
US Naval Research Laboratory, Washington, DC, USA

Susanne Fischer · Peer Rechenbach
Ministry of the Interior, Free and Hanseatic City of Hamburg, Germany

A. Talamelli et al. (eds.), *Progress in Turbulence V*,
Springer Proceedings in Physics 149,
DOI: 10.1007/978-3-319-01860-7_22,

is heavily influenced by buildings and other obstructions. Flow and dispersion models of different complexity have been developed in the past. Although they have been reasonably successful in some cases, most of them are still limited in scope. Especially in cases where obstacle effects dominate the dispersion of the hazardous cloud, these models are either too simplistic and thus unable to cope with the geometric complexity, or they are much too slow and thus not able to provide immediate guidance for the persons in charge of the rescue operations.

Recent progress in the fields of computer hardware development, numerical mathematics and scientific computing opens up the potential for improvements. In an effort jointly carried out by the Ministry of the Interior of the Free and Hanseatic City of Hamburg, by the US Naval Research Laboratory, Washington DC, and by the Meteorological Institute of the University of Hamburg, a new emergency management tool for the Hamburg inner city area has been developed. This tool provides, nearly instantaneously, the space-time-structure of airborne hazardous clouds. It is based on NRL's high-resolution large eddy simulation (LES) contaminant transport model (FAST3D-CT) which provides the detailed velocity and turbulence fields within the urban domain. The database created by the model is subsequently converted to an efficient form suitable for use in a second model (CT-Analyst) which runs on a laptop and comes with an interface as is common in computer games. The system is fast because results are pre-computed for a large number of meteorological situations. In case of an accident predictions are based solely on already existing knowledge. The system is easy to handle due to its user-friendly interface. Subsequently details of the new emergency management tool for the city of Hamburg will be presented.

2 The Large Eddy Simulation Model

The LES simulations were carried out at the Laboratories for Computational Physics and Fluid Dynamics of the US Naval Research Laboratory in Washington. Their FAST3D-CT three-dimensional flow simulation model (Boris, 2002; Cybyk, et al, 1999) is based on the scalable, low dissipation Flux-Corrected Transport (FCT) convection algorithm (Boris and Book, 1973, 1976). FCT is a high-order, monotone, positivity-preserving method for solving generalized continuity equations with source terms. The particular FCT convection algorithm in FAST3D-CT was modified by Patnaik et al (2005).

Relevant physical processes simulated in FAST3D-CT include complex building vortex shedding, flows in recirculation zones, and approximating the dynamic subgrid-scale turbulent and stochastic backscatter. The model has the potential to also incorporate stratification, solar heating, urban greenery etc., but these features have not been used here. Emphasis was laid on capturing the effects of unsteady flow on the evolving pollutant concentration distributions.

The simulation code is designed to run efficiently on shared-memory computers. Computational grids involving about 200 million cells were typically used in the presently discussed simulations. This requires about 20 GB of memory which

is now tractable on advanced computers. The challenge of high-resolution grids is not so much one of computer memory but one of computer speed. More details of the physical models in FAST3D-CT are given in Patnaik et al. (2005) and omitted here for brevity.

Runs were made separately for two domain sizes; A larger domain of 16km x 12km with a resolution of 10 m, and a smaller domain of 4km x 4km (Fig. 1a) with a resolution of 2.5 m. With the exception of the upper part of the domains the cells were horizontally and vertically unstretched. Also shown in Fig. 1a is the area modeled in the wind tunnel (diagonal rectangle, see section 4.2). Fig. 1b gives an impression of the high resolution geometry. 18 wind directions were calculated. Different wind speeds were accounted for by scaling the results according to the appropriate similarity laws. The CPU time needed per run for one wind direction and a one hour real time episode in the small domain was approximately six days.

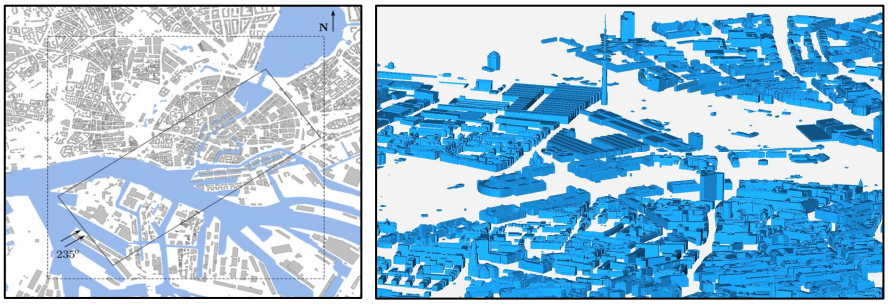

Fig. 1 (a) Top view (from OpenStreetMap) on the 4km x 4km domain. Lake Alster, River Elbe and the city centre are landmarks which provide orientation. Also shown is the 3.7km x 1.4km section modeled in the wind tunnel. (b) Sample of the 3D high-resolution geometry. The Hamburg Fair ground, the TV tower and parts of Hamburg University are easily identifiable.

For the dispersion calculations a passive, inert, gaseous tracer has been used. Passive means that the released substance drifts with the wind and spreads and dilutes due to atmospheric and obstacle generated turbulence. Buoyancy forces are neglected which, however, does not mean that the relevant substance needs to have the same density as the surrounding air. It is assumed only that the densimetric Froude number of the released cloud is well above 1. Inert means that the released gas over the period of interest neither reacts chemically nor deposits. This leads to conservative results. These are common assumptions which need not necessarily be introduced but seem to be adequate for the purpose under discussion here. With additional effort they could easily be avoided, and the FAST3D-CT code already contains the necessary physics for these additional processes.

3 The Emergency Management Tool

After the detailed 3D simulations for 18 wind directions are pre-computed for the coverage region, they are handed over to NRL's emergency management tool CT-Analyst® through a new data structure called Dispersion Nomografs™. CT-Analyst extends these results to all wind directions, speeds, sources, and source locations. These "nomografs" are generated well in advance, so manager using CT-Analyst in an emergency need not wait for supporting analyses (Boris, 2002).

Fig. 2a elucidates the basic method applied. The LES model provides for each grid point the local mean wind vector and the wind directional variation. Starting from a chosen source position the plume envelop can be determined by selecting at the right and left plume edge the worst case directional deviation from the mean wind vector, thereby determining the total area over which the pollutant is able to spread at all. The magnitudes of the local wind vectors determine the speed with which the cloud moves through the urban geometry. The method works likewise for instantaneous puffs and for continuous plumes, since the latter can be regarded as being made up from a series of individual puffs. Simultaneous discharges from multiple sources can be handled as well. Last but not least, the method allows placing sensors at many locations inside the domain and back-tracking the signal to an up to then unknown source location.

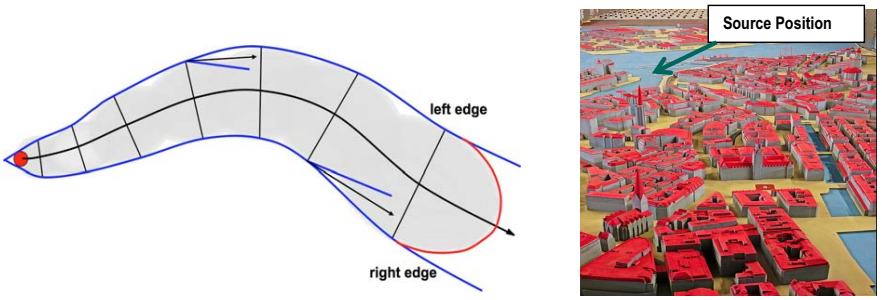

Fig. 2 (a) Top view on a plume dispersing in an environment in which obstacles effect plume shape and direction. The left and right plume edges are determined from the mean and turbulent velocity field computed by the LES model in a narrow 2.5m grid. (b) Geometrical detail of the physical model of Hamburg in the wind tunnel and indication of the source position during the field tests.

Although the immediate knowledge of the total area over which a pollutant can spread is certainly the most important information for a first responder, the second question concerns the pollutant concentrations. For these only conservative estimates are provided. Since the sources can be anywhere in the domain, the huge number of possible concentration fields are not directly calculated by the LES model. Instead of this, the plume edges in combination with a plume profile assumption are used to determine the local mean concentrations as a function of

source strengths, simply by applying the mass conservation principle. Variability around the mean value is roughly estimated from mean to peak ratios determined for a few spills released at representative positions in LES model experiments. Taking into account that reasonable thresholds for short time peak concentrations are often not available, this seems to be an acceptable constraint.

4 Validation of the Emergency Management System

In order to demonstrate the quality of the emergency management system, validation data sets have been generated in field and wind tunnel experiments.

4.1 Field Experiments

Two short field campaigns were carried out in addition to the wind tunnel experiments. Such field tests are always limited in scope. As was described in more detail in Schatzmann and Leitl (2011), it is nearly impossible gaining reliable test data for complex CFD models in such experiments. The atmosphere is intrinsically time dependent and never steady state. The commonly assumed 15 min or 30 min quasi-steady episodes exhibit a large inherent variability. Data obtained over such short periods of time are not representative for the assumed mean wind velocity and direction. And even worse, in urban canopy layers it proves to be nearly impossible to determine a position at which a wind vector representative for the dispersing cloud could be measured. Nevertheless comparisons with field data are vital for building confidence in the quality of numerical and physical model predictions; whenever possible they should be carried out. To perform field measurements in a vibrant metropolitan area is, however, hardly feasible. Permission for carrying out dispersion experiments was granted only for a few early morning hours at 2 weekends. With strong support by fire-fighters and police of the city of Hamburg small amounts of SF_6 were released upwind from the city centre from a boat positioned at river Elbe. In cooperation with scientists from the Forschungszentrum Jülich about 20 automated bag samplers were distributed over the inner city area (Fig. 3a). The probes were subsequently analyzed by using gas chromatography.

Early morning observations are always somewhat of a problem. During the first observational period at April 16, 2011, there was high pressure over Hamburg with clear skies and large radiative cooling of the surface. Such weather situations are subject to stratification and inversion layers, and this was indeed the case as the measurements at the Hamburg TV-Mast (http://www.wettermast-hamburg.zmaw.de) approximately 10 km apart from the site clearly indicate. As becomes evident from Fig 4a, there was a strong inversion above the 110 m measurement platform (Fig 4b) although the wind speed at higher altitudes was quite strong. As smoke experiments carried out at the end of the intensive operation period

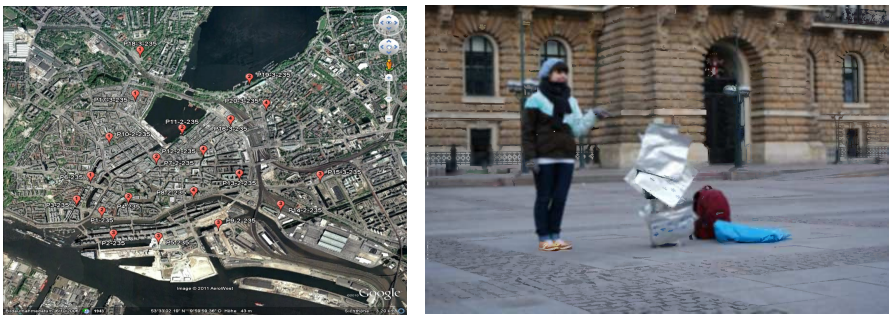

Fig. 3 (a) Measurement positions during the field experiments (from Google Earth) and (b) picture of an automated bag sampler rig (under surveillance of a student) in front of the Hamburg town hall

showed, there were even more inversions near the ground. None of the altogether 8 ultra-sonic-anemometers which were operated simultaneously at different locations around the test site provided a wind speed and direction which matched the movement of the smoke cloud.

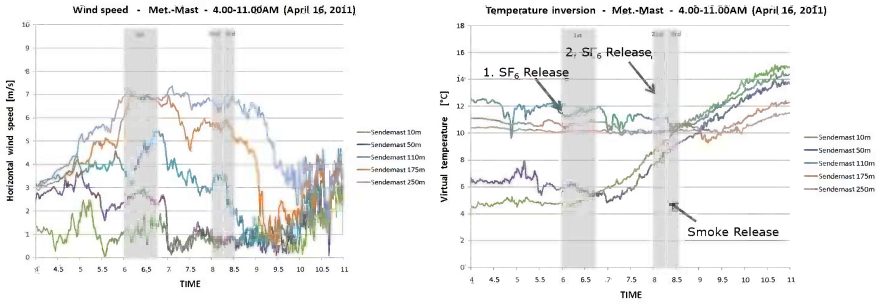

Fig. 4 Wind velocities (a) and virtual potential temperatures (b) measured during the first experimental period at 5 different height levels at a TV mast located about 10 km apart from the test site at the eastern edge of Hamburg

With the second field experiment we waited until a really stormy weekend arrived, with winds from the favored directional sector. Although highly fluctuating with time, wind speed and direction were much more uniform compared to the first campaign (Fig 5b). This finding was fully corroborated by the measurements performed at different height levels at the Hamburg TV mast. In contrast to Fig. 4, in the second phase the boundary layer was well mixed. The wind directions in the lowest 250 m above ground were always around 220°, independent of height and time, and the velocity profile only slightly increased with height.

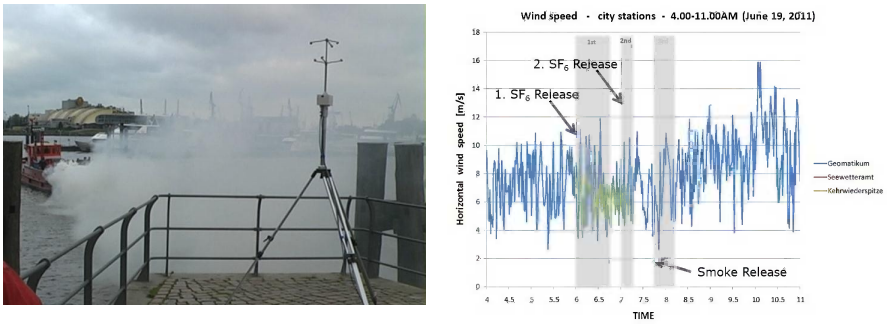

Fig. 5 Second campaign at June 19, 2011: (a) Picture from the highly meandering smoke plume and from the ultra sonic anemometer located near to the source at 'Kehrwiederspitze'. (b) Wind velocity versus time trace measured simultaneously at 2 different stations during the intensive operation period on June 19, 2011.

The automated samplers were spread over an area much wider than the expected cloud width in order to identify not only polluted but unpolluted areas as well. Although the time resolution of the field data is insufficient for the purpose of LES model validation, the overall agreement was generally fair. A comparison of measured and predicted concentrations is presented in Figure 6.

However, since the bag samplers average over an intermittently fluctuating contaminant supply rate, large variability bars would have to be added to the measurements. The magnitude of these bars remains unknown since short-time experiments do not provide the information necessary for statistical analyses (see Schatzmann and Leitl, 2011).

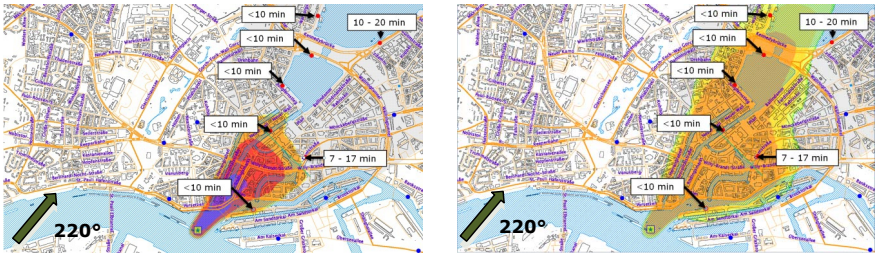

Fig. 6 Second campaign at June 19, 2011. Bag sampler positions are shown with red dots polluted and blue dots unpolluted. The bag-samplers operated time-staggered with suction intervals of 10 min. Comparison of cloud contours predicted by the emergency management tool with measured results (a) 5 min after the release and (b) 10 min after the release.

Further comparisons between field data, wind tunnel data and numerical results are under preparation and will be published soon. They also comprise FTIR measurements which were carried out by the Technical University of Hamburg-Harburg in combination with Bruker Sigma. Additionally, a second wind tunnel experiment is presently carried out in which the field tests of the second campaign are replicated with boundary conditions as they were met during the field experiments. This will allow comparing not only arrival times and the contaminated area but local mean and peak concentration levels as well.

4.2 Wind Tunnel Experiments

Prior to the field tests a first wind tunnel experiment was carried out in the large boundary layer wind tunnel 'Wotan' of Hamburg University. This tunnel has a total length of 25 m with a test section which is 4 m wide and 3 m high and contains a flow establishment section of about 18 m length. The wind tunnel is equipped with an adjustable ceiling allowing a ±0.25 m height change of the test section. An approach flow boundary layer matching the scale of the Hamburg model (1:350) was generated. The boundary layer properties were controlled and documented similarly as described in Schatzmann and Leitl (2011) for another wind tunnel investigation. Non-intrusive flow measurements were carried out with an optical LDA fiber probe with a focal length of 800 mm. To measure high resolution concentration time series a fast flame ionization detector was used. Fig. 1a shows the location of the (in full scale) 3700m long and 1400m wide area modeled in the wind tunnel and Fig. 2b a section of the physical model. Under steady-state mean flow conditions numerous instantaneous and continuous clouds were released at multiple positions.

The subsequent results from the validation exercise with respect to the mean and turbulent flow field are taken over from the paper by Hertwig et al. (2011). It should be mentioned that the wind tunnel experiments and LES simulations were done at the same time in different locations, i.e. neither side knew the results of the other side beforehand (blind testing).

22 measurement locations within the model domain were chosen and time series of the resulting velocity and concentration fields were monitored. For each position highly resolved time series of the horizontal wind components (and partly also for the vertical component) were taken in densely spaced profiles and horizontal flow layers. The selection was made to include areas of the city that feature characteristic urban flow situations that also pose challenges to numerical models. Thus, the locations include narrow street canyons, complex intersections, and measurement points close to the ground. Wind detectors in the numerical calculations were deployed to match the specified locations in the wind-tunnel experiment as closely as possible. The nearest neighbor extraction was chosen in order to avoid contamination of the results by interpolating data in order to have an exact spatial match. This procedure led to slight offsets of the x, y, and z positions of the comparison points that were in the range of a few centimeters up to a

maximum of 1.75m. Experimental and numerical data were homogenized by referencing all velocities and their derivatives to a reference wind speed at a fixed location. This monitoring point was defined at a height of 49m above the river Elbe at approximately 1km upstream distance from the city center (above the source, see Figure 2b). All results which are subsequently presented were obtained for a wind direction of 235°.

Although the emphasis of the analyses was put on the comparison of time-series characteristics, the starting point of the study was set by the validation of the mean flow. Figure 7 shows comparisons of vertical profiles of the stream wise velocity component from wind-tunnel measurements and FAST3D-CT simulations. The inflow is approaching from left to right. Scatter bars attached to the experimental values represent the reproducibility of the data based on repetition measurements under identical boundary conditions. The profile locations differ in the arrangement of the surrounding buildings. Figure 7a shows velocity profiles above the river Elbe (the location is identical with the reference point above the source location indicated in Figure 2b). Being situated well upstream of the densely built-up city centre, the good agreement between experimental and numerical profiles mirrors a good match of the mean inflow conditions. A good agreement is also found for positions at which the flow is strongly influenced by the building structure (Figs 7b and 7c).

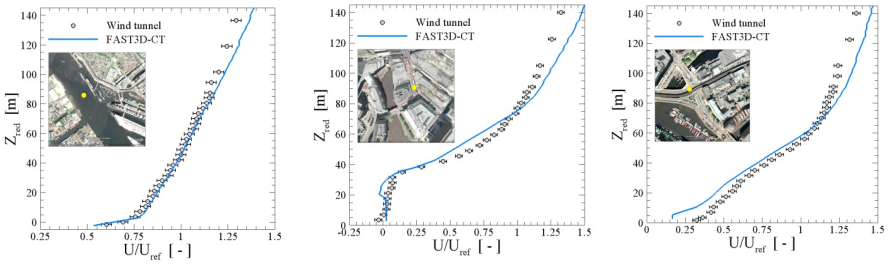

Fig. 7 (a)-(c): Comparison of mean stream-wise velocity profiles at various locations. Area images extracted from Google Earth.

For some of the compared locations, a slight trend towards an under prediction of velocities can be observed at elevations below the mean building height (approx. H_{mean}~35m by averaging over the city center) as seen in Figure 7c. In contrast, higher wind speeds than in the reference measurements are found at heights larger than $2.5H_{mean}$. The slight offsets observed within the street canyon might be explained by the close proximity of building walls and the effect of their physical treatment inside the simulation. The stronger acceleration well above the canopy has to be investigated further and might reflect an excess of TKE in the numerical inflow prescription.

A comparison of horizontal flow fields in terms of mean horizontal wind speed vectors is presented in Figure 8 for different heights above ground. The test case is

represented by the flow entering a courtyard. The large gray arrows indicate the inflow direction. The overall comparison is again quite good, although strong directional deviations at the lowest measurement plane are detected (see Figure 8a; z = 3.5m in the experiment and 2.75m for the numerical simulation). It has to be noted that this is also the lowest computational level of the simulation, which is a possible explanation for the offsets. At this first node the results are strongly influenced by the boundary constraints and the flow did not have enough time to evolve physically.

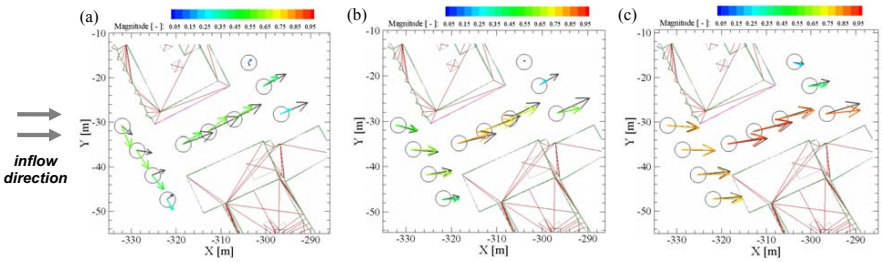

Fig. 8 Mean horizontal velocity vectors of flow entering a courtyard at heights of (a) 3.5m, (b) 17m, and (c) 30m. Gray vectors represent wind-tunnel measurements. Color-coded vectors are from the numerical simulation with FAST3D-CT.

Next, experimental and numerical time series were analyzed in terms of frequency distributions and spectral characteristics of the signals. It has to be noted that both signals differ in their length and their time resolution under full-scale conditions. While the 170s measurement time in the wind tunnel results in a full-scale length of 16.5 hours, the length of the numerical time series is 4.5 hours only. Especially at low elevations within street canyons the full-scale temporal resolution of 2Hz of the FAST3D-CT signals is better than the scaled wind-tunnel data rate that is strongly affected by the local seeding conditions that influences the experimental data rate.

First, the frequency distributions of instantaneous horizontal wind speeds and wind directions were evaluated. Figure 9a shows the location for such a test. The mean horizontal wind speeds U_h and wind directions are compared in terms of vertical profiles shown in Figures 9b and 9c, respectively. At each of the profile heights, the fluctuations about these means were investigated.

Figure 10 shows wind-rose diagrams of horizontal wind speeds and directions observed (Figure 10a) and simulated (Figure 10b) at four different heights within the street canyon profile. At first view the graphs show that the model predicts the deflection of wind directions inside the canopy quite well, together with the adjustment to the wind direction of the inflow at roof-top level and well above at 57.75m (i.e. $1.65H_{mean}$). The spread about the central direction is largest at roof-top height and smallest at the highest elevation in both the experiment and the

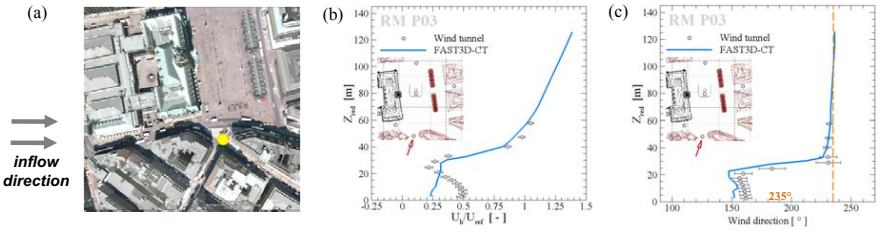

Fig. 9 (a) Profile measurement location at a complex intersection; image extracted from Google Earth. (b) Mean horizontal wind speed and (c) wind direction profiles from wind-tunnel measurements and FAST3D-CT calculations.

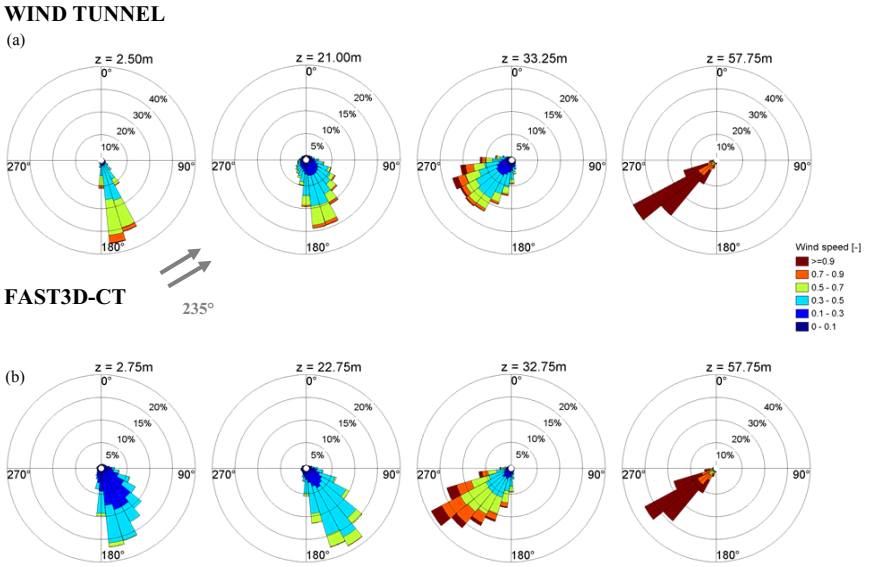

Fig. 10 Wind-rose diagrams showing frequency distributions of horizontal wind speeds and wind directions for wind-tunnel measurements (a) and FAST3D-CT simulations (b) at four different heights within and above a street canyon (same location as in Figure 8a). Large grey arrows indicate the inflow direction. Wind velocities non-dimensionalized with the reference wind speed.

simulation. However, discrepancies in velocity magnitudes are observed inside the canopy, especially for the lowermost point at 2.5m and 2.75m, respectively. As discussed earlier in connection with the mean flow validation, the lower magnitudes are most likely due to the influence of wall boundary conditions prescribed at the ground and at upright building surfaces. Despite these differences the analysis indicates that the LES code is able to reproduce the directional fluctuation levels caused by unsteady flow effects quite reliably.

Auto-spectral energy densities of the turbulent stream-wise velocity component are studied in order to analyze the spectral content associated with different eddy structures found in the flow. The spectra were obtained using an FFT algorithm. In order to make the spectra interpretable in terms of characteristic energetic ranges, two averaging techniques are used. First, the time series is separated into fragments of equal lengths and it is averaged over the spectra obtained from these subsamples. Next, this averaged spectrum is smoothed by taking the mean over equal intervals with respect to the logarithm of frequency. Original values are only kept for the lowest frequencies that are connected to the largest structures in the flow.

Figures 11a-c show scaled frequency spectra obtained from numerical and experimental velocities at various locations at heights of 17.5m (~$0.5H_{mean}$) and 45.5m (~$1.3H_{mean}$), respectively. A very good agreement of the production and energy-containing range of the spectra is found at all positions. The energetic peaks associated with integral length scale eddies coincide very well for the measurements shown in Figures 11b and 11c, whereas at the position above the river (Figure 11a) the peak is shifted for more than a decade towards higher frequencies. This offset might have been caused by the shorter overall signal length of the numerical time series. In order to investigate this further, next analyses will concentrate on comparisons of integral length scales that can be determined from autocorrelation time scales invoking Taylor's hypothesis.

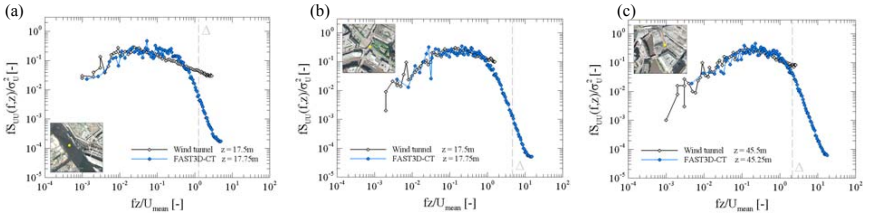

Fig. 11 (a)-(c) Auto-spectral energy densities of the fluctuating stream-wise velocity component from wind-tunnel measurements and simulations with FAST3D-CT at various locations within the city at heights of 17.5m (~$0.5H_{mean}$) and 45.5m (~$1.3H_{mean}$). The dashed lines separate the low frequency parts of the spectra that can be directly resolved by the numerical model given the grid resolution of Δ=2.5m and the respective mean wind speeds from the subgrid-scales affected by numerical diffusion. Area images are extracted from Google Earth.

Common to all of the numerical spectra is their fast roll-off in the high frequency range that marks the onset of the influence from the dissipation scheme. At most of the investigated locations this influence becomes noticeable approximately one decade after the spectral peak was reached resulting in a shortened extent of the inertial range. In consideration of the fact that FAST3D-CT was particularly designed to simulate dispersion processes in urban areas, the very good match of the energy-containing ranges associated with eddies that play a dominant role for scalar transport confirms the model's fitness for that purpose. However, it should

be studied whether an extension of the inertial range is possible in order to add to the physical character of the LES.

Another objective of the validation study was to validate the predicted danger zones of CT-Analyst. A danger zone marks the area which can be reached by a released tracer for a selected source location and a selected mean wind direction. For this analysis two different source locations and a wind direction of again 235° were selected. The tracer was released continuously during the measurements. Figure 12 shows the result of this comparison for the two dispersion scenarios. The marked area indicates in each case the predicted danger zone by CT-Analyst. The triangles and squares in Figure 12 represent the results of the wind tunnel measurements. A triangle states that no concentration was detected during a 4 minute wind tunnel measurement, and a square indicates that within the 4 minute measurement a concentration above instrument threshold was exceeded at least once. Hence the area between a triangle and a square marks the edge of the wind tunnel plume. It has to be considered that due to the model scale of 1:350 a 4 minute wind tunnel measurement would correspond to nearly a 24 hour measurement at full scale under identical mean weather conditions. In order to analyze the effect of the release rate the measurements were repeated for different release rates. In line with theory it was found that increasing the release rate by a factor of ten has no effect to the size of the danger zone.

Further comparisons with respect to local mean and peak concentrations will be done as soon as the results from the second wind tunnel campaign become available. These experiments will be an exact repetition of the conditions which were met during the second field tests.

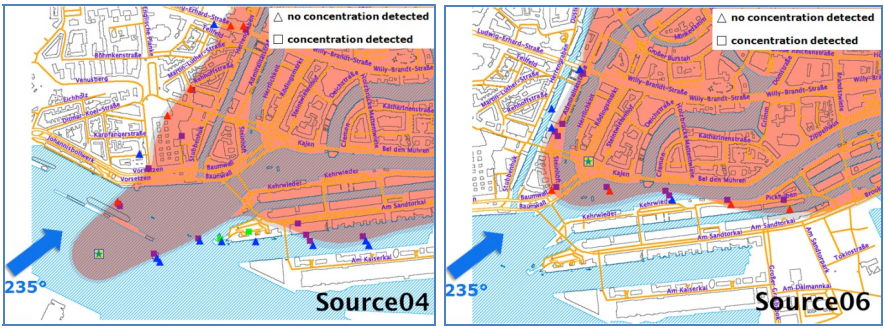

Fig. 12 Comparison of the predicted and measured danger zones for two different dispersion scenarios within the city center of Hamburg. Wind from 235 °.

5 Conclusions

Accidental or deliberate releases of harmful agents in urban areas can produce a tremendous challenge to emergency response staff even if the amount of the released substance is small and the scale of the threat limited. This is partly caused

by the fact that the dispersion process in complex geometries is driven by complex wind flows and turbulent diffusion. From a strict physical point of view, the source sizes, release rates or (mostly short time) durations of release events often restrict the use of tools which are based on mean flow and dispersion modeling because in the atmosphere the assumed mean conditions do not exist for relevant time periods less than many hours of constant weather.

Therefore it is necessary to move forward to more sophisticated modeling techniques which have the potential to deal with the unsteady behavior of local scale dispersion in complex geometries in a more consistent way. As was shown, technical progress has advanced and a new generation of CFD models is ready to be applied in the context of dispersion predictions for hazardous clouds resulting from accidental releases in urban or industrial environments. Although these models of LES type are very demanding with respect to computational hardware and time resources, they can be applied before an emergency occurs. In combination with an intelligent tool which excerpts the relevant information from the simulated CFD results first responders receive immediate decision making assistance.

A prototype of such an emergency management system adjusted to the geometry of the city of Hamburg has been developed and validated with data from appropriate wind tunnel and field experiments. The results obtained so far are promising. In spring 2012 the new emergency management system was handed over to Hamburg's city authorities. It is now being tested under realistic operating conditions.

Acknowledgements. Financial support by the German Federal Office of Civil Protection and Disaster Assistance as well as by the Parliament of the Free and Hanseatic City of Hamburg is gratefully acknowledged. Parts of the wind-tunnel model construction costs were covered through a grant from Hamburg University's KlimaCampus.

The authors are grateful for technical support from the Hamburg fire and police departments, the Forschungszentrum Jülich, Bruker-Sigma, THW Hamburg, the German Weather Service and Ingo Lange, Michael Offermann, Christine Peeck and Anastasia Tatarinova from the Meteorological Institute who provided the Ultra-Sonic-Anemometer data.

References

Boris, J.P., Book, D.L.: Flux-Corrected Transport I, SHASTA, A Fluid Transport Algorithm that Works. J. Comput. Phys. 11, 8–69 (1973)

Boris, J.P., Book, D.L.: Solution of the Continuity Equation by the Method of Flux-Corrected Transport. Methods in Comput. Phys. 16, 85–129 (1976)

Boris, J.P.: The Threat of Chemical and Biological Terrorism: Preparing a Response. Comp. Sci. and Eng. 4, 22–32 (2002)

Cybyk, B.Z., Boris, J.P., Young, T.R., Lind, C.A., Landsberg, A.M.: A Detailed Contaminant Transport Model for Facility Hazard Assessment in Urban Areas. AIAA Paper 99-3441. AIAA, Washington DC (1999)

Harms, F., Hertwig, D., Leitl, B., Schatzmann, M., Patnaik, G.: Characterization of transient dispersion processes in an urban environment. In: Proceedings of the 14th International Conference on Harmonisation within Atmospheric Dispersion Modelling for Regulatory Purposes, Kos, Greece, October 2-6 (2011)

Hertwig, D., Peeck, C., Harms, F., Patnaik, G., Leitl, B., Schatzmann, M.: Characterization of transient dispersion processes in an urban environment. In: Proceedings of the 14th International Conference on Harmonisation within Atmospheric Dispersion Modelling for Regulatory Purposes, Kos, Greece, October 2-6 (2011)

Patnaik, G., Boris, J.P., Grinstein, F.F., Iselin, J.: Large Scale Urban Simulations with FCT. In: Kuzmin, D., Löhner, R., Turek, S. (eds.) High-Resolution Schemes for Convection-Dominated Flows: 30 Years of FCT, pp. 105–130. Springer (2005)

Schatzmann, M., Leitl, B.: Issues with validation of urban flow and dispersion CFD models. Journal of Wind Engineering and Industrial Aerodynamics 99, 169–186 (2011)

Turbulent Rayleigh-Bénard Convection in Air: How Uniform Is the Local Wall Heat Flux at Finite Aspect Ratio?

Ronald du Puits, Robert Kaiser, Johannes Rilk, and André Thess

Abstract. In our talk we present a visualization of the flow field inside the boundary layer in highly turbulent Rayleigh-Bénard convection in air. Sequences were captured at various positions along the heated bottom plate in a rectangular cell of $2.5 \times 2.5 \times 0.6\,\mathrm{m}^3$ at a Rayleigh number of $\mathrm{Ra} = 1.3 \times 10^{10}$. They demonstrate that the velocity field may not be considered as uniform over the entire surface of the plate and, therefore, the distribution of the local heat flux becomes non-uniform as well. Local heat flux measurements using an infrared camera show that in the specific case this quantity varies by at least $\pm 10\%$ depending on the local flow condition at distinct areas of the plate surface.

1 Introduction

Phenomenological scaling theories on heat transport in turbulent Rayleigh-Bénard convection (RB) frequently base on the assumption of a virtually infinite lateral extent of the cell [1, 2, 3]. In this case the mean fields of velocity and temperature are not affected by the sidewall(s). In particular, the local heat flux along the surface of the heated bottom and the cooled top plates is uniformly or at least periodically distributed. On the other hand, it is well known that in RB cells of small aspect ratios $\Gamma = L/H$ (H - height, L - lateral extent of the cell) of the order of one and less a large-scale circulation (LSC) evolves that does not homogeneously fill the space between the plates [4]. If the LSC often referred to as mean wind passes the top and the bottom plates the local heat flux is enhanced along its path while in areas out of the mean wind the heat flux is lower than its spatial averaged mean. Since the aspect ratio of the cell affects the global flow structure the distribution of the local heat flux at the surface of the horizontal plates may also depend on the geometry.

Ronald du Puits · Robert Kaiser · Johannes Rilk · André Thess
Ilmenau University of Technology, POB 100 565, Ilmenau, 98684, Germany
e-mail: ronald.dupuits@tu-ilmenau.de

A. Talamelli et al. (eds.), *Progress in Turbulence V*,
Springer Proceedings in Physics 149,
DOI: 10.1007/978-3-319-01860-7_23,

2 Experimental Set-Up

We have performed a series of measurements of the local heat flux at the surface of the heating plate in a rectangular RB cell with aspect ratios $\Gamma_x = 1$ and $\Gamma_z = 0.26$ (see Figure 1). The working fluid is air and both Prandtl number $\mathrm{Pr} = \nu/\kappa$ and Rayleigh number $\mathrm{Ra} = (\beta g \Delta T H^3)/(\nu\kappa)$ are fixed at $\mathrm{Pr} = 0.7$ and $\mathrm{Ra} = 1.3 \times 10^{10}$, respectively. The boundary layer flow visualization has been performed using a 2 W laser in continuous wave mode. In combination with special optics a light sheet of 70 mm in height and about 2 mm in thickness has been generated according to the position in Figure 1. Adding cold-atomized droplets of Di-Ethyl-hexal-sebacate of about 1 μm size to the air flow the velocity field in the proximity of the heated bottom plate becomes visible and the motion of particles could be tracked by a digital photo camera CANON EOS 600D.

The local heat flux has been measured using an infrared camera. To this purpose the surface of the heating plate has been covered with a thin layer of a synthetic material with a well-defined heat conductivity. This layer generates a temperature drop being proportional to the local heat flux. Assuming that the temperature distribution beneath the synthetic layer is uniform (or at least known) the temperature field at the upper side represents the distribution of the local wall heat flux. In order to increase the accuracy of the method local heat flux sensors of very small thickness have been placed at various positions along the surface of the heating plate.

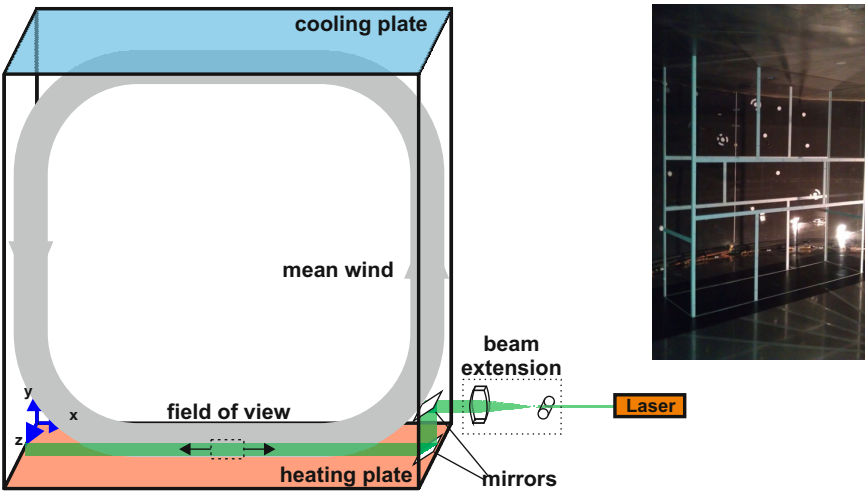

Fig. 1 Set-up of the boundary layer visualization in turbulent Rayleigh-Bénard convection. The rectangular test cell with the dimensions of $2.5 \times 2.5 \times 0.6$ m^3 is embedded in the large scale experiment "Barrel of Ilmenau" (please visit www.ilmenauer-fass.de for detailed information) using its heating and cooling plates with uniform temperature as bottom and top bound. The photo on the right shows the rectangular test cell.

3 Results

In Figure 2 a snapshot of the boundary layer flow captured above the center of the heating plate is shown.

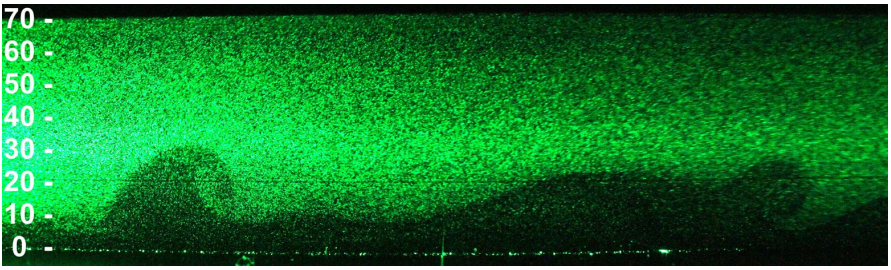

Fig. 2 Boundary layer in turbulent Rayleigh-Bénard convection in air at Ra $= 1.3 \times 10^{10}$. The mean wind is from left to right. The scale on the left hand side is the distance z from the heating plate in units of millimeter, $z = 0$ mm corresponds to the surface of the plate.

The large-scale circulation above the plate surface is from left to right as indicated in Figure 1. The picture illustrates how thermal plumes evolve as buoyancy driven boundary layer instabilities and how they interact with the mean wind. In the talk a

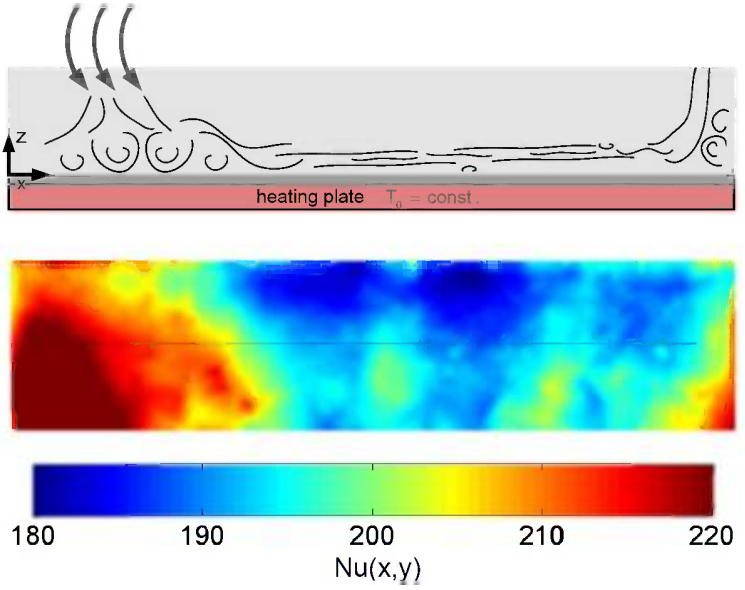

Fig. 3 Caricature of the flow field at the heated bottom plate along the mean wind as obtained from flow visualization and the time-averaged heat flux distribution $\langle Nu_L(x,y)\rangle_t$ measured at its surface. The color plot shows the full 2.5 x 0.6 m sized area of the heating plate.

few sequences from distinct areas of the heating plate have been presented showing the very different behavior of the boundary layer flow at various locations with respect to the mean wind.

Figure 3 shows both a caricature of the boundary layer flow structure at the heating plate derived from the flow visualization and the measured heat flux distribution at its surface. The heat flux is expressed in terms of a local Nusselt number $\mathrm{Nu}_\mathrm{L}(x,y) = (-q(x,y)H)/(\lambda\Delta T)$. The highest value is measured at the area of the plate surface where the falling plumes impinge the bottom plate. Along the path of the mean wind the local heat flux decreases and achieves its minimum at the center of the cell. The plot clearly demonstrates that the assumption of a uniform heat flux at the surface of the horizontal plates represents a strong simplification particularly at small aspect ratios $\Gamma \leq 1$. In the specific case studied here it quantity varies by more than $\pm 10\%$ depending on the local flow condition.

4 Conclusion

In our talk we demonstrated that the assumption of a uniform heat flux distribution along the surface of the heating (and the cooling) plate might be a too strong simplification in turbulent Rayleigh-Bénard convection at aspect ratios $\Gamma \leq 1$ and moderate Rayleigh number. For the first time a detailed map of this quantity could be generated using infrared camera technology. We are planning to apply this technique at the full-size RB experiment of 7.0 m in diameter and 6.3 m in height.

Acknowledgements. The authors wish to acknowledge the support of the Deutsche Forschungsgemeinschaft under the grant numbers PU 436/1-1 and PU 436/3-1, the financial contribution of the Thüringer Ministerium für Bildung, Wissenschaft und Kultur as well as the European Commission in the COST action MP 0806 for the work reported in this paper.

References

1. Kraichnan, R.H.: Turbulent thermal convection at arbitrary Prandtl number. Phys. Fluids 5, 1374–1389 (1962)
2. Siggia, E.D.: High Rayleigh Number Convection. Annu. Rev. Fluid Mech. 26, 137–168 (1994)
3. Grossmann, S., Lohse, D.: Scaling in thermal convection: a unifying theory. J. Fluid Mech. 407, 27–56 (2000)
4. Sun, C., Xia, K.-Q., Tong, P.: Three-dimensional flow structures and dynamics of turbulent thermal convection in a cylindrical cell. Phys. Rev. E 72, 026302 (2005)

A Gas Discharge Normal to a Wake: Experimental Investigation of the Plasma-Flow Interaction

Marco Belan

Abstract. An experimental investigation has been conducted to study the interaction of a gas discharge with the wake generated by a flat plate normal to the free airstream. The free discharge and the free airstream are orthogonal to each other and the electric forces are of the same order as the inertial forces in the absence of the discharge. The facilities include devices for local discharge current measurements, a hot wire anemometer and a visualization system. The analysis of the time histories of the cathodic currents suggests that the flow-discharge configuration considered here may give rise to a coupling between the flow and the electric fields oscillations.

1 Introduction

The phenomenon of the electric discharge in a gas has been of interest to engineers and physicists for many years. In particular, the flow induced by a non-thermal plasma stream in a ionized region of a gas, also known as electric wind, may give rise to important applications in itself and in relation with other phenomena in a variety of fields, such as fluid dynamics, heat and mass transfer, chemical reactions and so forth. In fluid dynamics, several efforts have been made to gain a better understanding of the interaction between airstreams and discharges of this kind, and many theoretical, experimental and numerical results have been published, see reviews [1, 2]. On the other hand, a wide range of studies is devoted to flow and turbulence control through plasma-based devices, as outlined in [3].

The airstream–discharge interaction may take place at different energy levels for the two phenomena involved; in many studies, focused on technical applications, the discharge energy density is considered definitely higher than the airstream energy density. However, a deeper comprehension of these interactions could arise

Marco Belan
Politecnico di Milano, Dipartimento di Scienze e Tecnologie Aerospaziali,
via La Masa 34 - 20156 Milano, Italy
e-mail: marco.belan@polimi.it

A. Talamelli et al. (eds.), *Progress in Turbulence V*,
Springer Proceedings in Physics 149,
DOI: 10.1007/978-3-319-01860-7_24,

from examining the whole range of possibilities between the limiting cases of a pure airflow and a fluid subject exclusively to electrical forces. Such wide range investigation can also be important from the point of view of turbulence–flow control, where the unsteady phenomena can reach high levels of complexity, and the useful applications correspond in general to well energized actuators that force the airflow at some specific location.

Within this context, the present experiment can be considered as an intermediate case, where the effects of the pure discharge and the pure airstream are comparable. This experiment deals with the interaction of a gas discharge with the flow past a bluff body, here a flat plate normal to the free stream. The same plate plays also the role of the discharge anode, whereas the cathode, located at the wall of the test section, is parallel to the free stream. This makes the main directions of airstream and discharge orthogonal each other. The resulting plasma-flow interactions can be basically characterized by few parameters, namely the gas density ρ, the airflow velocity scale U, the ion mobility μ_i, a spatial scale L for the discharge, typically related to the electrodes length (here also to the body span), and the time-averaged discharge current i. These parameters may be combined to obtain the dimensionless electrohydrodynamic number $N_{EHD} = i/(\rho \mu_i U^2 L)$, which represents the ratio of discharge-induced body force to inertial force on a gas volume: when this number is very small with respect to the unity, the airflow is scarcely affected by the electric field, whereas a large number indicates that the electric field controls the airflow, as in many plasma actuators. In this experiment, N_{EHD} is always less than 0.75 and typically bounded in the range 0.005 to 0.25, what means that the physics is neither airflow-dominated nor discharge-dominated. In other words, the N_{EHD} range is selected in such a way as to study a plasma-flow interaction where the discharge electric energy and the airflow kinetic energy are comparable.

2 Experimental Setup

In the electrohydrodynamic number N_{EHD}, the parameter actually common to discharge and airstream is the length L. Since electrical and inertial forces scale differently, the desired values of N_{EHD} turn out to be easily achievable in a small size facility, where L can take affordable values. A sketch of the relevant experimental setup is shown in Fig. 1. The fluid is air at atmospheric pressure and room temperature. The humidity, a crucial parameter for gas discharges, was less than 40% in all tests; in this range the discharge regimes can be easily identified by the relevant currents. The airstream flows inside a small wind tunnel and meets a metallic flat plate at 90° incidence in a test section of size $L \times H = 80 \times 50$ mm. The considered velocity range is 3 to 6 m/s, and the Reynolds number of the plate ranges from 1500 to 3200. The plate spans the center of the test section, parallel to the L side, it has a chord $c = 8$mm, a thickness of 0.5mm and is chamfered at both sides. It is also connected to the positive pole of a DC power supply through a ballast resistor, $R_b = 1\text{M}\Omega$, and in this way it acts as an anode of length $\sim L$, driven at voltages between 17 and 19kV. The cathode consists of an array of plane electrodes, located

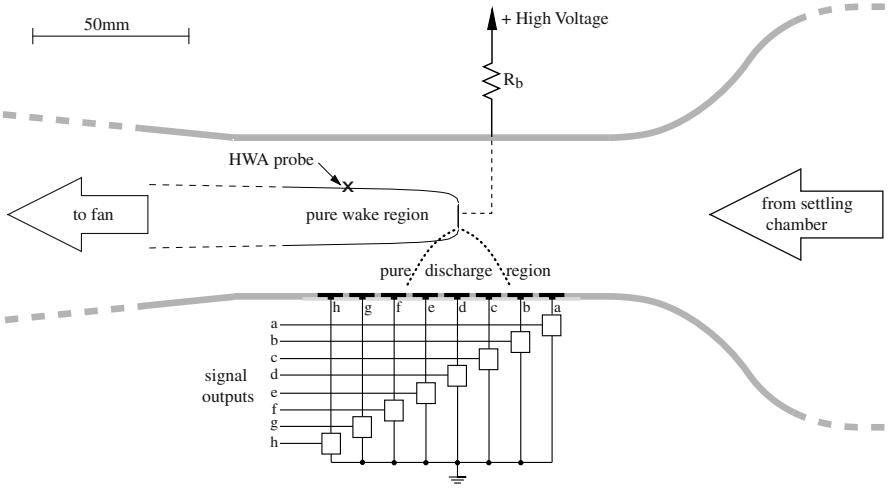

Fig. 1 Experimental setup, scaled coordinates. The flat plate is centered vertically on cathode d). The pure wake zone (without discharge) is sketched by thin lines, the pure discharge zone (without airflow) is sketched by dotted lines.

on a wall of the test section. Each electrode is connected to ground through a low impedance measuring device, which can be a 1kΩ resistor or a suitable voltage transformer, depending on the particular test which is being performed. The multiple cathodes a)... h) allow to gain information about the spatial distribution of the discharge as a function of time. The output signals are digitally acquired by standard devices, sampling up to 48kHz. A hot wire probe can be used to measure the velocity power spectrum in the wake. The probe position for the best detection of the vortex shedding frequency is shown in Fig. 1. The facilities include also a smoke generator and a camera for the visualization of flow and discharge patterns.

3 Results and Discussion

The unsteadiness of the pure wake, without discharge, can be basically characterized by measuring the dominant frequency f in the power spectrum of the HWA signal, that is the Strouhal number $St = fc/U$ in dimensionless form. The measured value 0.168, corrected for solid blockage by the formula used in experimental literature [4], turns out to be $St = 0.136$, which agrees very well with the known blockage free value [5, 6] in the Reynolds range under consideration. The relevant dimensional frequencies vary from 60 to 130Hz. The gas discharge under study, depending on the current intensity, belongs to two known regimes, the corona or glow discharge and the filamentary or breakdown streamer discharge [7]. In the absence of airstream, the time-averaged current density exhibits a standard symmetric spatial distribution with the maximum value on cathode d). The unsteadiness of the discharge is characterized by a typical high frequency pulsation in the kHz band

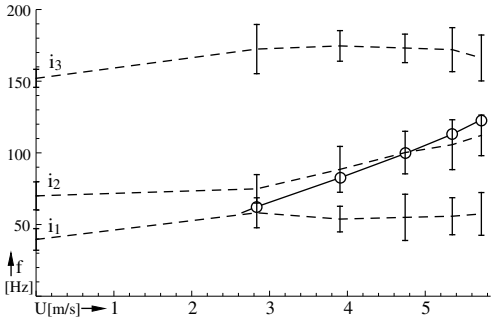

Fig. 2 Discharge burst frequencies and vortex shedding frequency. Dashed lines: burst frequencies for 3 current levels, identified by the total time-averaged discharge currents $i_1 = 40\mu$A, $i_2 = 70\mu$A and $i_3 = 140\mu$A, measured at $U = 0$ m/s. Solid line: natural Strouhal frequency of the pure wake in the absence of the discharge.

known as flashing corona [2] and a low frequency pulsation that appears at the highest currents (filamentary regime) due to repetitive current bursts, in the 100 Hz band. In this experiment, the high frequency pulsations lie in the range from 1.5 to 3.5kHz, whilst the low frequencies are generally lower than 200Hz. These frequencies can be measured by spectral analysis of the signals or also by direct counting of the bursts through a threshold algorithm. When both the airstream and the discharge are present, several phenomena can be observed. A smoke wire visualization reveals that the typical wake patterns are deflected toward the cathodic wall, whereas a visualization based on the weak light emitted from the discharge, obtained by means of an intensified camera, reveals that the discharge is deflected downstream. These effects are related to the intensities of discharge current and flow velocity in an intuitive way, which can be expressed by the value of the N_{EHD} number; unfortunately, a presentation of these results cannot be included here for reasons of space. About the unsteady behaviour of the plasma-flow system, other interesting results can be obtained by analyzing the time history of the cathodic output signals. Under the influence of the airstream, the outputs a), b), c) decrease rapidly whilst the outputs d)... f) maintain a good level. The output d) exhibits in general a dense, continuous spectrum, whilst the outputs e), f), g), h) have similar spectral properties, including high flashing frequencies and low burst frequencies. Both frequencies increase with the discharge current, but the flashing frequency lying in the kHz band remains independent of the airspeed U, whilst the burst frequency instead turns out to depend on U. The best S/N ratio is found on output f), that gives rise to Fig. 2, where the discharge is established at $U = 0$ m/s for 3 different currents, then the burst frequencies are measured for several flow velocities and shown in comparison with the Strouhal frequencies of the pure wake. In general, the burst frequencies are weakly raised by the interaction with the airstream. In particular, at the lowest current level i_1, the burst frequency is only slightly influenced by the airstream, this phenomenon is more evident when the frequency approaches the natural pulsation of the wake (lowering the current below this level leads to a glow discharge with rare non repetitive bursts). At the intermediate level i_2, the burst frequency appears to be strongly influenced by the airflow, and seems to grow together with the wake frequency in

the considered airspeed range. At the highest level i_3, the burst frequency returns to be weakly influenced by the airstream; further increases of the current lead subsequently to the transition to spark regime.

In conclusion, the presented results suggest that the flow-discharge configuration considered here may give rise to a coupling between the oscillatory behaviours of the flow field and the discharge stream. At the present state of the work, a complete understanding of the underlying physics cannot yet be reached, but it is worth to add some comments: first, a simple interpretation of the current waveform as a periodic deflection of the discharge due to the wake is not satisfactory. Actually, the bursts exist even without airflow, provided that the current is high enough, because of the voltage–current characteristic of the discharge and the intrinsic capacitance of the circuit. When both the airflow and the wake are present, a possible mechanism for the coupling could be the enhanced ion transport each time that a vortex rolls up toward the cathodic wall creating a favourable velocity zone. Then, the coupling would take place when the natural frequencies of the two phenomena are close enough. At present, this mechanism must be considered as a mere hypothesis, and other interpretations may also arise as consequences of different kind of measurements. Therefore, a more articulated investigation of this phenomenon will be the object of a further work.

References

1. Chang, J.S., Watson, A.: Electromagnetic hydrodynamics. IEEE Trans. Dielectr. Electr. Insul. 5(1), 871–895 (1994)
2. Fridman, A., Chirokov, A., Gutsol, A.: Non-thermal atmospheric pressure discharges. J. Phys. D: Appl. Phys. 38, R1–R24 (2005)
3. Moreau, E.: Airflow control by non-thermal plasma actuators. J. Phys. D: Appl. Phys. 40, 605–636 (2007)
4. Ota, T., Okamoto, Y., Yoshikawa, H.: A correction formula for wall effects on unsteady forces of two-dimensional bluff bodies. J. Fluids Eng. 116, 414–418 (1994)
5. Roshko, A.: On the wake and drag of bluff bodies. J. Aeronaut. Sci. 22, 124–132 (1955)
6. Chen, J.M., Fang, Y.C.: Strouhal numbers of inclined flat plates. J. Wind Eng. Ind. Aerodyn. 61, 99–112 (1996)
7. Gallo, C.F.: Corona – A Brief Status Report. IEEE Trans. Ind. Appl. IA-13(6), 550–557 (1977)

Mixing due Pulsating Turbulent Jets

Holger Grosshans, Alexander Nygård, and Laszlo Fuchs

Abstract. Combustion efficiency and the formation of soot and/or NOx in Internal-Combustion engines depends strongly on the local air/fuel mixture, the local flow conditions and temperature. Modern diesel engines employ high injection pressure for improved atomization, but mixing is controlled largely by the flow in the cylinder. By injecting the fuel in pulses one can gain control over the atomization, evaporation and the mixing of the gaseous fuel. We show that the pulsatile injection of fuel enhances fuel break-up and the entrainment of ambient air into the fuel stream. The entrainment level depends on fuel property, such as fuel/air viscosity and density ratio, fuel surface-tension, injection speed and injection sequencing. Examples of enhanced break-up and mixing are given.

1 Introduction

Steady turbulent jets generate large scale vortices which enhance the large scale mixing and the entrainment of ambient fluid into the jet. The shear-layer of the jet produces also small scale turbulent eddies that are responsible for the local mixing. For many applications, such as a fuel jet injected into a combustion chamber, the time and space that is allowed for mixing is limited. One has observed in the past

Holger Grosshans
Lund University, Division of Fluid Mechnics,
SE-22100 Lund, Sweden
e-mail: holger.grosshans@energy.lth.se

Alexander Nygård · Laszlo Fuchs
KTH - Mechanics, Osquarsbacke 18, 100 44 Stockholm
e-mail: {alexander,lf}@mech.kth.se

Laszlo Fuchs
Lund University-Fluid Mechanics,
SE-22100 Lund, Sweden

A. Talamelli et al. (eds.), *Progress in Turbulence V*,
Springer Proceedings in Physics 149,
DOI: 10.1007/978-3-319-01860-7_25,

that pulsatile injection, instead of a continuous one, enhances entrainment and mixing. In [1] one considers mixing in jets subject to some means of jet exit nozzle pattern excitations. [1] note that even relatively minor changes to the exit flow pattern of a round jet, through changes to the exit nozzle profile are found to propagate downstream into the far field. [2] studied impulsively started incompressible turbulent jets with emphasis on the transient phase. [3] and [4] measured the characteristics of air jets intermittently discharged into ambient fluid. This type of jet shows a much higher rate of entrainment than do steady or pulsed jets at the same mass flow. In the LDV measurements of [4] a pulsed subsonic jet with significant no-flow period between pulses has been studied. It was shown that such a jet has much higher entrainment than steady or partially pulsed jets of the same mass flow. The effect of pulsations is observed up to distances of 50 nozzle diameters. Similar findings of the effects of jet unsteadiness have been observed by [5] in their gravity-driven flow in which they used dyed fluid from a vertical tube flowing into a large water tank. The measurements revealed that the portion of the unsteady jet corresponding to *the deceleration phase* dilutes more than the steady jet. By using acid-base neutralization reaction, one could show that the jet mixes in a shorter distance than the steady jet. Modern diesel engines use common rail injectors. The injectors can be steered electronically with respect to duration and frequency of injection. [6] studied a single nozzle of such an injector. The axial velocity of the droplets was studied. The radial distribution of the normalized axial mean velocity was similar to that of the free gas jet within $r/r_{0.5} = 1.0 - 1.5$ ($r_{0.5}$ is the radius where the jet velocity attains half of the velocity at the center-line) regardless of time. The effects of intermittent injections on entrainment were not considered. Experiments and experience in the diesel engine industry indicated the benefits of staged/multiple injection of fuel. The initial purpose has been to generate stratified charges, but it has been observed that enhanced mixing is attained at the end of the injection pulse. A related engineering solution is using rotating fuel injectors. There have been some attempts to explain the observed effect of mixing at the end of injection. [7] proposed a 1-D model for studying mixing of an inert diesel spray. The main assumptions of the model are the mixing-controlled hypothesis. The authors claim that by making some further assumptions the model would enable the estimation of the distribution of properties within the spray as well as the tip penetration. A more detailed analysis by [8, 9] using also a 1-D model, indicates the formation of a so called entrainment wave. This entrainment wave propagates at the centreline twice as fast as the jet [8, 9].

2 Models and Methods

The liquid jet is injected into a quiescent air, where it undergoes an initial break-up. The flow is assumed to be incompressible both in the liquid as well as in the gaseous phase. The liquid-gas interface is handled by the so called Volume Of Fluid (VOF) approach [10]. Large Eddy Simulations (LES) is used for handling this transitional flow such that it is practically equivalent to Direct Numerical Simulation (DNS) in larger parts of the domain, since in these regions all scales are resolved. At regions

where the resolution is incomplete the approach becomes to be LES. The influence of the liquid-gas density ratio, ρ_l/ρ_g, the Weber number, $We = \rho_g U_{inj} d_{jet}/\sigma$, and the injection timing parameters T_1 and T_2 is studied as shown in Tab. 1. T_1 corresponds to the duration of one injection pulse, T_2 corresponds to no injection. At injection the jet has a constant speed of U which is changed to zero at off state.

Table 1 Characteristics of the simulations

CASE	Re_{jet}	$\frac{\rho_l}{\rho_g}$	$\frac{\mu_l}{\mu_g}$	We_{jet}	T_1	T_2
vof.aI	9300	1	2.8	10^8	10	10
vof.aII	9300	20	2.8	10^8	10	10
vof.bI	9300	1	2.8	10^8	10	20
vof.bII	9300	20	2.8	10^8	10	20
vof.cII	9300	20	2.8	500	10	10

3 Results

Two of the cases are shown below. The first case is a single phase jet but with $\mu_l/\mu_g = 2.8$. Fig. 1 depicts the injection of five jet pulses. The first injected blob disintegrates not only at its leading edge but even more at its trailing part. This is the effect of enhanced entrainment of ambient air due to the strong deceleration as the injection is halted, leading to the suction of ambient air towards the tail of the blob. At the fifth injection one may note the disintegrated jet even though one may notice the centroids of the previously injected blobs. Fig. 2 depicts a different case with relatively stronger surface tension effects. The dominating break-up mechanism is different as compared to the previous case. In the former case the gas inertia is large compared to the surface tension force per unit of interfacial are. The resulting break-up generates many droplets much smaller than the jet diameter and is called catastrophic. In latter case the breakup is of shear type. Additionally, one may also observe that due to the low speed the jet breaks up at its tail in the first wind induced regime. A measure of the entrainment is the speed of the jet along the center-line. As ambient air is entrained the speed of the jet decreases. Fig. 3(a) depicts the stream-wise velocity along the jet axis at two different locations. The delay between the leading edge of the jet pulses as they pass the two monitoring points is 5.7 t^* ($t^* = d_{jet}/U$). The corresponding time delay for the tail of the blob is only 4.3 t^*. The entrainment wave speed is the ratio of these two time delays, which is about 1.3 which is considerably smaller than the factor 2 seen is the experiments and the 1D model. The corresponding plot for the case in Fig. 2 is depicted in Fig. 3(b). In this case the time delays for the leading and trailing edges are 4.3 and 2.2, respectively. This case is closer in its parameter range to the experimental one and hence also the entrainment wave speed is predicted very well (i.e. equals to 2).

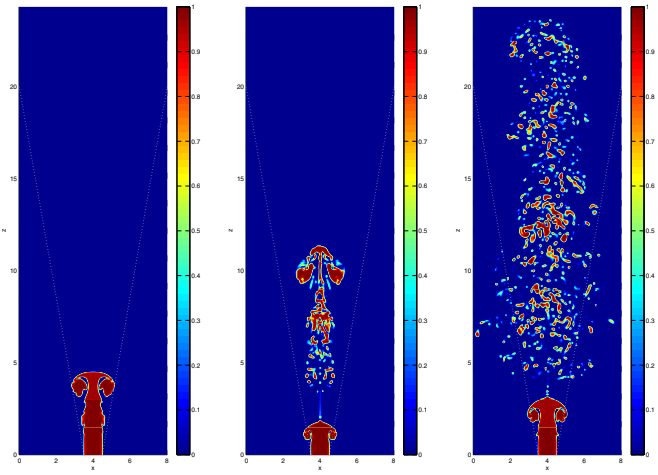

(a) (b) (c)

Fig. 1 First (Fig. 1(a)), second (Fig. 1(b)) and fifth (Fig. 1(c)) injection pulse. At the end of injection of the first blob, ambient fluid is penetrating the blob from behind and when the second blob is injected the first one starts to disintegrate (right frame). $\rho_l/\rho_g = 1$, $\mu_l/\mu_g = 2.8$, $Re = 9300$ and $We = 10^8$. The injection and pause intervals are equally long.

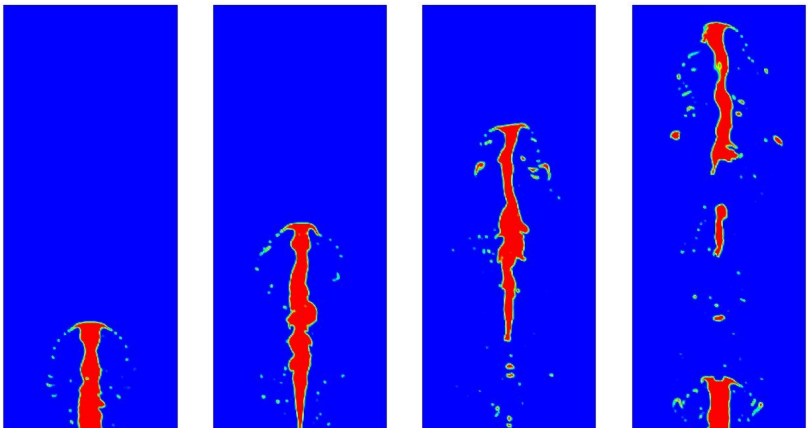

(a) (b) (c) (d)

Fig. 2 Injection of a liquid jet: The red regions correspond to the liquid phase as it disintegrates. Note the disintegration at the tail of the jet. The density ratio is 20, injection time over pause time is 2, $We = 500$.

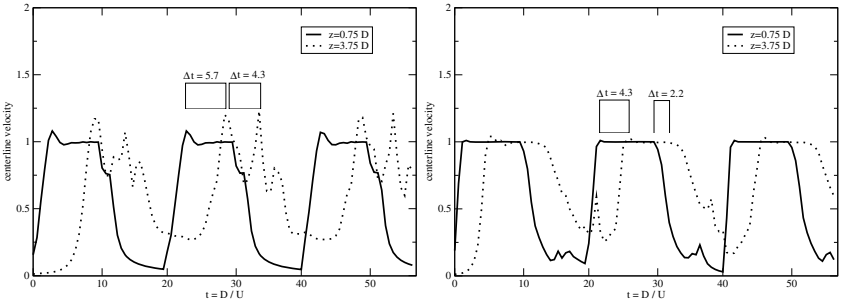

Fig. 3 Center-line axial velocity of the jet vs. time. Solid line corresponds to a point located 0.75 diameters downstream, dashed line to a point 3.75 diameters downstream. The flow in Fig. 3(a) corresponds to the case shown in Fig. 1, Fig. 3(a) to Fig. 2.

4 Conclusion

The effects of intermittent injection of a jet has been studied numerically. The influence of the gas-liquid density ratio, the We number and the injection frequency has been investigated. It can be concluded, that for certain parameters the tail of a injected blob travels twice the speed than the head. This agrees with experimental and analytical results, but is not generally valid for all parameters. Increased air entrainement is indicated, which effects not only the tail but the whole blob.

References

1. Nathana, G.J., Mia, J., Alwahabib, Z.T., Newbolda, G.J.R., Nobesa, D.S.: Impacts of a jet's exit flow pattern on mixing and combustion performance. Progress in Energy and Combustion Science 32, 496–538 (2006)
2. Joshi, A., Schreiber, W.: An experimental examination of an impulsively started incompressible turbulent jet. Experiments in Fluids 40, 156–160 (2006)
3. Tanaka, Y.: On the Structure of Pulsed Jet. Bull. JSME 27, 1667–1674 (1984)
4. Bremhorst, K., Hollist, P.G.: Velocity Field of an Axisymmetric Pulsed, Subsonic Air Jet. AIAA 28, 2043–2049 (1990)
5. Johari, H., Paduano, R.: Dilution and mixing in an unsteady jet. Experiments in Fluids 23, 272–280 (1997)
6. Doudou, A.: Turbulent flow study of an isothermal diesel spray injected by a common rail system. Fuel 84, 287–298 (2005)
7. Pastor, J.V., López, J.J., García, J.M., Pastor, J.M.: A 1D model for the description of mixing-controlled inert diesel sprays. Fuel 87, 2871–2885 (2008)
8. Musculus, M.P.B., Kattke, K.: Entrainment Waves in Diesel Jets. In: SAE, vol. 01(1355) (2009)
9. Musculus, M.P.B.: Entrainment waves in decelerating transient turbulent jets. Journal of Fluid Mechanics 638, 117–140 (2009)
10. Lörstad, D., Fuchs, L.: High order surface tension VOF-model for 3D bubbly flows with high density ratio. Journal of Computational Physics 200, 153–176 (2004)

DNS of Stable Spatially-Developing Turbulent Thermal Boundary Layers under Weak Stratification

Guillermo Araya, Luciano Castillo, and Kenneth Jansen

Abstract. Direct Numerical Simulations (DNS) of spatially-developing turbulent thermal boundary layers under stratification are performed. It is well known that the transport phenomena of the flow is significantly affected by buoyancy, particularly in urban environments where neutral, stable and unstable atmospheric boundary layers are encountered. In the present investigation, the Dynamic Multi-scale approach (DMA) by Araya *et al.* [3] for turbulent inflow generation is extended to thermally stratified boundary layers. Furthermore, the proposed DMA is based on the original rescaling-recycling method by Lund *et al.* [12]. The two major improvements are: (i) the utilization of different scaling laws in the inner and outer parts of the boundary layer to better absorb external conditions such as inlet Reynolds numbers, streamwise pressure gradients, buoyancy effects, etc. ([4]), (ii) the implementation of a dynamic approach ([3]) to compute scaling parameters from the flow solution without the need of empirical correlations for the friction velocity and friction temperature as in Lund *et al.* [12] and Kong *et al.* [11], respectively.

1 Introduction

Stratification mainly occurs in a natural setting and possesses significant consequences on key areas such as wind energy, urban aerodynamics, pollen/contaminant dispersion to name a few. Furthermore, stable conditions are reached whenever the bottom surface is colder than the freestream air. In addition, under stable conditions, turbulence is generated by shear and destroyed by negative buoyancy and viscosity. Therefore, the strength of turbulence in the stable boundary layer (SBL) is much

Guillermo Araya · Luciano Castillo · Kenneth Jansen
Department of Mechanical Engineering, National Wind Resource Center,
Texas Tech University, Lubbock, TX, 79409, USA
e-mail: araya@mailaps.org

Luciano Castillo
University of Colorado at Boulder, Boulder, CO 80309, USA

A. Talamelli et al. (eds.), *Progress in Turbulence V*,
Springer Proceedings in Physics 149,
DOI: 10.1007/978-3-319-01860-7_26,

weaker in comparison to the neutral and unstable boundary layers [8]. As a result, the stable boundary layer is also much thinner and characterized by smaller eddy motions, as a consequence field measurements and numerical simulations (LES) have found enormous difficulties [6]. Actually, this problem of SBL is indeed very similar to boundary layers under favorable pressure gradients (FPG) in which the external pressure gradient reduces the large scales of turbulence, and, thus the production of the turbulent kinetic energy and shear Reynolds stresses are diminished as well [2]. Finally, in the present investigation we have focused on stable conditions and by means of extensive and highly accurate DNS, we have tried to shed some light on the physical aspects of stable boundary layers.

2 The Dynamic Multi-scale Approach (DMA)

Araya *et al.* [3] introduced an improved version of the rescaling-recycling method by Lund *et al.* [12], originally devised only for zero pressure (ZPG) flows. The DMA considers different scaling laws in the inner and outer zones of the boundary layer, therefore, different external conditions such as streamwise pressure gradients, Reynolds numbers and stratification can be better absorbed. Table 1 shows the proposed thermal scaling laws used for the thermal boundary layers and successfully employed in [4]. Moreover, these thermal scaling laws have been obtained by performing a similarity analysis over the governing equations of the flow [13]. Furthermore, Table 2 depicts the velocity scaling functions considered in the proposed turbulent inflow generation method base on the equilibrium similarity by [9] (referred henceforth as GC97) and the classical scales. The GC97 scaling laws have already been tested in [1] and [3] in the rescaling process with high quality results including higher order statistics. It can be observed that different scales are used by GC97 in the inner and outer regions contrary to the classical approach, which is based on a single scaling, mainly the friction velocity, u_τ. Furthermore, the corresponding length scales are $y^+ = yu_\tau/\nu$ (inner) and $\bar{y} = y/\delta$ (outer) in the GC97 and classical approaches of Table 2. It is worth noting that the proposed inflow generation method has been developed in such a way to apply any other scaling laws from the literature. Thus, the method is very versatile and can be easily expanded to absorb other external conditions, such as compressibility and freestream turbulence.

Table 1 Thermal scaling functions

Variable	**Type**	**Proposed Scaling**			
		Inner		Outer	
		Length scale	T_{si} and T'_{si}	Length scale	T_{so} and T'_{so}
$\overline{\Theta}$	Mean temp.	$y_T^+ = \frac{yU_\infty}{\nu}\sqrt{S_t}$	$Pr\sqrt{S_t}(\Theta_w - \Theta_\infty)$	$y_T = \frac{y}{\delta_T}$	$(\Theta_w - \Theta_\infty)\frac{\delta_T}{\delta_T^*}$
θ'	Fluctuating temp.				

Table 2 Velocity scaling functions

Variable	Inner		Outer	
	Classical	Equilibrium similarity	Classical	Equilibrium similarity
$\overline{U}, u', w'$	u_τ	u_τ	u_τ	U_∞
$\overline{V}, v'$	U_∞	u_τ	U_∞	$U_\infty d\delta/dx$

In order to calculate the friction velocity (u_τ) and fiction temperature (Θ_τ) at the inlet plane, power law variations are assumed (i.e., $u_\tau/U_\infty \sim Re_\delta^\gamma$ and $\Theta_\tau/\Theta_\infty \sim Re_{\delta_T}^{\gamma_T}$). At each timestep, γ and γ_T are computed dynamically based on the mean flow solution downstream. As a consequence, there is no need for empirical correlations as in the Lund's method [12]. The reader is referred to [3] for details and method validation in turbulent boundary layers without buoyancy.

3 Numerical Details

Figure 1 shows a schematic of the thermal boundary layer with the corresponding inner and outer regions. DNS of the Navier-Stokes and heat transfer equations for incompressible attached flows have been performed in momentum/thermal spatially-developing boundary layers. Isothermal conditions are prescribed at the wall for the temperature field. The Boussinesq approximation is used to model buoyancy along the wall-normal direction in the momentum equation. Two ZPG cases are simulated in this paper: neutral and stable. For the neutral case, the momentum thickness Reynolds number (Re_θ) range is 2600-2987 while 2993-3610 for the stable case. The bulk Richardson number ($Ri_\theta = g\beta\theta(\Theta_\infty - \Theta_w)/U_\infty^2$) is zero in the neutral case and 0.001 in the stable case. The idea of imposing a low Richardson number is to analyze the effects of weak stratification in the boundary layer. Furthermore, the initial conditions for the stable case are prescribed from the neutral case. In addition, domain dimensions ($L_x^+ = 7421, L_y^+ = 2330, L_z^+ = 1153$), mesh resolution ($\Delta x^+ = 18.6, \Delta y^+_{min} = 0.46, \Delta y^+_{max} = 18.6, \Delta z^+ = 9.3$) and number of grid points ($N_x = 400, N_y = 150, N_z = 125$) in the stable case are very similar than those of the neutral case, whose grid resolution and domain dimension suitability have been demonstrated in Araya *et al.* [3].

The local gradient Richardson number ($Ri_l = g\beta(\partial\Theta/\partial y)/(\partial U/\partial y)^2$) is shown in Fig. 2 at Re_θ = 3200 for the stable case. As observed, the gradient Ri_l is lower than the critical value of 0.25 in most of the boundary layer, except at the edge of the boundary layer. Furthermore, the Ri_l follows a linear increasing trend from the wall up to $y^+ \approx 50$, where $Ri_l \approx 0.01$. Therefore, the level of stratification introduced in the near wall region is low; however, significant decreases of the skin friction (C_f) and Stanton number (S_t) are seen for the stable case in figs. 3 (a) and 3 (b), respectively. In other words, under stable conditions, the flow tends to laminarize and the heat transfer between the wall and the flow is much poorer than that of the neutral case. Comparable behaviors of the C_f and S_t have been reported by

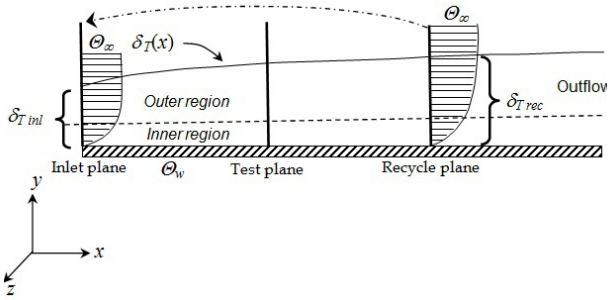

Fig. 1 Schematic of the thermal boundary layer with different regions

Araya *et al.* [5] for DNS in a turbulent channel under local blowing at the wall. This may reveal that in a turbulent boundary layer under stable conditions, the low speed streaks in the near wall region are pushed up due to buoyancy, which provokes the skin friction reduction. However, further investigation should be carried out to confirm it.

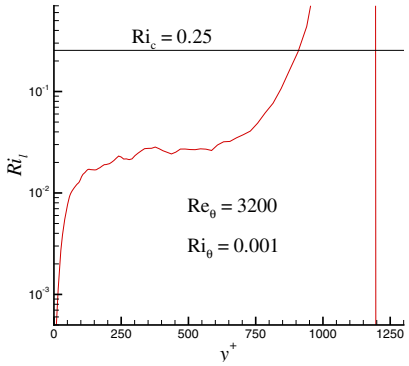

Fig. 2 Local Richardson number along y^+

Moreover, the effects of weak buoyancy can be appreciated far from the wall, as well: the Reynolds normal stresses in outer units show a decrease when stable conditions are applied (see Fig. 4). However, the most meaningful reductions (up to 17%) can be observed in the Reynolds shear stresses in Fig. 5 (a) and the wall-normal turbulent heat fluxes in Fig. 5 (b). Similar findings have been obtained by Hattori *et al.* [10] at much lower Reynolds numbers. Notice the good agreement of present DNS in the neutral case (without buoyancy) with experimental data by DeGraaff & Eaton [7] at $Re_\theta = 2900$. Figure 6 shows iso-contours of instantaneous

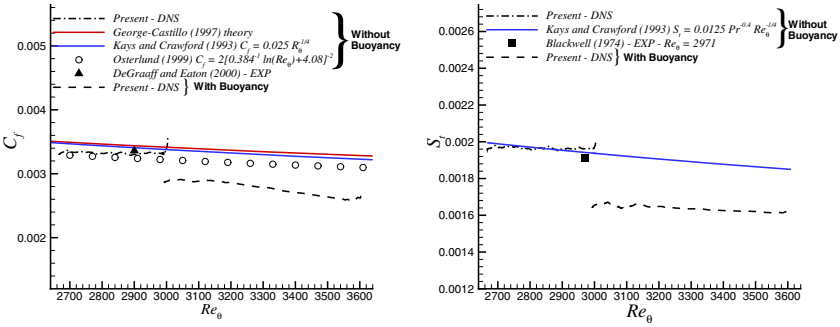

(a) (b)

Fig. 3 Skin friction (a) and Stanton numbers (b) along the streamwise direction

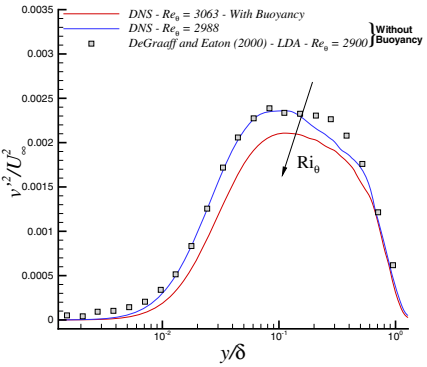

Fig. 4 Reynolds normal stresses in outer units

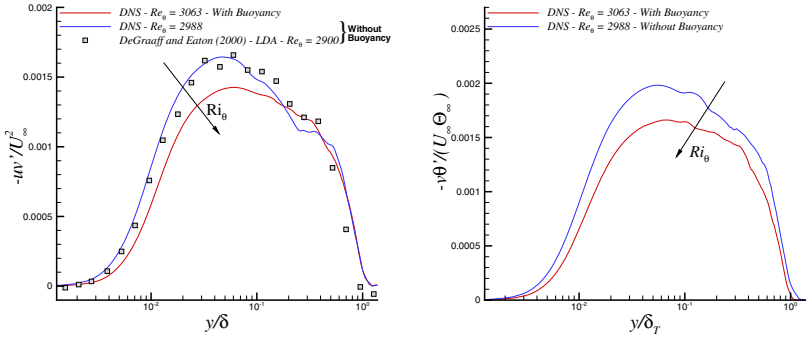

(a) (b)

Fig. 5 Reynolds shear stresses (a) and wall-normal turbulent heat fluxes (b) in outer units

temperature fluctuations at $y^+ \approx 5$ for the neutral and stable cases in the near wall region. It is observed that the stable condition provokes a suppressing effect on the high temperature streaks (i.e., high speed streaks) in spite of the weak level of stratification imposed. A similar behavior has been observed for FPG flows [2].

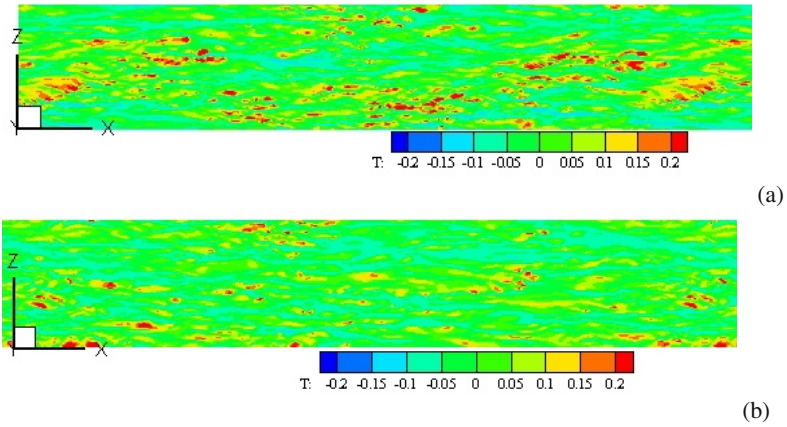

Fig. 6 Iso-contours of temperature fluctuations at $y^+ \approx 5$ for: (a) neutral and (b) stable conditions

4 Final Remarks

A Dynamic Multi-scale Approach (DMA) is introduced to generate realistic turbulent inflow conditions at the inlet of a computational domain in stable boundary layers. Present DNS have demonstrated significant modifications in the near wall region despite the weak stratification level introduced. The most significant effects of stratification have been identified as decreases of Reynolds shear stresses and wall-normal turbulent heat fluxes (up to 17%) for a bulk Richardson number of 0.001.

References

1. Araya, G., Jansen, K., Castillo, L.: Inlet condition generation for spatially-developing turbulent boundary layers via multi-scale similarity. Journal of Turbulence 10(36), 1–33 (2009)
2. Araya, G., Cal, R.B., Castillo, L.: Energy budget analysis for favorable pressure gradient turbulent boundary layers using Direct Numerical Simulations. In: 8th ERCOFTAC Symposium on Eng. Turbulence Modelling and Measurement, Marseille, France (2010)
3. Araya, G., Castillo, L., Meneveau, C., Jansen, K.: A dynamic multi-scale approach for turbulent inflow boundary conditions in spatially evolving flows. J. of Fluid Mechanics 670, 518–605 (2011)

4. Araya, G., Castillo, L.: DNS of turbulent thermal boundary layers up to $Re_\theta = 2300$. Int. Journal of Heat and Mass Transfer 55(15-16), 4003–4019 (2012)
5. Araya, G., Leonardi, S., Castillo, L.: Steady and time-periodic blowing/suction perturbations in a turbulent channel flow. Physica D 240, 59–77 (2011)
6. Basu, S., Porte-Agel, F.: Large-Eddy Simulation of Stably Stratified Atmospheric Boundary Layer Turbulence: A Scale-Dependent Dynamic Modeling Approach. J. of the Atmospheric Sciences 63, 2074–2091 (2005)
7. DeGraaff, D.B., Eaton, J.K.: Reynolds-number scaling of the flat-plate turbulent boundary layer. J. of Fluids Mechanics 422, 319–346 (2000)
8. Garratt, J.R.: The atmospheric boundary layer. Cambridge University Press (1992)
9. George, W.K., Castillo, L.: Zero-pressure-gradient turbulent boundary layer. Appl. Mech. Rev. 50, 689–729 (1997)
10. Hattori, H., Houra, T., Nagano, Y.: Direct numerical simulation of stable and unstable turbulent thermal boundary layers. Int. Journal of Heat and Fluid Flow 28, 1262–1271 (2007)
11. Kong, H., Choi, H., Lee, J.: Direct numerical simulation of turbulent thermal boundary layers. Physics of Fluids 12(10), 2555–2568 (2000)
12. Lund, T.S., Wu, X., Squires, K.D.: Generation of turbulent inflow data for spatially-developing boundary layer simulations. J. Comp. Phys. 140, 233–258 (1998)
13. Wang, X., Castillo, L.: Asymptotic solutions in forced convection turbulent boundary layers. J. of Turbulence 4, 1–18 (2003)

An Experimental Study of a Rotating-Disk Turbulent Boundary-Layer Flow

Shintaro Imayama, R.J. Lingwood, and P. Henrik Alfredsson

Abstract. The azimuthal velocity distribution in a turbulent boundary layer (TBL) on a rotating disk is explored using hot-wire anemometry and compared with those of the two-dimensional TBL over a flat plate.

1 Introduction

The turbulent boundary layer on a rotating disk (RDTBL) in an otherwise quiescent fluid has a three-dimensional velocity distribution with an inflection point in the radial component. The aim of this study is to investigate both the mean and fluctuating azimuthal velocity distribution using hot-wire anemometry and to compare these distributions with those of the two-dimensional TBL (2DTBL) over a flat plate.

The rotating-disk experimental set-up was identical to the one used by ref. [1], see their figure 1. A hot-wire probe, with a single sensor made of platinum, is operated by a constant temperature anemometer (CTA) with an overheat ratio of 0.8. The sensor has a diameter of 1.3 μm and its length (L^*) is 0.3 mm. The signal from the CTA is digitalized by a 16 bit A/D converter at a sampling rate of 2880 data points per disk rotation during a sampling time of 60 seconds.

The location of the hot-wire sensor with respect to the disk surface is obtained through a comparison with a gauge block with height 1.000 mm put next to the sensor (figure 1(a)). The calibration of the hot wire is performed using the laminar velocity profile however the highest velocity calibration datum for the TBL is obtained by extrapolating the anemometer voltage to the wall (figure 1(b)). A typical hot-wire calibration curve obtained by using various rotational speeds and heights is shown in figure 1(c). The calibration data are fitted by a fourth-order polynomial, resulting in a deviation of less than $\pm 1.0\%$ except in the very low velocity region.

Shintaro Imayama · R.J. Lingwood · P. Henrik Alfredsson
Linné Flow Centre, KTH Mechanics, SE-100 44 Stockholm, Sweden
e-mail: {shintaro,lingwood,phal}@mech.kth.se

R.J. Lingwood
University of Cambridge, Cambridge, CB23 8AQ, UK

A. Talamelli et al. (eds.), *Progress in Turbulence V*,
Springer Proceedings in Physics 149,
DOI: 10.1007/978-3-319-01860-7_27,

Table 1 Experimental conditions and DNS data. T01 and T02 are the two experimental profiles presented here. 2D01 and 2D02 are profiles for a 2DTBL flow taken from ref. [3]. $R = r^*(\Omega^*/\nu^*)^{1/2}$, where r^* is the radius of the disk at the measurement position, Ω^* is the rotational speed of the disk, and ν^* is the kinematic viscosity of the fluid. The Reynolds number based on friction velocity is defined as $Re_\tau = v_\tau^* \delta_{99}^* / \nu^*$, where v_τ^* is the friction velocity and δ_{99}^* is defined as the height the velocity is 1% of V_w^*. δ_{95}^* corresponds to the height where the velocity is 5% of V_w^*. The Reynolds number based on momentum loss thickness δ_2^* is defined as $Re_\theta = V_w^* \delta_2^* / \nu^*$. H is the shape factor $H = \delta_1^*/\delta_2^*$, where δ_1^* is the displacement thickness. The skin friction is defined as $c_f = 2(v_\tau^*/V_w^*)^2$. The viscous length is defined as $\ell^* = \nu^*/v_\tau^*$ and the non-dimensional hot-wire length $L^+ = L^*/\ell^*$.

Case	R	Re_τ [-]	Re_θ [-]	r^* [mm]	V_w^* [m/s]	δ_{99}^* [mm]	$\delta_{95}^*/\delta_{99}^*$ [-]	δ_1^* [mm]	δ_2^* [mm]	H [-]	v_τ^* [m/s]	c_f [-]	ℓ^* [μm]	L^+ [-]
T01	668	885	1714	210	32.0	9.3	0.60	1.08	0.81	1.34	1.43	0.00399	10.5	28.6
T02	698	1011	1935	220	33.5	10.4	0.59	1.16	0.87	1.33	1.46	0.00380	10.3	29.2
2D01		492	1420				0.78			1.43		0.00388		
2D02		974	3032				0.78			1.40		0.00319		

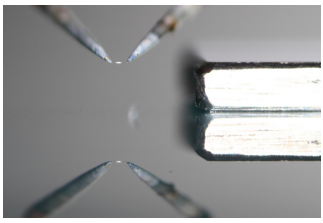

(a)

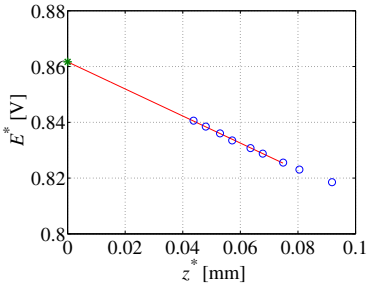

(b)

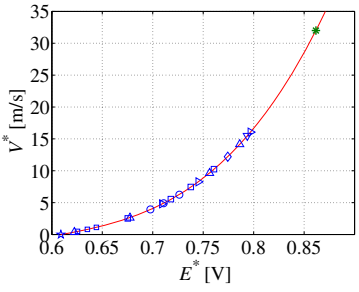

(c)

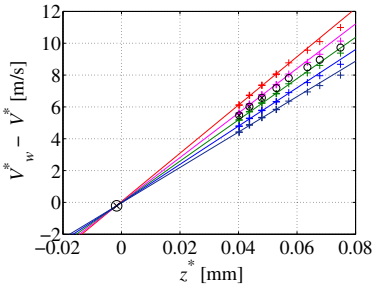

(d)

Fig. 1 Details of the procedure of the hot-wire calibration and wall shear stress determination. (a) hot-wire height calibration, (b) estimation of wall voltage ($*$) using TBL profile near-wall region, (c) hot-wire calibration curve including the estimated wall voltage ($*$), (d) wall position estimation.

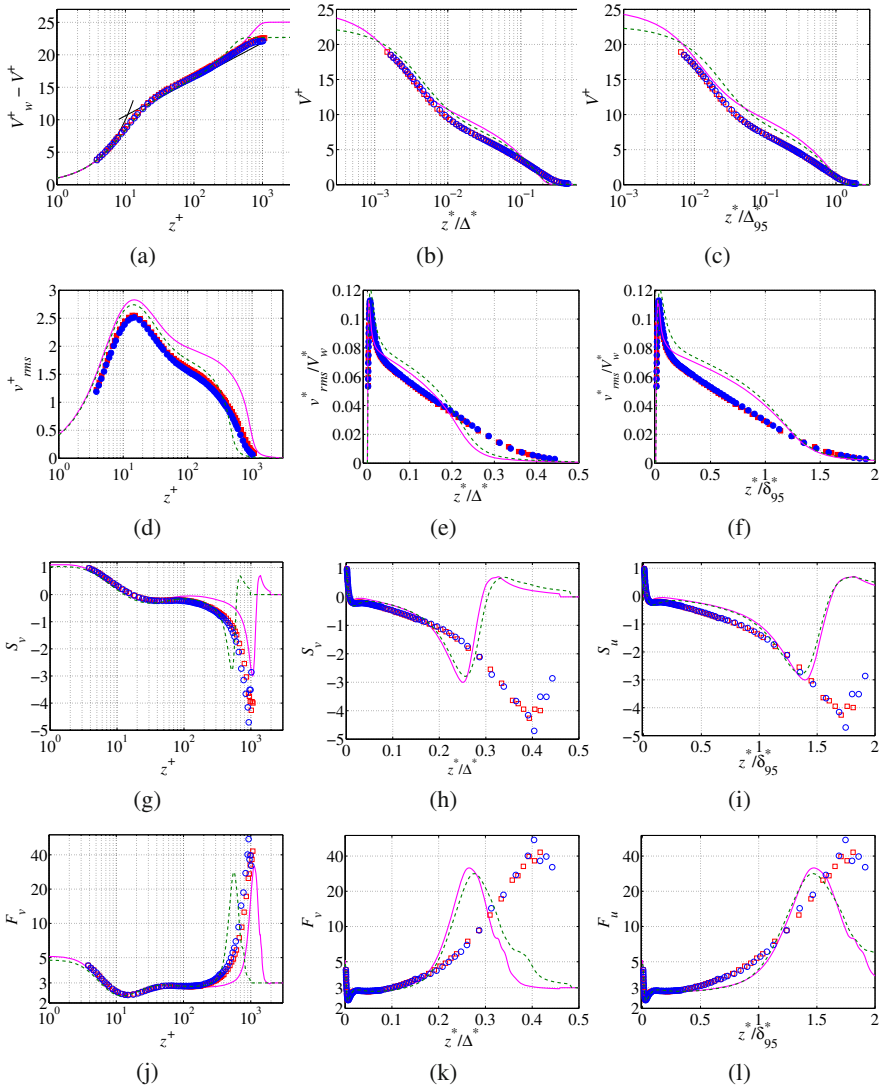

Fig. 2 Mean, rms, skewness and flatness profiles versus wall-normal distance (z) scaled by the inner scale (ℓ^*), Rotta-Clauser boundary-layer thickness defined as $\Delta^* = \delta_1^* V_w / v_\tau^*$ and boundary layer thickness, where the symbols and lines indicate T01 (◯), T02 (□), 2D01 (dashed line) and 2D02 (solid line), respectively. V^+ is the non-dimensional azimuthal mean velocity given as $V^+ = V^*/v_\tau^*$. The straight line corresponds to the logarithmic law with the Kármán constant $\kappa = 0.41$ and logarithmic intercept of 5.0. v_{rms}^+ is the non-dimensional intensity of the velocity fluctuation ($v_{rms}^+ = v_{rms}/v_\tau^*$) with spatial resolution corrections to the data from the hot-wire probe in RDTBL. S_v and F_v are the skewness and flatness of the velocity fluctuations given as $S_v = \overline{v^{*3}}/v_{rms}^{*3}$ and $F_v = \overline{v^{*4}}/v_{rms}^{*4}$, respectively, where the overline indicates the averaging. The skewness in T01 and T02 is multiplied by -1.

2 Results and Discussions

The azimuthal friction velocity is estimated by measuring the velocity distribution in the near-wall region. Ref. [2] has shown that the cumulative distribution functions (CDF) of the fluctuating streamwise velocity in 2DTBL is self-similar in the viscous sublayer. Figure 1(d) presents the mean azimuthal velocity profile in the near-wall region with five different values of the CDF, namely 0.2, 0.3, 0.4, 0.5 and 0.6. The self-similar behaviour makes the extrapolated lines meet at the position of the wall and the estimated wall position indicated by $\otimes$, shows an error of about 2 μm and less than 1 % in the velocity. Then the azimuthal wall-shear stress is calculated by the slope of the velocity profile in the self-similar region. In contrast to the velocity profile in figure 9 in ref. [2] where heat conduction to the wall gives too high readings, figure 1(d) shows no increase of the mean velocity near the wall, indicating that wall interference is negligible here. Since heat convection from the sensor is high due to the high velocities near the disk, the effect of heat conduction to the wall is negligible, indicating that the main problem of hot-wire measurement close to a stationary wall is heat conduction rather than, e.g. blockage by the hot-wire probe.

In figure 2, a comparisons between the RDTBL and the 2DTBL for the mean, rms, skewness and flatness distributions are shown using three different length scales, the inner scale, Rotta-Clauser and the 95% boundary-layer thickness (for specifications of the cases see table 1). The two flows show nice agreement in inner-scaling for the inner layer (figure 2(a, g, j)) except for the rms profiles (figure 2(d)) despite with spatial resolution corrections of the hot-wire probe by ref. [5]. However differences between the two flows are clearly observed in the outer region where there is no obvious wake component (figure 2(a), also pointed out by ref. [4]), much smaller rms (figure 2(d)) and larger values of both skewness and flatness (figure 2(g,j)) for the RDTBL. The almost linear decrease of v^*_{rms}/V^*_w with z^*/δ^*_{95} shown in figure 2(f) in the region $0.1 < z^*/\delta^*_{95} < 1.0$ is in agreement with ref. [6]. It is clear that neither the Rotta-Clauser boundary-layer thickness nor δ^*_{95} are appropriate outer scales to compare with 2DTBL.

Acknowledgement. This work is supported by the Swedish Research Council.

References

1. Imayama, S., Alfredsson, P.H., Lingwood, R.J.: A new way to describe the transition characteristics of a rotating-disk boundary-layer flow. Phys. Fluids 24, 031701 (2012)
2. Alfredsson, P.H., Örlü, R., Schlatter, P.: The viscous sublayer revisited–exploiting self-similarity to determine the wall position and friction velocity. Exp. Fluids 51, 271–280 (2011)
3. Schlatter, P., Örlü, R.: Assessment of direct numerical simulation data of turbulent boundary layers. J. Fluid Mech. 659, 116–126 (2010)
4. Littell, H.S., Eaton, J.K.: Turbulence characteristics of the boundary layer on a rotating disk. J. Fluid Mech. 266, 175–207 (1994)
5. Smits, A.J., Monty, J., Hultmark, M., Bailey, S.C.C., Hutchins, N., Marusic, I.: Spatial resolution correction for wall-bounded turbulence measurements. J. Fluid Mech. 676, 41–53 (2011)
6. Itoh, M., Hasegawa, I.: Turbulent boundary layer on a rotating disk in infinite quiescent fluid. JSME Int. J. 37, 449–456 (1994)

DNS of Rotating Turbulent Plane Poiseuille Flow in Low Reynolds- and Rotation-Number Ranges

Takahiro Ishida, Takahiro Tsukahara, and Yasuo Kawaguchi

Abstract. We performed a series of direct numerical simulation (DNS) of the rotating turbulent channel flow in low Reynolds-number and rotation-number ranges, in order to investigate presence or absence of turbulent stripe, i.e., large-scale laminar-turbulent banded pattern, in the rotating Poiseuille flow and to elucidate the transitional process in terms of structures including longitudinal roll cells induced by the Coriolis force. As a result, we found that the turbulent stripe occured only in flows with weak (or no) spanwise system rotations and coexisted with the roll cell under a limited condition. We investigated relationships between the dominant-structure alterations and the changes of rotation-number dependencies of statistics.

1 Introduction

Turbulent Poiseuille flow with spanwise system rotation includes the suction side and the pressure side, where turbulence would be either attenuated or enhanced. In the suction side, where the system rotation has the same direction as the vorticity of the mean shear, the flow becomes stable or sometimes laminarized. In the pressure side, where their directions are opposite to each other, the Coriolis force may give rise to roll cells (RC). The structure of RC is an array of large-scale longitudinal vortices aligning in the spanwise direction with regularity [1]. It has been known that the spanwise size of a counter-rotating vortex pair in RC is 4–6δ and 2–3δ (δ, the channel half width) for the plane Couette and Poiseuille flows, respectively, under spanwise system rotations. Figure 1(a) shows a diagram of RC that occurs in a channel. Black and gray cylinders in the figure represent longitudinal vortices, which rotate in the clockwise and counter-clockwise directions, respectively.

Reducing the Reynolds number from a fully-developed turbulent flow, the large-scale structure named 'turbulent stripe' (TS) was found to occur spontaneously by

Takahiro Ishida · Takahiro Tsukahara · Yasuo Kawaguchi
Tokyo University of Science, Noda, Chiba 278-8510, Japan
e-mail: {j7512609,tsuka,yasuo}@ed.tus.ac.jp

A. Talamelli et al. (eds.), *Progress in Turbulence V*,
Springer Proceedings in Physics 149,
DOI: 10.1007/978-3-319-01860-7_28,

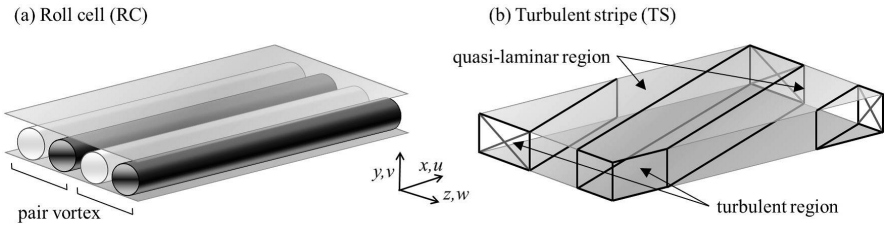

Fig. 1 Diagrammatic illustrations of large-scale organized structures in plane channel flows

recent studies. The structure of TS consists of large-scale turbulent and (quasi-) laminar bands, which incline at a certain degree to the streamwise direction. The stream- and spanwise wavelengths of a pattern of TS were reported as $\lambda_x^+ \approx 5000$ and $\lambda_z^+ \approx 2000$, respectively, in the plane Poiseuille flow at $\mathrm{Re}_\tau = 80$ based on the friction velocity u_τ and the channel half width δ [2, 3], although those wavelengths might be influenced by the finite-length calculation domain with periodic boundaries. Figure 1(b) schematically illustrates the structure of a single band of TS captured in the minimal domain, showing an elongation of a turbulent band in the diagonal direction of the domain. In the turbulent region, there occur low- and high-speed streaks and fine-scale vortices, while they are almost absent in the quasi-laminar region. According to previous studies, TS would be considered as a common state during the transitional regime in various flow systems: such as plane Poiseuille flow and plane Couette flow [3, 4]. In particular, the stabilizing rotation allows TS in the plane Couette flow to persist in a wider range of the Reynolds number [5]. In the rotating plane Poiseuille flow (RPPF), an occurrence of TS has not been reported in any Reynolds number, because RC in the pressure side was dominant [6]. We speculate TS would occur in the suction (stable) side in RPPF. Therefore, we investigate presence or absence of TS in RPPF and elucidate the transitional process in terms of structures including TS and RC, by means of direct numerical simulation (DNS).

2 Numerical Procedures

The incompressible-fluid channel flow we consider here is driven by a uniform pressure gradient in x and subjected to a positive system rotation along the spanwise (z) axis with an angular velocity Ω. Hence, the pressure and suction sides are bottom- and top-side halves of the channel, respectively. Strictly speaking, a border between stabilized and destabilized regions should be demarcated based on the Bradshaw number, $\mathrm{Br} = S(S+1)$, where $S = 2\Omega/(-\mathrm{d}\overline{u}/\mathrm{d}y)$ [1, 7]. In this study, we decided to simply define the border of two regions at the channel center, since the maximum of the mean velocity $\overline{u}$ did not significantly change in height because of low rotation numbers. The periodic boundary conditions are imposed in the x and z directions and the non-slip condition is applied on the wall surface. The fundamental equations are the equation of continuity and the following Navier-Stokes equation:

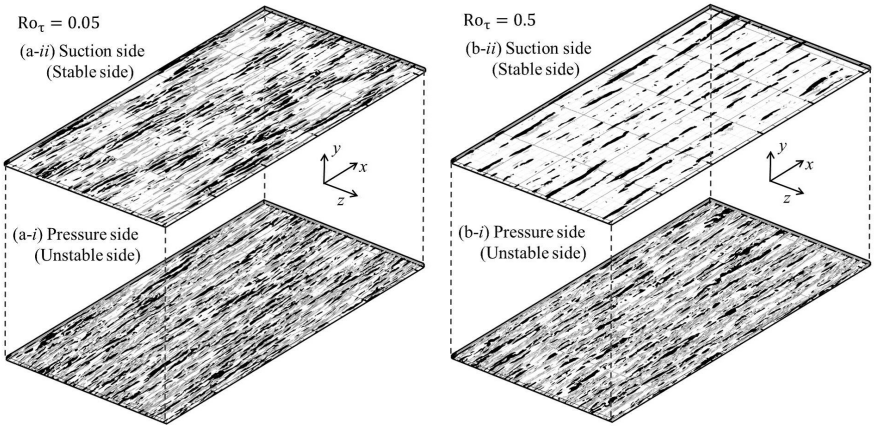

Fig. 2 Visualization of instantaneous flow fields at $\mathrm{Re}_\tau = 80$ for (a) $\mathrm{Ro}_\tau = 0.05$, (b) $\mathrm{Ro}_\tau = 0.5$. For each figure, (i) and (ii) show the stable and the unstable sides, respectively. Black isosurface, $u'^+ > 3$; gray, $u'^+ < -3$. The mean flow moves from bottom-left to top-right.

$$\frac{\partial u_i^+}{\partial t^*} + u_j^+ \frac{\partial u_i^+}{\partial x_j^*} = -\frac{\partial p^+}{\partial x_i^*} + \frac{1}{\mathrm{Re}_\tau} \frac{\partial^2 u_i^+}{\partial x_j^* \partial x_j^*} - \mathrm{Ro}_\tau \varepsilon_{i3k} u_k^+ \tag{1}$$

Note that the superscripts of $+$ and $*$ indicate the quantities normalized by the wall units and the outer scale, respectively, and ε_{ijk} means the Eddington's epsilon. The finite difference method was adopted for the spatial discritization. For the time integration, the second-order Crank-Nicolson and Adams-Bashforth schemes were used for the wall-normal (y) viscous term and the other terms, respectively.

A series of DNS has been made for $\mathrm{Re}_\tau = 54$–80 and $\mathrm{Ro}_\tau = 2\Omega\delta/u_\tau = 0.0$–$1.5$. We employed a large computational domain of $102.4\delta \times 2\delta \times 51.2\delta$ with grids of $2048 \times 192 \times 1024$ in the x, y, and z directions. The present domain size was chosen to capture several bands of TS, according to the earlier DNS results. Indeed, three or four TS bands were observed to exist stably, as described in the following section.

3 Results and Discussion

Some examples of three-dimensional visualization of instantaneous flow fields at $\mathrm{Re}_\tau = 80$ are given in Fig. 2, where each side is separately shown. Note that the field presented in (a) is obtained for a low rotation number of $\mathrm{Ro}_\tau = 0.05$, while that in (b) is for a relatively high value of $\mathrm{Ro}_\tau = 0.5$. Here, the isosurfce values of the streamwise velocity fluctuations are set at $u'^+ = \pm 3$, so that it allows us to extract streaky structures in the near-wall regions clearly. From observation of their distributions in instantaneous fields, we can detect the structures of TS and RC. For instance, if a focus is placed on the suction side shown in Fig. 2(a-*ii*), the streaks exhibits a spatially intermittent pattern in the field, giving rise to several

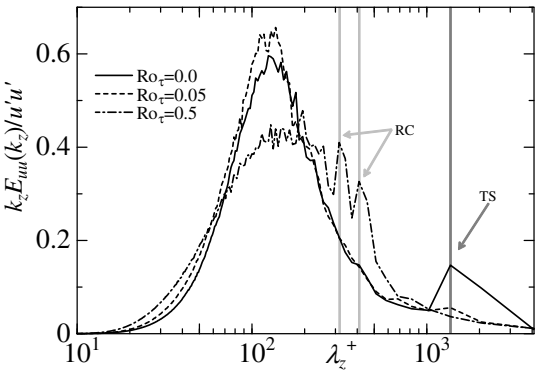

Fig. 3 Pre-multiplied energy spectra of u' as a function of spanwise wavelength (λ_z) at $y^+ = 34$ in the pressure side for $\mathrm{Re}_\tau = 80$. Note that $k_z = 2\pi/\lambda_z$.

bands of locally strong turbulence, in accordance with the result in the non-rotaing case (figure not shown). It implies that the flow in this side of channel be dominated by TS. On the other hand, we confirmed that TS occured in the RPPF and found a transitional state (in terms of the dominant structure) in the pressure side, where both TS and RC coexisted in the flow field, as shown in Fig. 2(a-*i*). Although difficult to detect from the given figure, low-speed streaks are remarkably elongated in x and probably along RC. Hereafter, such a transitional state between TS and RC as Ro_τ increases gradually is labeled as either Tr1 or Tr2. In the regime of Tr1, TS seems to be more dominant than RC, while RC is stronger than TS in Tr2. At high Ro_τ, the flow field given in Fig. 2(b) apparently involves only RC, and TS cannot be determined. The low-speed streaks are very prominent compared to high-speed ones in the pressure side (b-*i*), because ejecting fluid motions due to RC are enhanced, whereas sweeping motions from the core region are relatively weak. In the suction side (b-*ii*), the flow should be stabilized by the Coriolis force and so the streaks observed in this side might be induced passively by RC in the pressure side, resulting in the dominancy of high-speed streaks in the suction (stable) side.

In the present study, we have determined the dominant structure on the basis of flow visualizations (as like Fig. 2) and statistics. Figure 3 represents spanwise pre-multiplied energy spectra of u' in the buffer layer of the pressure side, for different rotation numbers. In this spectrum, a wavelength giving a peak/spike represents the spacing of an energetic structure. That is, we can quantitatively determine the dominant structure in the flow field from this plot. In particular, Fig. 3 shows that the primary peak in the spectra has been taken at $\lambda_z^+ \approx 100$, corresponding to the well-known spacing of the near-wall streaky structures. It can be clearly seen that there exists an additional peak at $\lambda_z^+ = 1500$, which indicates the spanwise spacing of the TS patterns, for $\mathrm{Ro}_\tau = 0$ and 0.05, but the peak is obviously damped in the latter case. At $\mathrm{Ro}_\tau = 0.5$, such a peak in $\lambda_z^+ > 10^3$ completely disappears and several spikes exist in a range of $\lambda_z^+ = 300$–400, which should be relevant to RC. Although not presented, the streamwise wavelength of TS has been detected at $\lambda_x^+ = 4100$.

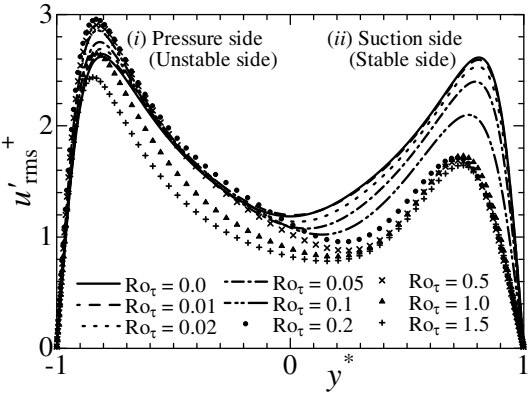

Fig. 4 Rotation-number dependency of streamwise turbulent intensity (root-mean-square of streamwise velocity fluctuation) at $\mathrm{Re}_\tau = 80$

On the basis of the present DNS results, we have classified various turbulent states about each side. As the rotation number Ro_τ is increased from stationary with a fixed Reynolds number in the present range of $\mathrm{Re}_\tau = 54$–80, the state of turbulent flow changes gradually, revealing a transitional process of TS→Tr1→Tr2→RC both for the suction side and the pressure side. If an emphasis is placed on the scenario observed at $\mathrm{Re}_\tau = 80$, the rotation numbers at which the respective structure transitions arise in the pressure side are $\mathrm{Ro}_\tau = 0.02$ (for TS→Tr1), 0.05 (for Tr1→Tr2), and 0.1 (for Tr2→RC). As for the suction side, each transition is found to be delayed to somewhat higher values: for instance, $\mathrm{Ro}_\tau = 0.05$ for TS→Tr1, and 0.2 for Tr2→RC. Therefore, any footprint of TS cannot be detected even in the stable side of RPPF at $\mathrm{Ro}_\tau \geq 0.2$. We found that the dependencies on the rotation number described above were more or less unchanged for $\mathrm{Re}_\tau = 54$–80, although TS in $\mathrm{Re}_\tau = 54$ clearly remained in both channel halves even for slightly higher Ro_τ.

It is interesting to note that the transitional values with respect to Ro_τ, at which the dominant structure changes from TS to Tr1 or from Tr2 to RC, correspond to those with respect to the statistics described in the following. Although figures are not shown, the wall-normal profile of the mean velocity become unchanged practically for $\mathrm{Ro}_\tau \leq 0.05$, corresponding to the TS and transition states (Tr1, Tr2). Moreover, the profile becomes asymmetric and then decreases gradually for $\mathrm{Ro}_\tau \geq 0.2$ in conjunction with the appearance of RC. The wall-normal height, at which the Reynolds shear stress $-\overline{u'v'}$ is zero, shifts from the center to the suction side with increasing Ro_τ. For $\mathrm{Ro}_\tau \geq 0.2$, this height almost unchanges, maybe because RC is dominant. Figure 4 presents the root-mean-square values of the streamwise velocity fluctuation. In the suction side, u'^{+}_{rms} drastically decreases as $\mathrm{Ro}_\tau = 0 \rightarrow 0.2$, while it almost remains irrespective of Ro_τ for $\mathrm{Ro}_\tau \geq 0.2$. In the pressure side, u'^{+}_{rms} shows a trend of monotonic increase for $\mathrm{Ro}_\tau \leq 0.5$, but monotonically decreases for $\mathrm{Ro}_\tau > 0.5$ with increasing Ro_τ. It can be seen that u'^{+}_{rms} does not depend on Ro_τ, once TS disappears completely. This relationship implies that the transitional process from TS to RC significantly affects statistics.

In summary, we found that TS, which spontaneously occured in the non-rotating transitional Poiseuille flow, would remain only in flows with weak spanwise rotations which has not been reported in the literature. Moderate rotations gave rise to coexistence of TS and RC. Johnston & Halleen [1] reported RC was present for $\mathrm{Ro_m}(=2\Omega\delta/u_\mathrm{m}) > 0.04$ (u_m, the bulk mean velocity) and absent for $\mathrm{Ro_m} \leq 0.02$. In the range of $0.02 < \mathrm{Ro_m} \leq 0.04$, the flow was unsteady and sometimes RC form, decay, wash-out, and wave in a very unsteady manner. In a DNS study [7], the different numbers of RC vortices was identified by increasing rotation rates up to $\mathrm{Ro_m} = 0.2$ and 0.5, respectively, and the scale of RC tends to diminish with increasing $\mathrm{Ro_m}$. This implies that the wall-normal size of RC may change. In the present study, we observed turbulent motions that were affected by RC in the range of $0.02 < \mathrm{Ro}_\tau < 0.05$ ($0.014 < \mathrm{Ro_m} < 0.037$), but RC did not completely develop. For $\mathrm{Ro}_\tau > 0.1$ ($\mathrm{Ro_m} > 0.075$), RC develops in the whole domain. The $\mathrm{Ro_m}$-dependency of RC is consistent with the literature [1], and the dominant region of RC is in good agreement with those obtained by Krisroffersen & Andersson [7]. For $\mathrm{Ro}_\tau \geq 0.2$, TS disappeared, resulting in monotonic Ro_τ-dependencies of statistical results.

Acknowledgements. This work was supported by a KAKENHI Grant-in-Aid, #22760136. The present simulations were performed by SX-9 at Cyberscience Center, Tohoku University.

References

1. Johnston, J.P., Halleen, R.M.: Effects of spanwise rotation on the structure of two-dimensional fully developed turbulent channel flow. J. Fluid Mech. 56, 533–557 (1972)
2. Tsukahara, T., Seki, Y., Kawamura, H., Tochio, D.: DNS of turbulent channel flow at very low Reynolds numbers. In: Proc. 4th Int. Symp. Turbulence and Shear Flow Phenomena, pp. 935–940 (2005)
3. Tsukahara, T., Kawaguchi, Y., Kawamura, H., Tillmark, N., Alfredsson, P.H.: Turbulent stripe in transitional channel flow with/without system rotation. In: Proc. 7th IUTAM Symp. Laminar-Turbulent Transition. IUTAM Bookserie, vol. 18, pp. 421–426 (2010)
4. Prigent, A., Grégoire, G., Chaté, H., Dauchot, O., van Saarloos, W.: Large-scale finite-wavelength modulation within turbulent shear flows. Phys. Rev. Lett. 89, 014501 (2002)
5. Tsukahara, T., Tillmark, N., Alfredsson, P.H.: Flow regimes in a plane Couette flow with system rotation. J. Fluid Mech. 648, 5–33 (2010)
6. Iida, O., Fukudome, K., Iwata, T., Nagano, Y.: Low Reynolds number effects on rotating turbulent Poiseuille flow. Phys. Fluids 22, 085106 (2010)
7. Krisroffersen, R., Andersson, H.I.: Direct simulations of low-Reynolds-number turbulent flow in a rotating channel. J. Fluid Mech. 256, 163–197 (1993)

The Characteristics of Turbulence in Curved Pipes under Highly Pulsatile Flow Conditions

A. Kalpakli, R. Örlü, N. Tillmark, and P. Henrik Alfredsson

Abstract. High speed stereoscopic particle image velocimetry has been employed to provide unique data from a steady and highly pulsatile turbulent flow at the exit of a 90 degree pipe bend. Both the unsteady behaviour of the Dean cells under steady conditions, the so called "swirl switching" phenomenon, as well as the secondary flow under pulsations have been reconstructed through proper orthogonal decomposition. The present data set constitutes – to the authors' knowledge – the first detailed investigation of a turbulent, pulsatile flow through a pipe bend.

1 Introduction

Turbulent flow through curved pipes occurs in a number of industrial applications and has recently re-attracted the attention of scientists, mainly due to the oscillatory character of the vortices formed in a pipe bend [1–5]. Such oscillations are known to cause fatigue in piping systems. On the other hand, in some technical applications, the turbulent flow is superposed with a pulsating motion which often is of much higher frequency. This kind of flow is for example prevalent in different components of the Internal Combustion Engine (ICE) such as the exhaust manifold. Numerical simulations of such flow systems are generally favoured [6], however these need to be validated against experiments in which the main physical features of interest are captured, in order to assess the accuracy and limitations of the simulations. Studying the fundamental fluid dynamics governing the engine's functionality would lead to better understanding of the gas exchange system and consequently lead to more efficient management of the exhaust gases. However, there is barely any experimental data available in the literature when it comes to turbulent, pulsatile flow through curved pipes and existing studies are predominantly on laminar, pulsatile flows [7–9]. The present work aims at filling this gap in the literature by providing

A. Kalpakli · R. Örlü · N. Tillmark · P. Henrik Alfredsson
CCGEx & Linné Flow Centre, KTH Mechanics, SE-100 44 Stockholm, Sweden
e-mail: ramis@mech.kth.se

A. Talamelli et al. (eds.), *Progress in Turbulence V*,
Springer Proceedings in Physics 149,
DOI: 10.1007/978-3-319-01860-7_29,

2D3C (2-dimensional, 3-component) data from high-speed stereoscopic particle image velocimetry (PIV) measurements. Both a steady and a highly pulsatile turbulent flow in a generic geometry related to engine components are considered. The study provides insight into the secondary flow structures with the aid of proper orthogonal decomposition (POD). In particular, the low frequency oscillatory motion (so called "swirl switching") in steady flows as well as the secondary, in-plane motion under pulsatile flow conditions will be illuminated.

2 Experimental Set Up and Measurement Technique

The experiments were conducted in the CICERO laboratory at KTH CCGEx, a centre focussing on gas exchange research for ICE. A compressor installation facility delivers air at a maximum mass flow rate of 500 g/s at 6 bar, under either steady and pulsating flow conditions. The pulsatile motion is created by rotating a valve with its rotation rate being set by a frequency controlled AC motor. In order to ensure steady flow conditions, the mass flow rate is additionally monitored by a hot-film type mass flow meter (ABB Thermal Mass Flow meter FMT500-IG). The reader is referred to Ref. [10] for details on the CICERO laboratory, and the pulsatile flow rig.

A 90° pipe bend is connected to the pipe flow rig (see figure 1) and measurements are taken at the immediate vicinity of the bend exit. The diameter of the pipe is $D = 40.5$ mm and the curvature radius is $R_c = 51$ mm. The data presented here were acquired using high-speed stereoscopic PIV at pipe cross-sections 0.2 and 2 pipe diameters downstream the 90° pipe bend section (see figure 1). A laser light sheet of 1 mm thickness was produced by a Nd-YLF laser (Pegasus, 10 kHz maximum frequency, New Wave Research). The laser was externally triggered by the valve rotation in order to enable phase averaging of the snapshots. Two high-speed C-MOS

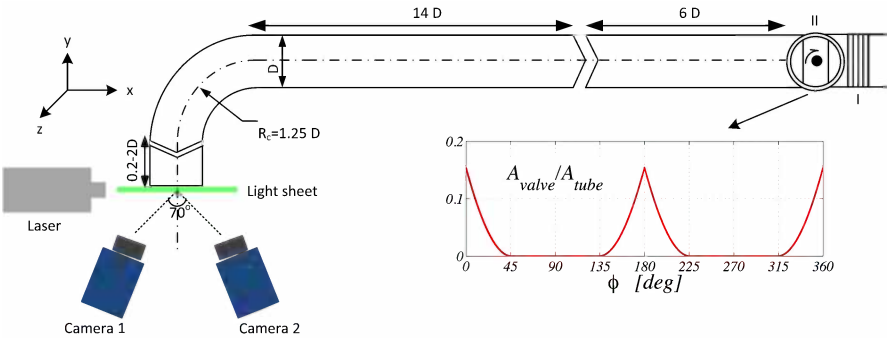

Fig. 1 Geometrical configuration used in the experiments and camera set up for the stereoscopic PIV measurements *(top view)*. Pipe diameter $D = 40.5$ mm and curvature radius $R_c = 51$ mm, I) smoke injection inlet, II) rotating valve. Insert depicts the relative open valve area change as function of the revolution angle.

cameras (Fastcam APX RS, Photron, 3000 fps at full resolution 1024×1024 pixels, 10 bit) were positioned at an angle of approximately 70° between their viewing axes (Figure 1). The 105 mm Nikon Nikkor lenses of the cameras were adjusted using a Scheimpflug adapter. The data sets consist of 1000 snapshots taken at a sampling frequency of 1 and 1.5 kHz for the steady and pulsating flow cases, respectively. The vector fields were calculated using the commercial software Davis (Lavision GmbH). A multi-pass iteration procedure was chosen for increased resolution starting with an interrogation window of 64×64 pixels and decreasing to 16×16 pixels with an overlapping area of 50%. Details of the set-up and parameters of the stereoscopic PIV measurements are documented in Ref. [11].

3 Results and Discussion

For the experiments the flow parameters used correspond to a Dean number of $De = 15 \times 10^3$, defined as the product of curvature ratio ($\gamma = D/(2R_c) = 0.4$) and Reynolds number (based on bulk velocity and D), and a Womersley number, defined through $\alpha = D/2\sqrt{\omega/\nu} = 58$ (with ω and ν denoting the angular frequency of the imposed pulsations and kinematic viscosity, respectively) in case of the pulsatile flow. Throughout this paper only POD reconstructed snapshots are shown, in order to focus on the most energetic structures, which in the present study has been been utilised mainly as an in-homogenous spatial filter. For details on the use of POD as

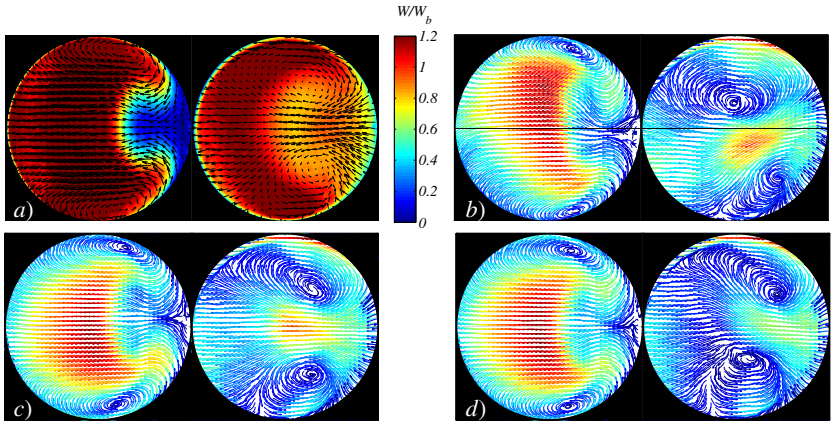

Fig. 2 *a)* Time-averaged flow field 0.2 *(left)* and 2 *(right) D* downstream the 90° pipe bend. The streamwise velocity component (scaled by the bulk speed) is shown as the contour map and the in-plane components as the vectors. The largest time-averaged in-plane velocity component is around 30 % of the bulk velocity. *b–d)* Subsequent snapshots (reconstructed by means of the first 4 POD modes) for the 0.2 *(left)* and 2 *(right) D* stations, showing the magnitude of the in-plane velocity components as the coloured vectors. Highest value (*red*) equals to 50 % of the bulk velocity.

a tool to extract large scale structures from PIV data and for a similar (steady) flow case as the one shown here the reader is referred to Ref. [5, 12].

Figure 2*a)* shows the time-averaged flow field 0.2 and 2 *D* downstream the pipe bend, with the streamwise velocity component shown as the background contour map and the in-plane components as the vectors. The mean flow fields exhibit the main characteristics of flow fields in curved pipes, i.e. the high velocity fluid in the centre of the pipe tends to move outwards, being greatly affected by centrifugal forces, while slow-moving fluid particles close to the pipe walls move inwards thereby creating a C-shaped streamwise velocity distribution. This behaviour induces two counter rotating cells, the so-called *Dean vortices*, which are apparent in the vector field and are – due to the sharp curvature of the present pipe bend – much closer located to the pipe walls than in cases with a milder curvature (cf. Ref. [3]). While previous studies in steady turbulent flow through pipe bends with milder curvature ratios have reported a low-frequency oscillatory motion of the Dean cells [1, 3, 5], such a behaviour is not apparent from the snapshots depicted in figure 2*b–d)* for the 0.2 *D* station. In fact, the instantaneous flow field resembles to a large extent its time-averaged counterpart. Further downstream, on the other hand, at the 2 *D* station, the flow starts to recover from the sharp bend as apparent from the mean streamwise velocity distribution where the Dean cells move away from the wall. In the instantaneous flow field, as observed in flows with a milder curvature ratio, the Dean cells, depict an unsteady behaviour, i.e. the Dean cells

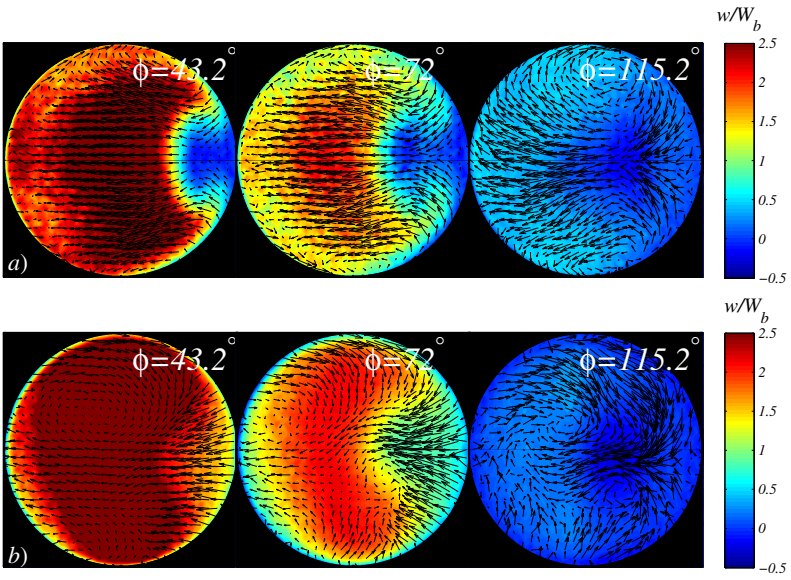

Fig. 3 Reconstructed pulsating flow field using the first 4 POD modes, *a)* 0.2 and *b)* 2 *D* downstream the bend, for three valve angles (cf. figure 1 for the relative valve area change)

"switch" between three states: a symmetric one, and two in which either the upper or lower cell appears as the dominant one.

When it comes to the pulsatile flow case, the flow field is dictated by the imposed pulsatile motion, and the aforementioned unsteady behaviour of the Dean cells is replaced by a secondary flow that is determined through the pulsatile motion. As apparent from figure 3, the highest velocity reaches around three times the bulk speed, while at the end of the deceleration phase back flow with a magnitude of almost the bulk speed sets in. The shown three different phase angles along the deceleration phase depict, that the flow is characterised by a net secondary flow from the inner to the outer wall and cell-like structures at the start and end of the deceleration phase, respectively. To the authors' knowledge, this is the first experimental investigation revealing the secondary flow pattern for a pipe bend under turbulent, pulsatile flow conditions.

Acknowledgements. This research was done within KTH CCGEx, a centre supported by the Swedish Energy Agency, Swedish Vehicle Industry and KTH.

References

1. Rütten, F., Schröder, W., Meinke, M.: Large-eddy simulation of low frequency oscillations of the Dean vortices in turbulent pipe bend flows. Phys. Fluids 17, 035107 (2005)
2. Ono, A., Kimura, N., Kamide, H., Tobita, A.: Influence of elbow curvature on flow structure at elbow outlet under high Reynolds number condition. Nuclear Eng. Design 241, 4409–4419 (2010)
3. Kalpakli, A., Örlü, R., Alfredsson, P.H.: Dean vortices in turbulent flows: rocking or rolling? J. Vis. 15, 37–38 (2012)
4. Sakakibara, J., Machida, N.: Measurement of turbulent flow upstream and downstream of a circular pipe bend. Phys. Fluids 24, 041702 (2012)
5. Kalpakli, A., Örlü, R.: Turbulent pipe flow downstream a 90 degree pipe bend with and without superimposed swirl. Int. J. Heat Fluid Flow (2013), http://dx.doi.org/10.1016/j.ijheatfluidflow.2013.01.003
6. Hellström, F.: Numerical computations of the unsteady flow in turbochargers. PhD thesis, KTH Mechanics, Sweden (2010)
7. Sumida, M.: Pulsatile entrance flow in curved pipes: effect of various parameters. Exp. Fluids 43, 949–958 (2007)
8. Timité, B., Castelain, C., Peerhossaini, H.: Pulsatile viscous flow in a curved pipe: Effects of pulsation on the development of secondary flow. Int. J. Heat Fluid Flow 31, 879–896 (2010)
9. Jarrahi, M., Castelain, C., Peerhossaini, H.: Secondary flow patterns and mixing in laminar pulsating flow through a curved pipe. Exp. Fluids 50, 1539–1558 (2010)
10. Laurantzon, F., Tillmark, N., Örlü, R., Alfredsson, P.H.: A flow facility for the characterization of pulsatile flows. Flow Meas. Instrum. 26, 10–17 (2012)
11. Kalpakli, A., Örlü, R., Tillmark, N., Alfredsson, P.H.: Pulsatile turbulent flow through pipe bends at high Dean and Womersley numbers. J. Phys.: Conf. Ser. 318, 092023 (2011)
12. Meyer, K., Pedersen, J.M., Özcan, O.: A turbulent jet in crossflow analysed with proper orthogonal decomposition. J. Fluid Mech. 583, 199–227 (2007)

Nonlinear Development of Unstable Modes and Formation of Coherent Vortex Structures in Weakly Supercritical Zonal Shear Flows

S.V. Shagalov and G.V. Rybushkina

Abstract. This study explores the nonlinear development of the barotropic instability in weakly supercritical horizontally sheared zonal currents in the presence of vertical stratification. The energy exchange between unstable normal modes and the flow is shown to be confined to the common critical layer-region where the modal wave speed matches the flow velocity. A closed system of equations governing the evolution of instability wave amplitudes and critical layer vorticity distributions is derived with the aid of an asymptotic procedure. The dependence of the evolutionary scenarios of the flow on the values of the supercriticality and dissipation parameters is examined within the framework of qualitative and numerical analysis of the obtained equations. Nonlinear growth and saturation of the unstable barotropic and baroclinic modes lead to development of periodic coherent structures in the vorticity distribution inside the common modal critical layer. These structures take on the appearance of two-dimensional vortex chain or three-dimensional baroclinic vortex pattern depending on the flow regime at the stage of the instability equilibration.

1 Introduction

Exploring the development of the shear-flow (barotropic) instability in rotating fluid [4] has continued to attract considerable attention because of its relevance to the formation of large-scale vortex structures [2, 3] and transition to turbulence [5, 6] in horizontally sheared atmospheric and oceanic zonal flows. The physical mechanism feeding the instability near its onset in a weakly dissipative zonal flow is restricted to resonant extracting the kinetic energy from the flow by weakly unstable normal modes in the relatively thin critical layer (CL) surrounding a level where the wave speed of a marginal mode matches the mean flow [1, 5, 6]. The studies [5, 6] seem to

S.V. Shagalov · G.V. Rybushkina
Institute of Applied Physics , Nizhny Novgorod, Russia
e-mail: {shagalov,ryb}@appl.sci-nnov.ru

A. Talamelli et al. (eds.), *Progress in Turbulence V*,
Springer Proceedings in Physics 149,
DOI: 10.1007/978-3-319-01860-7_30,

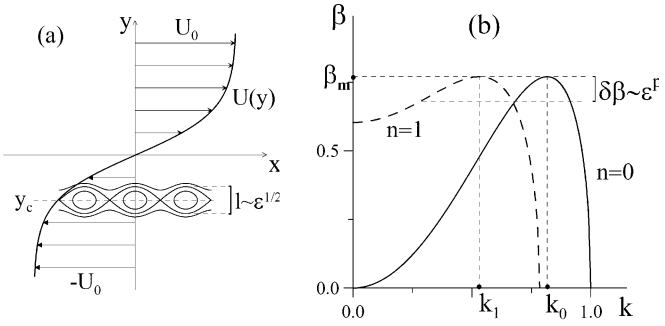

Fig. 1 (a) Schematic illustration of the cat's eye streamline pattern in the nonlinear CL of a zonal mixing layer. (b) The stability boundaries of the barotropic mode (a solid line) and the main baroclinic mode (a dashed line) for the zonal flow $U = \tanh y$.

be the first to perform an asymptotic analysis of transition to turbulence and chaotic advection in parallel shear flows on the basis of the nonlinear CL concept.

2 Description of the Model, Scalings and Evolution Equations

The objective of this research is to extend the asymptotic CL approach to exploration effects arising from the stable density stratification in a weakly dissipative barotropically unstable flow on a horizontal plane rotating with angular velocity Ω_0. Being specified by a mixing layer velocity profile $U(y)$ most typical of the Antarctic polar vortex periphery [7], the background flow is assumed to be directed along the zonal x-axis and varies in the meridional y-direction (Fig. 1(a)). The β-effect (variation of Coriolis parameter $f = 2\Omega_0$ with y) is included. A simple model of density stratification in the vertical z-direction with constant buoyancy frequency N is adopted.The flow is furthermore confined in the vertical direction between two rigid horizontal boundaries at $z = 0$ and $z = 1$.

According to the linear inviscid theory based on the Rayleigh-Kuo's theorem [4] the basic flow is capable of supporting barotropic and baroclinic unstable normal modes whenever the constant meridional gradient β of the Coriolis parameter f is less than a critical value $\beta_m = (U'')_{\max}$. The nondimensional variables are related to their (primed) dimensional counterparts through $(x,y) = (x',y')/L$, $z = z'/H$ and $\beta = \beta' L^2/U_0$, where L and H are a shear scale length and a depth of stratified fluid respectively. A notable feature of the problem is that all marginal modes corresponding to $\beta = \beta_m$ have the same phase speed c. As a consequence, weakly unstable normal modes adjacent to marginal modes for the values of β close to β_m grow in the flow due to the interaction with the common CL in the vicinity of $y = y_c$ where $U(y) = c$ (Fig. 1(a)). Only two unstable modes (the barotropic mode and the main baroclinic one) sharing common CL are shown to develop in the flow near the instability onset provided that some restriction is imposed on the value of the Burger

number $B = (NH/fL)^2$ (Fig. 1(b)). Supercriticality of an inviscid flow defined as $\delta\beta = \beta_m - \beta$ is expressed through a small amplitude parameter ε: $\delta\beta = \varepsilon^p \beta_1$. To capture effects arising from small dissipation a dimensionless viscosity parameter ν (an inverse Reynolds number defined through the parameter of turbulent viscosity) is also scaled in terms of ε: $\nu = \varepsilon^{3/2}\nu_*$. The scaling of $\delta\beta$ allows the regimes of quasi-steady ($p = 1$) and time-dependent ($p = 1/2$) CL to be considered. Outside the CL a solution to potential-vorticity equation describing the flow dynamics [4] is sought as a series in ε for the total streamfunction

$$\psi = \int_{y_c}^{y} (U - c)\, dy + \varepsilon \left\{ 2Re \sum_{n=0,1} A_n(\tau_1)\varphi(y)\cos(\pi n z) e^{ik_n\xi} \right\} + \varepsilon^{p+1}\psi^{(p+1)} + \ldots, \tag{1}$$

where the $O(\varepsilon)$ term satisfying the rigid-lid boundary conditions at $z = 0$ and $z = 1$ accounts for the slowly growing instability waves. The complex amplitude functions A_0 and A_1 depend on the slow variable $\tau_1 = \varepsilon^p t$; $\psi^{(p+1)} = \psi^{(p+1)}(\xi, y, z, \tau_1)$, $\xi = (x - ct)$ is a streamwise coordinate in a frame of reference moving with the common phase speed c of the marginal modes having wavenumbers k_0 and k_1 (Fig. 1(b)) and common latitudinal structure $\varphi(y)$. The regular asymptotic expansion scheme breaks down near the level $y = y_c$ and asymptotic series become disordered for $y - y_c = O(\varepsilon^{1/2})$ (see, e.g., [1, 6]). At this stage rescaled cross-stream coordinate should be introduced to search for asymptotic solutions inside the CL surrounding the critical level $y = y_c$. The scaling of ν ensures that the viscous scale of the CL $l_\nu = (\nu/k_0 U_c')^{1/3}$ and the nonlinear scale $l_n = (|\psi_c|/U_c')^{1/2}$ are $O(\varepsilon^{1/2})$ and hence viscous and nonlinear effects may be of comparable importance inside the CL. An analysis of the asymptotic expansions outside and inside the CL and the matched asymptotics formalism (see also [6, 1]) are employed to derive a closed system of equations governing the evolution of the instability modes amplitudes a_j ($j = 0, 1$) and CL vorticity distribution $\Omega = \Omega(\xi, \eta, z, t)$

$$\frac{da_0}{dt} = i\varphi_c^2 \frac{k_0}{J} \int_0^1 dz \int_{-\infty}^{\infty} \left\langle \Omega e^{-ik_0\xi} \right\rangle d\eta\,, \tag{2}$$

$$\frac{da_1}{dt} = i\varphi_c^2 \frac{2k_1}{J} \int_0^1 \cos(\pi z)\, dz \int_{-\infty}^{\infty} \left\langle \Omega e^{-ik_1\xi} \right\rangle d\eta, \tag{3}$$

$$\frac{\partial\Omega}{\partial t} + U_c'\eta\frac{\partial\Omega}{\partial\xi} - 2Re\left\{ \sum_{n=0,1} ik_n a_n \cos(\pi n z)\, e^{ik_n\xi} \right\} \frac{\partial\Omega}{\partial\eta} = F(\xi, z, t) + \nu\frac{\partial^2\Omega}{\partial\eta^2}, \tag{4}$$

where F contains terms describing supercriticality and nonlinearity, $\langle \ldots \rangle$ and $(\ldots)_c$ denote local averaging over zonal coordinate ξ and evaluation at $y = y_c$ respectively, $a_j = \varepsilon\varphi_c A_j$, $\eta = y - y_c$, J is a functional of modal profile $\varphi(y)$ and $U(y)$. Being written in terms of physical variables, equations (2)-(4) combine both variants of $\delta\beta$ scaling and allow one to study the shear flow dynamics over relatively wide range of supercriticality.

3 Results

Under sufficiently small supercriticality with $\delta\beta \ll \nu^{2/3}$ the CL-flow is shown to evolve in a quasi-steady weakly nonlinear regime. In this case equations (2)-(4) may be reduced to a set of two coupled Landau-Stuart amplitude equations describing simultaneous development of the unstable normal modes

$$\frac{da_j}{dt} = \gamma_j a_j + a_j \sum_l \rho_{jl} |a_l|^2 + a_j \sum_{l,m} \alpha_{jlm} |a_l|^2 |a_m|^2 \quad (j = 0, 1), \tag{5}$$

where $\gamma_j = \pi k_j \varphi_c^2 \delta\beta / JU_c'$ is the linear growth rate of the j-wave and ρ_{jl}, α_{jlm} are real coefficients. A qualitative analysis of the system (5) based on the phase-plane description (see, e.g., [8]) was performed. It has been revealed that the primary effect of the nonlinear interaction between modes within the CL is the suppression of the baroclinic mode and saturation of the instability in barotropic regime as a result. The physical mechanism of this effect is based on the nonlinear interaction of the modes with the second-order "beat-wave" vorticity perturbations induced in the CL. At the higher level of supercriticality ($\delta\beta \sim \nu^{1/3}$) nonlinearity and time dependence play a significant role in the CL and development of the instability can no longer be described by the weakly nonlinear equations (5). It is shown with the aid of numerical analysis of the equations (2)-(4) that in this case the flow exhibits competition between modes and depending on the initial conditions for the mode amplitudes the instability saturates in pure barotropic or baroclinic regime (Fig. 2(a),(b)).

This evolutionary scenario is accompanied by development of periodic coherent structures in the vorticity distribution inside the common modal CL taking the form of the two-dimensional barotropic vortex chain or the three-dimensional baroclinic vortex pattern at the stage of the instability equilibration. Figure 3 shows the snapshots of the final state potential vorticity field

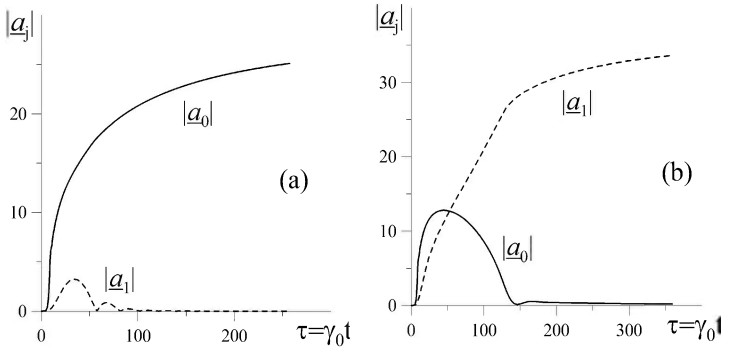

Fig. 2 (a), (b) The time evolution of the normalized mode amplitudes $\underline{a}_j = a_j / U_c' l_\nu^2$ in the regime of the nonlinear time-dependent CL for different initial conditions

$$Z = -\frac{1}{3!}U_c^{IV}\eta^3 + \delta\beta\eta - \frac{U_c^{IV}}{U_c'}\eta Re\left(a_0 e^{ik_0\xi} + a_1\cos\pi z e^{ik_1\xi}\right) + \Omega(\xi,\eta,z,t) \quad (6)$$

for the barotropic and baroclinic regimes of the instability saturation for different values of vertical coordinate z .

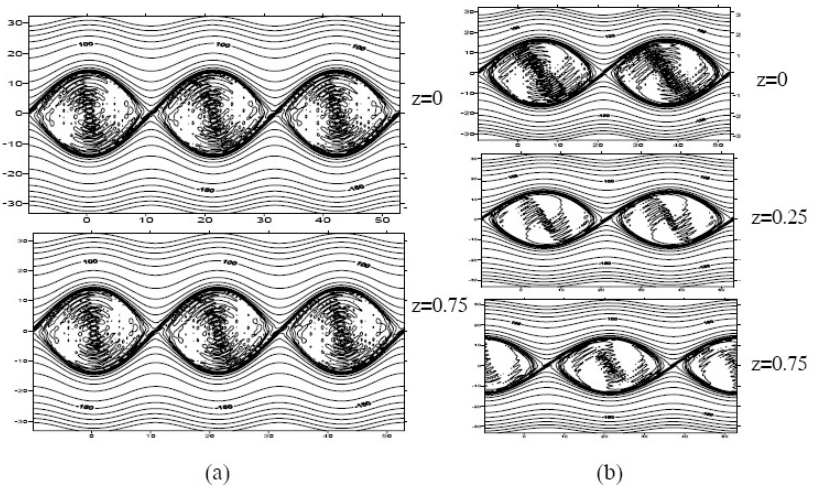

Fig. 3 Computed constant-potential vorticity Z contours in the barotropic (a) and baroclinic (b) regimes of the instability saturation for different values of vertical coordinate z

4 Concluding Remarks

In this study an asymptotic approach based on the critical layer concept is used to analyze the nonlinear development of barotropic instability in a horizontally sheared, stratified zonal flow. The contribution of the baroclinic (three-dimensional) unstable normal modes to different scenarios of the barotropic instability is explored. It has been shown that in the absence of resonant interaction between unstable normal modes characteristics of the instability crucially depend on the value of the supercriticality. Transition from the regime of the baroclinic mode suppression to the regime of competition between modes with the supercriticality increasing has been revealed.

Acknowledgement. The work was carried out with financial support from the Russian Foundation for Basic Research (project No. 12-05-01115-a).

References

1. Churilov, S.M.: The nonlinear stabilization of a zonal shear flow instability. Geophys. Astrophys. Fluid Dyn. 46(3), 159–175 (1989)
2. Flierl, G.R., Malanotte-Rizzoli, P., Zabusky, N.J.: Nonlinear waves and coherent vortex structures in barotropic beta-plane jets. J. Phys. Oceanogr. 17, 1408–1438 (1987)
3. Maejima, Y., Iga, K., Niino, H.: Upper-tropospheric vortex street and its formation mechanism. In: SOLA, vol. 2, pp. 80–83 (2006)
4. Pedlosky, J.: Geophysical Fluid Dynamics. Springer, Berlin (1982)
5. Reutov, V.P., Shagalov, S.V., Rybushkina, G.V.: The onset of turbulence in a shear flow on the beta-plane. An asymptotic approach based on the critical layer theory. In: Frish, U. (ed.) Advances in Turbulence VII, pp. 483–486. Kluwer, Dordrecht (1998)
6. Shagalov, S.V., Reutov, V.P., Rybushkina, G.V.: Asymptotic analysis of transition to turbulence and chaotic advection in shear zonal flows on a beta-plane. Izvestiya, Atm. Ocean. Phys. 46, 95–108 (2010)
7. Tomikawa, Y., Yoshiki, M., Sato, K.: A neutral wave observed in the Antarctic polar vortex. J. Meteor. Soc. Japan 84, 97–113 (2006)
8. Weiland, J., Wilhelmsson, H.: Coherent Non-Linear Interaction of Waves in Plasmas. International series in natural philosophy, vol. 88. Pergamon Press, Oxford (1977)

Reactive Continuum Mixtures under the Influence of Electromagnetic Fields

Martina Costa Reis and Adalberto Bono Maurizio Sacchi Bassi

Abstract. In this work, we present the equations of balance of mass, linear and angular momenta, energy, and entropy for reactive continuum mixtures under the influence of electromagnetic fields. We assume that the mixture is a polar continuum whose constituents are electric charge and/or electric dipole moment carriers immersed in a Newtonian fluid. From the mass balance equation, properties of real and potential electrolytes were related to the terms of mass production. In addition, from the linear and angular momenta balances, it was shown that the stress tensor is not symmetric due to the polar nature of both the constituents and the mixture. Moreover, the energy balance equation for the mixture reveals that the energy flux vector should not be interpreted as the heat flux vector from the classical continuum mechanics. The balance laws presented in this work may offer a theoretical tool to investigate mass transport and thermoelectric phenomena in electrolyte solutions as well as in bio and geological fluids.

1 Introduction

The study of the electrodynamics of deformable and reactive bodies interests chemists, physicists and engineers. Some authors [4, 5] have demonstrated that many physical and biological processes are influenced by electromechanical interactions, so that several continuum models, varying in degree of complexity, have been developed. However, despite the many models available, the electrodynamics of deformable and reactive bodies has not been appropriately described in the literature yet.

Thus, the aim of this work is to present the balance laws for reactive mixtures under the influence of electromagnetic fields. This is done by superposing the

Martina Costa Reis · Adalberto Bono Maurizio Sacchi Bassi
Department of Physical Chemistry, Institute of Chemistry,
University of Campinas-UNICAMP, Brazil
e-mail: {marreis,bassi}@iqm.unicamp.br

A. Talamelli et al. (eds.), *Progress in Turbulence V*,
Springer Proceedings in Physics 149,
DOI: 10.1007/978-3-319-01860-7_31,

quasi-electrostatic theory on the continuum theory of mixtures. The results of this work may be useful for modeling the thermomechanical behavior of electrolyte solutions and bio and geological fluids too.

2 Dynamics of Electrolyte Solutions

We assume that electrolyte solutions are continuum mixtures whose polar constituents may carry electric charges and/or electric dipole moments. In describing electrolyte solutions as electrically polarizable and conducting media, we assign an inner structure to the mixture. Briefly, electrolyte solutions are considered micropolar mixtures whose macroscopic behavior is strongly influenced by microscopic properties, such as molecular motion, electric dipole moments and size of particles.

Maxwell's equations of electromagnetism are considered under the quasi-electrostatic approximation [6]. All equations are written in their component forms by considering a Cartesian coordinate system, and all quantities relative to the individual constituents of the mixture, named partial quantities, are labeled by an index a. Furthermore, time derivatives of the fields $\psi(\mathbf{x},t)$ following the motion of the mixture are denoted by $\dot{\psi}$, whereas time derivatives of the fields $\psi^a(\mathbf{x}^a,t)$ following the motion of the constituent are expressed by $\grave{\psi}^a$. Besides, brackets represent the anti-symmetry of second order tensors.

2.1 Kinematics

Let $\mathscr{B}$ be a micropolar mixture of n constituents $\mathscr{B}^a$ with $a = 1,...,n$, such that a particle of $\mathscr{B}^a$ is represented by X^a. Besides, let a region of the Euclidean space $\mathscr{E}$ be simultaneously occupied by n particles, one from each constituent [2]. Thus, if $\mathbf{X}^a$ is the material coordinate in some reference configuration, the motion $x_i^a = x_i^a(\mathbf{X}^a,t)$ of constituent a is a smooth function of space and time with velocity and acceleration respectively given by:

$$v_i^a \equiv \frac{\partial x_i^a(\mathbf{X}^a,t)}{\partial t}, \qquad a_i^a \equiv \frac{\partial^2 x_i^a(\mathbf{X}^a,t)}{\partial t^2}. \tag{1}$$

Each particle X^a undergoes the rotation ω_i^a, as well as the displacement set above. These rotations are independent of mixture vorticity, w_i, and are not described by the spin tensor, but by an orthogonal tensor, I_{ij}^a, which accounts for the average moment of inertia of molecules of $\mathscr{B}^a$ [3]. By assuming that particles behave as rigid bodies, one has

$$s_i^a = I_{ij}^a \omega_j^a, \tag{2}$$

where s_i^a is the spin field, a quantity that represents the internal angular momentum of the molecules of $\mathscr{B}^a$.

2.2 Balance Laws

For a multi-constituent system, the local balance equation of mass for the constituent a is given by

$$\dot{\rho}^a + \rho^a v^a_{i,i} - c^a = 0\,, \tag{3}$$

where ρ^a is the mass density of a, and $c^a = \sum_{b=1}^{n} \left(c^{ba} - c^{ab} \right)$, being c^{ba} the rate of mass conversion from constituent b to constituent a as result of a chemical reaction. The charge density of each constituent a, q^a, may be obtained from $q^a = \rho^a z^a$, where z^a is the charge *per* unit mass of constituent a.

The introduction of c^{ba} is very important to define two kinds of electrolytes: the potential electrolytes and the real ones. Potential electrolytes are those which dissociate into ions through chemical reactions with solvent molecules. Most solutions of potential electrolytes contain small ionic concentrations, thus the effects of ion-ion interactions are frequently neglected. The behavior of these solutions is mainly governed by the equilibrium position of the reaction between the potential electrolyte and the solvent. Hence, until kinetic equilibrium is reached, c^{ba} and c^{ab} are different for the same point of the mixture at the same time. On the other hand, real electrolytes are those which generate ions in solution through physical interactions between the ions present in the ionic solid and the solvent molecules. Usually, real electrolytes are completely ionized when dissolved in water, so that the final solutions consist only of solvated ions and solvent molecules. For these solutions, the dependence of their properties on concentration is determined by the ion-ion interaction force [1].

For a micropolar mixture whose constituents are chemical species, which may carry electric charge and/or electric dipole moments, each constituent experiences mechanical as well as chemical and electrical forces. Then, the local balance equations of linear momentum for each constituent and mixture are, respectively,

$$\begin{gathered} \rho^a \dot{g}^a_i - T^a_{[ij],j} - \rho^a b^a_i - q^a E^a_i - P^a_i E^a_{i,j} - m^a_i = 0\,, \\ \rho \dot{g}_i - T_{[ij],j} - \rho b_i - q E_i - P_i E_{i,j} = 0\,, \end{gathered} \tag{4}$$

where $\rho g_i = \sum_{a=1}^{n} \rho^a g^a_i$ is the total linear momentum density, $T_{[ij]} = \sum_{a=1}^{n} \left(T^a_{[ij]} - \rho^a u^a_i u^a_j \right)$ is the total stress tensor, u_i is the translational diffusion velocity, $\rho b_i = \sum_{a=1}^{n} \rho^a b^a_i$ is the mechanical body force density, $qE_i = \sum_{a=1}^{n} q^a E^a_i$ is the coulombic force density, m^a_i is the linear momentum production that accounts for the chemical interaction of constituent a with other constituents, and P_i is the polarization vector defined by $P_i = \rho p_i$, such that p_i denotes the dipole moment. The linear momentum production, m^a_i, can be split up into two parts: a part that comes from the thermochemical interactions of a with other constituents and another part that follows from the chemical production of mass of constituent a.

Unlike single fluids, the stress tensor for continuum mixtures contains two contributions: the first one, named inner part, is the sum of all partial stress tensors, and the second one, named partial diffusive stress tensor, describes the transfer of linear momentum caused by the diffusive motion of each constituent of the mixture. Moreover, as the dynamics of the whole mixture must not be changed by the interactions among the constituents, one necessarily has $\sum_{a=1}^{n} m_i^a = 0$.

The local balance equations of spin for each constituent and mixture are, respectively,

$$\begin{gathered} \rho^a \mathring{s}_i^a - C_{ij,j}^a + \tfrac{1}{2}\varepsilon_{ijk} T_{[jk]}^a - \varepsilon_{ijk} P_j^a E_k^a - \rho^a l_i^a - \tau_i^a = 0\,, \\ \rho \dot{s}_i - C_{ij,j} + \tfrac{1}{2}\varepsilon_{ijk} T_{[jk]} - \varepsilon_{ijk} P_j E_k - \rho l_i = 0\,, \end{gathered} \tag{5}$$

where $\rho s_i = \sum_{a=1}^{n} \rho^a s_i^a$ is the spin density, $C_{ij} = \sum_{a=1}^{n} \left(C_{ij}^a - \rho^a s_i^a u_j^a\right)$ is the coupling stress tensor, $\rho l_i = \sum_{a=1}^{n} \rho^a l_i^a$ is the mechanical body coupling force, and τ_i^a is the spin production due to the electromechanical interactions of a with other constituents and the chemical production of mass of constituent a. According to Eq. 5, there exists an electromagnetic body coupling force acting on polar molecules given by $\varepsilon_{ijk} P_j E_k$ which contributes to the time change of spin and to the antisymmetry of the stress tensor. In fact, Eq. 5 shows that the stress tensor of each constituent will be symmetric if, and only if, simultaneously s_i^a is a time constant, C_{ij}^a is a solenoidal field, $\tau_i^a = 0$, $l_i^a = 0$, and P_i^a and E_i^a are aligned. As expected, the same conclusions hold for the whole mixture too.

At this point, it should be emphasized that body coupling forces can also act on particles of apolar fluids, but, in this case, they are equivalent to body forces, so they only modify non-internal degrees of freedom. On the other hand, these body coupling forces work upon the internal degrees of freedom of structured fluids, inducing fluid flow.

The local energy balance equations for each constituent and mixture are, respectively,

$$\begin{gathered} \rho^a \mathring{\varepsilon}^a + h_{i,i}^a + S_{i,i}^a - T_{[ij]}^a v_{i,j}^a - \tfrac{1}{2}\omega_i^a \varepsilon_{ijk} T_{[jk]}^a - \\ C_{ij}^a \omega_{i,j}^a - \rho^a r^a - \rho^a E_i^a \mathring{p}_i^a - E_i^a i_i^a - \vartheta^a = 0\,, \\ \rho \dot{\varepsilon} + h_{i,i} + S_{i,i} - T_{[ij]} v_{i,j} - \tfrac{1}{2}\omega_i \varepsilon_{ijk} T_{[jk]} - C_{ij}\omega_{i,j} - \rho r - \rho E_i \dot{p}_i - E_i i_i = 0\,, \end{gathered} \tag{6}$$

where $\rho\varepsilon = \sum_{a=1}^{n} \left(\rho^a \varepsilon^a + \frac{1}{2}E^{a2} + \frac{1}{2}\rho^a u^{a2} + \frac{1}{2}\rho^a s_i^a \varsigma_i^a\right)$ is the density of internal energy, being the total kinetic energy split up into translational and rotational kinetic energies, ς_i^a is the angular diffusion velocity, $h_i = \sum_{a=1}^{n} \left\{ h_i^a - T_{[ij]}^a u_i^a - C_{ij}^a \varsigma_i^a + \left[\frac{1}{2}\rho^a \varepsilon^a + \frac{1}{2}E^{a2} + \frac{1}{2}\rho^a u^{a2} + \frac{1}{2}\rho^a s_i^a (\varsigma_i^a - \omega_i)\right] u_i^a \right\}$ is

the energy flux vector, S_i^a is the Poynting's vector, $\rho r = \sum_{a=1}^{n} \rho^a r^a$ is the energy supply due to mechanical body forces, i_i is the conduction current, and ϑ^a is the energy production. The last two terms on the right-hand side of Eq. 6.2 respectively describe the rate of work done by the constituents which are carriers of electric dipoles, and the Joule effect. Moreover, the heat flux vector for the mixture involves not only the contribution of partial heat fluxes, but also the stress powers and the coupling stresses over the diffusive movement, and the convective energy flux associated to diffusion. Consequently, the energy flux vector, h_i, should not be interpreted just as the heat flux vector, ϕ_i.

Additionally to Eqs. 3-6, the behavior of reactive continuum mixtures under influence of electromagnetic fields must also obey the entropy principle. The entropy principle for each constituent and mixture respectively are

$$\begin{aligned} \rho^a \dot{\eta}^a + \Phi^a_{i,i} - \rho^a \sigma^a - \rho^a \pi^a = 0\,, \\ \rho \dot{\eta} + \Phi_{i,i} - \rho \sigma \geq 0\,, \end{aligned} \tag{7}$$

where $\rho \eta = \sum_{a=1}^{n} \rho^a \eta^a$ is the the specific entropy density, $\Phi_i = \sum_{a=1}^{n} (\Phi_i^a + \rho^a \eta^a u_i^a)$ is the entropy flux, $\rho \sigma = \sum_{a=1}^{n} \rho^a \sigma^a$ is the entropy supply density, and $\rho \pi = \sum_{a=1}^{n} \rho^a \pi^a \geq 0$ is the entropy production density. Note that the entropy production for each constituent may take any value, provided that the entropy production for the whole mixture is a non-negative quantity. Furthermore, unlike the Coleman and Noll exploitation method [7] of the entropy principle, Φ_i and $\rho\sigma$ are not *a priori* assumptions, but constitutive functions on which thermodynamic restrictions must be placed. In fact, with Φ_i and $\rho\sigma$ given by the previous expressions, the main constitutive assumptions adopted by Coleman and Noll, $\Phi_i = \frac{1}{\theta}\phi_i$ and $\sigma = \frac{1}{\theta} r$, clearly do not hold, where θ stands for the empiric temperature.

3 Concluding Remarks

In this work, we discussed the dynamics of reactive micropolar mixtures under influence of electromagnetic fields. We described the electrolyte solution as a discontinuous medium on the microscopic scale, such that the intrinsic motion of the molecules of each constituent is taken into account. Moreover, we presented balance equations of mass, linear and angular momenta, energy, and entropy. Mass production terms were used to distinguish the nature of potential and real electrolytes. The results obtained from the balance equation of linear momentum indicated that the stress tensor is the sum of the partial stress tensors minus the sum of the diffusive coupling stresses. Indeed, we showed that the manifestation of torques on polar molecules is closely related to the inner structure of the fluid and causes the lack of

symmetry of the stress tensor. We also demonstrated that the vector h_i should not be interpreted as the heat flux vector, ϕ_i, from the classical continuum mechanics. Thus, the well-known Clausius-Duhem inequality does not apply to reactive continuum mixtures, so that other entropy principles, for instance, the Müller-Liu entropy principle, should be employed to impose restrictions on the constitutive responses of the body.

Acknowledgements. Martina Costa Reis acknowledges financial support from the Brazilian National Counsel for Scientific and Technological Development (CNPq) and German Academic Exchange Service (DAAD). The authors are also indebted to Professor Yongqi Wang for his pertinent comments about the equations.

References

1. Bockris, J.O'.M., Reddy, A.K.: Modern Electrochemistry: Ionics. Kluwer, Boulder (1998)
2. Bowen, R.M.: The thermochemistry of a reacting mixture of elastic materials with diffusion. Arch. Rational Mech. Anal. (1969), doi: 10.1007/BF00247461
3. Condiff, D.W., Dahler, J.S.: Fluid mechanical aspects of antisymmetric stress. Phys. Fluids (1964), doi: 10.1063/1.1711295
4. Eringen, C.A., Maugin, G.A.: Electrodynamics of Continua. Springer, New York (1990)
5. Hutter, K., van de Ven, A.A.F., Ursescu, A.: Electromagnetic Field Matter Interactions in Thermoelastic Solids and Viscous Fluids. Springer, Berlin (2006)
6. Melcher, J.R.: Continuum Electromechanics. MIT Press, Massachusetts (1981)
7. Truesdell, C.A., Noll, W.: The Non-Linear Field Theories of Mechanics, 3rd edn. Springer, Berlin (2004)

Sound Generating Flow Structures in a Thick Orifice Plate Jet

Emma Alenius

Abstract. The aim of this work is to study sound generating flow structures in a thick circular orifice plate jet, placed in a circular duct. Large eddy simulations (LES) are performed for two jet Mach numbers, 0.4 and 0.9. Characteristic frequencies in the flow, and their corresponding flow structures, are identified with dynamic mode decomposition (DMD). The results show that a tonal noise is generated at frequencies where the jet displays strong ring vortices, in the plane wave range. The main sound generating mechanisms seems to be a fluctuating mass flow at the orifice opening and a fluctuating surface force at the plate sides, caused by the ring vortices. The frequencies are believed to be chosen, and strengthened, by a feedback mechanism between the orifice in- and outlet.

1 Introduction

When air flows through a thick orifice, a jet is formed inside and downstream of the orifice, generating sound. In this work we study sound generating flow structures in a circular orifice jet, confined in a circular duct. Simulations are an important tool for studying the flow structures; they can give insight into what happens in areas where it is difficult to perform measurements. Here, compressible large eddy simulation (LES) is used in order to capture both the sound generating flow structures and the acoustics.

Orifice jets have been shown to exhibit similar, although more 3D, coherent structures as nozzle jets, which have been more extensively studied in literature, [7, 6]. The jet shear layer is unstable to small perturbations, which grow exponentially and roll up into axisymmetric vortex rings close to the nozzle exit and helical structures further downstream [3]. The passing of axis-symmetric vortex rings has been shown to give rise to a periodic acceleration of the jet core fluid [5]. The most unstable

Emma Alenius
Competence Center for Gas Exchange (CCGEx) and MWL, KTH, Stockholm, Sweden
e-mail: ealenius@kth.se

A. Talamelli et al. (eds.), *Progress in Turbulence V*,
Springer Proceedings in Physics 149,
DOI: 10.1007/978-3-319-01860-7_32,

frequency of the jet shear layer is very sensitive to low level coherent background perturbations [2]. Thus, a feedback mechanism can occur when the jet impinges on an object, giving upstream propagating coherent disturbances that excite the shear layer at the point of separation [8]. For a ducted orifice plate, a similar feedback mechanism can generate a high amplitude tonal noise, so called whistling, due to interaction with reflecting duct ends [11].

The focus of this paper is flow structures that generate a tonal noise in a 2 cm thick orifice plate jet, with non-reflecting duct ends. The flow structures are studied using dynamic mode decomposition (DMD), which is a method to extract structures corresponding to characteristic frequencies in the flow [10]. Simulations are performed for an orifice with an area contraction ratio of 0.36, and at two flow speeds, corresponding to jet Mach numbers of 0.4 and 0.9.

2 Models and Methods

In this study LES is used since direct numerical simulations (DNS) are too expensive, and Reynolds average Navier Stokes (RANS) models are too dissipative and problematic at the time-scales related to the sound generation. The idea with LES is to resolve the large energy containing scales, which are coupled to the geometry, while the small scales are modeled. This model should account for the effects of the small, unresolved, scales on the resolved ones, where the most important effect is dissipation of kinetic energy. An alternative to using an explicit model for the sub-grid scales is implicit LES, where the numerical dissipation in the discretization scheme is assumed to account for the dissipation by the sub-grid scales. In the simulations it is also made sure that the spatial resolution is good enough to resolve a part of the inertial sub-range, as required in an LES.

The LES have been performed with the general compressible CFD code Edge, which is a node based finite volume code, see [1]. The spatial discretization uses a formally second order central scheme, with a Jameson type of artificial dissipation [4] added to the inviscid terms. For the temporal discretization an explicit, low storage, four stage, second order accurate Runge-Kutta scheme is used.

In DMD the flow is decomposed into a temporal part, consisting of frequencies ω_j and growth rates β_j, and a spatial part, with flow structures/modes ϕ_j corresponding to these frequencies. Mathematically this is formulated as:

$$\mathbf{u}(\mathbf{x},t) = \sum_{j=1}^{\infty} \eta_j \mathrm{e}^{(\beta_j - i\omega_j)t} \phi_j(\mathbf{x}),$$

where $\mathbf{u}$ is the velocity, t is the time and η_j is an amplitude. In order to compute the modes a linear tangent approximation is done, where $\mathbf{A}$ is assumed to connect the flow field $\mathbf{u_{m+1}}$ with the flow field at the previous time $\mathbf{u_m}$. That is, $\mathbf{u_{m+1}} = \mathbf{A}\mathbf{u_m}$. The eigenvalues and eigenvectors of $\mathbf{A}$ now correspond to the DMD eigenvalues and

modes. However, in real problems A becomes very large, so the problem is rewritten to give approximate DMD eigenvalues and modes. In this work a method based on the singular value decomposition of the snapshot matrix (containing the velocity field at 3000 time instants) is used. For more information about DMD and how it is computed see [9] and [10].

3 Results

High sound levels are generated at certain frequencies, which depend on the flow speed, see Fig. 1. These frequencies correspond to jet instabilities, as seen in Fig. 2 of the DMD mode spectra. Studying the shape of the modes at the lower flow speed, Fig. 3, it is observed that the two modes that generate a tonal noise are axisymmetric, while no noise seems to be generated by the azimuthal mode. This is explained by the fact that only plane waves, which have variables that are constant over duct cross-sections, are studied, and if the fluctuations of an azimuthal mode are integrated over a cross-section the result is zero. The fact that only axisymmetric modes generate a tonal noise at these frequencies also applies to the higher mass flow case.

The generated sound can be correlated to a fluctuating mass flow at the orifice openings and a fluctuating surface force at the plate sides, indicating that these are the main sound generating mechanisms. These fluctuations are caused by the periodic passing of strong vortex rings, which drive an oscillation of the jet core fluid.

The strong axisymmetric vortices at specific frequencies are believed to be caused by a feedback mechanism. When a vortex reaches the downstream edge a pulse is generated and propagates to the upstream edge, where it triggers a new vortex. This hypothesis is supported by the correlation of the mass flow at the orifice inlet and outlet, having a maximum for a time delay corresponding to the upstream acoustic propagation speed.

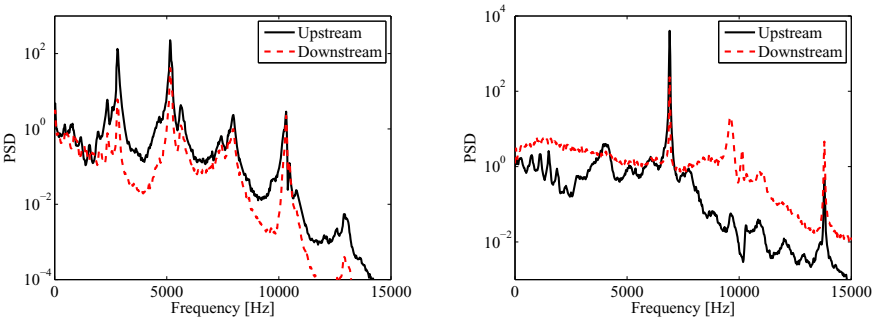

Fig. 1 Power spectral density of the plane wave sound generated by the Mach 0.4 jet to the left and the Mach 0.9 jet to the right

Fig. 2 DMD mode spectra

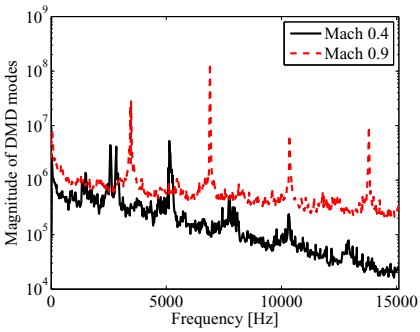

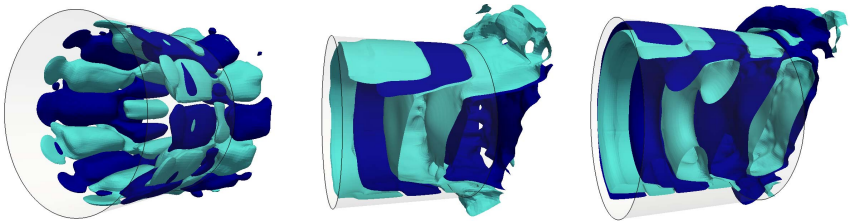

Fig. 3 DMD modes at 2600 Hz (left), 2800 Hz (middle) and 5150 Hz (right), for the Mach 0.4 jet. Iso-surfaces of a positive and a negative axial velocity.

References

1. Eliasson, P.: EDGE, a Navier-Stokes Solver for Unstructured Grids. FOI-Swedish Defence Research Agency (2001)
2. Gutmark, E., Ho, C.M.: Preferred modes and the spreading rates of jets. The Physics of Fluids 26, 2932–2938 (1983)
3. Ho, C.M., Huerre, P.: Perturbed free shear layers. Annu. Rev. Fluid Mech. 16, 365–422 (1984)
4. Jameson, A., Schmidt, W., Turkel, E.: Numerical Solutions of the Euler Equations by Finite Volume Methods Using Runge-Kutta Time-Stepping Schemes. AIAA paper 81-1259 (1981)
5. Jung, D., Gamard, S., George, W.K.: Downstream Evolution of the Most Energetic Modes in a Turbulent Axisymmetric Jet at High Reynolds Number. Part 1. The Near-Field Region. J. Fluid Mech. 514, 173–204 (2004)
6. Meslem, A., El Hassan, M., Nastase, I.: Analysis of jet entrainment mechanism in the transitional regime by time-resolved PIV. J. of Visualization 14, 41–52 (2011)
7. Mi, J., Nathan, G.J., Nobes, D.S.: Mixing characteristics of axisymmetric free jets from a contoured nozzle, an orifice plate and a pipe. J. Fluids Eng. 123, 878–883 (2001)
8. Rockwell, D., Naudascher, E.: Self-sustained oscillations of impinging free shear layers. Annu. Rev. Fluid Mech. 11, 67–94 (1979)
9. Rowley, C.W., Mezić, I., Bagheri, S., Schlatter, P., Henningson, D.S.: Spectral Analysis of Nonlinear Flows. J. Fluid Mech. 641, 115–127 (2009)
10. Schmid, P.J.: Dynamic mode decomposition of numerical and experimental data. J. Fluid Mech. 656, 5–28 (2010)
11. Testud, P., Aurégan, Y., Moussou, P., Hirschberg, A.: The whistling potentiality of an orifice in a confined flow using an energetic criterion. J. Sound Vib. 325, 769–780 (2009)

Sound Generation in Plane Couette Flow: A Failure of Lighthill's Analogy

Jan-Niklas Hau, George Chagelishvili, George Khujadze,
Martin Oberlack, and Alexander Tevzadze

Abstract. The linear mechanism of acoustic wave generation by initially pure vortex perturbations embedded in a two-dimensional, inviscid and unbounded Couette flow is investigated by Kelvin-mode analysis and direct numerical simulations (DNS). Our results show a misleading representation of the linear sources of aerodynamic sound generation by Lighthill's acoustic analogy approach, not taking the strong anisotropy of the linear generation of acoustic waves by pure vortex mode perturbations in non-normal shear flow systems into account. DNS confirm the importance of linear sound production in the range of validity of rapid distortion theory (RDT), herein being superior compared to the nonlinear mechanism despite the common opinion.

1 Introduction

Aerodynamic sound generation is a major subject of fluid dynamics, with applications in wide areas of engineering problems, even extending to the astrophysical context (helio- and astroseismology). The framework for modern aero-acoustic research was accomplished by Lighthill's pioneering work [3] and the derivation of the acoustic analogy (AA). Particularly, Lighthill's statement [4] that linear sound generation can be increased by a mean shear flow, due to the linear terms in the so-called source term $\mathscr{S}$, is one of the motivations of the presented research. This

Jan-Niklas Hau · George Khujadze · Martin Oberlack
Chair of Fluid Dynamics, TU Darmstadt, Petersenstr. 30, 64287 Darmstadt, Germany
e-mail: hau@fdy.tu-darmstadt.de

George Chagelishvili
E. Kharadze Abastumani Astrophysical Observatory, Ilia State University, Tbilisi 0160, Georgia & M. Nodia Institute of Geophysics, Tbilisi State University, Tbilisi 0128, Georgia

Alexander Tevzadze
Faculty of Exact and Natural Sciences, Javakhishvili Tbilisi State University, Tbilisi 0128, Georgia

A. Talamelli et al. (eds.), *Progress in Turbulence V*,
Springer Proceedings in Physics 149,
DOI: 10.1007/978-3-319-01860-7_33,

has the dual purpose of: *i*) Rethinking Lighthill's AA approach [3, 4] in the light of the breakthrough of the hydrodynamic stability community in the 1990s (e.g. [1, 9] and references herein) that was followed by the understanding of phenomena introduced by the non-normality of non-uniform flow systems. In nonuniform/shear flows the set of governing equations describing the dynamics of are non-normal. Hence, the operators in the mathematical formalism of shear flow modal analysis are non-normal and the corresponding eigenmodes non-orthogonal (see e.g. [9]). This fact leads to strong interference phenomena among the eigenmodes, which are not captured by the classic modal analysis, and can be circumvented by the so called non-modal approach; *ii*) Comparing the efficiency of the linear and nonlinear mechanisms of aerodynamic sound generation at different Mach numbers, $\mathscr{M}$, and RDT parameters, $\mathscr{D}$, of the embedded flow eddies.

Our investigation is performed by means of Kelvin-mode analysis as well as direct numerical simulations (DNS) of the Navier-Stokes equations, focusing on the dynamics in the spectral plane, as this analysis facilitates grasping the basic physics of acoustic wave generation. Herein, the linear generation of acoustic waves by initially pure vortex perturbations embedded in a two-dimensional, inviscid and unbounded plane Couette flow with constant/homogeneous shear ($\mathbf{V}_0 = (Ay, 0)$, shear parameter $A > 0$ without the loss of generality), uniform pressure and density distribution is investigated. Thence, we can focus entirely on phenomena induced by the non-normal nature of the underlying base flow system, which appears partially in jets, and subsequently shed some light on the open question for the *true sources* of aerodynamic sound, which are still not properly defined, [2].

2 Results

The ability of wave-generation by pure vortex mode perturbations in the linear limit as gained by Kelvin-mode analysis [1] is illustrated in Fig. 1*a*)-*c*). Herein, the ability of wave-generation is regarded for different Mach numbers based on the initial perturbation $\mathscr{M} = A/(k_{x0}c_s)$ and, moreover, for different ratios of initial (subscript 0) wavenumbers $\beta = k_{y0}/k_{x0}$, in spanwise (k_y) and streamwise (k_x) direction, whilst c_s denotes the speed of sound.

By comparing Fig. 1*a*) and *b*) it becomes evident that acoustic wave spatial Fourier harmonics (SFH) are generated just at the time τ^* of the vortex SFH crossing the line of $k_y = 0$ ($\tau^* = k_{y0}/Ak_{x0}$) at sufficiently high values of $\mathscr{M}$, when compressibility effects come into play [1]. The specific time behaviour is due to the linear drift induced in spectral space by the flow system non-normality. Passing the critical time τ^*, henceforth, leads to an excessive energy-extraction ($E_{\mathbf{k}}$) from the shear flow by the newly generated wave SFH. On the other hand it is observed in Fig. 1*c*) that the vortex SFH, initially located in regions of $\beta < 0$, decay, incapable of generating sound waves, as they do not bear the ability to cross the line of $k_y = 0$, which contradicts Lighthill's acoustic analogy in the linear limit, as to be shown.

In order to validate the obtained results by DNS, which were carried out with the PLUTO code [6], pure vortex mode perturbations are inserted into the flow, being

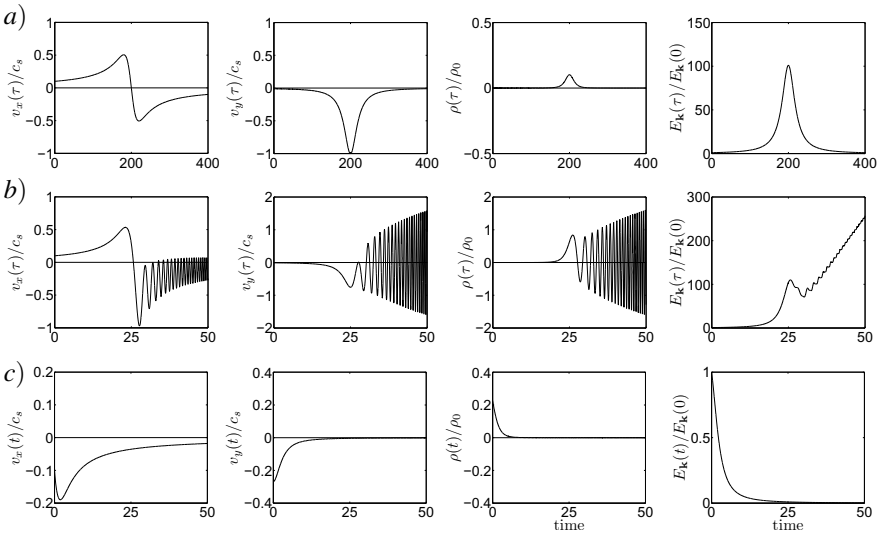

Fig. 1 The figure shows the evolution of SFH in terms of normalised velocity and density perturbations ($v_x(\tau)/c_s$, $v_y(\tau)/c_s$ and $D \equiv \mathrm{i}\rho(\tau)/\rho_0$) and its normalised energy ($E_{\mathbf{k}}(\tau)/E_{\mathbf{k}}(0)$) at *a*) $\mathscr{M} = 0.05$; *b*) $\mathscr{M} = 0.40$ for equally $\beta = k_{y0}/k_{x0} = 10$ and *c*) $\mathscr{M} = 0.40$ for $\beta = k_{y0}/k_{x0} = -1 \cdot 10^{-5}$. Evolving in the shear flow, the initially imposed vortex SFH (with $\beta > 10$, respectively adjusted A) transiently grows and retains its aperiodic nature, whereas the one initially located at $\beta < 0$ undergoes immediate attenuation. Note that the ordinate is adjusted to the respective amplitude after the moment of wave-generation, and the abscissa due to the increased speed of drift.

stochastically localised in the spanwise (y) and homogeneous in the streamwise (x) directions, respectively. The initial stochastic velocity perturbation distribution at $t = 0$ (see Fig. 2(a)) is given by

$$v_x(\mathbf{x},0) = Be^{-(y/2hd)^4} \int\int \frac{k_y^2}{k_{y0}^2} e^{-\left[\frac{(k_x-k_{x0})^2}{\Delta k_x^2}+\frac{k_y^2}{k_{y0}^2}\right] 2\pi \mathrm{i}\zeta_p(\mathbf{k})} \zeta_a(\mathbf{k}) e^{\mathrm{i}\mathbf{x}\cdot\mathbf{k}} \mathrm{d}\mathbf{k}$$

whereas initial density $\rho(0)$ and spanwise velocity perturbations $v_y(0)$ can be calculated from the linearised Navier-Stokes equations. Herein, $\zeta_a(\mathbf{k}), \zeta_p(\mathbf{k}) \in [0,1]$ are random numbers depending on $\mathbf{k} = (k_x, k_y)$, h and d denote the box-size and localisation scale in y-direction, respectively, with $\mathbf{x} = (x,y)$. The perturbation spectrum is centred along the k_x-axis at $k_x = k_{x0}$, which half-width Δk_x satisfies the condition $\Delta k_x \ll k_{x0}$ – allowing to easily distinguish between linearly and nonlinearly generated acoustic waves – and the k_y-axis at $k_y = k_{y0}$. The perturbations are inserted in the physical plane, extending from $-h \leq x,y \leq h$ with $h = 10$, at the parameters $A = 4$, $d = 2$, $k_{x0} = 5$, $k_{y0} = 50$, $\Delta k_x = 2$ and amplification factor $B = 10^5$, $B = 10^6$, accordingly. By choosing a the value of $\beta = 10$ we can assure, that the initial perturbations have sufficient time to amplify transiently and, hence, in combination

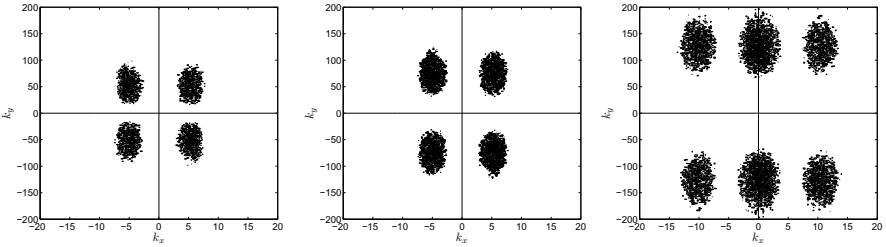

(a) $v_x(t=0)$ **(b)** $\mathscr{S}_1(t=0)$ **(c)** $\mathscr{S}_{\mathrm{nl}}(t=0)$

Fig. 2 Contour plots of (a) stream-wise velocity perturbation distribution v_x and (b) linear $\mathscr{S}_1$ and (c) nonlinear $\mathscr{S}_{\mathrm{nl}}$ source prediction by Lighthill at $t=0$

with $\mathscr{M}=0.8$ strong linear wave emergence is expected (compare Fig. 1*a*) and *b*)). Moreover, the proposed choice of the amplification factor B assures that we operate in the range of validity of RDT. This approximation holds for shear rates, A, and amplitudes, B, of the initial stochastic perturbations the inequality $\mathscr{D}=A/(k_{x0}q)\gtrsim 1$ is met, [10]. Herein, q is the characteristic velocity of the largest energy containing scales, located around k_{x0} in the spectral plane.

The presented set of parameters allows us to perform a comparative analysis *(i)* of linear ($\mathscr{D}\simeq 10^3$) and weakly nonlinear ($\mathscr{D}\simeq 10$) sound generation by stochastic perturbations in an unbounded Couette flow and *(ii)* of the results from DNS and Lighthill's AA. The initial spectra of the linear $\mathscr{S}_1$ and nonlinear $\mathscr{S}_{\mathrm{nl}}$ sources as predicted by [3] for the embedded perturbations are presented in Fig. 2(b)-(c), showing that $\mathscr{S}_1$ is distributed in all quadrants of **k**-space and, consequently, predicting immediate acoustic wave-generation in all regions of k_y/k_x. Although, often reworked (e.g. [7, 8]) the failure is of fundamental nature, consistently leading to a similar distribution of the linear sources in spectral space. This prognosis is in contradiction with the results obtained by Kelvin-mode analysis, while latter is nicely confirmed by our DNS (see Figs. 3-4).

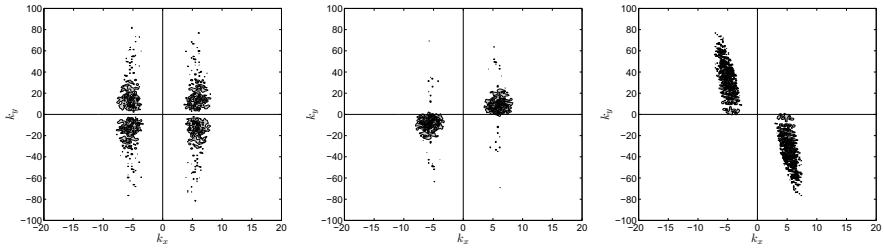

(a) $t=0$, $|\rho|_{\max}=2$ **(b)** $t=2.4$, $|\rho|_{\max}=4$ **(c)** $t=40$, $|\rho|_{\max}=2.5\cdot 10^3$

Fig. 3 Temporal evolution of vortex mode perturbations in **k**-space in terms of ρ. The scaling varies continuously between the range of $\pm|\rho|_{\max}$ with $\mathscr{D}\simeq 10^3$.

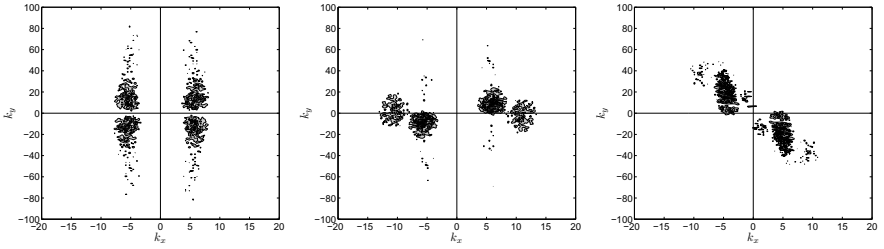

(a) $t = 0$, $|\rho|_{\max} = 2 \cdot 10^2$ **(b)** $t = 2$, $|\rho|_{\max} = 4 \cdot 10^2$ **(c)** $t = 40$, $|\rho|_{\max} = 1.3 \cdot 10^5$

Fig. 4 Identical to Fig. 3 for the case of fortified nonlinear mechanisms, $\mathscr{D} \simeq 10$

The time evolution of density perturbations ρ of initially pure vortex mode SFH in $\mathbf{k}$-space are shown in these figures for $\mathscr{D} \simeq 10^3$ (Fig. 3) and $\mathscr{D} \simeq 10$ (Fig. 4). As one can see, only those vortex SFH coming from regions of $\beta > 0$ amplify and are thence responsible for linear sound generation, while those, initially located in regions of $\beta < 0$, decay and do not bear the potential of triggering wave emergence despite the prediction of Lighthill's AA (see Fig. 2(b)-(c)). These results are in perfect agreement with the results gained by Kelvin-mode analysis, that have been presented in Figs. 1b) and c), respectively. Although the fortified nonlinear mechanisms ($\mathscr{D} \simeq 10$) lead to the appearance of additional structures around $k_x = 2k_{x0}$ and $k_x = 0$ – some mixture of wave and vortex mode SFH – those forthwith decay (see Fig. 4), hence being inferior compared to the linear mechanism of sound generation in plane shear flows.

3 Conclusion

Summarising, the present results show a failure of Lighthill's AA for non-normal flow systems comprising linear sources of aerodynamic sound generation. Taking advantage of the ability of Kelvin-mode analysis to capture strong non-normal effects in shear flow systems, we are able to extract the true sources of linear sound. Moreover, it was shown and proven by DNS that the linear sound dominates over the nonlinear one at moderate and high Mach numbers up to rather large amplitudes of the stochastic perturbations at which RDT is still valid ($\mathscr{D} \gtrsim 1$). The strong character of linear aerodynamic sound generation bears the potential of efficient nonlinear wave-generation, which are able to travel to the (near) far-field, and hereby strongly contradicts the common view that linear sources are negligible in many applications [5]. The basic character of the failure, which is an unambiguously connected phenomena induced by the non-normality of nonuniform flow systems, makes it for many applications unfeasible to remain in the framework of the AA "ideology" in general.

References

1. Chagelishvili, G.D., Tevzadze, A., Bodo, G., Moiseev, S.S.: Linear Mechanism of Wave Emergence from Vortices in Smooth Shear Flows. Phys. Rev. Lett. 79, 3178–3181 (1997)
2. Goldstein, M.E.: On Identifying The True Sources of Aerodynamic Sound. J. Fluid Mech. 526, 337–347 (2005)
3. Lighthill, M.J.: On Sound Generated Aerodynamically – I. General theory. Proc. R. Soc. Lon. Ser.-A 211, 564–587 (1952)
4. Lighthill, M.J.: On Sound Generated Aerodynamically – II. Turbulence as a Source of Sound. Proc. R. Soc. Lon. Ser.-A 222, 1–32 (1954)
5. Lilley, G.M.: On the Noise From Jet. In: AGARD Conference Proceedings No.131 on Noise Mechanisms, Brussels, Belgium (1974)
6. Mignone, A., Bodo, G., Massaglia, S., Matsakos, T., Tesileanu, O., Zanni, C., Ferrari, A.: PLUTO: A Numerical Code for Computational Astrophysics. Astrophys. J. Suppl. Ser. 170, 228–242 (2007)
7. Phillips, M.O.: On the Generation of Sound by Supersonic Turbulent Shear Layers. J. Fluid Mech. 9, 1–28 (1960)
8. Powell, A.: Theory of Vortex Sound. J. Acoust. Soc. Am. 36, 177–195 (1964)
9. Schmid, P.J., Henningson, D.S.: Stability and Transition in Shear Flows. Applied Mathematical Sciences, vol. 142, pp. 337–347 (2001)
10. Simone, A., Coleman, G.N., Cambon, C.: The Effect of Compressibility on Turbulent Shear FLow: A Rapid-Distortion-Theory and Direct-Numerical-Simulation Study. Proc. R. Soc. Lon. Ser.-A 330, 307–338 (1997)

Using an Inflow Turbulence Generator for Leading Edge Noise Predictions

Thomas P. Lloyd, Mathieu Gruber, Stephen R. Turnock, and Victor F. Humphrey

Abstract. Inflow turbulence noise is often the dominant noise mechanism in turbomachines. It has been shown that the sound pressure level is related to the intensity and integral length scale of the turbulence. We utilise a methodology for generating turbulence with prescribed intensity and length scales within a detached eddy simulation. This is applied to a case of homogeneous isotropic turbulence impinging on a non-symmetric aerofoil at high Reynolds number (2.1×10^5). The sound pressure level is estimated using Curle's compact acoustic analogy, and compared to experimental data and analytical estimates. The intensity of the inflow turbulence is higher than expected, though it exhibits approximately homogeneous and isotropic characteristics. While the general shape of the predicted noise spectrum is correct, the magnitude differs from the experimental results by up to 17 *dB*. Reasons for this are elaborated, and improved predictions based on a flat plate are presented.

1 Introduction

Broadband noise of turbomachines has become an important design consideration in numerous applications, including axial fans, marine propulsors and wind turbines. *Leading edge* (or *inflow turbulence*) noise has been shown to dominate when the flow into the rotor is turbulent [1]. In case of a marine propeller, this occurs when the turbulent boundary layer of the hull enters the propulsor. For tidal turbines, the

Thomas P. Lloyd · Stephen R. Turnock · Victor F. Humphrey
Faculty of Engineering and the Environment, University of Southampton,
Southampton, SO17 1BJ, UK
e-mail: {T.P.Lloyd,S.R.Turnock,V.F.Humphrey}@soton.ac.uk

Mathieu Gruber
Department of Acoustic, Snecma Villaroche, Rond point rene Ravaud, REAU,
77550 Moissy-Cramayel, France
e-mail: mathieu.gruber@snecma.fr

A. Talamelli et al. (eds.), *Progress in Turbulence V*,
Springer Proceedings in Physics 149,
DOI: 10.1007/978-3-319-01860-7_34,

inflow turbulence may be due to the oceanic boundary layer or the turbulent wakes from upstream turbines.

Amiet [2] derived an analytical model showing that the far field acoustic pressure is proportional to the integral length scale (L) and square of the turbulence intensity (I^2). As such, the measurement or specification of these quantities is important in the investigation of inflow turbulence noise. Measurements have also focussed on the leading edge noise of fixed aerofoils [3, 4]. The inflow turbulence is grid-generated, thus generating approximately homogeneous, isotropic turbulence.

One computational approach is to generate synthetic inflow turbulence [5, 6]. These studies have illustrated that predicting not only the noise, but also the inflow turbulence characteristics correctly is not easily achievable. In this study, we present validation of a computational methodology for predicting leading edge noise, using experimental data for homogeneous isotropic turbulence [4]. The intention is to apply this to inhomogeneous and anisotropic cases in the future.

2 Simulation Details

The simulation setup is based on measurements made of leading edge noise of a NACA 65(12)10 fixed at zero degrees angle of attack in a planar jet [4]. We use the OpenFOAM simulation environment, and employ the improved delayed detached eddy simulation (IDDES) modelling approach, with $k-\omega$ SST turbulence model. This has been chosen since IDDES allows considerable unsteadiness inside the boundary layer without the need for large eddy simulation (LES) grid quality at the wall.

The simulation parameters are as follows. A freestream velocity of 20 ms^{-1} results in a chord-based Reynolds number of 2.1×10^5, and Mach number of 0.059. The inflow turbulence is generated using the method of Kornev *et. al.* [7], with $I = 2.1\%$ and $L = 0.005m$. A structured multi-block grid is used, with the spanwise domain width equal to $10\%c$. The mean Δy_1^+ is 1.6, whilst $\Delta z^+ = 40$, with a total of $4M$ cells are used. The computational time step is 1×10^{-6} s. Data is sampled at 10 kHz for 4 flow-throughs of the domain.

3 Results

Results are presented in terms of the inflow turbulence characteristics, and aeroacoustic predictions. Figure 1 shows properties of the inflow turbulence. The inflow turbulence is observed to be approximately homogeneous and isotropic; in fact the numerical result shows the turbulence intensity to be more homogeneous than the experiments. The mean velocity profile agrees well with the experiment, while the turbulence intensity is over-predicted.

Figure 2(a) confirms that the target mesh cut-off frequency of ≈ 2 kHz has been achieved, and lies inside the inertial subrange. The integral length scale has been estimated, using a temporal autocorrelation and Taylor's hypothesis, as 0.0054 m, approximately 8% higher than that of the experiment. We note however that the

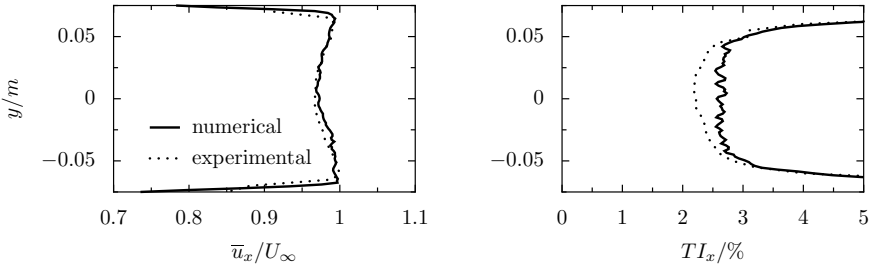

(a) Mean velocity. (b) Turbulence intensity.

Fig. 1 Characteristics of the inflow turbulence: normalised streamiwse profiles across the jet height

integral length scale in the experiment was deduced by curving fitting to a von Kármán spectrum and not via autocorrelation. Hence there may be experimental error associated with the prescribed value.

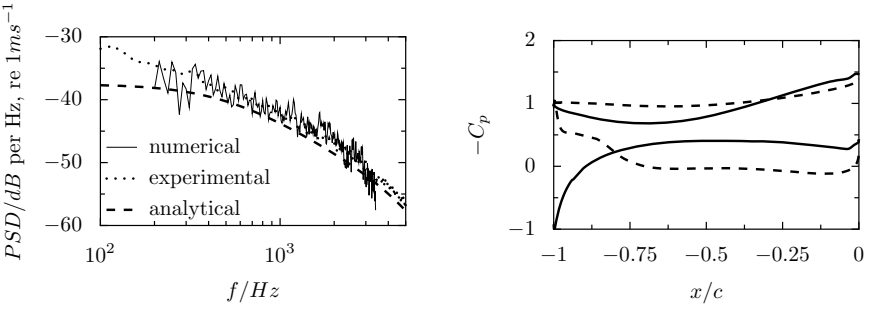

(a) Power spectral density of the jet velocity at $x = -0.2m, y = 0m$, compared to von Kármán model.

(b) Normalised chordwise mean (bottom) and *rms* (top) surface pressure: dash - pressure side; solid - suction side.

Fig. 2 Jet velocity spectrum and aerofoil surface pressure coefficient

The estimated sound pressure level (SPL) is presented in Figure 3. The source strength has been estimated using only the first 10% of the aerofoil chord, as in [6], in an attempt to isolate the leading edge noise source. The unexpectedly large magnitude of the SPL at high frequencies has been attributed to flow separation on the aerofoil pressure side close to the leading edge. This leads to an artificially strong trailing edge noise source, as also observed by Deniau *et. al.* [6]. This can be visualised in Figure 4(b). The main reason for the difference between experimental and numerical results is the omission of turbulence trip strips in the simulations. Hence the development of the turbulent boundary layer is delayed (Figure 4(a)), causing large laminar trailing edge noise. Future simulations will include some form of trip strip to replicate the experiments more closely.

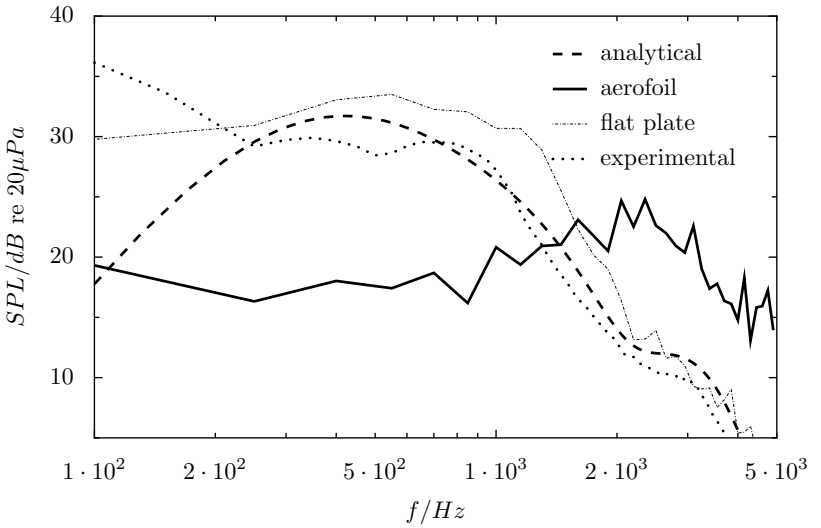

Fig. 3 Sound pressure level at observer $1m$ above trailing edge

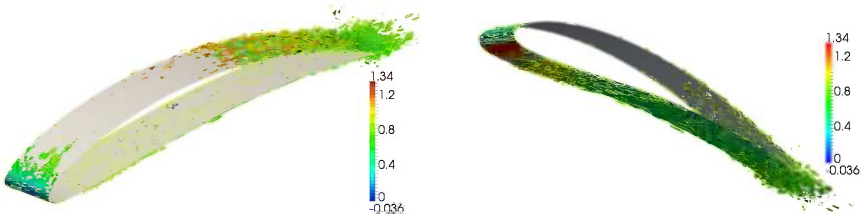

(a) Suction side (b) Pressure side

Fig. 4 Isosurface of $\lambda_2 = 10^7$, coloured by streamwise mean velocity

The inability of Amiet's analytical model to predict the low frequency noise is evident from Figure 3. Aerofoil numerical result shows the correct spectral shape at low frequency, suggesting that this method offers an advantage over the analytical prediction in this frequency range. This has been confirmed by performing the same simulations for a flat plate of equivalent chord and relative thickness 0.02. This result is presented in Figure 3. A correction has been included for the difference in thickness between the aerofoil and flat plate [8], although this effect is dominant at higher frequencies. Significant improvement is observed for the flat plate case, since issues surrounding the turbulent boundary layer are somewhat negated; there is no spurious trailing edge noise source.

4 Conclusions

The method used replicates the mean velocity profile of the planar jet very well, but over-predicts turbulence intensity by up to 30%. For the case presented, the inflow turbulence is divergence free. The method must be modified for future cases concerning anisotropic or inhomogeneous turbulence, so as to maintain the divergence free condition. The magnitude of the SPL error for the aerofoil case is up to $17dB$; improvements are observed for a flat plate, where comparison of the data is allowed by applying a thickness correction. Grid design in combination with IDDES can have a significant impact on the magnitude of the predicted acoustic sources. It is our intention to refine the grid close to the leading edge in order to predict this source with greater accuracy. Including trip strips in the simulation is to be considered, as a way to remove the unexpected trailing edge noise sources presented here.

Acknowledgements. Experimental data was collected by MG as part of the FLOCON project. Gratitude is expressed to Prof. Richard Sandberg for providing the $k-\omega$ *SST* implementation of IDDES, and Evgeny Shchukin for the inflow generator. The authors acknowledge the use of the IRIDIS HPC facility at the University of Southampton. TPL acknowledges the financial support of a University of Southampton Postgraduate Scholarship, dstl and QinetiQ.

References

1. Moreau, S., Roger, M.: Competing broadband noise mechanisms in low-speed axial fans. AIAA Journal 45, 48–57 (2007)
2. Amiet, R.K.: Acoustic radiation from an airfoil in a turbulent stream. J. Sound Vibrat. 300, 407–420 (1975)
3. Devenport, W.J., Staubs, J.K., Glegg, S.A.: Sound radiation from real airfoils in turbulence. J. Sound Vibrat. 329, 3470–3483 (2010)
4. Gruber, M.: Airfoil noise reduction by edge treatments. Ph.D. thesis, Uni. Southampton (2012)
5. Christophe, J., Anthoine, J., Rambaud, P., Schram, C., Moreau, S.: Prediction of incoming turbulent noise using a combined / semi-empirical method and experimental validation. In: West-East High Speed Flow Field Conference, November 19-22 (2007)
6. Deniau, H., Dufour, G., Boussuge, J.-F., Polacsek, C., Moreau, S.: Affordable compressible LES of airfoil-turbulence interaction in a free jet. AIAA Paper No. 2011-2707 (2011)
7. Kornev, N.V., Kröger, H., Turnow, J., Hassel, E.: Synthesis of artificial turbulent fields with prescribed second-order statistics using the random spot method. Proc. App. Math. Mech. 7, 47–48 (2007)
8. Roger, M., Moreau, S.: Extensions and limitations of analytical airfoil broadband noise models. Int. J. Aeroac. 9, 273–306 (2010)

A Mixed RANS/LES Model Applied to the Channel Flow

Antonella Abbà and Massimo Germano

Abstract. In the paper we present some preliminary results related to a new LES approach, the mixed RANS/LES modelling technique that should exploit both the experience accumulated in RANS modelling, particularly near the wall, and the LES capabilities. This new approach was first presented to the APS/DFD Meeting of Baltimore in 2012 [1] and represents a particular application of the general Hybrid RANS/LES filtering technique. Here in particular we have applied this new mixed RANS/LES modelling technique to the channel flow in the particular case of exact RANS databases as regards the RANS model and the no-model and the dynamic anisotropic model as regards the LES aspect. The results are interesting and promising for a simple implementation in different codes with different models.

1 The Mixed RANS/LES Model

The difficult dialogue between RANS, the Reynolds Averaged Navier-Stokes equations based on the statistical average, and LES, the Large Eddy Simulation based on the filtering approach, has been revived recently by practical needs. Hybrid RANS/LES methods for the simulation of turbulent flows have been proposed in order to reduce computational cost in a wide range of complex industrial applications [2]. The related scenario of models is very complex and difficult to classify [3], and many blending techniques are highly empirical. Exact hybrid RANS/LES, HRL, equations have been recently derived [4] by applying to the Navier-Stokes equations a hybrid filtering operator which linearly combines a LES average and the RANS statistical mean with an additive blending factor, generally function of space

Antonella Abbà
Politecnico di Milano, Dip. di Scienze e Tecnologie Aerospaziali
e-mail: antonella.abba@polimi.it

Massimo Germano
Politecnico di Torino, Dip. di Ing. Meccanica e Aerospaziale
e-mail: massimo.germano@polito.it

A. Talamelli et al. (eds.), *Progress in Turbulence V*,
Springer Proceedings in Physics 149,
DOI: 10.1007/978-3-319-01860-7_35,

and time. These hybrid equations are formally exact, they can be implemented with every code and with any combination of RANS and LES models and some preliminary investigations [5, 6] have shown that notwithstanding challenges and difficult issues the additive hybrid method is an interesting and viable approach to simulate turbulent flows. In order to better understand the basic peculiarities of this procedure we have studied in this paper the simple case of a *constant* additive blending factor. In this case we have mixed RANS/LES equations and in the paper we apply this procedure to the simulation of the turbulent flow in a channel. In particular we pay attention to low resolution grids and simple modelling assumptions in order to better understand the peculiarities of the method and the ability to develop and to control the turbulent fluctuations. We stress the fact that a constant blending factor both in the bulk of the channel and near the wall is rather unusual in a hybrid model, but we really think that this preliminary study will be an important step to better clarify the different roles of the new terms introduced in the mixed equations by the new RANS/LES mixing technique. In particular it removes the terms introduced by the non commutativity of a variable RANS/LES filter with the derivatives, and permits to better understand the importance of the terms peculiar to this new approach and physically related to the mixed subgrid RANS/LES stress.

The general governing equations for the incompressible channel flow are

$$\frac{\partial u_k}{\partial x_k} = 0 \quad ; \quad \frac{\partial u_i}{\partial t} + \frac{\partial \left(u_i u_k\right)}{\partial x_k} = -\frac{\partial p}{\partial x_i} + f_i + \frac{1}{Re_\tau}\frac{\partial^2 u_i}{\partial x_k \partial x_k}$$

$$f_1 = \frac{\partial P}{\partial x_1} = \cos(\alpha) \quad ; \quad f_2 = \frac{\partial P}{\partial x_2} = \sin(\alpha) \quad ; \quad f_3 = 0 \tag{1}$$

where as usual the quantities are referred to the friction velocity u_τ and the channel half-width h, α is the rotation angle between the coordinates system and the mean flow [7] and f_i are constant forcing terms related to the mean pressure gradient along the channel. In the present paper we will assume $\alpha = 0$, (the channel is oriented as usual with the mean flow), and we remark that Re_τ is the Reynolds number based on the friction velocity and the channel half-width. These equations are solved for $0 \le x_1 \le 2\pi$, $0 \le x_2 \le \pi$, $-1 \le x_3 \le 1$, the velocity components u_i are zero at the walls and are provided with periodic conditions in the x_1 and x_2 directions.

Let us now apply to these equations a mixed additive RANS/LES average $\mathscr{H}$ such that

$$\mathscr{H} = k\mathscr{F} + (1-k)\mathscr{E} \tag{2}$$

where $\mathscr{E}$ is the statistical RANS operator, $\mathscr{F}$ an explicit or implicit filtering operator and k a constant blending factor. The resulting mixed RANS/LES equations are

$$\frac{\partial v_k}{\partial x_k} = 0 \quad ; \quad \frac{\partial v_i}{\partial t} + \frac{\partial \left(v_i v_k + \tau_{ik}\right)}{\partial x_k} = -\frac{\partial q}{\partial x_i} + f_i + \frac{1}{Re_\tau}\frac{\partial^2 v_i}{\partial x_k \partial x_k} \tag{3}$$

where v_i and q are the mixed components of the velocity and pressure and τ_{ik} the mixed subgrid stress. It results

$$v_i = \langle u_i \rangle_H = k w_i + (1-k)\bar{u}_i \;\; ; \;\; q = \langle p \rangle_H = k\pi + (1-k)\bar{p}_i \tag{4}$$

and

$$\tau_{ij} = \langle u_i u_j \rangle_H - \langle u_i \rangle_H \langle u_j \rangle_H = k\tau_f(u_i,u_j) + (1-k)\tau_e(u_i,u_j) + \frac{1-k}{k}(v_i - \bar{u}_i)(v_j - \bar{u}_j) \tag{5}$$

where w_i and π are the LES components of the velocity and pressure

$$w_i = \langle u_i \rangle_F \quad ; \quad \pi = \langle p \rangle_F \tag{6}$$

$\tau_f(u_i,u_j)$ and $\tau_e(u_i,u_j)$ the stresses associated to the filtering LES operator and to the RANS operator and where the overline indicates the statistical mean value

$$\bar{u}_i = \langle u_i \rangle_E \quad ; \quad \bar{p} = \langle p \rangle_E \tag{7}$$

These equations are numerically integrated in space with a second order centred finite difference scheme and in time with a three steps explicit Runge Kutta scheme, combined with a Projection Method.

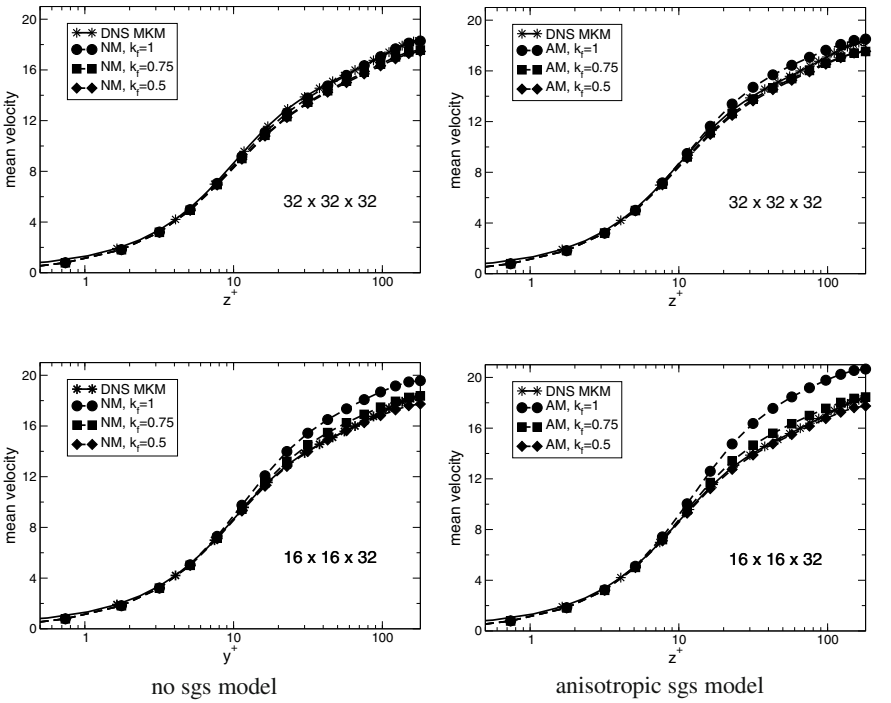

Fig. 1 Mean velocity profiles for different values of the blending factor k_f: results obtained without subgrid model (on the left side) and with the anisotropic subgrid model [8](on the right side) are compared with the DNS results [9]. The upper graphs are obtained with $32 \times 32 \times 32$ grid points, while the bottom ones with the lower resolution $16 \times 16 \times 32$.

2 Numerical Results

We start our exploration with a low Reynolds number, $Re_\tau = 180$, with a classical LES resolution, $32 \times 32 \times 32$, and a lower resolution $16 \times 16 \times 32$. As regards the particular subgrid model chosen to test the hybrid approach we have directed our

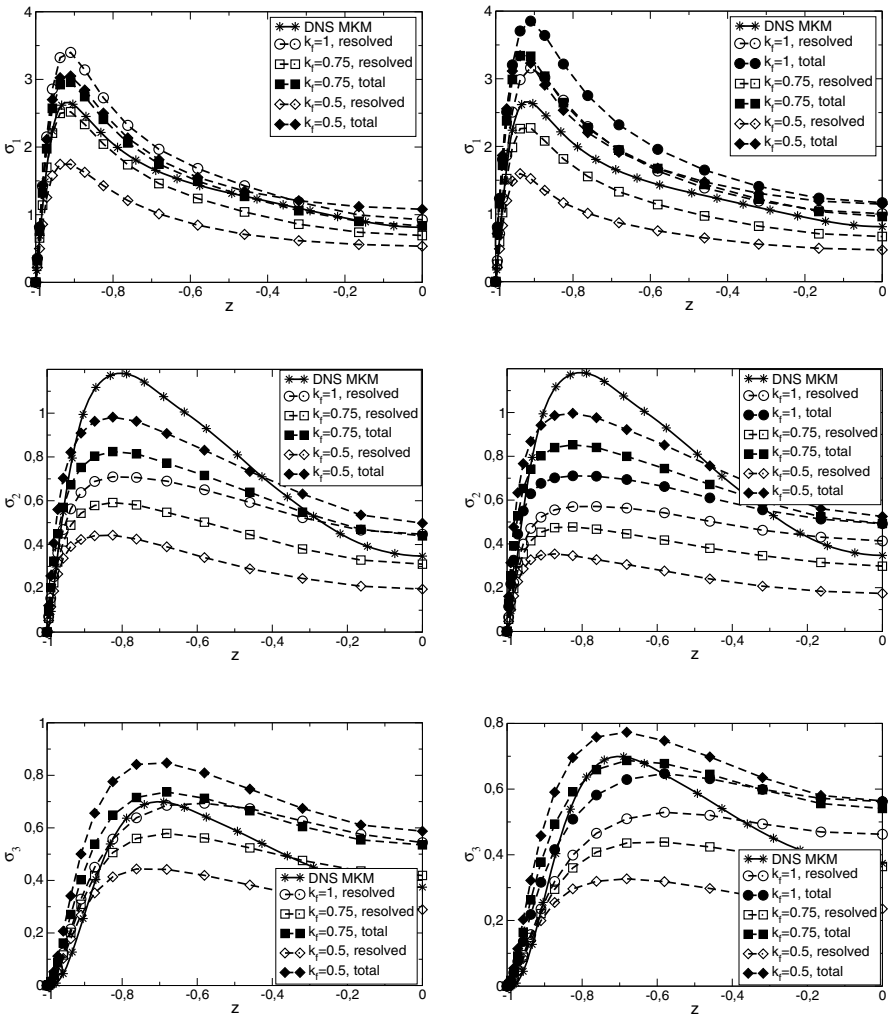

Fig. 2 Profiles of the rms of velocity components for different blending factors: results obtained without subgrid model (on the left side) and with the anisotropic subgrid model [8](on the right side) are compared with the DNS results [9](*continuous line*); *empty symbols* correspond to the resolved fluctuations, while the *filled symbols* represent the total (resolved + modelled) contribution; *circle*: $k_f = 1$; *square*: $k_f = 0.75$; *diamond*: $k_f = 0.5$. The results are obtained with the lower resolution $16 \times 16 \times 32$.

attention to the dynamic anisotropic model [8]. The no-model option has been explored first in order to have an idea of the peculiarities of the code, in particular as regards the dissipation of the numerical scheme. The constant blending factor assumes the value 1, that corresponds to pure LES, no-model (NM) or anisotropic model (AM), and the values 0.75 and 0.5. We examine the mean velocity profiles, and from figure 1 we deduce a considerable improvement of the Mixed RANS/LES procedure compared both to the LES no-model case and the LES anisotropic model, and the advantage is particularly evident at the lower resolution. Obviously due to the very low resolution these results are purely indicative, in particular we remark better results for the no-model case compared with the nisotropic model, but the general trend is positive both for a blending factor of 0.75 and 0.5. In figure 2 the predicted rms are presented for the same values of the blending factor and for the lower resolutions. Also in this case we register a positive trend in the results if compared to the pure LES case that corresponds to a blending factor of one. We remark again that we have deliberately chosen very coarse resolution levels in order to amplify the effect of the mixed RANS/LES approach. Obviously a practical use of the hybrid method proposed should cope with the problem of a varying blending factor near the wall and the related difficulties of the non commutative terms in the filtered equations.

3 Conclusion

Finally we can say that the present results reinforce and confirm the conclusions of previous more dedicated researches : notwithstanding issues and challenges this hybrid approach seems really a simple and viable tool for simulating turbulent flows. Obviously this flexibility has to be explored in more detail by applying the hybrid filtering approach to different codes and test flows, but we think that the test reported in the paper in the simple case of constant blending factors and for low resolution levels gives confidence in the practical application to industrial codes and complex engineering flows.

Acknowledgements. This work was partly supported by MIUR, PRIN 2009 Research Project Kinetic theory for fluid dynamics and microsystems.

References

1. Germano, M., Sanchez-Rocha, M., Menon, S.: Hybrid RANS/LES equations. 64th Annual Meeting of the DFD/APS, Bulletin of the APS 56(18), 77 (2011)
2. Sagaut, P., Deck, S.: Large eddy simulations for aerodynamics: Status and perspectives. Phil. Trans. R. Soc. A 367, 2849–2860 (2009)
3. Fröhlich, J., von Terzi, D.: Hybrid LES/RANS methods for the simulation of turbulent flows. Progress in Aerospace Sciences 44, 349–377 (2008)
4. Germano, M.: Properties of the hybrid RANS/ LES filter. Theoret. Comput. Fluid Dynamics 17, 225–231 (2004)

5. Sanchez-Rocha, M., Menon, S.: The compressible hybrid RANS/LES formulation using an additive operator. J. Comp. Phys. 228, 2037–2062 (2009)
6. Rajamani, B., Kim, J.: A Hybrid-Filter Approach to Turbulence Simulation. Flow Turbulence Combust. 85, 421–441 (2010)
7. Abbà, A., Rolfo, S., Germano, M.: LES of the channel flow in a non aligned system of coordinates. 13th European Turbulence Conference, Journal of Physics: Conference Series 318, 042041 (2011)
8. Abbà, A., Cercignani, C., Valdettaro, L.: Analysis of Subgrid Scale Models. Comp. Math. Appl. 46(4), 521–536 (2003)
9. Moser, R.D., Kim, J., Mansour, N.N.: Direct numerical simulation of turbulent channel flow up to $Re\_\tau = 590$. Phys. Fluid 11(4), 943–945 (1999)

Model Reduction Based on a Numerical Length Scale Analysis

Niklas Winkler and Laszlo Fuchs

Abstract. For the time being, the required computational cost to solve the 3D time-dependent flow prevents the use of such methods for internal flows at high Reynolds number in complex geometries. In this work we present a method based on a numerical length scale analysis to get a rational reduction of the full 3D governing equations for turbulent pipe flows. The length scale analysis quantifies the terms of the governing equations after changing the coordinate system into a curvilinear coordinate system with one coordinate aligned with the flow path. By retaining the most important terms or neglecting the (significantly) smallest terms, different reductions may be attained. The results for a double bent pipe, used to illustrate the approach, show that the most significant component of the viscous terms is the normal component. The convective terms are all important. The normal component is significant in the bends of the pipe due to centrifugal forces, while the spanwise component is most significant after the second bend due to a swirling motion.

1 Introduction

Low-order models, where the dimensionality has simply been reduced to decrease computational cost are today being used for machine design. One-dimensional models are e.g. used for engine manifolds [4], which assumes that the flow is uniform across the flow direction or two-dimensional models, which are used for turbine design [1] where the flow is computed on a stream surface between the blade rows with the assumption that no mass flow is crossing it.

Niklas Winkler
Competence Center for Gas Exchange (CCGEx) and Div. of Internal Combustion Engines, KTH, Stockholm, Sweden
e-mail: winkler@md.kth.se

Laszlo Fuchs
CCGEx and Dept. of Mechanics, KTH, Stockholm, Sweden
e-mail: lf@mech.kth.se

A. Talamelli et al. (eds.), *Progress in Turbulence V*,
Springer Proceedings in Physics 149,
DOI: 10.1007/978-3-319-01860-7_36,

The aim with this study is to show a concept to derive a reduced model based on a numerical length scale analysis of the terms in the governing equations, which has also been performed on the disturbance equations to study the disturbance growth in boundary layers [3]. By retaining the most important terms or neglecting the (significantly) smallest terms, different reductions may be attained. Dropping the smallest term, gives the so called Parabolized Navier-Stokes equations [2] or keeping the largest term, gives the boundary-layer equations, which was adopted by Prandtl in 1904 to the incompressible Navier-Stokes equations to derive the boundary-layer equations with the assumption that the flow in the boundary-layer is thin in the wall normal direction. Hence, the approach enables one to get a reduced model with assessed accuracy.

2 Method

To quantify the terms in the Navier-Stokes equations for a complex geometry, the terms have to be projected onto the flow path. Here we use a curvilinear coordinate system, with the main coordinate aligned with the flow path. The transformation is given by scaling factors h_i, which give a stretching of the field to transform it from the physical to the computational domain, with $i = S$ in the direction of the flow path, i.e. the streamwise, $i = \eta$ in the normal and $i = \xi$ in the spanwise direction,

$$h_S = \left|\frac{\partial \mathbf{r}}{\partial S}\right|, h_\eta = \left|\frac{\partial \mathbf{r}}{\partial \eta}\right|, h_\xi = \left|\frac{\partial \mathbf{r}}{\partial \xi}\right|, \tag{1}$$

where $\mathbf{r} = x\mathbf{e_x} + y\mathbf{e_y} + z\mathbf{e_z}$ is the position vector.

Considering incompressible Newtonian fluids, the Navier-Stokes equations are

$$\nabla \cdot \mathbf{u} = 0 \tag{2}$$

$$\frac{\partial \mathbf{u}}{\partial t} + (\mathbf{u} \cdot \nabla)\,\mathbf{u} = -\frac{1}{\rho}\nabla p + \nu \nabla^2 \mathbf{u}. \tag{3}$$

As a first approach we are mainly interested to compute the flow in the streamwise direction $\mathbf{e_S}$ and to quantify the influence from the other components. The terms can now be rewritten into curvilinear coordinates where the convective term in the streamwise direction becomes,

$$\begin{aligned}((\mathbf{u} \cdot \nabla)\,\mathbf{u}) \cdot \mathbf{e_s} = \tfrac{u_S}{h_S}\tfrac{\partial u_S}{\partial S} + \tfrac{u_\eta}{h_\eta}\tfrac{\partial u_S}{\partial \eta} + \tfrac{u_\xi}{h_\xi}\tfrac{\partial u_S}{\partial \xi} \\ + \tfrac{u_S u_\eta}{h_S h_\eta}\tfrac{\partial h_S}{\partial \eta} + \tfrac{u_S u_\xi}{h_S h_\xi}\tfrac{\partial h_S}{\partial \xi} - \tfrac{u_\eta^2}{h_S h_\eta}\tfrac{\partial h_\eta}{\partial S} - \tfrac{u_\xi^2}{h_S h_\xi}\tfrac{\partial h_\xi}{\partial S},\end{aligned} \tag{4}$$

where u_S, u_η, u_ξ are the velocity components in the streamwise, normal and spanwise direction and can be computed through the scaling factors. The first three terms in the momentum equation denotes convection of u_S in the three directions corresponding to $\mathbf{u} \cdot \nabla u$ in the Cartesian coordinate system. The four remaining terms account for the fact that the coordinate system is curved, which gives a contribution

to the convective terms of the momentum equation in $\mathbf{e_S}$. The fourth and fifth term corresponds to convection of u_η and u_ξ in $\mathbf{e_S}$. The sixth and seventh term correspond to convection of u_η and u_ξ in $\mathbf{e}_\eta$ and $\mathbf{e}_\xi$, which gives a contribution to the momentum equation in $\mathbf{e_S}$.

The viscous terms can be rewritten as,

$$\nu\nabla^2\mathbf{u} = \nu\nabla\cdot\Pi_{ij}, \tag{5}$$

where the terms of the stress tensor Π_{ij} are obtained from computing $\nabla\mathbf{u}$ for the curvilinear coordinates taking into account that the unit vectors are functions of the coordinates as e.g.

$$\Pi_{SS} = \frac{1}{h_S}\frac{\partial u_S}{\partial S} + \frac{u_\eta}{h_S h_\eta}\frac{\partial h_S}{\partial \eta} + \frac{u_\xi}{h_S h_\xi}\frac{\partial h_S}{\partial \xi}, \quad \Pi_{S\eta} = \frac{1}{h_\eta}\frac{\partial u_S}{\partial \eta} - \frac{u_\eta}{h_S h_\eta}\frac{\partial h_\eta}{\partial S}. \tag{6}$$

The viscous term of the momentum equations in the streamwise direction become,

$$\begin{aligned}\nabla\cdot\Pi_{ij}|_s = \tfrac{1}{h_S h_\eta h_\xi}[&\tfrac{\partial}{\partial S}\left(h_\eta h_\xi \Pi_{SS}\right) + \tfrac{\partial}{\partial \eta}\left(h_S h_\xi \Pi_{S\eta}\right) + \tfrac{\partial}{\partial \xi}\left(h_S h_\eta \Pi_{S\xi}\right)\\ &+h_\xi \Pi_{\eta S}\tfrac{\partial h_S}{\partial \eta} + h_\eta \Pi_{\xi S}\tfrac{\partial h_S}{\partial \xi} - h_\xi \Pi_{\eta\eta}\tfrac{\partial h_\eta}{\partial S} - h_\eta \Pi_{\xi\xi}\tfrac{\partial h_\xi}{\partial S}],\end{aligned} \tag{7}$$

where the first three terms correspond to $\nabla^2 u$ in the Cartesian coordinate system. The remaining terms compensate for the fact that the coordinate system is curved in a similar way as for the convective terms, Equation 4.

Quantifying the different convective and viscous terms will show the error a reduction of each term will give. However, even though the viscous terms are most certainly smaller than the convective terms, not all of them can be neglected if one would like to account for viscous effects in the spanwise plane. The pressure terms, i.e. the gradient of the pressure, has to balance the inertia terms and has therefore to be included in the reduced model.

The main limitation of the approach is for flow situations that do not have a dominating flow direction. Under such conditions the analysis would reveal that the reduction is inconsistent.

3 Results

The turbulent flow field, computed with the Large Eddy Simulation (LES) approach, of a double bent pipe, bent in different directions, for $Re = 25000$ is used to illustrate the concept. The magnitude of the viscous terms for each component computed from the Navier-Stokes equations in the streamwise direction with respect to the curvilinear coordinates for the double bent pipe are presented in Figure 1 and for the convective terms as the ratio between the normal and spanwise components compared to the streamwise component in Figure 2, as area-weighted averages across the streamwise direction based on 100 snapshots of the flow field.

The results show that the viscous term in the normal direction is approximately two orders of magnitude larger than the viscous term in the streamwise and

spanwise direction, respectively. This is due to that the normal component is large close to the boundary due to the large velocity gradient. Comparing the convection of the different velocity components shows that they are all in the same order of magnitude. The convective terms are all of great importance. The normal component is significant in the bends of the pipe due to centrifugal forces, while the spanwise component is most significant after the second bend due to a swirling motion.

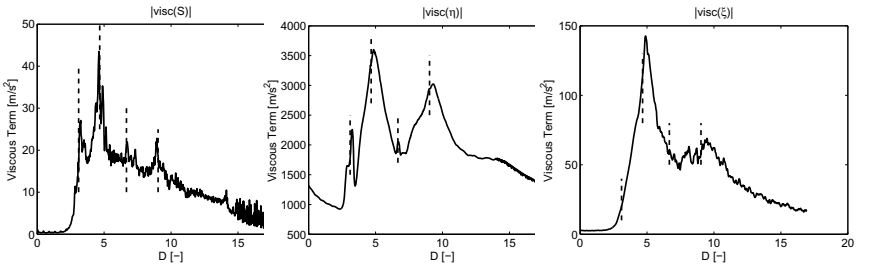

Fig. 1 Magnitude of the viscous terms in curvilinear coordinates, in "S", "η" and "ξ" directions from the momentum equation in $\mathbf{e_S}$, respectively. The dashed vertical lines show the locations of the bends.

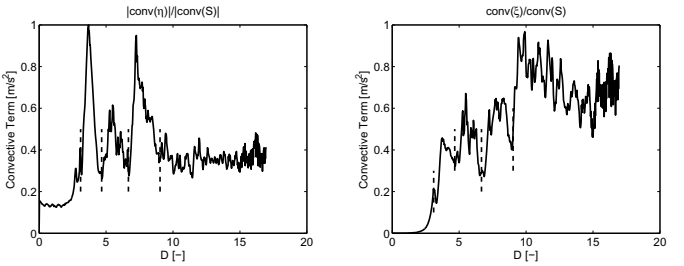

Fig. 2 Ratio of the magnitude of the convection of u_η and u_S, left and u_ξ and u_S, right, in $\mathbf{e_S}$, respectively. The dashed vertical lines show the locations of the bends.

References

1. Aungier, R.H.: Turbine aerodynamics: axial-flow and radial-inflow turbine design and analysis. Amer. Society of Mechanical (2006)
2. Tannehill, J.C., Andersson, D.A., Pletcher, R.H.: Computational fluid mechanics and heat transfer. Taylor & Francis Group (1997)
3. Tempelmann, D., Hanifi, A., Henningson, D.: Spatial optimal growth in three-dimensional boundary layers. J. Fluid Mech. 646, 5–37 (2010)
4. Winterbone, D.E., Pearson, R.J.: Theory of Engine Manifold Design: Wave action methods for IC engines. Prof. Eng. Publishing (2000)

A Quasi-optimal Spectral Method for Turbulent Flows in Non-periodic Geometries

Franco Auteri

Abstract. In this work, a quasi-optimal spectral solver for the incompressible Navier–Stokes equations is proposed which is able to treat nonperiodic geometries by construction. The method is based on a fractional-step time discretization recently proposed by Guermond and Minev. A Chebyshev–Galerkin spatial discretization is adopted to satisfy the LBB condition while maintaining an efficient treatment of the linear and nonlinear, dealiased, terms. A careful construction of the algorithm allows the computational complexity to grow as $CN^3 \log N$ in 3D.

1 Introduction

Fast solvers are necessary for the direct numerical simulation of turbulent flows. This is especially true when the transition process is concerned, since in this case a wide range of different space and time scales has to be resolved.

Two kinds of solvers have been mainly employed for DNS in non-periodic geometries: finite difference solvers [1] and spectral solvers based on the Fourier expansion, the non-periodic direction being treated by *ad hoc* strategies, see for instance [2].

Despite providing a more sound mathematical formulation, spectral solvers based on polynomials have been considered unattractive so far when more than one direction is characterized by non-periodic boundary conditions, since the computational complexity of the solver growed as N^4 in the available solvers, N being the polynomial basis degree. In this work this limitation is addressed, and the computational complexity of the proposed solver scales as $N^3 \log N$.

The construction of the present solver is based on two key elements. First, a 1D Helmholtz solver able to cope with Dirichlet and Neumann boundary conditions while retaining a quasi-optimal computational complexity. The key idea to obtain

Franco Auteri
Politecnico di Milano, Dipartimento di Ingegneria Aerospaziale
e-mail: auteri@aero.polimi.it

A. Talamelli et al. (eds.), *Progress in Turbulence V*,
Springer Proceedings in Physics 149,
DOI: 10.1007/978-3-319-01860-7_37,

such solvers is to convert the Neumann or mixed problem to their Dirichlet counterpart, an operation which takes at most $7N$ operations. Second, a direction splitting fractional step method, recently proposed by Guermond and Minev [3], which allows to reduce both the velocity step and the pressure correction step to the solution of a sequence of one dimensional Helmholtz equations. In this way, a quasi-optimal spectral solver is obtained.

2 Time Discretization

The equations to be solved are the Navier–Stokes equations, supplemented by Dirichlet boundary conditions for velocity. A second order Crank–Nicolson scheme with explicit treatment of the nonlinear term is employed to discretize the problem in time,

$$\begin{cases} \dfrac{\mathbf{u}^{k+1}-\mathbf{u}^k}{\Delta t} - \dfrac{\nu}{2}\nabla^2(\mathbf{u}^{k+1}+\mathbf{u}^k) = \mathbf{f}^{k+1/2} - (\mathbf{u}_\star^{k+1/2}\cdot\nabla)\mathbf{u}_\star^{k+1/2} - \nabla p_\star^{k+1/2} \\ \nabla\cdot\mathbf{u}^{k+1} = 0, \end{cases} \tag{1}$$

where $p_\star^{k+1/2} = p^{k-1/2} + \phi^{k-1/2}$ represents the pressure predictor and $\mathbf{u}_\star^{k+1/2} = (3\mathbf{u}^k - \mathbf{u}^{k-1})/2$ the extrapolated velocity.

The discretized Navier–Stokes equations are split by the fractional-step, pressure-correction algorithm proposed in [3]. Velocity is then obtained by the sequence of 1D equations

$$\begin{aligned} \frac{\mathbf{z}^{k+1}-\mathbf{u}^k}{\Delta t} &= \mathbf{f}^{k+1/2} + \nu\nabla^2\mathbf{u}^k - (\mathbf{u}_\star^{k+1/2}\cdot\nabla)\mathbf{u}_\star^{k+1/2} - \nabla p_\star^{k+1/2} \\ \frac{\mathbf{w}^{k+1}-\mathbf{z}^{k+1}}{\Delta t} - \frac{\nu}{2}\partial_{xx}(\mathbf{w}^{k+1}-\mathbf{u}^k) &= 0, \\ \frac{\mathbf{v}^{k+1}-\mathbf{w}^{k+1}}{\Delta t} - \frac{\nu}{2}\partial_{yy}(\mathbf{v}^{k+1}-\mathbf{u}^k) &= 0, \\ \frac{\mathbf{u}^{k+1}-\mathbf{z}^{k+1}}{\Delta t} - \frac{\nu}{2}\partial_{zz}(\mathbf{u}^{k+1}-\mathbf{u}^k) &= 0. \end{aligned} \tag{2}$$

Each equation requires to solve ordinary differential equations only.

To compute the pressure field first the following cascade of 1D Neumann elliptic problems has to be solved

$$\begin{cases} (1-\partial_{xx})\psi = -\dfrac{1}{\Delta t}\nabla\cdot\mathbf{u}^{k+1}, & \partial_x\psi|_{\xi=\pm1} = 0 \\ (1-\partial_{yy})\varphi = \psi, & \partial_y\varphi|_{\eta=\pm1} = 0 \\ (1-\partial_{zz})\phi^{k+1/2} = \varphi, & \partial_z\phi^{k+1/2}|_{\zeta=\pm1} = 0 \end{cases} \tag{3}$$

to compute the auxiliary variable $\phi^{k+1/2}$, then the pressure is updated by the mass problem:

$$p^{k+1/2} = p^{k-1/2} + \phi^{k+1/2} - \chi \frac{\nu}{2} \nabla \cdot (\mathbf{u}^{k+1} + \mathbf{u}^k). \tag{4}$$

As reported in [3], the algorithm is stable for $0 \leq \chi \leq 1$. The numerical tests reported in [4] show that the choice $\chi = 1$ leads to the most accurate solver.

3 Space Discretization

After time discretization we are led to the solution of a cascade of one-dimensional elliptic problems for velocity and pressure. To treat these problems efficiently, it is convient to expand the unknowns by a Chebyshev polynomial basis, so that FFT can be used for forward and backward transformation. For instance, velocity is expanded as follows:

$$\mathbf{u}(\xi, \eta, \zeta) = \sum_{i=0}^{I} \sum_{j=0}^{J} \sum_{m=0}^{M} \hat{T}_i(\xi) \hat{T}_j(\eta) \hat{T}_m(\zeta) \mathbf{u}_{i,j,m}. \tag{5}$$

A similar expansion is employed for the pressure, but a smaller polynomial degree $\hat{I} = I - 2$, $\hat{J} = J - 2$, $\hat{K} = K - 2$ is employed in each direction to satisfy the LBB condition.

The selected basis functions $\hat{T}_m(\zeta)$ are those proposed by Jie Shen [7] since they lead to better conditioned operators, allow a trivial enforcement of Dirichlet boundary conditions and preserve the quasi-optimal computational complexity of the algorithm. The basis functions are defined as

$$\hat{T}_0(\xi) = 1, \quad \hat{T}_1(\xi) = \xi, \quad \hat{T}_i(\xi) = T_{i-2}(\xi) - T_i(\xi), \quad i \geq 2, \tag{6}$$

where $T_i(\xi)$ represents the i-th degree Chebyshev polynomial.

Neumann boundary conditions for the pressure are converted to Dirichlet boundary condition by a simple and efficient procedure to retain the quasi-optimal computational complexity. A similar procedure can be adopted to treat mixed boundary conditions [4].

4 Results and Discussion

Convergence tests have been performed to assess the spectral accuracy in space and the second order accuracy in time of the method. In table 1, for instance, space convergence results are reported for the test case reported in [3].

Table 1 Space convergence results for velocity, $L^2(\omega)$ norm of the error, test reported in [3]

N	8	10	12	16
Error	9.7×10^{-7}	1.2×10^{-7}	9.9×10^{-9}	2.6×10^{-11}

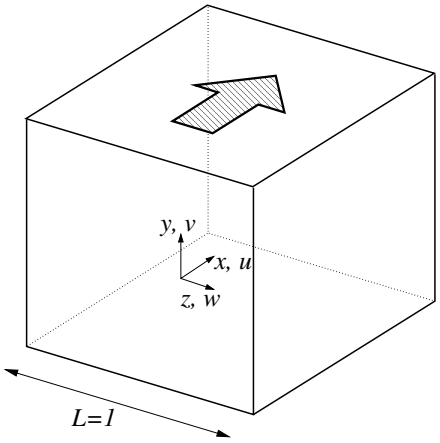

Fig. 1 Sketch of the geometry of the cavity

Then the turbulent flow in a regularized cubic driven cavity has been simulated for a Reynolds number based on the cavity side and on the lid velocity of 12000, see the sketch reported in figure 1.

A dealiased spatial discretization has been adopted with 96^3 degrees of freedom for each velocity component and 94^3 degrees of freedom for the pressure. The time step was $\Delta t = 0.00125$, the time being adimensionalized with respect to the cavity side and lid velocity. In figure 2 the velocity profile of the mean x component of the velocity computed on the symmetry plane for $x = 0$ is reported. The mean has been computed over 150 time units, with a sample every 0.125 time units. In figure 3 the velocity profile of the mean y component of the velocity computed on the

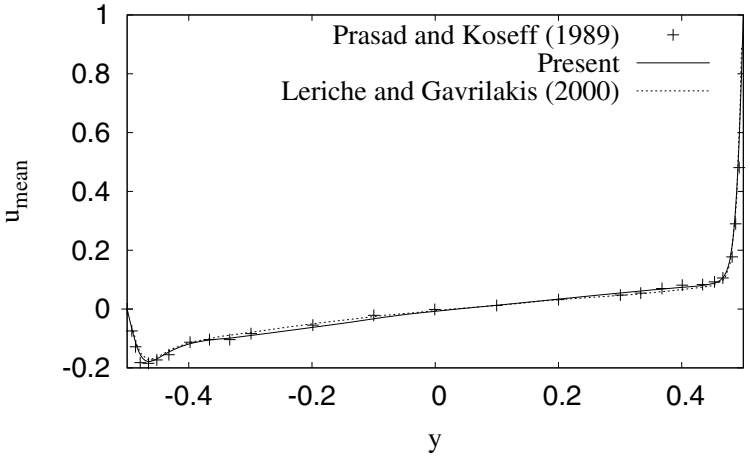

Fig. 2 Mean x component of the velocity field for $x = 0$ and $z = 0$. Comparison with results from Leriche & Gavrilakis and Prasad & Koseff, see [5].

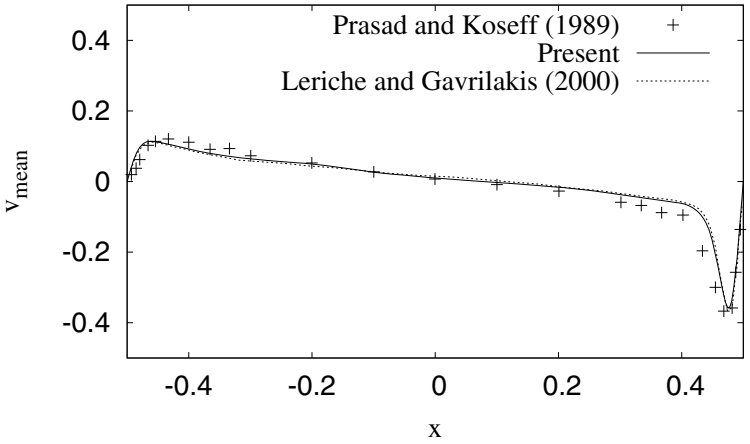

Fig. 3 Mean y component of the velocity field for $x = 0$ and $z = 0$. Comparison with results from Leriche & Gavrilakis and Prasad & Koseff, see [5].

same line and during the same time interval is also reported. As shown in the figure, these results are in very good agreement with analogous results reported by Leriche and Gavrilakis [5] despite the lower resolution and lower mean time. The reference results reported by Leriche and Gavrilakis were computed by a *projection diffusion* method [6], a fractional-step method, and a collocation spatial discretization on the Gauss–Chebyshev points using a nonstaggered grid. In their algorithm, the linear systems arising from the space and time discretization are solved by a diagonalization procedure requiring $O(N^4)$ operations, which is therefore sub-optimal.

Acknowledgements. This work started during a visit to LadHyx (École Polytechnique, Paris). The kind hospitality of P. Schmid and LadHyx personnel is gratefully acknowledged. This work was partially supported by the European Commission - Capacities Area - Research Infrastructures under the HPC-EUROPA2 project (project number: 228398).

References

1. Siemens, M.P., Jimenez, J., Hoyas, S., Mizuno, Y.: J. Comput. Phys. 228
2. Bertolotti, F.P., Herbert, T., Spalart, P.R.: J. Fluid Mech. 242
3. Guermond, J.-L., Minev, P.D.: Comput. Meth. Appl. Mech. Eng. 200
4. Auteri, F.: A quasi-optimal 3D Chebyshev Navier–Stokes solver (2012) (in preparation)
5. Leriche, E., Gavrilakis, S.: Phys. Fluids 12
6. Leriche, E., Labrosse, G.: SIAM J. Scient. Comput. 22
7. Shen, J.: SIAM J. Sci. Comput. 64

On Subgrid-Scale Model Implementation for a Lee-Wave Turbulent Patch in a Stratified Flow above an Obstacle

Sergey N. Yakovenko, T. Glyn Thomas, and Ian P. Castro

Abstract. Results of application of a subgrid-scale (SGS) model to describe turbulence arising in a stably stratified flow above an obstacle are shown for high Schmidt/Prandtl numbers. An appropriate SGS Schmidt/Prandtl number is 0.3 for the case of weakly unstable stratification in the internal wave breaking region. Use of the SGS model allows us to remove numerical noise and obtain adequate spectra, as well as fine details of secondary instabilities during the transition to turbulence.

1 Introduction

Studies (via DNS) of turbulence in breaking internal waves require fine grids when the Schmidt/Prandtl number Sc is high, as for salinity stratification in water. The finest grid used in [1], with well over one billion cells, was estimated to be insufficient to capture all scales of the density field: the scalar dissipation microscale is much smaller than both the mesh size and the Kolmogorov microscale of the velocity field. Runs at Sc = 700 using under-resolved DNS with no SGS models, i.e. implicit large-eddy simulation (ILES), have inadequate resolution of the dissipation range as illustrated by spectra (Fig. 1). The density field generates (numerical) noise which remains not only in the wave-breaking turbulent patch itself, but also in the surrounding fluid (Fig. 2) where one would expect very low noise levels due to strongly stable stratification. It is therefore a challenging to resolve adequately fine details of the flow at $Sc \gg 1$. Similar difficulties may arise at Reynolds numbers observed in environmental flows (higher than the Re = 4000 of [1]).

Sergey N. Yakovenko
Khristianovich Institute of Theoretical and Applied Mechanics, Siberian Branch, Russian Acade-my of Sciences, Novosibirsk 630090, Russia
e-mail: yakovenk@itam.nsc.ru

T. Glyn Thomas · Ian P. Castro
Faculty of Engineering and the Environment, University of Southampton, Highfield, Southampton SO17 1BJ, UK
e-mail: {tgt,i.castro}@soton.ac.uk

A. Talamelli et al. (eds.), *Progress in Turbulence V*,
Springer Proceedings in Physics 149,
DOI: 10.1007/978-3-319-01860-7_38,

2 Results and Discussion

To overcome the problems of insufficient resolution, SGS models of Smagorinsky type for velocity and density are applied at Sc = 700 using the standard value of Smagorinsky constant, $C_s = 0.1$, and the same boundary conditions, sponge layers, and refined uniform grid as in the DNS at Sc = 1 [1]. To check transient behaviour, two preliminary LES runs with the SGS Schmidt/Prandtl number, $\mathrm{Sc}_{sgs} = 1$ and 0.3 (the latter has been used in buoyant jet studies [2]), begin from the data of the under-resolved ILES at Sc = 700 for $t = 35$ (where transient processes are finished, and the quasi-steady period begins). By $t \sim 40$ the spatial spectra curves collapse into one and do not vary for $t > 40$. So $t \sim 42.5$ is chosen for comparison of spanwise spectra, and temporal spectra are obtained for $40 \leq t \leq 50$, to exclude the transient period when the effect of the SGS model insertion has settled down.

The preliminary runs produce a viscous range in the high wave-number spectra which move away from the ILES Sc = 700 results and towards the Sc = 1 results. However, $\mathrm{Sc}_{sgs} = 1$ leads to insufficient improvement in the density spectra and to only partial damping of the numerical density noise. The latter still exists, e.g. in front of the turbulent patch and under it where one may expect laminar-like behaviour due to strongly stable stratification. In contrast, for $\mathrm{Sc}_{sgs} = 0.3$ the larger eddy diffusivity has essentially removed this noise from the density distributions, see Fig. 2, and the spectra almost coincide with those for DNS (with $C_s = 0$) at Sc = 1, see Fig. 1. Thus, spectra obtained inside the patch, and density distributions inside and around it indicate that $C_s = 0.1$ and $\mathrm{Sc}_{sgs} = 0.3$ as in [2] are more suitable to predict adequately the under-resolved density field. This is confirmed by other studies (e.g. [3, 4]) where $\mathrm{Sc}_{sgs} \sim 1$ only for very stable stratification, whereas for less stable, neutral and unstable cases it is, typically, from 0.25 to 0.50. In our case, slightly unstable (mean) density distributions, produced by the overturning and breaking of the internal wave, remain inside the patch [1]. This unstable density-field feature does not disappear completely (when turbulence activity destroys the recirculation structure in the wave-breaking region) and serves in fact to maintain the turbulent patch.

The next LES run was started from $t = 0$, and 'white-noise' perturbation was applied at $t = 7.5$ as in [1] (to break the 2D symmetry assigned by initial conditions). For the fine grid as used in [1] and at Re = 4000, the SGS viscosity is almost everywhere below the molecular one (see e.g. Fig. 3), except at some (separated) points during transition to turbulence. However, for most times and in most areas, the SGS diffusivity at $\mathrm{Sc} \gg 1$ is much larger than the molecular one, so has a considerable effect (Fig. 1, 2). Note, the SGS viscosity and diffusivity distributions look like the vorticity invariant ones because both depend on local velocity gradients and indicate the existence of large structures with the (non-dimensional) spanwise wavelengths $\lambda_y \sim 2$, heavily modulated by the range of smaller turbulent eddies (Fig. 3).

Moreover, we can still capture fine details of the transition, in particular, growth of the mushroom-like convective structures (Fig. 4) arising from the Rayleigh–Taylor instability (RTI). They have small wavelengths ($0.2 \leq \lambda_y \leq 1.0$ at $19 \leq t \leq 26$) which tend to increase with time up to $\lambda_y \sim 2.5$ at $30 \leq t \leq 35$ according to the corresponding spanwise spectra. The RTI development looks very similar to that

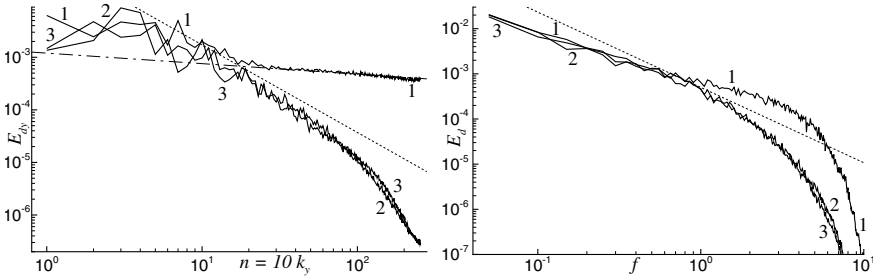

Fig. 1 Spanwise density spectra for $t = 42.5$ averaged at $1.8 \le x \le 2.3$, $2.4 \le z \le 2.9$ (left); temporal ones at $x = 2.19$, $z = 2.97$ averaged along the span (right): 1 – ILES at Sc = 700, 2 – DNS at Sc = 1, 3 – LES at Sc = 700 and $\mathrm{Sc}_{sgs} = 0.3$, straight lines show the '–5/3' and '–1' power laws

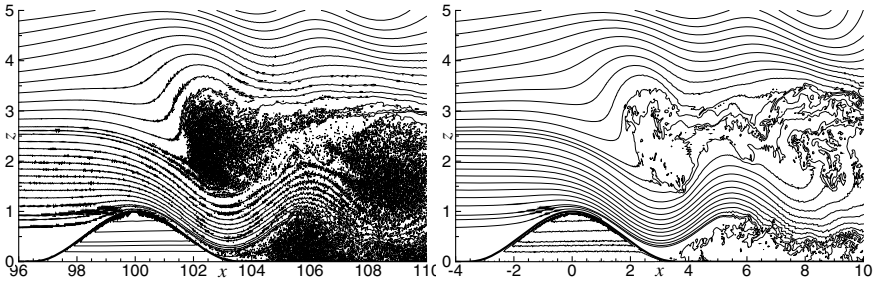

Fig. 2 Density contours for $t = 35$ and $y = 5$ in ILES (left) and LES (right) at Sc = 700

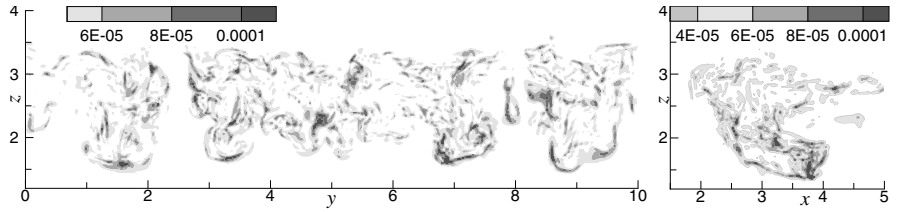

Fig. 3 Subgrid-scale eddy viscosity for $t = 35$ at a position $x = 2.5$ just behind the hill (left) and $y = 5$ in LES at Sc = 700 (the non-dimensional value of the molecular viscosity was $\nu = 1/\mathrm{Re} = 0.00025$)

in experiments on a flow with an unstable, step-like density gradient [5], where the mixed layer depth increased linearly with time, and the number of convective elements decreased with time, through the mechanism of subsequent pairing. The same scenario of structures' growth with their interaction and merging was also proposed for the RTI evolution of the interface between two immiscible fluids [6], but the mixed region width was in that case quadratically dependent on time.

The behaviour of filtered velocity and density fields during the quasi-steady period of the developed turbulent patch, shown by density and vorticity invariant

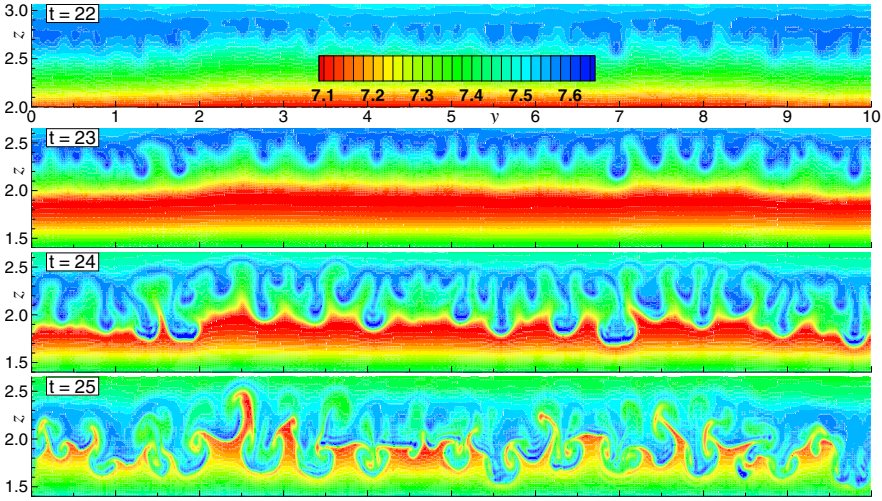

Fig. 4 Density contours for $t = 22$, 23, 24, 25 and $x = 2.5$ in LES at Sc = 700

contours and by fluid particle pathlines, demonstrates that the patch stays practically unchanged at $t \geq 35$ and looks closely like those obtained in the DNS at Sc = 1 in [1]. The statistical moments of the velocity field obtained within the turbulent patch in the LES computations at Re = 4000 and Sc = 700 (by spanwise and time averaging during the quasi-steady period of the developed turbulence) are also expected to be nearly the same as those in [1]. In both cases we get the same energy-containing and inertial spectral ranges, and the unresolved velocity fluctuations are negligible in comparison with the resolved ones due to the small SGS viscosity, so the corresponding contributions to the statistical moments are insignificant.

Acknowledgements. The study has been supported by RFBR (grant 12-01-00050-a) and EPSRC (grants EP/C008561/1, EP/D044073/1).

References

1. Yakovenko, S.N., Thomas, T.G., Castro, I.P.: A turbulent patch arising from a breaking internal wave. J. Fluid Mech. 677, 103–133 (2011)
2. Zhou, X., Luo, K.H., Williams, J.J.R.: Study of density effects in turbulent buoyant jets using large-eddy simulation. Theoret. Comput. Fluid Dynamics 15, 95–120 (2001)
3. Mason, P.J., Brown, A.R.: On subgrid models and filter operations in large eddy simulations. J. Atmos. Sci. 56, 2101–2114 (1999)
4. Porte-Agel, F.: A scale-dependent dynamic model for scalar transport in large-eddy simulations of the atmospheric boundary layer. Boundary-Layer Meteorol. 112, 81–105 (2004)
5. Voropayev, S.I., Afanasyev, Y.D., van Heijst, G.J.F.: Experiments on the evolution of gravitational instability of an overturned, initially stably stratifed fluid. Phys. Fluids A 5, 2461–2466 (1993)
6. Youngs, D.L.: Numerical simulation of turbulent mixing by Rayleigh–Taylor instability. Physica D 12, 32–44 (1984)

Author Index